Optimal design of line-start permanent magnet synchronous motors of high efficiency

Vera Elistratova

N° d'ordre : 278

ECOLE CENTRALE DE LILLE

THESE

Présentée en vue
d'obtenir le grade de

DOCTEUR

En

Spécialité : Génie Electrique

Par

Vera Elistratova

DOCTORAT DELIVRE PAR L'ECOLE CENTRALE DE LILLE

Titre de la thèse :

«CONCEPTION OPTIMALE D'UNE GAMME DE MOTEURS SYNCHRONES A DEMARRAGE DIRECT A HAUTE PERFORMANCE ENERGETIQUE»

Soutenue le 6 Novembre 2015 devant le jury d'examen :

Président	**G. BERTHIAU**	**Professeur**	**IREENA-Univ-Nantes**
Rapporteur	**N. TAKORABET**	**Professeur**	**GREEN – Univ-Lorraine**
Rapporteur	**F. WURTZ**	**Directeur de recherche**	**G2ELAB – Univ- Grenoble**
Examinateur	**G.KREBS**	**Maître de Conférences**	**GeePs-Univ-Paris Sud**
Directeur de thèse	**M. HECQUET**	**Professeur**	**L2EP-EC Lille**
Co-directeur	**P. BROCHET**	**Professeur**	**L2EP-EC Lille**
Co-Encadrant	**D. VIZIREANU**	**Ingénieur de Recherches**	**EDF R&D Clamart**

Thèse préparée dans le Laboratoire d'Électrotechnique et d'Électronique de Puissance (L2EP)
Ecole Doctorale SPI 072 (Lille I, Lille III, Artois, ULCO, UVHC, EC Lille)
PRES Université Lille Nord-de-France

Acknowledgments

My deep gratitude goes first to Professor Pascal BROCHET, the associated professor of Ecole Centrale de Lille and the President at University of Technology of Belfort Montbéliard who hearty welcomed me in his team «Optimization» in 2010. I am very grateful to him for his valuable advices, powerful support, very nice personality and especially for his belief in me. My appreciation also extends to Professor Michel HECQUET, the associate professor of Ecole Centrale de Lille who expertly guided me through my graduate education and who shared with me the excitement of three years of discovery. His personal generosity and unwavering enthusiasm for electrical engineering helped sustain a positive and productive atmosphere in which to do science.

I want to express my sincere acknowledgments to Darius VIZIREANU, an engineer researcher of department THEMIS at EdF R&D, for his valuable remarks, important suggestions and sharing his experience during my work.

I want to thank Mr. Lucas ORSATTO, the student-interns who made valuable contribution to the development of our software.

I would like to thank the regional institution of Nord-PdC MEDEE IV and EDF for the financial support of this research work.

I would like to express my hearted acknowledgments to Mr. Noureddine TAKORABET, Professor of University of Lorraine, and Mr. Frédéric WURTZ, the Professor of University of Grenoble, who do us the honor of participating in the jury as reporters.

I also thank all the administrative, technical and professor staff of Ecole Centrale de Lille and my colleagues for perfect working conditions and support. Among them I would like to thank personally Juliana and Bruno IAMAMURA, Evgeny TARASOV, Xavier CIMETIERE, Mathias FAKAM, Patricio LA DELFA, Heloïse DUTRIEUX, Kongseng BOUNVILAY, Simon THOMY, Christophe RYMEK, Guido CHIAPPORI and Frédéric GILLON for their help and support. Working among such people helped me a lot in my research.

Finally I would like to acknowledge with gratitude the support and love of my family - my husband Dmitry, my parents Igor and Margarita and my grandfather Vasily. They all kept me going, and this dissertation would not have been possible without them.

Contents

Résumé détaillé de la thèse

Contexte:

Pour réduire les émissions de gaz à effet de serre, les principaux axes de développement sont les économies d'énergie et la production d'énergie « verte » produisant une quantité faible de polluants lorsqu'elle est transformée en énergie finale. Pour cette énergie, en France, l'objectif fixé par le Grenelle de l'Environnement pour 2020 est de réaliser 23% d'augmentation de consommation à partir des sources d'énergie renouvelable.

Concernant l'encouragement des économies d'énergies, dans des pays de l'Union Européenne et au niveau national, un système de certificats d'économie d'énergie a été mis en place. Dans ce cadre, dans un premier temps, les producteurs/distributeurs d'énergies doivent mettre en place des actions qui génèrent une diminution de la consommation énergétique de leur clientèle afin de bénéficier de ces certificats d'économie d'énergie.

Les moteurs électriques représentent la charge électrique la plus importante pour l'industrie car les systèmes dans lesquels ils sont utilisés représentent environ 70% de l'électricité consommé par l'industrie. Leur consommation annuelle d'électricité en 2005, dans l'espace communautaire, s'élève à 1067 TWh. Ceci représente un impact environnemental de 427 millions de tonnes d'émission de CO2. Selon les estimations, si aucune mesure spécifique n'est adoptée pour limiter cette consommation, celle-ci devrait atteindre 1252 TWh en 2020. Il existe un potentiel total d'amélioration de l'efficacité énergétique des systèmes à moteurs électriques de l'ordre de 20 à 30%. Les principaux facteurs d'une telle amélioration sont l'utilisation des variateurs de vitesse et l'utilisation de moteurs à bon rendement énergétique.

En 2009, la norme CEI 60034 pour la mesure du rendement des moteurs électriques a été modifiée et actuellement elle propose une norme unifiée internationalement qui classe les moteurs à induction basse tension dans de nouvelles classes de rendement : IE3 Rendement premium, IE2 Haut rendement, IE1 Rendement standard. Il est prévu d'intégrer prochainement dans la norme la classe de rendement IE4 (Super-Premium) avec l'objectif de réduire les pertes d'environ 15% par rapport à classe IE3. La Commission Européenne envisage déjà l'introduction d'une norme IE5 (Ultra-Premium) qui pourrait réduire les pertes de 20 à 25 % par rapport à l'IE4 (Figure 1). À compter du 1er janvier 2015, en conséquence des directives adoptées, seuls les moteurs IE3 sont autorisés pour un fonctionnement en ligne direct, bien que les moteurs IE2 avec variateur de vitesse soient aussi admis pour la plage de puissance de 7,5 - 375kW. Cette nouvelle norme définit aussi des exigences en matière d'éco-conception pour la commercialisation et la mise en service de moteurs. Ainsi, les nouveaux moteurs achetés doivent respecter cette norme d'efficacité.

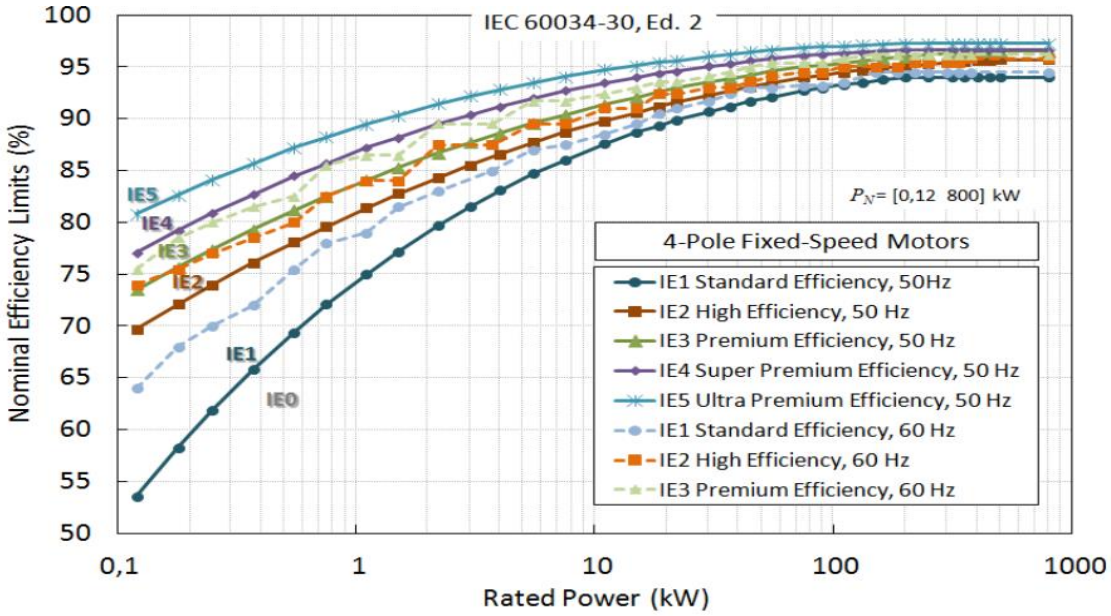

Figure 1 Norme CEI 60034-30-11 (2eme édition)

Pour les moteurs asynchrones (MA) de faibles et de moyennes puissances (<100kW) avec un taux d'utilisation supérieur à 5000h/an, le coût d'un variateur peut s'avérer onéreux et sans gain d'efficacité pour les applications à vitesse constante. En plus, les études récentes montrent que des moteurs synchrones à aimants présentent un meilleur rendement par rapport aux moteurs asynchrones pour un volume donné. En revanche, ces moteurs synchrones présentent le désavantage de ne pas être capable de démarrer directement sur le réseau. Ainsi, l'hybridation apparaît comme une solution pour améliorer le rendement des moteurs pour les applications ne nécessitant pas de la variation de vitesse.

Objectif de la thèse:

L'objectif de l'étude est de dimensionner une gamme de moteurs « hybrides » de type LSPMSM (Line Start Permanent Magnet Synchronous Motors), intégrant les avantages des deux technologies : l'auto-démarrage de la technologie asynchrone et les bonnes performances énergétique en régime permanent de la technologie synchrone à aimants permanents en répondant aux nouveaux enjeux d'efficacité énergétique et en ajoutant à cela les aspects économiques. Ainsi, dans le cadre de cette thèse, on souhaite se doter d'une méthodologie de conception et d'optimisation multi-physique utilisable en avant-projet pour réaliser le dimensionnement de ces machines électriques.

Chapitre 1

Le premier chapitre rappelle la situation actuelle sur le réchauffement climatique en raison de la croissance constante de la production d'énergie.

Dans ce contexte, des plans et des mesures internationales sur le changement climatique sont introduites comme moyen de lutte contre le gaspillage énergétique et l'effet de serre. L'un d'entre eux concerne l'augmentation de l'efficacité énergétique afin de réduire de 20% par rapport aux niveaux prévus la consommation d'énergie dans l'Union européenne (UE) d'ici 2020.

Ensuite, une attention particulière est portée à l'examen des principaux types de moteurs électriques utilisés pour des applications à vitesse constante afin de choisir l'un des plus efficaces. Comme résultat, le moteur synchrone à aimant permanent à démarrage direct (LSPMSM) est choisi pour être le plus intéressant en apportant un bon compromis entre efficacité et les aspects technico-économiques.

Ce chapitre présente également des défis et des enjeux de conception et de réalisation appliqués à différentes topologies du rotor d'un LSPMSM, qui sont les suivants: démagnétisation, couple pulsant (couple de détente et les ondulations de couple), couple de freinage et les spécificités de fabrication. Différentes études bibliographiques ont pu montrer qu'afin de répondre à nos besoins, nous devions utiliser un LSPMSM avec un rotor à aimants enterré (Figure 2).

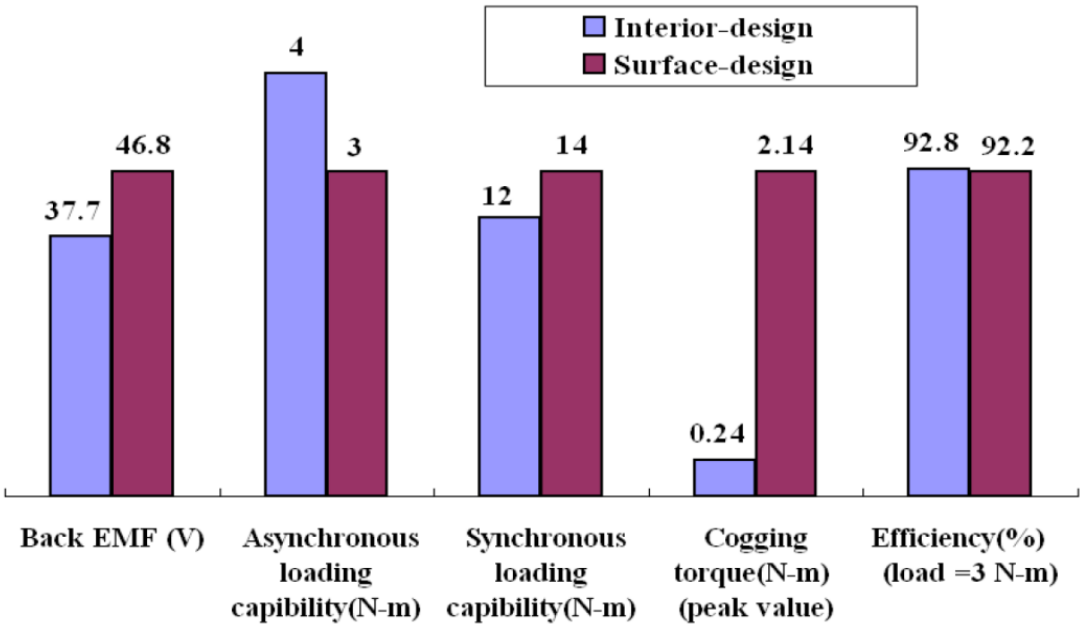

Figure 2 Comparaison des caractéristiques de LSPMSM avec différentes structures de rotor

La sélection de quelques structures rotoriques les plus intéressantes seront étudiées dans cette thèse (Figure 3).

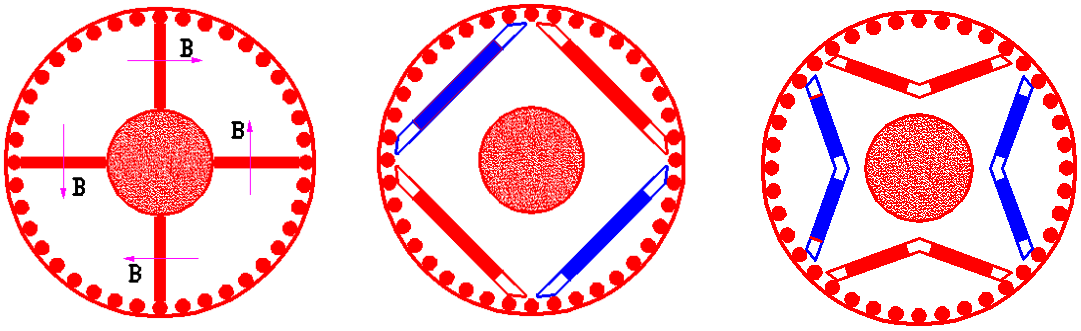

a) b) c)

Figure 3 Trois configurations de rotor à l'étude: (a) Rotor à aimants radiaux, (b) Rotor à aimants en série, (c) Rotor à aimants en V

Finalement, une brève revue des différentes techniques de conception et de modélisation appliquée aux problèmes électro-magnétiques est donnée. Les avantages et inconvénients de chacune d'entre elles sont illustrés.

À l'issue de ce chapitre, la méthode analytique pour la conception de LSPMSM et la méthode numérique éléments finis pour les taches de modélisation spécifique comme l'étude dynamique et de validation des modèles analytiques sont choisies comme les plus adaptées aux objectifs globaux de la thèse.

Chapitre 2

Le deuxième chapitre commence par une discussion sur les méthodes analytiques utilisées pour la conception des machines LSPMSM. Pour des raisons économiques, il a été décidé de conserver le stator et le bobinage du LSPMPM identiques au moteur asynchrone de la même puissance. Cela nous permet de simplifier la conception et de passer d'un moteur asynchrone à un LSPMSM uniquement en changeant le rotor. Ci-dessous la figure présente la démarche de conception des machines LSPMSM choisie.

Selon la Figure 4 la première étape de conception est le dimensionnement des paramètres principaux d'une machine asynchrone de la même puissance. Le dimensionnement de ce genre de moteurs est connu. Notre modèle propose un calcul thermique simplifié à une dizaine de nœuds (Annexe B). L'intérêt de ce modèle de dimensionnement est de nous permettre très rapidement de converger vers une solution de bobinage et de choix de la denture stator – rotor en fonction de la puissance souhaitée.

Ensuite, à partir du diagramme vectoriel dans l'axe d et q du référentiel de Park, nous pouvons déduire les équations d'alimentation de LSPMSM en régime établi pour chacune des trois architectures retenues en prenant en compte leurs spécificités géométriques. Ces équations ont été ensuite utilisées dans une étude paramétrique afin de connaitre l'influence des paramètres principaux (entrefer, géométrie d'aimants) sur les inductances Ld et Lq et la force électromotrice E_0 et, en conséquence, sur les performances des machines étudiées.

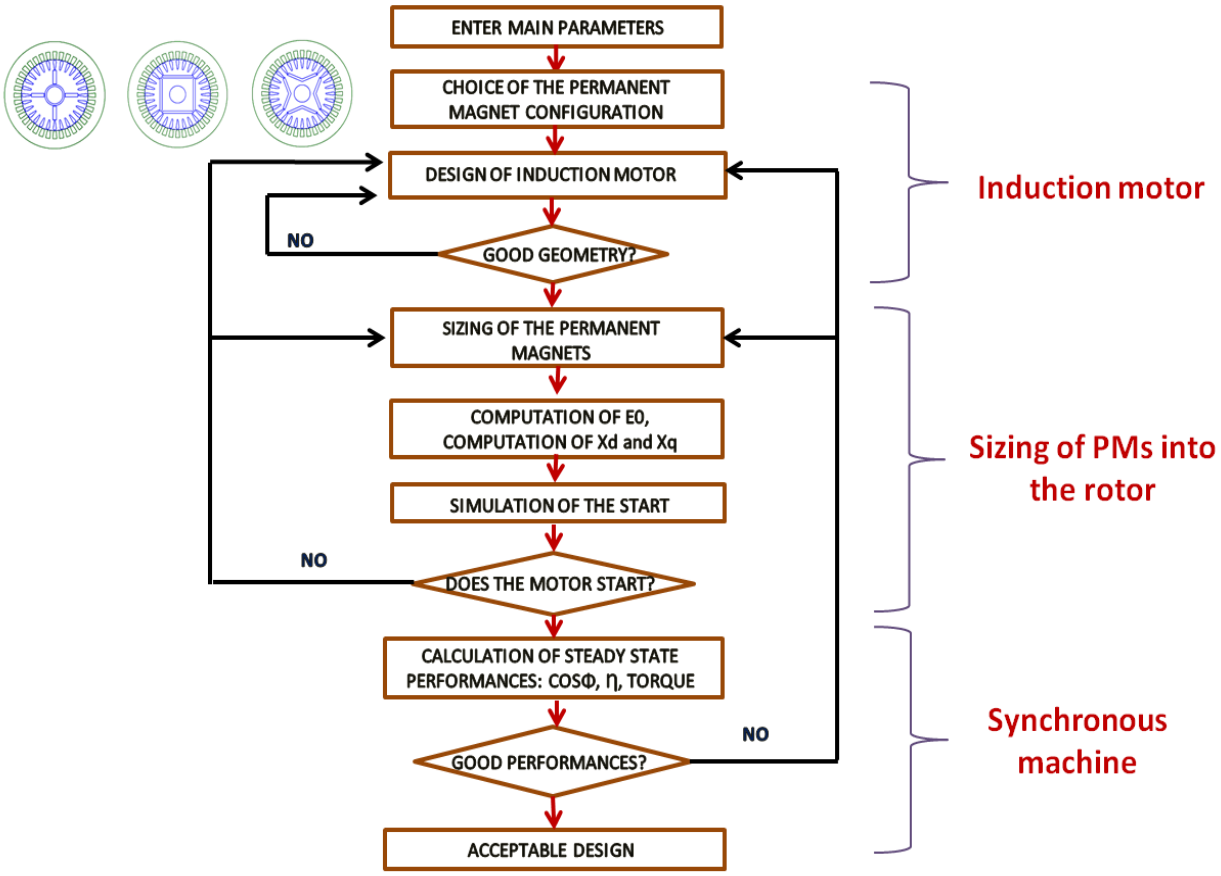

Figure 4 Démarche de conception pour LSPMSM

Se basant sur ces équations analytiques, un outil de dimensionnement a été réalisé. Les architectures retenues ont été évaluées en établissant des feuilles de calculs analytiques qui intègrent le dimensionnement électrique, magnétique, et thermique. Ces calculs ont été ensuite validés par des calculs éléments finis pour deux puissances (7.5kW et 18.5kW) et les solutions les moins prometteuses ont été retirées en appliquant les critères de qualités imposées par le cahier des charges. Les résultats obtenus sont présentés sous forme d'un front de Pareto pour deux types de cages d'écureuil : classique et avec des sections de barres réduites (Figure 5 et Figure 6).

Au vu des résultats d'optimisation et pour des raisons économiques, nous n'avons réalisé que 2 des 3 machines sélectionnées qui ont présenté une meilleure performance énergétique: LSPMSM avec un rotor à aimants en série et le LSPMSM avec un rotor à aimants en V. Dans les deux cas, la cage d'écureuil est réduite ce qui correspond au cas de la Figure 6.

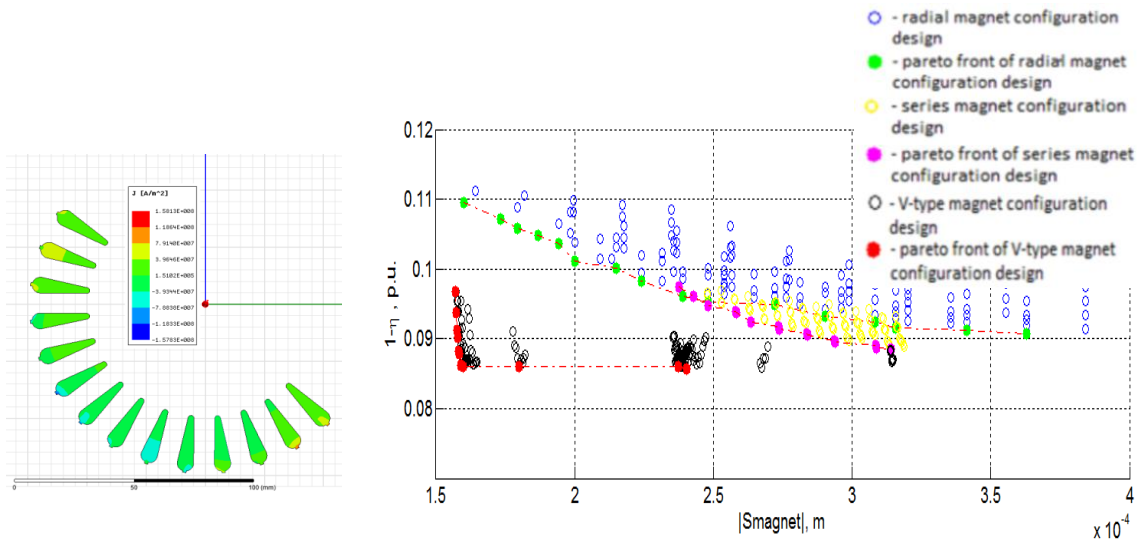

(a) (b)

Figure 5 Résultats d'optimisation : (a)Vue d'une cage classique (sans les aimants) ; (b) Front de Pareto entre l'efficacité par rapport à la surface d'aimants dans le cas de cage classique

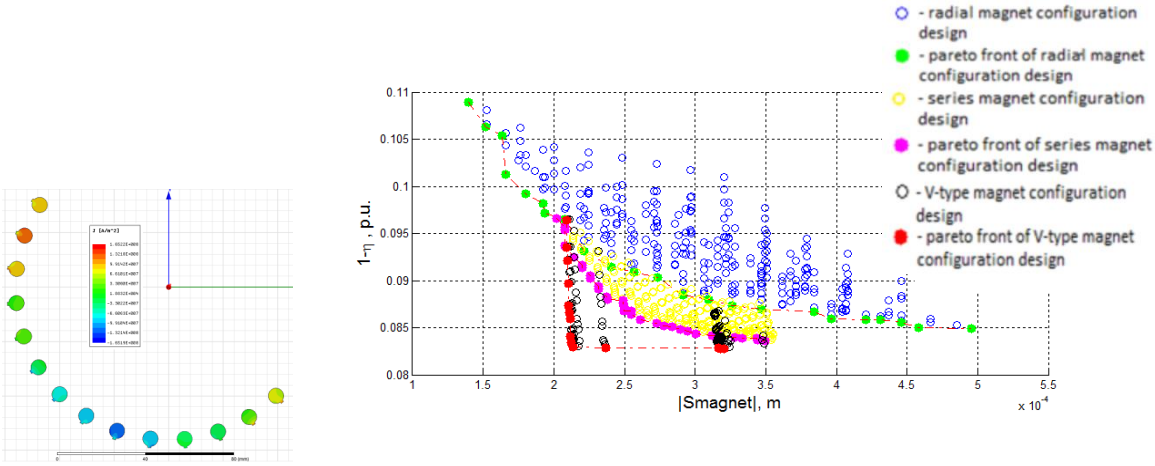

(a) (b)

Figure 6 Résultats d'optimisation : (a)Vue d'une cage non-classique (limitation de la section des barres) ; (b) Front de Pareto entre l'efficacité par rapport à la surface d'aimants

Chapitre 3

L'objectif principal du troisième chapitre est la spécification et la fabrication de deux prototypes de LSPMSM permettant la vérification des modèles analytiques et numériques présentés dans le deuxième chapitre mais aussi validant les performances souhaitées des LSPMSM en comparaison avec une machine asynchrone. La première partie du chapitre concerne le dimensionnement détaillé de deux prototypes de LSPMSM et la prédiction de leurs performances pendant le démarrage et en régime établi.

Pour cela, des études en dynamique par éléments finis (Maxwell – Ansys) en prenant en compte la courbe B(h) du matériau (Annexe D) ont permis de comparer les différentes machines au niveau du temps de démarrage avec une inertie totale imposée. De plus,

une étude sur la démagnétisation des aimants a permis d'observer leur niveau d'induction lors des phases les plus pénalisantes (Figure 7). Suite à ces études, nous avons pu valider les topologies retenues en ajustant le volume d'aimants.

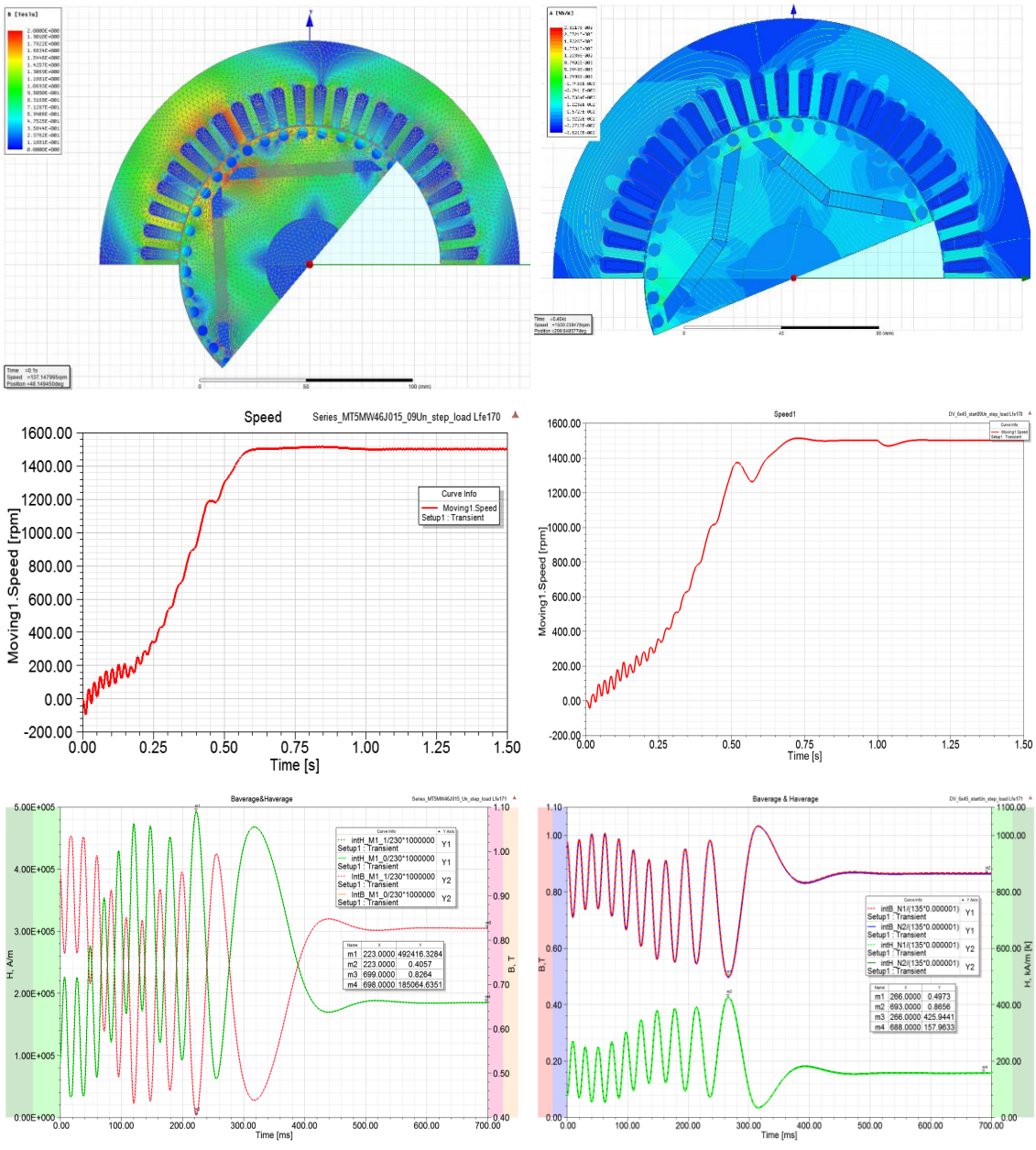

(a) (b)

Figure 7 Valeurs moyennes de l'induction et de la force du champ magnétique des aimants lors du démarrage de LSPMSMs modélisés par éléments finis : (a) LSPMSM avec le rotor à aimants en série de 5x46 mm^2, (b) LSPMSM avec le rotor à aimants en V de 6x45 mm^2

La deuxième partie de ce chapitre concerne la réalisation des prototypes. Les 2 machines reprennent un stator de machine asynchrone du marché d'une puissanse de

7.5KW et les 2 topologies de rotors retenues dans le chapitre précédent sont réalisées : un rotor à aimants en série, un rotor à aimants en 'V'. Afin de valider la partie asynchrone de la méthodologie de conception, un moteur asynchrone commercial de'une même puissance a été aussi acheté.

De nombreux essais ont été réalisés : électrique et thermique afin de valider les performances en comparaison avec une MAS de référence (stator identique pour les 3 réalisations). Ci-dessous les quelques photos des réalisations des 2 prototypes sélectionnés (Figure 8).

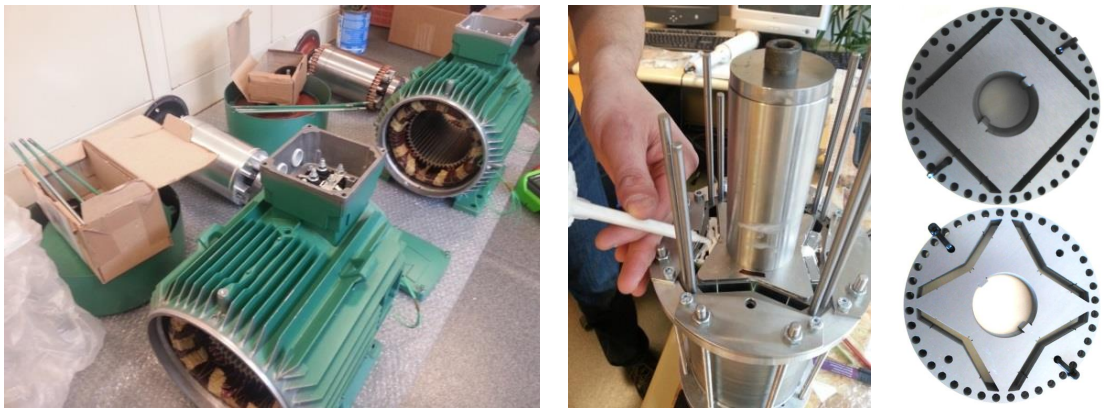

Figure 8 Réalisations des prototypes à partir de machines asynchrones du marché (à gauche), montage des aimants (au centre) et 2 types de tôles rotoriques (à droite)

Les Figure 9 et 10 présentent les performances de deux prototypes réalisées et un moteur asynchrone commercial en régime stationnaire leur comparaison avec les normes CEI.

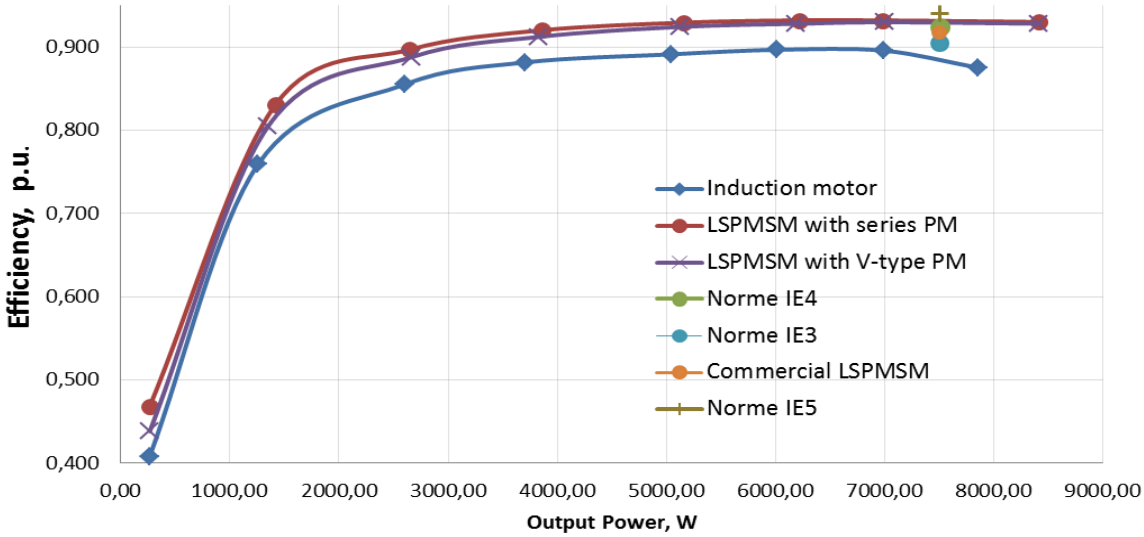

Figure 9 Comparaison de 3 moteurs (ligne bleue – moteurs asynchrone d'origine, ligne rouge – moteurs LSPMSM série, ligne violette – LSPMSM V-type : rendement en fonction de la puissance de sortie.

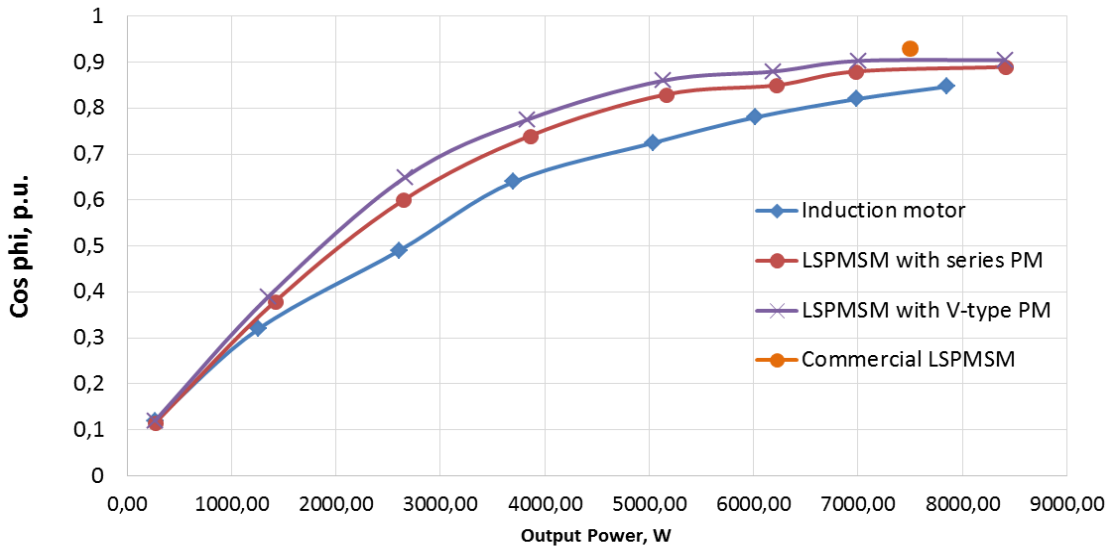

Figure 10 Comparaison de 3 moteurs (ligne bleue – moteur asynchrone d'origine, ligne rouge – moteurs LSPMSM série, ligne violette – LSPMSM V-type : facteur de puissance en fonction de la puissance de sortie

Les différents résultats obtenus montrent un gain de 3,5% à 4% sur le rendement en comparaison avec des machines asynchrones commercialisés de type IE2 ce qui représente un gain important au niveau énergétique. En reprenant la norme CEI 60034-30, le niveau de rendement obtenu par nos prototypes correspond à un IE4 Super Premium Efficiency Class et par conséquent l'investissement dans un LSPMSM peut être déjà justifié d'un point de vue économique.

L'optimisation de la machine a permis aussi un gain de 1,2% en comparaison avec un moteur commercialisé de type LSPMSM de même puissance. Cependant, le facteur de puissance est légèrement plus faible pour nos prototypes. Par contre, nos machines ont un facteur de puissance nettement supérieur à celui de la machine asynchrone.

De plus, des essais d'échauffement des enroulements du moteur LSPM et du moteur asynchrone commercial en fonction de la charge des moteurs ont été réalisés (Figure 11). Au bout de 2,5 heures, l'échauffement du bobinage de LSPMSM est de 40,8 Kelvin (K) et celui de la machine asynchrone est de 69,3K. Les valeurs d'échauffement de 2 moteurs sont inférieures à la valeur critique donnée par le cahier de charge : 80K. Le fait que l'échauffement de LSPM soit considérablement inférieur (de 41%) à l'échauffement du MAS est expliqué par l'absence de pertes rotoriques pendant le régime stationnaire.

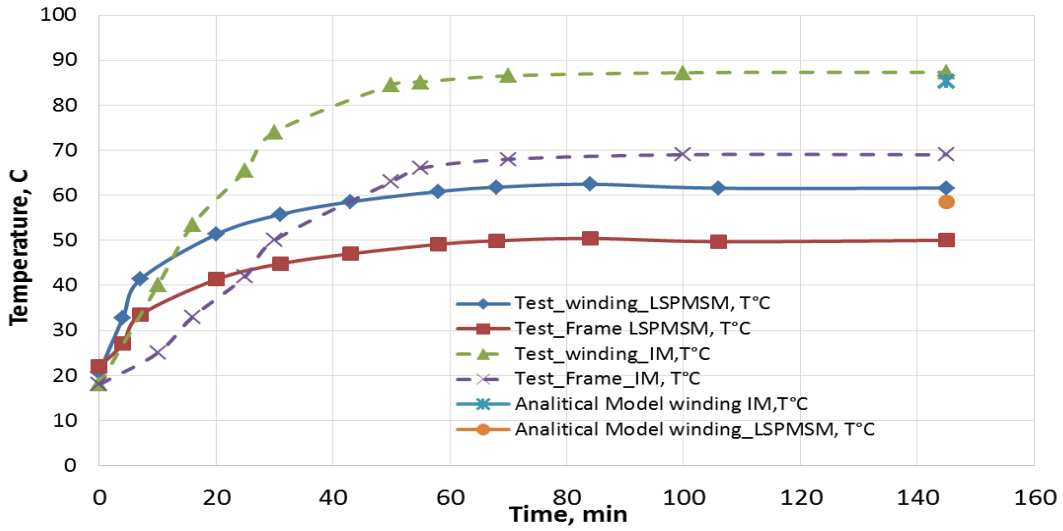

Figure 11 Evolution des températures lors de l'essai d'échauffement sur un moteur asynchrone et un moteur LSPMSM

Conclusion

Ce travail de thèse répond à un besoin d'actualité dans le domaine des machines électriques industrielles et plus particulièrement d'être capable de choisir un moteur électrique le plus adapté aux applications à vitesse constante à haute performance énergétique, mais aussi de se munir d'une méthodologie de conception et d'optimisation multi-domaine utilisable en avant-projet pour réaliser le dimensionnement.

Des études bibliographiques réalisées ont permis un choix sur le LSPMSM. Parmi toutes les configurations existantes de rotor, seulement 3 types de rotors ont été retenus comme les plus appropriés aux objectifs de la thèse. Ensuite, pour chacune des configurations choisies un modèle de conception analytique a été développé.

Il faut aussi rappeler que pour des raisons économiques, nos modèles de conception se basent sur le stator d'une machine asynchrone commerciale.

A l'issu de cette étude, un outil de dimensionnement a été réalisé en utilisant le couplage entre Matlab et Maxwell 2D. Les architectures retenues ont été évaluées en établissant des feuilles de calculs analytiques qui intègrent le dimensionnement électrique, magnétique, et thermique. Ces calculs ont été ensuite validés par des calculs éléments finis pour deux puissances (7.5kW et 18.5kW).

Grâce aux résultats de notre outil deux prototypes de LSPMSM de 7.5kW ont été réalisés et les résultats de leurs essais ont montré un gain important sur le rendement, le facteur de puissance ainsi que sur comportement thermique en comparaison avec des machines asynchrones commercialisés.

Introduction

The growths in energy price along with stricter environment regulations emphasize the importance of life-cycle costs of innovative technologies. At the same time, there is constantly growing regulating pressure on industry enforcing it to optimize electricity consumption and to implement measures for improving energy efficiency.

As electrical motors consume about 70% of electricity in the industry, the European minimum efficiency regulation has a significant impact on their design and application. For instance, in 2011 the second edition of the International Electrotechnical Commission (IEC) 60034-30 has been presented, where a new Ultra-Premium Efficiency (IE5) Class has been introduced. According to these new requirements, starting from1 January 2015, only the motors with a rated output of 7.5 kW to 375 kW corresponding to IE3 class are allowed to be used providing that they are not equipped with a variable speed drive. Besides, from 1 January 2017, all motors with a rated output of 0.75 kW to 375 kW shall not be less efficient than the IE3 efficiency level or shall meet the IE2 efficiency level and be equipped with a variable-speed drive (VSD). Thus, the tightening regulation implies that the newly purchased electrical motors must meet the new more stringent standards of efficiency.

Previous studies proved that permanent magnet motors can offer higher efficiency than standard induction motors used in the modern industry. Therefore, even the applications that were exclusively limited to induction motors can now benefit from the advantages of permanent magnet motors. In regard to constant-speed applications with direct mains operation, the induction motors still have some cost advantage, although new developments in line-start permanent magnet synchronous motors (LSPMSM) make the last ones a cost-effective alternative during their life-cycle.

The objective of the study is to determine a line-start permanent magnet synchronous motor design general strategy for incorporating the advantages of both technologies: self-start asynchronous technology and good energy performance of synchronous permanent magnet technology. The elaborated strategy will be a bases for the developing a multi-physical generic model (and a software) fast enough to be combined with an optimization procedure. The model must be able to define the most efficient rotor structure for the imposed LSPMSM rotor configuration. The validity of the model has to be verified by virtual modelling and real prototyping.

The work consists of several chapters:

Chapter 1 presents the introduction and motivation of the thesis. It begins with a brief overview presenting actual situation with regard to global warming as a result of energy production growth. After that, some international outlooks and measures on climate change are introduced. The comparison of the new standard and the old one is provided in the dedicated part of the chapter.

Further, particular attention is drawn to the examination of the main types of electric motors used for constant-speed applications. The line-start permanent magnet

synchronous motor is selected to be the most promising in terms of technico-economic assessment.

The chapter also presents design challenges and peculiarities in regard to different LSPMSM rotor topologies. A procedure for selection of the three of the most promising LSPMSM rotor structures which will be studied in the thesis.

The last part of the chapter gives general information about modelling techniques used for the calculation of electrical machine characteristics. A brief examination of numerical, analytical and combined methods helps to define the most-corresponding one for the thesis objectives.

The second chapter begins with a discussion about analytical methods used for LSPMSM design presentation of the transient d-q equivalent circuit for LSPMSM. Along with that Chapter 2 is focused on the formalization of a LSPMSM design strategy. It integrates technical features of both motor technologies: self-start asynchronous mode and steady-state performance of synchronous permanent magnet motor and takes into account geometry peculiarities for each of the three selected LSPMSM rotor structures. Based on this strategy the implementation of the dedicated design software is introduced. The developed software will be tested and validated by commercial finite element software Ansoft/Maxwell.

As soon as a general definition of the optimization problem is stated and discussed, the optimization technique may be chosen. With the use of the developed software and integrated in it optimization technique the three selected configurations of LSPMSM rotor topologies are to be analyzed for all variants of design vector. The combinations of design variables belonging to the feasible domain and defined by optimization constraints have to be presented in the form of Pareto frontier in order to choose several the most efficient LSPMSM rotor structures for their farther prototyping.

The main goal of Chapter 3 is sizing and realization of two prototypes based on two of the three selected LSPM rotor configurations defined in the first chapter. The Chapter 3 also presents the experimental validation of the numerical models whose implementation was introduced in Chapter 2. The built prototypes were tested in starting operation, steady state and both no-load and full load operations. The experimental tests have to justify the implementation of the LSPMSM instead of the conventional IM and to show the gap in efficiency and power factor for these two.

In conclusion of Chapter 3 the thermal behavior of the realized prototypes is also discussed and compared with the thermal behavior of commercial IM.

Finally, the general conclusion is presented with perspective future use, development and application of provided models and software. The main contributions of the thesis are also included in the general conclusion.

The present study is carrying out in the Laboratoire d'Electrotechnique et d'Electronique de Puissance de Lille (L2EP) and financed by EDF R&D and MEDEE IV.

Context of the thesis

1.1. Introduction

The first chapter begins with a brief overview presenting actual situation with regard to global warming as a result of energy production growth. After that, some international plans and measures on climate change are introduced. One of them, increasing of energy efficiency to save 20% of the European Union (EU) energy consumption by 2020, is, then, discussed in particular. In order to reach this objective, the European Union adopted a new international standard for electric motors efficiency IEC 60034-30. The comparison of the new standard and the old one will be provided in the following part of the chapter.

Then, special attention is paid to the examination of the main types of electric motors used for constant-speed applications in order to choose the most efficient one. In the issue, the line-start permanent magnet synchronous motor is selected to be the most interesting in terms of technico-economic assessment.

The chapter also presents design challenges and specific design issues applied to different LSPMSM rotor topologies. This discussion allows selection of several of the most interesting LSPMSM rotor structures which will be studied along the thesis.

Finally, a brief overview of various design and modeling techniques applied to electro-magnetic problems is made. The advantages and drawbacks of each of them are illustrated. Based on this discussion, the most adapted method meeting the global goal of the thesis consisting in developing of a multi-physical generic model fast enough to be integrated into an optimization procedure will be chosen.

1.2. Environmental constraints and energy development

1.2.1. Global warming and its consequences

Global warming also known as climate change is the observed century-scale rise in the average temperature of the oceans and the atmosphere which reflects an increase in the amount of heat at Earth's surface. Since the early 20th century, the global air and sea surface temperature has increased about 0.8 °C [ACC 2011], with about two-thirds of the increase occurring since 1980 (Fig.1. 1).

There are the following indicators of global warming:

- Loss of mass of polar ice sheets in the Antarctic and Greenland;
- Melting of ice floes;
- A reduction in the surface area and thickness of glaciers;
- Increase in average ocean levels;
- Increase in the frequency of heat waves;

- Disruptions to the water cycle, which may lead to very heavy rainfall (flooding) or prolonged droughts;
- Changes in ecological systems (flowering dates, harvest times, migrations of animal species).

Climate change has effects on human systems that are difficult to quantify: it has both obvious and not-so-obvious consequences:

- Influence of heat waves on particularly vulnerable populations (older people, newborns or persons with respiratory problems, particularly asthma);
- Poor air quality affects vulnerable people suffering from cardio-respiratory problems.
- Besides, changes in pollen production are one of the reasons why allergies are on the rise in most countries;
- Migrations of insects carrying epidemics (malaria, calenture) can lead to the extension of the areas at risk of these epidemics;
- Climate changes also affect farm production and fishing resources, which can be cause of undernutrition and shortage of drinking water and bad harvests.
- Finally, extreme weather-related events (tsunamis, floods) can give rise to epidemics such as cholera.

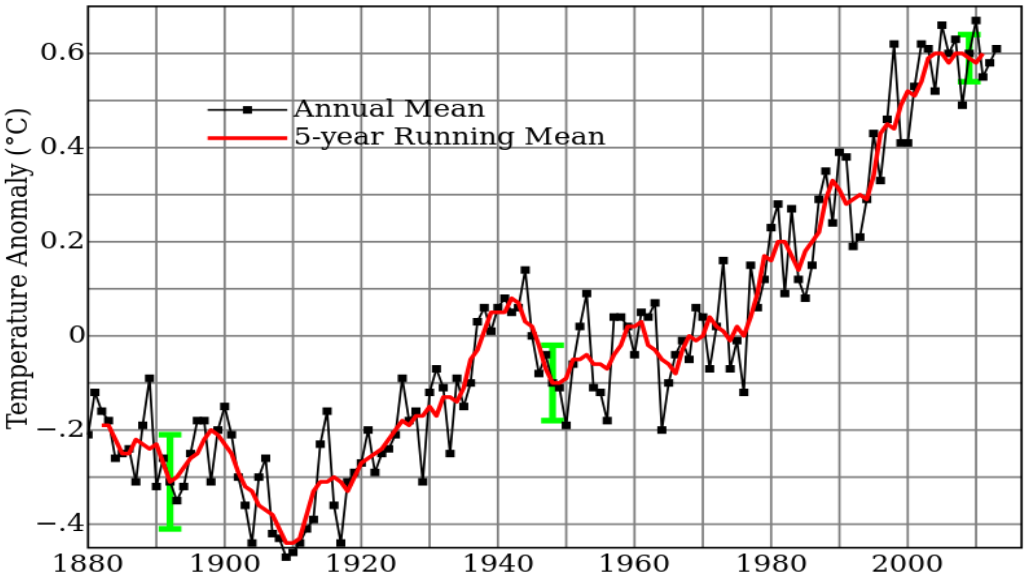

Fig.1. 1 Global mean land-ocean temperature change from 1880–2013 (the green bars show uncertainty estimates) [HANSEN_10]

1.2.2. Part played by greenhouse gases in climate regulation

There are many factors, both natural and human, that can cause changes in Earth's energy balance and provoke climate change, including changes in atmospheric

composition (e.g., increased concentrations of greenhouse gases), cycles of solar activity, volcanic eruptions, and variations in Earth's orbit around the Sun.

Emission of greenhouse gases (especially CO_2) has a significant role in climate regulation. By trapping a part of the infrared rays, they allow the Earth to have an average temperature of 15 °C instead of -18 °C. However, since the nineteenth century, humankind has greatly increased the amount of greenhouse gases in the atmosphere.

While the growth of the global warming has acquired a steady tendency the other factors causing climate change haven't changed their perennial cyclic nature (Fig.1. 2). Thus the constant increase in concentrations of greenhouse gases is responsible for the broken Earth's energy balance and as follows in the global temperature rise.

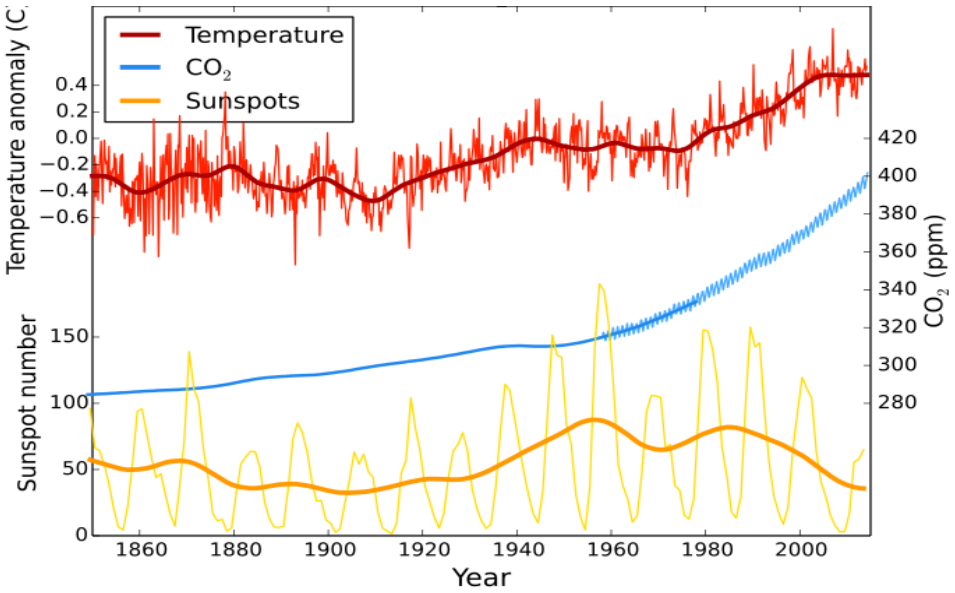

Fig.1. 2 Variation of temperature anomalies, solar activity and CO2 concentration during the last two centuries [WIKI 15]

1.2.3. Global energy development

For the past years global energy development and hence the extraction of fossil fuels have a steadily increasing trend. A large amount of this energy has been converted to electricity Fig.1. 3 [KWES 14].

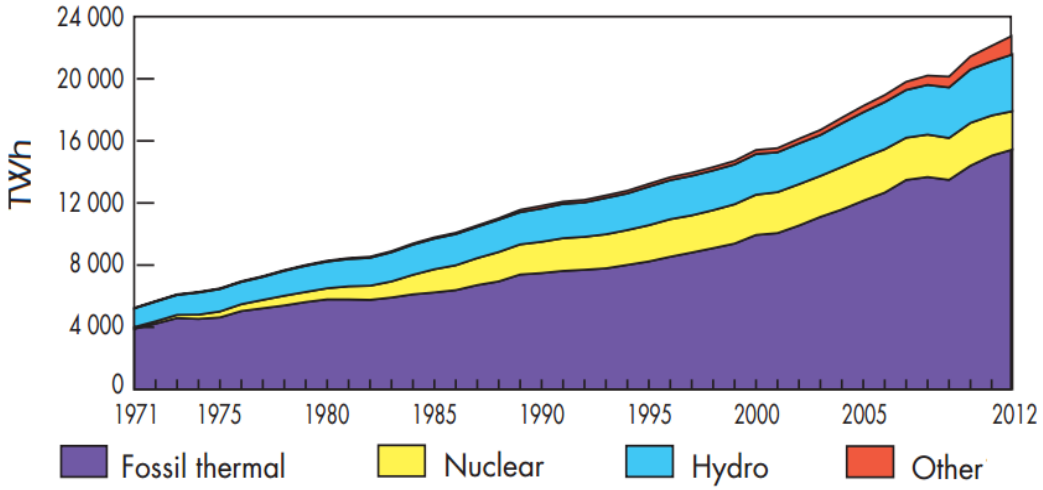

Fig.1. 3 World electricity generation from 1971 to 2012 by different types of fuel [KWES_14]

According to Global Energy Statistical Yearbook [GESY_2014] worldwide net electrical energy generation in 2013 was already 23.133 TWh (Fig.1. 4).

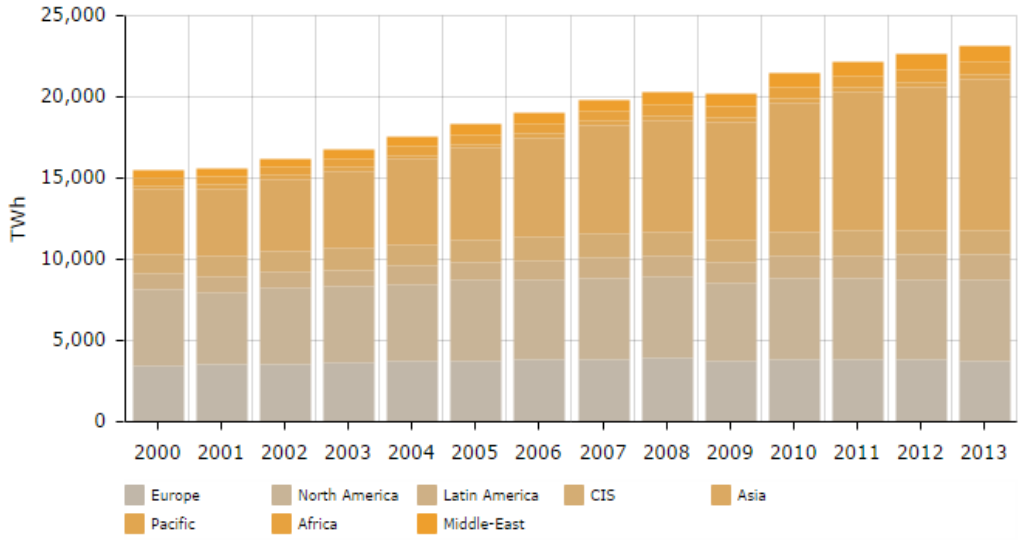

Fig.1. 4 Worldwide electricity production [GESY_2014]

Assuming an efficiency of 33.5% for net electricity generation, it was estimated that around 40% of total world energy production is converted to electrical energy. At the same time the share of fossil fuels in electricity generation in 2012 was estimated at 67.9% (Fig.1. 5a).

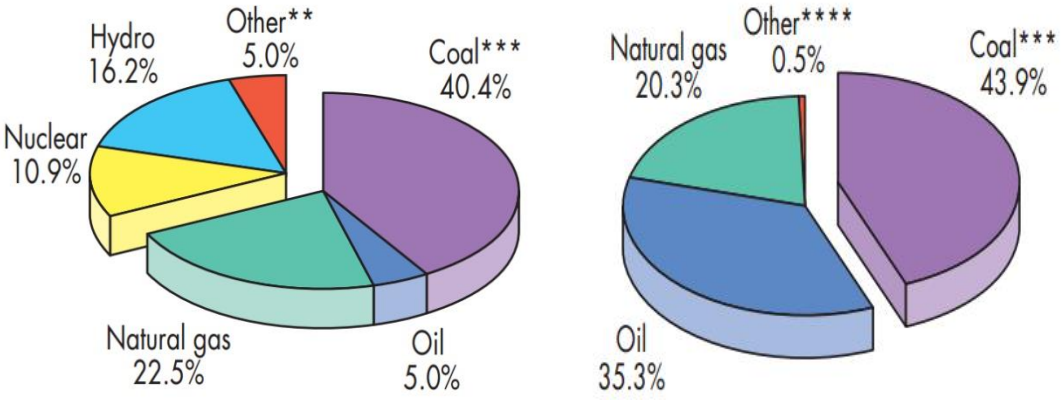

a) b)

Fig.1. 5 Share of different fuels: (a) in worldwide electricity generation in 2012, (b) in worldwide CO2 emission [KWES_14]

According to estimates presented in Key world energy statistics [KWES_14], the main portion of greenhouse gases is produced by fossil fuels (see Fig.1. 5b). Therefore the electricity generation plays an undeniable role in the worldwide air pollution and global warming.

1.3. New efficiency standards for AC motors as measures against climate change

1.3.1. European Union plan on climate change

In order to resist climate change, a large number of agreements and treaties have been recently ratified by the international community. One of the last ones is the Copenhagen Accord [FCCC/CP/2009/L.7], which endorses the continuation of the Kyoto Protocol. According to this document, global emissions (mainly CO2) have to be reduced as to hold the increase in global temperature below 2 degrees Celsius. The plan consisted in four proposals:

- To reduce emissions of greenhouse gases by 20% by 2020 taking 1990 emissions as the reference
- To increase energy efficiency to save 20% of EU energy consumption by 2020
- To reach 20% of renewable energy in the total energy consumption in the EU by 2020
- To reach 10% of biofuels in the total consumption of vehicles by 2020.

1.3.2. Shares of world electricity consumption by different sectors

In paragraph 1.2.3 it has been shown that a large amount of primary energy resources is converted to electric energy. According to Key World Energy Statistics [KWES_14] in 2012 electricity is used primarily by industry (42.3%), households and the commercial sector (56.1%), while transport (1.6%) is a rather small share.

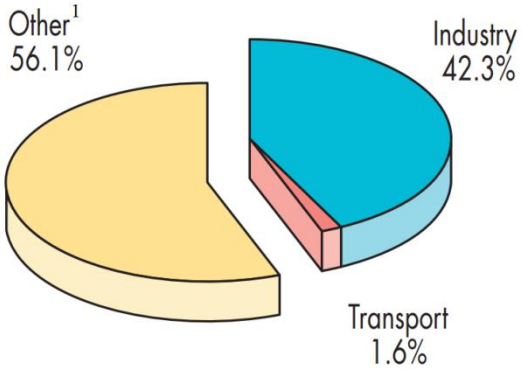

Fig.1. 6 Shares of world electricity consumption in 2012[KWES_14][1]

Electric motors is one of the main sources of electricity consumption at households the same as in industry: it has about 50% in overall global electricity demand (Fig.1. 7) and this expense is up to 70% in the industrial processes in Europe [EEPOEMDS_11], [MESURES803]. As so, they are responsible for a huge share of emission of CO_2. Therefore, optimization of electric motor efficiency is crucial for energy saving and emission reduction.

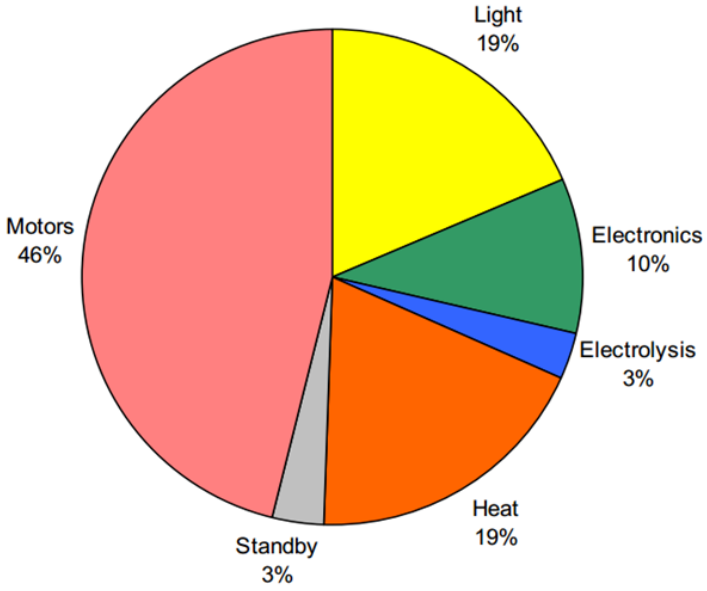

Fig.1. 7 Estimated share of global electricity demand by end-use in 2006 [EEPOEMDS_11]

Under different estimates there is a total potential of improving the energy efficiency of electric motors in the range of 20-30%. The main factors in such improvements are the use of variable speed drives and the use of energy efficient motors.

[1] [1] Includes agriculture, commercial and public services, residential, and non-specified other

1.3.3. New standard on efficiency classes for low voltage AC motors

In order to promote efforts for the use of energy-optimized motors also in Europe, the European Commission and the CEMEP (European Committee of Manufacturers of Electric Machines and Power Electronics) issued a voluntary accord of motor manufacturers on efficiency classification with three efficiency classes [SIEMENS 09]:

- EFF1 for motors of high efficiency classes
- EFF2 for motors of standard efficiency classes
- EFF3 for motors of low efficiency classes

In 2008 the European Union has adopted a new international standard for electric motors efficiency IEC 60034-30, also called "ECODESIGN" [IEC600034-30 08]. The standard is applied to two- to six-pole motors from 0.75 to 375 kW at voltage up to 1000V. This helps to align energy efficiency standards to the countries of the European Union and to set targets to generate eco-design term energy savings.

The first edition of IEC 60034 defines new efficiency classes for motors and harmonizes the currently different requirements for induction motor efficiency levels around the world. It puts an end to the difficulties encountered by manufacturers producing motors for the global market. Motor users benefit through the availability of transparency and facility to understand information. The new standard defines three IE (International Efficiency) efficiency classes for single-speed, three phase cage induction motors. The standard also introduced IE4 (Super Premium Efficiency), a future level above IE3 which intended to be informative, since no sufficient market and technological information were available to allow IE4 standardization and more experience with such products was required. Comparison made between the new IEC efficiency classification and the old CEMEP efficiency classification (Table.1. 1) shows that the new standards have become stricter and more rigid.

Table.1. 1 IEC efficiency classification vs. CEMEP efficiency classification

Premium efficiency	IE3	Premium
High efficiency	IE2	Comparable to EFF1
Standard efficiency	IE2	Comparable to EFF2

The second edition of the IEC 60034-30 Standard is now being prepared, and the IE4 classification will be included in it. Moreover, a new Ultra-Premium Efficiency (IE5) Class has been introduced, which, although not yet defined in detail, is envisaged for potential products [IEC600034-30 11]. The levels of the IE5 Efficiency Class are envisaged to be introduced by the next edition of the IEC 60034-30 standard. The goal is to reduce the losses of IE5 by 20% relative to IE4. In Fig.1. 8 the IE5 limits assuming 20% loss reduction in the IE4 limits are also drawn [BRUNNER 11].

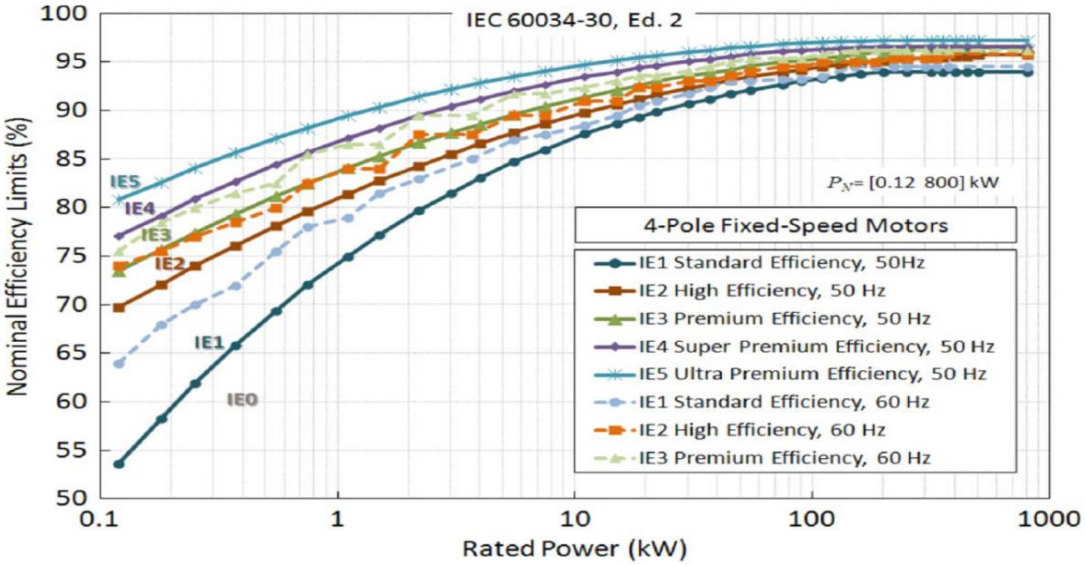

Fig.1. 8 Nominal efficiency class limits proposed in the second edition of IEC 60034-30, for four-pole motors (0.12–800-kW power range) [ALMEIDA_14]

1.4. Choice of an efficient electric motor for constant-speed application

1.4.1. Run-down on motor market

Due to new efficiency performance standards being enacted by governments around the world, share of high-efficiency motors on motor market is changing. If in 2012 high-efficiency motors accounted for only 28 percents of global motor shipments, by 2017 it is expected that the higher-efficiency motor shipments will grow up to 62 percent of motor market [CASSELL_14].

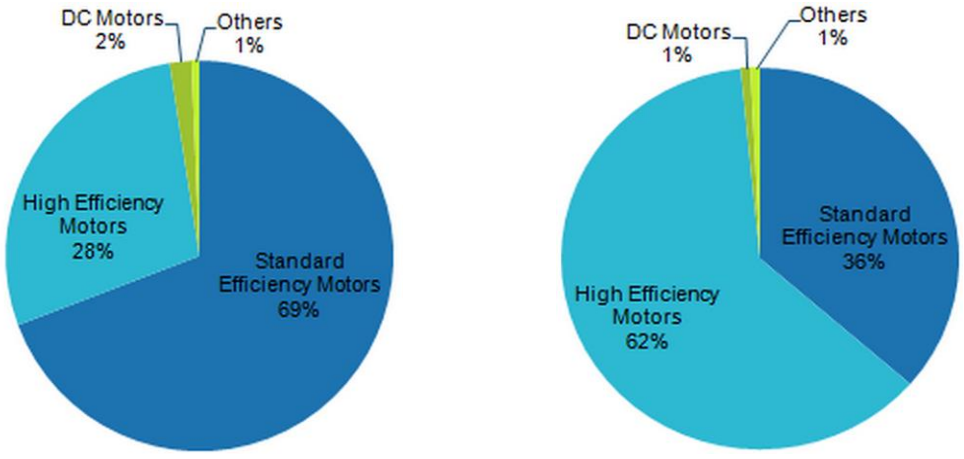

(a) (b)

Fig.1. 9 Share of different types of electric motors; (a) market share in 2012, (b) market share in 2017 [CASSELL_14]

1.4.2. Induction motors

Until recently induction motors (IM) thanks to their low manufacturing cost and robust structure have been widely applied for industrial constant-speed applications such as pumps, fans, pumps, air conditioners and etc.

However, as the speed of the IM rotor is below synchronous speed there is always an induced current in the IM rotor cage bars. This current generates large copper losses which are about 30% of total loss (Fig.1. 10) and lowers the motor efficiency [FUCHSLOCH_08].

In addition the IM, because of its inductive behavior, suffers from a low power factor, resulting in a reduction in the capacity of electricity distribution systems by increasing current flow and voltage drops. This may lead to the losses rise in transmission lines and overheating and premature failure of motors and other inductive equipment. A low power factor can also cause extra losses in stator windings of induction motors. Besides, a number of public utilities charge customers by an additional fee if their power factor is less than a minimum.

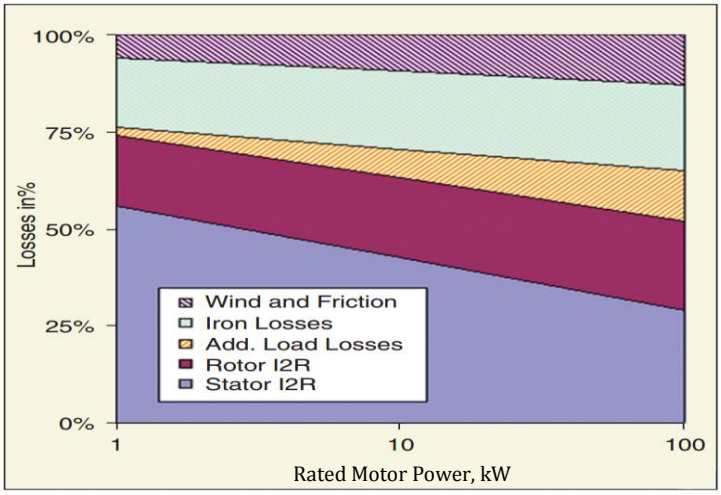

Fig.1. 10 Typical loss distribution in induction motor [FUCHSLOCH_08]

As public worries about the environment and global warming is ever increasing, the prospect of improving the energy efficiency of running the vast number of IMs currently installed in industry is of particular interest. High efficiency motors are needed in a large variety of industrial products in order to save electrical energy [HASSANPOUR_09]. With legislation tightening the demand for higher efficiency motors is set to increase while IMs start getting technical and economic limits of performance improvement.

1.4.3. Permanent magnet synchronous motor

In the last quarter-century great progress in the development of new high-energy rare-earth permanent magnets (PMs) such as Samarium-Cobalt (SmCo) and Neodymium-Iron-Boron (NdFeB) has been achieved. Fast advancement in PM materials increased a number of studies about designing of a cost-effective energy-saving permanent magnet synchronous motor (PMSM) [GIERAS_10].

For many applications PMSMs can replace IMs as the first ones can be designed smaller in size but more efficient as compared to an asynchronous machine [FENG_12], [DING_11], [KURIHARA_04]. However a PMSM cannot be started up without using a variable frequency drive (VFD). The presence of VFD reduces the overall efficiency and significantly raises the price of the system. A simplified block diagram of open loop voltage-to-frequency control of PMSM is shown in Fig.1. 11.

Therefore, the hybridization (behaving like an IM during the start and a PMSM during the steady state) looks like a good solution to improve motor performance for applications that do not require the speed variation.

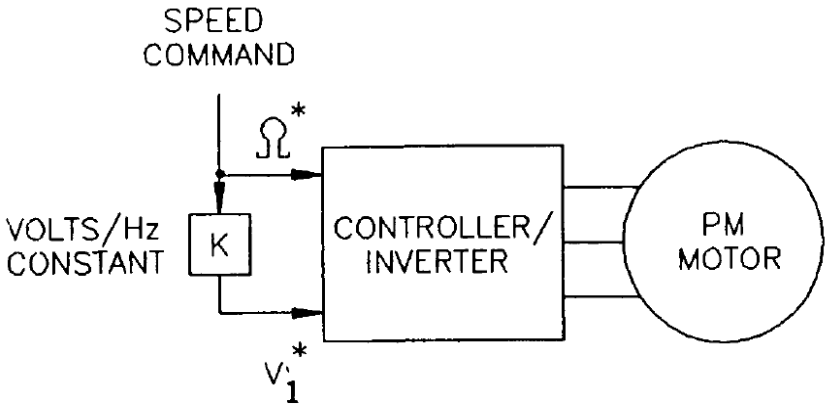

Fig.1. 11 Simplified block diagram of open loop voltage-to-frequency control of PMSM [GIERAS_10]

1.4.4. Line-start permanent magnet synchronous motor

A permanent magnet synchronous motor that produces asynchronous starting torque is usually called the line-start permanent magnet synchronous motor (LSPMSM). The LSPMSM can be immediately used instead of conventional induction motors for applications where the motor is to be connected directly to the mains, for example, in pumps, air conditioners and fans. Once started, it runs at synchronous speed without "slip" losses reducing by that means the total loss by 30% and consequently improving an efficiency of 85% to 89% for the same output power [HENDERSHOT_10].

In [HASSANPOUR_09] the variations of efficiency, power factor and the product of these two characteristics of a three-phase LSPMSM is compared with those of an induction motor of the same power rating (see Fig.1. 12). It is demonstrated that a well-designed LSPMSM shows the absolute superiority over the standard IM.

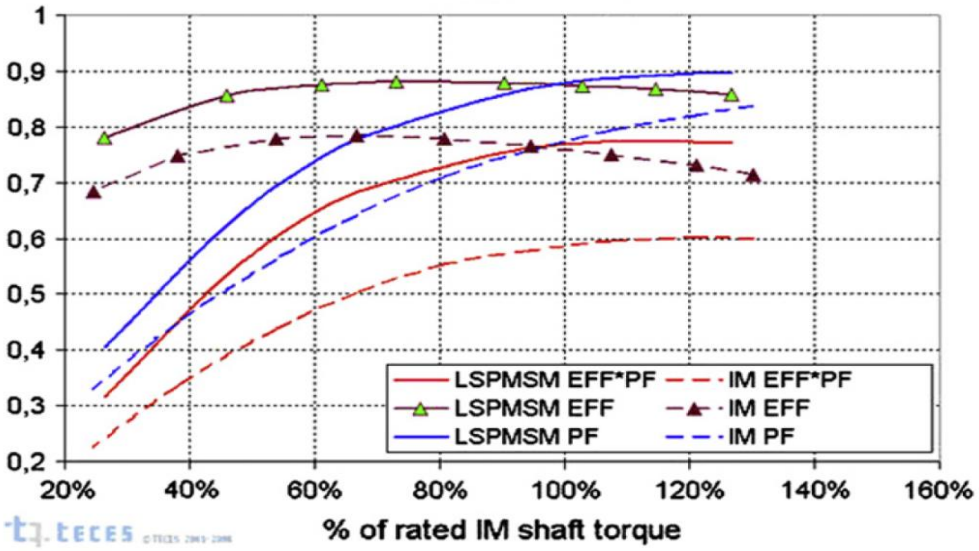

Fig.1. 12 Efficiency (EFF) and power factor (PF) characteristics of the tree-phase line-start permanent magnet synchronous motor and induction motor [HASSANPOUR_09]

The LSPMSM has however rotor losses during the start sequence, and thus if the application includes a multitude of large inertia starts in short time intervals, this must be taken into account when determining the required motor size. In such applications the benefits of a LSPMSM are less prominent.

1.4.5. Comparative technico-economic study of LSPMSM and IM

In [ALMEIDA_14] three 7.5-kW four pole commercial motors with different efficiency classes from one of the largest motor manufacturers are now considered, whose main characteristics are presented in Table.1. 2.

The prices with a typical 40% discount for the IE2 IM, IE3 IM and IE4 LSPMSM models are 328€, 378€, and 764€, respectively. The efficiency gain of the IE4 LSPMSM with regard to the IE2 and IE3 IMs is respectively 4.0% and 1.5%.

Assuming 5840 h/year of operation and 0.07 €/kWh even if the LSPMSM has a much longer payback than that for the IE3-Class IM when replacing an IE2-Class IM, its life-cycle cost will be lower. For example, neglecting the possible stator rewinding and bearing replacement costs, during a 15-year period, the estimated energy savings value is 1458€ and 2295 € for the IE3-Class IM and IE4-Class LSPMSM. For a 15-year period it represents the equivalent to approximately 29 and 5 times their extra initial cost (or price difference, with respect to IE2-Class IM), respectively. In that 15-year period these motors will consume an amount of energy with a value equivalent to nearly 137 and 67 times their price (with 40% discount), respectively [ALMEIDA_14].

Table.1. 2 Main characteristics of commercial IE1, IE2-, IE3-, and IE4-class 7.5-kw 4-pole motors [ALMEIDA 14]

IEC Class	Motor Type	IEC Frame	Weight, kg	Power density, W/kg	Moment of Inertia, kgm2	Rated Speed, r/min	Full-load torque, Nm	Full-load efficiency, %	Full-Load Power factor, p.u.	Price, %
IE1	IM	132M	64.5	116.3	0.0465	1455	49.3	87.0	0.84	--
IE2	IM	132M	72.0	104.2	0.0528	1455	49.3	89.0	0.86	100
IE3	IM	132M	78.0	96.2	0.0642	1465	48.9	91.5	0.85	115
IE4	LSPMSM	132M	61.5	122.0	0.0500	1500	47.8	93.0	0.93	233

Considering that the IE2 IM needs to be rewound or repaired, the rewinding plus bearing replacement price is 175 € (46% of the price of a new IE3), the original motor efficiency is maintained after repair, and the payback time for the additional cost associated with the decision of replacing the damaged IE2 motor by a new IE3 or IE4 motor, instead of its rewinding, would be 2.1 and 3.8 years, respectively, which is still very attractive, particularly for the IE3 motor. Considering a damaged IE1 IM, if the customer decides to replace it instead of repairing, the payback time for the additional investment in a new IE3 or IE4 motor, would be 1.1 and 2.5 years, respectively, being an attractive option for both cases.

Moreover if a LSPMSM is well-designed it can significantly surpass an IE3 IM of the same power in the range of performances and hence in terms of material consumption. It means that for the same output power and speed and higher power factor, a LSPMSM with smaller frame size compared to IE3 IM can be used. Table.1. 3 presents material consumption, start-up and running performance comparison between a LSPMSM prototype of 19.0kW and a premium efficient induction motor of the same power range [FENG 11].

Table.1. 3Performance and material consumption comparison [FENG_11]

Performance	LSPMSM 19kW 4 Pole	Premium IM 19kW 4 Pole (class IE3)
Efficiency	95.8%	93.9%
Power Factor	97.0%	89.8%
Starting Torque (PU)	236.0%	132%
Starting Current (A)	252.5	290.7
Minimum Torque (PU)	115%	132%
Maximum Torque (PU)	265%	253%
Core Laminations (kg)	82.9	124.4
Winding Copper (kg)	11.2	21.9
Cage Aluminum (kg)	1.86	3.61
PM Material (kg)	3.55	N/A
Frame Size	F254T	F284T (one size bigger)

As the LSPMSM 19kW has smaller frame size, its consumption of core lamination, winding copper and cage aluminum is about 60% of the IE3 IM's consumption. Therefore in spite of the presence of 3.55kg of rare-earth magnets the total cost of LSPMSM is lower than this of the IE3 IM. This fact opens up new opportunities for saving energy and financial resources.

1.5. LSPMSM Design Challenges

1.5.1. Demagnetization

Nowadays the choice of PMs for LSPMSM is mainly making between rare-earth materials (i.e., samarium-cobalt SmCo and neodymium iron-boron NdFeB) and ferrite magnets. Fig.1. 13 presents demagnetization curves for different permanent magnet materials.

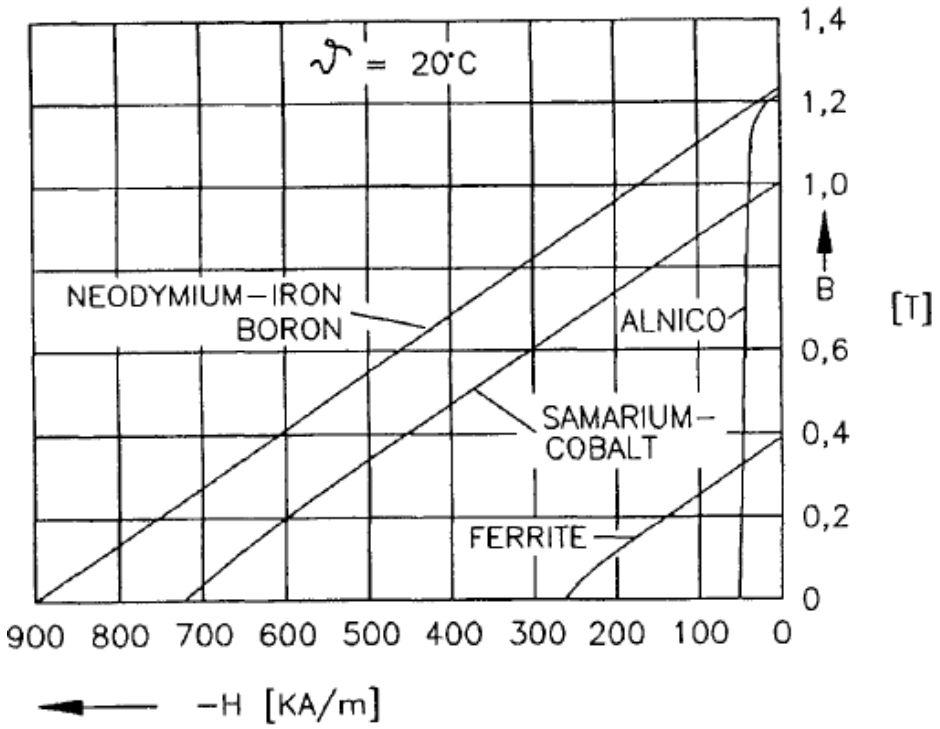

Fig.1. 13 Demagnetization curves for different permanent magnet materials [GIERAS_10]

Despite being considered rather expensive, high temperature range and chemical resistance of rare-earth materials make them more advantageous. In particular, SmCo magnets can be used in situations where operating temperatures will exceed 260°C. As a result, in applications requiring a strong, corrosion resistant magnet that will be exposed to high temperatures, SmCo remains unmatched [EAMAGNETICS_15].

As the PMs are often placed in the d-axis main flux path and the magnet relative permeability is close to one, the choice of magnet greatly affects the d-axis magnetizing inductance. High energy density magnets, i.e. rare-earth, allow a larger d-axis inductance than what is possible with ferrite magnets, resulting in a high power factor and high efficiency over a larger supply voltage range [MODEER_07].

Fig.1. 14 shows dependency of the intrinsic demagnetization curve from the temperature. Increase in temperature results in decrease in the remanent flux density B_r. The effect is approximately linear. The coercively of magnets H_c also decreases or increases depending on the temperature range [GIERAS_10].

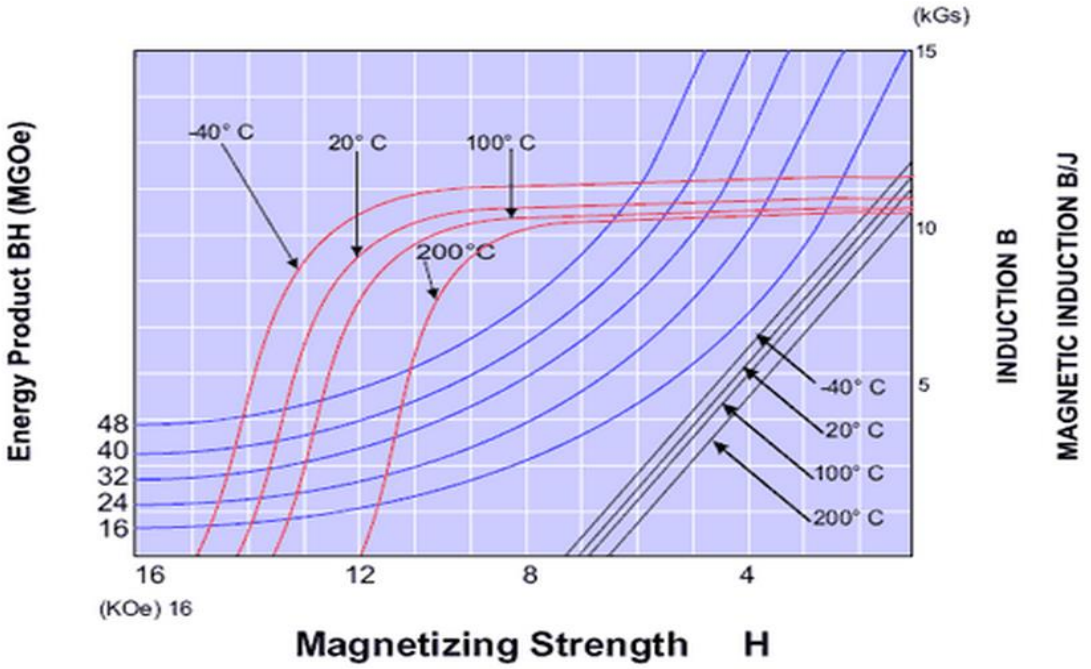

Fig.1. 14 Comparison of B - H and Bi - H demagnetization curves and their variations with the temperature for $Sm_2Co_{17}XG$ 26/20 PMs [EAMAGNETICS_15]

As it follows from Fig.1. 14 there is a risk of demagnetization if the LSPMSM rotor is overheated or if there is too much induced current in the winding and in the rotor bars. Partial or complete demagnetization can occur during the motor startup [DING 11]. Therefore, it's very important to make correct estimate of the temperature rise in order to ensure that the LSPMSM can normally run without any stator winding insulation damaged and permanent magnet material demagnetization.

There are two principal causes of motor heating: copper losses and iron losses. If in an IM, rotor losses include two components i.e. iron loss and cage loss, in a LSPMSM, thanks to synchronous speed of the rotor, the cage loss vanishes to negligible eddy current loss caused by air gap space harmonics. Therefore, the rotor temperature of a LSPMSM is about 30% less than that of an IM with the same output power [FASQUELLE 07]. However, since the starting time of the LSPMSM may be slower than that of the induction motors, rotor overheating is to be verified during its design.

An adiabatic thermal model for 3 rotor configurations was developed in [DING 11]. According to this research paper, the calculated temperature rise of the surface-inset LSPMSM motor was less than 8°C, while the interior motors are less than 4°C. It seems logical as PMs buried in the rotor are better protected from demagnetization than PMs being arranged on the rotor surface and directly exposed to demagnetizing winding fluxes.

1.5.2. Pulsating torques

LSPMSMs may be used in many high performance applications in which a smoothness of torque is of essential importance. Thus, the pulsating torque which creates vibrations and acoustic noise in the motor and causes inaccuracy should be minimized.

The pulsating torque consists of two major components: the ripple torque and the cogging torque. The ripple torque is caused by the distortion of sinusoidal distribution of the magnetic flux density in the air gap. Then, in order to get a small ripple torque the rotor magneto-motive force (MMF) should preferably have a sinusoidal waveform. Furthermore, the rotor reluctance variations should be as smooth as possible in order to soften the torque pulsation caused by stator spatial harmonics and rotor reluctance difference. The cogging torque is, however, almost independent of the stator current and back-emf and is caused by the interaction of the stator teeth with the magnets.

Table.1. 4 lists some methods to minimize the cogging torque for PM motors with surface-magnet rotor (SPM) and interior-magnet rotor (IPM) [HEIKKILA_02], [PCT/KR2006/005572], [DING_11].

Table.1. 4 Different methods to minimize the cogging torque [HEIKKILA_02]

Methods	Rotor Configuration	Influence	Drawbacks
Increasing of air gap length	SPM/IPM	-Lower magnetic flux density, lower reluctance variation regarding the rotor	-Increasing of stray inductance; -Decreasing of flux density and torque
Using a fractional slot/pole	SPM/IPM	-Reduction of the stator MMF harmonics	-Requires often double-layer windings
Using a large number of slots/pole	SPM/IPM	-Frequency of cogging increases; -Permeance variation is reduced: uncovering one half tooth	-Low speed machines normally have many poles as a cause of which a large number of slot/pole may not be possible
Using thick tooth tips	SPM/IPM	-Avoiding of saturation of tooth tips	-Insufficient space for stator windings and as a result heating and lower efficiency
Keeping slot openings to a minimum	SPM/IPM	-Small notches due to stator slotting in flux density waveform	-Complicates installation of the winding wires into the slots
Using magnetic slot wedges	SPM/IPM	-Small notches due to stator slotting in flux density waveform	-Increases stator leakage flux; -Increases costs
Skewing of stator or/and rotor stack or magnets	SPM/IPM	-Complete harmonic elimination is possible, if the skewing angle is correct	-Automatic slot filling and mass production becomes difficult; -Manufacturing problems, expensive; -Reduction of back-EMF

Table 1.4 Different methods to minimize the cogging torque. Continuation

Shaped PM surfaces	SPM	-Reducing of pulsating components; -Decreasing of the harmonics of the air gap flux density	-Shaping of PMs is expensive
Shaped pole shoes	IPM	-Reducing of pulsating components; -Decreasing of the harmonics of the air-gap flux density	-Increasing of armature reaction
Optimization of magnet width	SPM	-Magnet width should be greater than the integer number of slot pitches	-Exact pole width is not easily achievable: small variation in the arc change can produce either high or small cogging harmonics
Asymmetrical magnet distribution/ shifting of PMs	SPM	-Reducing the cogging harmonics like skewing magnets; -Increasing of frequency; -Additive effect of symmetry is broken	-Reduction of back- EMF; -Eccentricity: vibration, bearings problems
Different PM pole arc width	SPM	-Additive effect of symmetry is broken	-Different shapes of PM are needed: expensive -The air-gap flux density is different from each pole; -Parallel paths in windings may not be used
Using of separated into two parts teeth	SPM/ IPM	-Increased number of interactions between PMs and slots; -Higher frequency: acoustic noise may fall over audibility -Attenuated peak value of cogging torque	-Effective only if number of notches was correctly selected and if the main harmonic is the highest (in comparison with other harmonics)
Air-gap winding	SPM/ IPM	-No teeth, no reluctance variations	-Mechanical arrangements; -Difficult winding cooling
Using lower magnetic flux density	SPM/IPM	-Variation of flux density is smaller and cogging torque decreases	-Affects significantly the torque

1.5.3. Braking torque

The LSPMSM starts as an induction motor by the resultant of two torque components [SOULARD 02], [HUANG 08] i.e. the asynchronous torque developed by winding damper (squirrel cage) and magnet opponent torque so-called braking torque (see Fig.1. 15).

$$T_{tot} = T_{mb} + T_{cage} \tag{1. 1}$$

Where T_{mb} is braking torque, T_{cage} is asynchronous torque developed by winding damper and T_{tot} is total torque produced by the resultant of these two torques.

Therefore throughout all the starting process the load torque must be less than the total torque developed by motor:

$$T_{load} < T_{tot} < T_{mb} + T_{cage} \tag{1. 2}$$

The braking torque is directly proportional to the back-EMF and q-axis reactance and inversely proportional to the product of the d- and q-axis reactances as may be seen below from eq. (1. 3) [SOULARD 02].

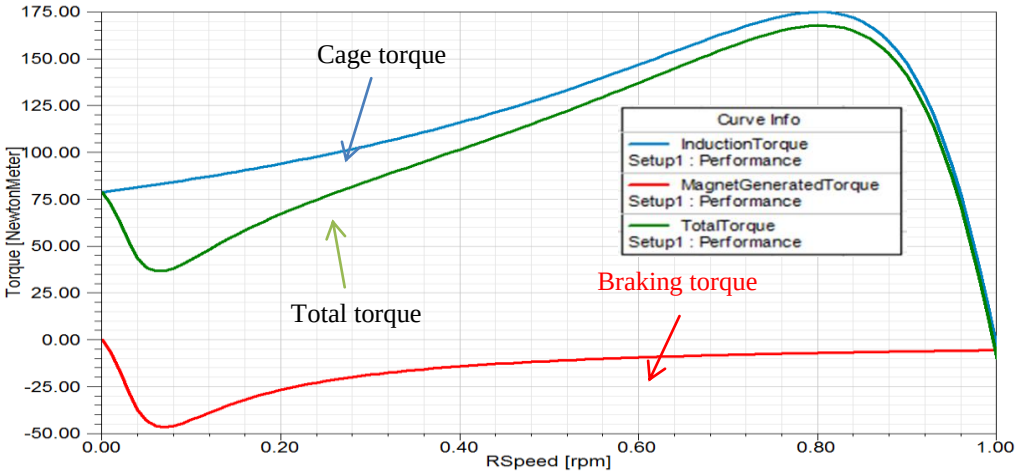

Fig.1. 15 Asynchronous torque/ speed curve of LSPMSM startup

$$T_{mb} = -\frac{3p}{\omega_r} \cdot (1-s) \cdot E_0^2 \cdot r_1 \cdot \frac{r_1^2 + X_q^2 \cdot (1-s)^2}{[r_1^2 + X_d \cdot X_q \cdot (1-s)^2]^2} \tag{1. 3}$$

where s is the slip, p is the number of poles, r_1 is the stator resistance, ω is the synchronous electrical speed, E_0^2 is the no-load EMF, X_d and X_q - d- and q-axis synchronous reactances. As it has been shown in Fig.1. 15, the magnet braking torque reduces the total torque and therefore complicates the motor pull-in process [MILLER 84].

The E_0^2 term in eq. (1. 3) shows that the magnet braking torque is strongly dependent on the electromotive force (EMF) produced by the PMs. At synchronous speed s=0, and if $r_1 \ll X_d$, the torque T_{mb} becomes approximately proportional to $(E_0/X_d^2) \cdot r_1$ and not zero at synchronous speed. At low speed, T_{mb} becomes inversely proportional to r_1. At an intermediate speed there is a maximum magnet braking torque. In low-power

LSPMSM where r_1 is relatively large, this occurs at a higher speed and the T_{mb} is flatter; in larger motors where r_1 is relatively small, the curve is more pointed and the peak occurs at a lower speed [HENDERSHOT_10].

1.5.4. Manufacturing and sizing

LSPMSMs use the same frame sizes as conventional IMs for the same motor rating. This makes them attractive replacements for conventional standard efficiency AC induction motors because mounting bolt locations and shaft heights are compatible [SOULARD_02], [TAKAHASHI_10].

However, even though for the same power the stator of a LSPMSM is the same as the stator of IM, its rotor topology is more complicated due to the presence of PMs. This imposes extra manufacturing restrictions on located PMs inside the rotor body. For example, welding of the rotor cage when PMs are already embedded into the rotor may degrade PMs characteristics and deteriorate motor performances. If PMs are too thin, besides from being brittle and so causing manufacturing problems, they become also more sensitive to demagnetization as the magnet reluctance is low and stray fields could more easily cause demagnetization.

Nonetheless, thanks to progressively developing magnetization technology, locating and magnetizing of PMs have become simpler and more cost effective than before [HO_12].

1.6. Choice of an efficient LSPMSM rotor topology

1.6.1. Variants of LSPMSM rotor

As it has been mentioned above, for economic reasons of the thesis, the stator and windings of the LSPMSM are identical to the IM for the same motor rating. This means that between the induction motor and the LSPMSM, only the rotor is changed.

From the point of the magnet arrangement a LSPMSM may be represented by two types: interior-magnet line-start permanent magnet synchronous motor (ILSPMSM) with magnets embedded in the rotor and surface-magnet line-start permanent magnet synchronous motor (SLSPMSM) with magnets mounted on its surface (see Fig.1. 16).

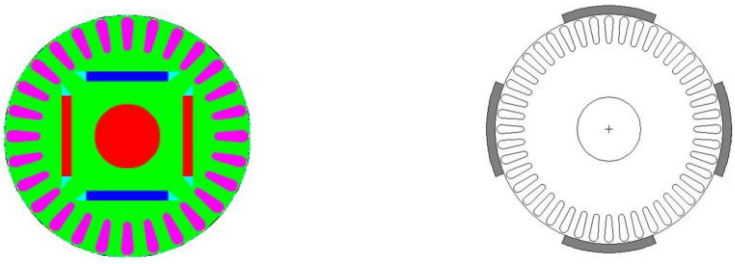

a) b)

Fig.1. 16 Two rotor structures of line-start permanent magnet synchronous motor: (a) interior-magnet line-start permanent magnet synchronous motor; (b) surface-magnet line-start permanent magnet synchronous motor

1.6.2. Interior-magnet LSPMSM vs. surface-magnet LSPMSM

ILSPMSM type has a conventional design of a LSPMSM with the robust structure and is hard to be demagnetized due to the squirrel cage protection.

The main advantage of the SLSPMSM is that its manufacturing is easier than one of interior-magnet rotor. Moreover, the SLSPMSM can provide larger permanent magnet synchronous torque via the shorter distance between the magnets and the stator winding.

As a result of less flux leakage and reluctance, the SLSPMSM is able to offer higher air gap flux density (Fig.1. 17a) than ILSPMSM and consequently higher output power. On the other hand, the bigger flux density will also create higher reluctance force and increased cogging torque (Fig.1. 17b) that could induce higher vibration as well as noise during rotation [HUANG 08].

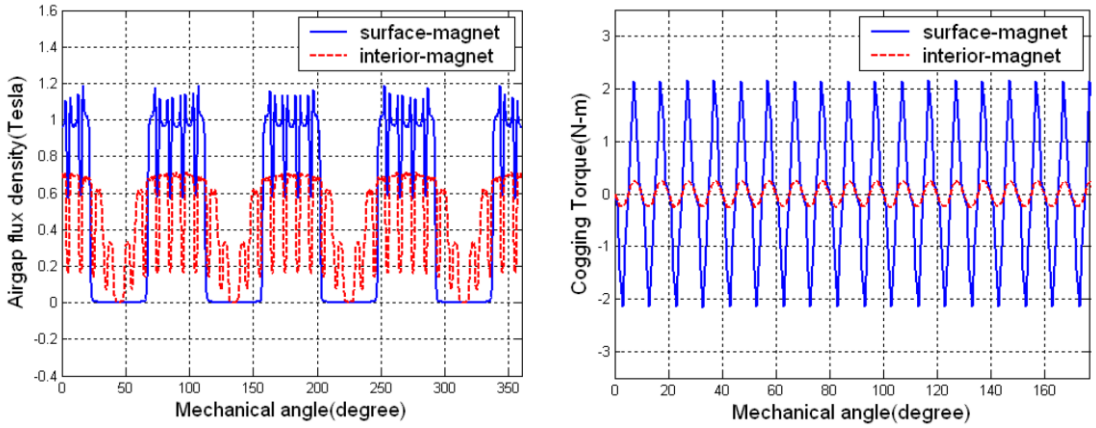

a) b)

Fig.1. 17 Comparison of characteristics of two LSPMs with different rotor structures: (a) Air gap flux density comparison; (b) Cogging torque comparison [HUANG 08]

The higher flux density created by the surface PMs increases the back-EMF that in its turn is proportional to the braking torque eqn. (1. 3). As the flux linkage and the reluctance torque of the SLSPMSM are higher (Fig.1. 17), the ILSPMSM will need less time to reach synchronous rotation.

At steady-state regime the main torques rotating a LSPMSM are the permanent magnet alignment torque T_{pma} and the synchronous reluctance torque T_{rel}:

$$T_{pma} = \frac{p}{2\omega_r} E_0 I_q \tag{1. 4}$$

$$T_{rel} = \frac{p}{2\omega_r} (X_d - X_q) I_d I_q \tag{1. 5}$$

where i_d, i_q refer to the d-axis and q-axis current. During synchronous rotation, the reluctance torque of the ILSPMSM is greater than one of SLSPMSM due to the bigger

difference of d-axis and q-axis reactance. As loading capability of the LSPMSM is determined by the combination of the permanent magnet alignment torque and the synchronous reluctance torque it means that the SLSPMSM has better synchronous loading capability for the same magnet volume (Fig.1. 18). Anyway it's not a standing rule and depends on the design geometry [FODOREAN 05], [FODOREAN 09].

Since the ILSPMSM has a larger synchronous reluctance torque at the synchronous speed, the steady-state current in the stator winding is smaller than that of the SLSPMSM at the same loading. The smaller steady-state current indicates that the ILSPMSM uses a lower input power but reaches the same output power as SLSPMSM. In other words, the interior type has a higher efficiency. In [HUANG 08] the influence of magnet arrangements on the transient and steady states operations for a LSPMSM 0.75kW were investigated and compared (Fig.1. 18).

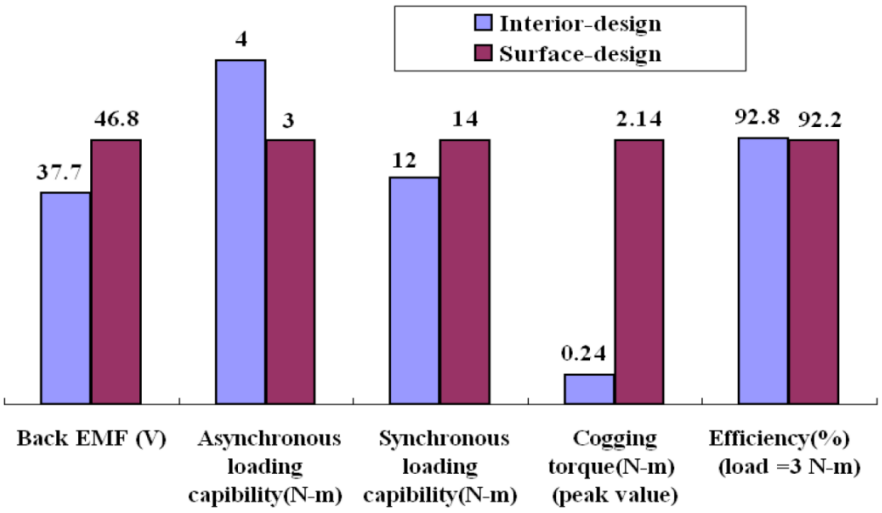

Fig.1. 18 Comparison of characteristics of two LSPMs of different rotor structures [HUANG 08]

According to given specification (see Appendix A) the designed motor has to start up under unfavorable conditions such as reduced rated voltage and high inertia of the load. According to Fig.1. 18 it is more reasonable to focus on the interior-magnet rotor structure.

1.6.3. Choice of an efficient ILSPMSM topology

In [UGALE 12], [RUAN 11], [HUANG 13] a performance comparison of LSPMSMs with different interior magnet rotor arrangements simulated for the same magnetic material and constant magnet volume (see Fig.1. 19 and Fig.1. 20) has been implemented.

It is has been shown that among all those architectures the spoke-, the interior-, the V-type- and the W-type magnet rotor topologies offer the overall good performance in terms of efficiency, power factor, load angle, starting torque and no-load current [UGALE 12]. Moreover, the spoke rotor presents the principle of concentration of the flux density that allows a significant increase of the magnetic field in the air gap over the residual flux density. This fact let utilization of cheaper magnet materials (SmCo instead of NdFeBr, for example). Despite of having good performances, W-type rotor has a

rather complicated geometry and consequently more complex and expensive fabrication process.

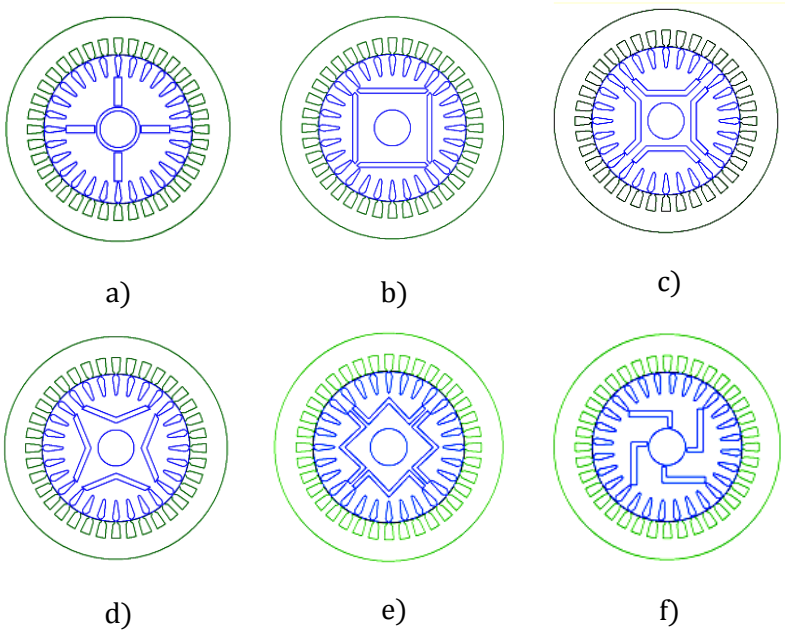

Fig.1. 19 Configurations of rotors for LSPM: (a) Spoke rotor (radial magnetic circuit structure), (b) series-type magnetic circuit structure, (c) U-type magnetic circuit structure, (d) V-type magnetic circuit structure, (e) W-type magnetic circuit structure, (f) Swastika magnetic circuit structure

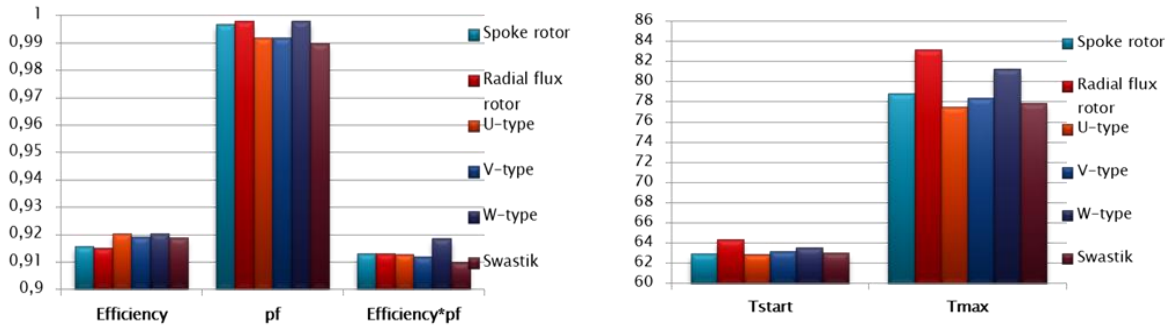

Fig.1. 20 Performance comparison of LSPMSM shown in Fig.1. 19

Thus, due to the presence of a large number of constraints that has to be taken into consideration, such as adequate performances, reluctance torque, costs of manufacture and the pay-back time, it's not an easy task to find the best compromise solution and the best PM rotor architecture. In this work, it was decided to focus on the analysis on three important rotor configurations that meet the major part of specification requirements (Appendix A): best product of power factor and efficiency (see Fig.1. 20) and being relatively simple to be manufactured. The preselected rotor configurations are the following: (a) rotor with radial magnetic circuit structure, (b) rotor with series-type

magnetic circuit structure, (c) rotor with V-type magnetic circuit structure (see Fig.1. 21). These three LSPMSM configurations will be studied along the rest of the thesis and special pre-design software predicting the behavior of each of them will be developed.

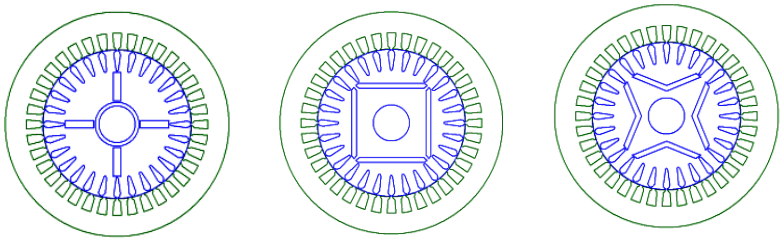

a) b) c)

Fig.1. 21 LSPMSM rotor configurations under study: (a) rotor with radial magnetic circuit structure, (b) rotor with series-type magnetic circuit structure, (c) rotor with V-type magnetic circuit structure

1.7. Choice of design and modeling techniques

As soon the LSPMSM configurations are preselected, it is possible to go in the search of the design and modeling methods adapted to the thesis objectives that consist in the developing of a multi-physical generic model which allow the calculation of the LSPMSM's steady-state characteristics. The model must be fast enough to be integrated into an optimization procedure. The goal of the optimization procedure is the selection of the most efficient LSPMSM rotor architecture and its manufacturing.

There are several methods which allow the steady-state characteristics calculations: analytical, permeance network method and numerical.

1.7.1. Numerical methods

The prompt evolution of the information technologies and computing facilities encourages the development of efficient methods which numerically solve electro-magnetic equations in two-dimensional/three-dimensional representation.

There is a set of different numerical techniques that makes possible to calculate the electromagnetic field in electrical machines. The most known of them are Finite Difference Method (FDM), Boundary Element Method (BEM), Finite Element Method (FEM), Discrete element method (DEM) and Finite Integration Technique (FIT) [LEMENACH 05].

All these methods allow modeling of numerous structures with a rather good accuracy. Being quite long at the origin of the implementation of different methods the computation time now is constantly reducing with the increasing speed of processors. These methods directly solve a system of partial differential equations, like Maxwell's equations serving as fundamentals of electromagnetism. This system of equations describes the physical behavior of the system and is based on low level assumptions. System of equations solving is based on numerical methods and provides, for example,

the value of a potential at any point of the studied domain structure in case of different physics problem like for mechanics, electromagnetism and thermodynamics.

The values of macroscopic quantities are then calculated thanks to the value of these potentials. FDM and FEM are very popular when an electromagnetic structure has to be analyzed. These methods help to take into account electrical, magnetic, thermal or mechanical phenomena. They are generally based on a spatial discretization of a structure into small triangular or rectangular surfaces in case of two-dimensional space, or into small tetrahedral or hexahedral volumes in case of three-dimensional space. The peaks of the geometric shapes are called the nodes and represent the number of unknowns of the system. The accuracy of the solution is therefore directly related to the mesh refinement.

After defining material characteristics of the studied structure and its boundary conditions (Neumann, Dirichlet, etc.), a set of partial differential equations (that can be non-linear) may be numerically solved [GIERAS_10]. If the values of the potentials at the nodes are calculated accurately, the rest of the defined geometry is found by interpolation. It gives an access to the different field maps of the studied structure life, for example, one of electrical motor (see Fig.1. 22)and thereby offering the possibility of getting the overall performance of the machine. In summary, this is a method that allows taking into account the microscopic and macroscopic, dynamic or static, two-dimensional or three-dimensional phenomena.

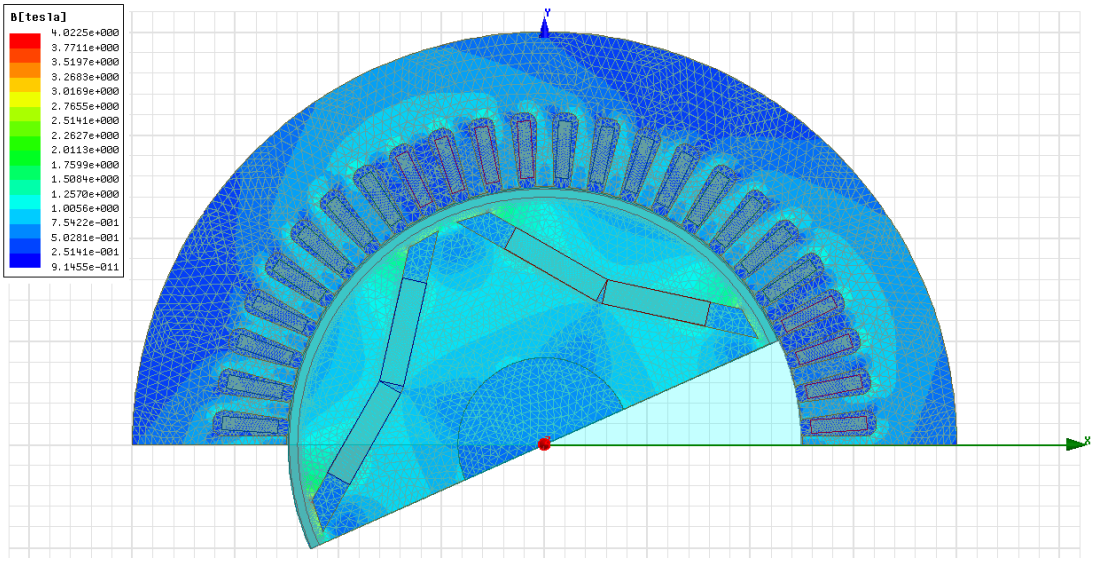

Fig.1. 22 2D finite-element representation of a LSPMSM: mesh and plot of flux magnitude

These different approaches are mostly presented in the form of a generic software. The user task consists in describing the studied structure geometry, the set of material characteristics (which may be relatively complex in view of the assembly of sheets for example), and finally, the realization of a mesh geometry. Cumbersomeness of implemented calculations depends on the size of the matrices related to the density of the mesh, and their inversions.

In a design phase, these methods are mainly used for the technical validation of proposed solutions. However, their coupling with optimization algorithms, especially in case of a multi-physical study, generally is not useable. Nonetheless, the methods let it possible for a small number of parameters coupled with adapted optimization methods based for example on substitution models [BRISSET_07], [GILLON_09].

1.7.2. Analytical methods

Unlike numerical methods, it is considered that analytical methods are based on an explicit formulation of variables characterizing the system. Analytical equations relate the functional variables of the system, so-called performances, to descriptive variables: geometric parameters, material characteristics, etc. These analytical equations can be written using different simplifying assumptions applied to descriptive values of the system. They have been widely used for problems in electrical engineering and cover a wide range of electromagnetic systems. These analytical models have been used long time before the first computers appearance.

Explicit links between all the variables help the designer to interpret the behavior of the studied system. This is especially useful when modeling some coupled phenomena. However, such simplicity can lead to permanent loss of certain information. Even if analytical models can more or less precisely describe the behavior of a system, the do that with the use of tough assumptions: linearity of the environment, neglecting the harmonics except the first one, etc.

There are a number of studies [DUBAS_09], [LEGRANGER_09], [GIERAS_10] where the magnetic flux density is analytically calculated by formal resolution of magnetic field partial differential equations. These models are of a very high accuracy, but require a high level of assumptions. The method is based on a geometrical simplification and representation of the machine by a cylinder (but with the possibility to take into account the saliency). This model is valid in the linear environment and can be used for description of the motor behavior under the assumption of infinite iron permeability.

Compared to the finite element model, the analytical formulation gives the possibility of utilization of highly efficient direct optimization algorithms such as Sequential Quadratic Programming (SQP). This approach has been successfully applied for design of electrical machines.

Other benefits of the analytical models are the short computing time and the easy model understanding due to explicit links between model parameters and physical phenomena. Such simplicity allows the implementation of the coupling between different physical domains and extension of these couplings to other areas such as economic, environmental, industrial, etc.

In contrast to numerical models, there are very few generic analytical models. There are models for every type of machine, using more or less rigid hypothesis. Therefore a good knowledge of the system in terms of engineering sciences is required before choosing a model and its associated assumptions.

In general, the electrical machine design requires the application of an analytical model leading to a first solution to be further refined by a finite element model or a lumped model. These models based on a set of explicit equations can be treated with a significant computation time reduction if some simplifying assumptions like linearity of the environment are made. Accuracy of models can be improved, for example, by adding a coefficient in order to integrate the saturation effect, but their effectiveness through optimal design is relative. In addition, for each new design structure, the designer has to adapt the model assumptions. If the designer works with a non-conventional machine, the model must be completely rebuilt.

The fully analytical formulation of the system allows the designer to compute all the partial derivatives of the objective function, which permits to exploit gradient type algorithms and to study the sensitivity of functional parameters in comparison to descriptive parameters.

1.7.3. Semi-analytical/ semi-numerical methods

Combined together, analytical and numerical models create a hybrid one like for example the distributed element model (also called transmission line model) or the lumped element model. In these models the formulation of the network elements is determined analytically, but the solution of the system equations is numerical. Consequently the method is called semi-analytical or semi-numerical. Transition from system of analytical equations to matrix is rather easy, especially using Kirchhoff's laws. Parameterization is possible for relatively similar configurations so the model geometry can reasonably vary [DO_10]. This model feature is very convenient for the design phase. Therewith, it is possible to obtain values of formal derivative, which is a real advantage.

Distributed element models (see Fig.1. 23) can describe the designed structure not like a discrete elements combination (lumped element model), but as a combination of infinitesimal elements by discretizing the network associated with an element in a finite number of smaller elements each comprising a part of the network. It involves the calculation of a new derivative respecting space, but gives more nodes. This additional information allows the user an access to a more important potential map of the studied machine and to gain in accuracy. In electrical engineering, these models are commonly used in the study of the cables and transmission lines.

The lumped element models (see Fig.1. 24), like permeance network models for the magnetic circuit or nodal network models for thermal modeling have an advantage of being based on Kirchhoff's laws and various associated theorems [PETRICHENKO_07]. Similarly to the numerical model, speed and accuracy of the model will largely depend on its granularity. Number of elements can also be increased in order to take into account such model specificity as transients, nonlinearities and multi-physical interactions.

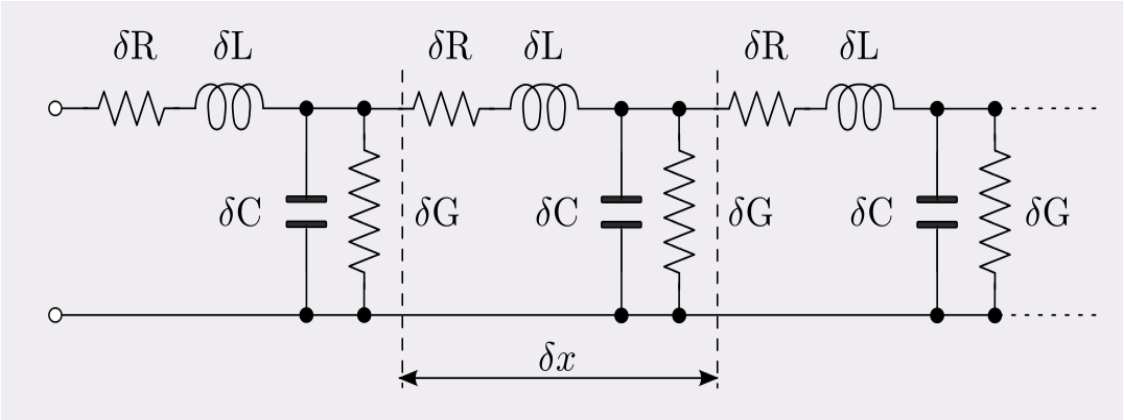

Fig.1. 23 Distributed element model applied to a transmission line

In some cases, the coefficient of saturation may be implanted in the permeance network when BH curve is considered for all the permeances, [PERHO 02]. Like numerical models, in lumped element models there is a direct link between studied phenomena and network discretization.

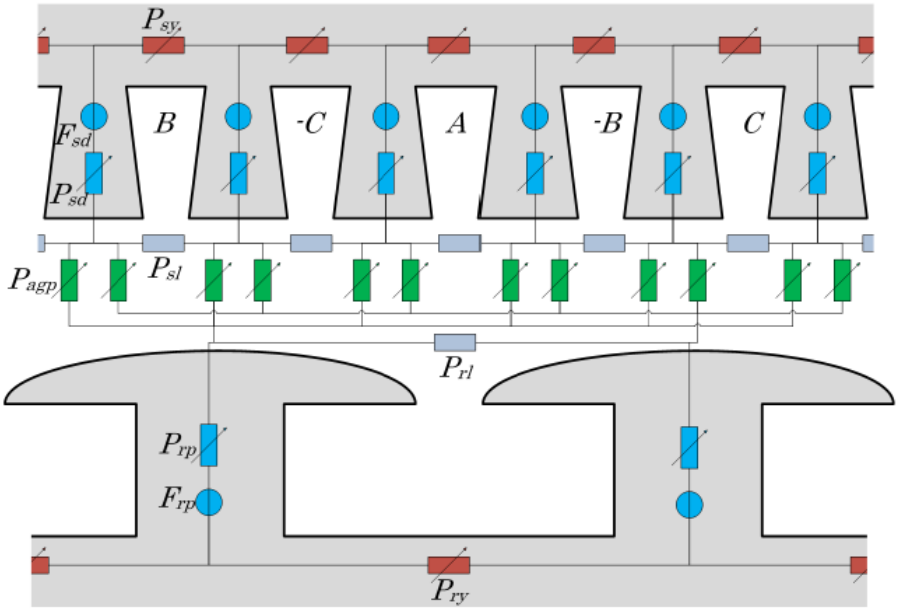

Fig.1. 24 Lumped element models applied to a synchronous generator [PETRICHENKO 07]

This is an essential element in this type of modeling. To visualize a specific physical phenomenon, the user has to be in the know which flux path is considered. Besides it is necessary to properly analyze the network topology based on the phenomena to be taken into account. This partitioning can be systematic for two-dimensional or three-dimensional networks.

There are very few generic commercial softwares based on lumped models. In view of electrical machine modelling there are "Motor-Cad®" dedicated to the electromagnetic performance of motors and generators and the optimization of their cooling and "ReluсTool®" dedicated to magnetics. In fact all complex physical phenomena

encountered in electrical machine like, for example, vibro-acoustic aspects, have difficulty with being introduced in the form of lumped element model [DOGAN_12].

The accuracy of these models is higher than one of purely analytical models. This requires fewer assumptions such as taking into account the movement of the rotor that allows the visualization of the teeth effects, induced currents in the solid parts of the studied machine, the intrinsic specificity of materials: local saturation, temperature sensitivity, etc. The method has some disadvantages: while its implementation it is necessary to have a notion about the fluxes paths inside the electrical machine that is sometimes difficult due to its high saturation. In addition, it may be rather complicated to determine the circuit elements like, for example, thermal coefficients for the distributed element models or the law of the air gap permeance variation for lumped element model [NEJDAR_11], [NAKAMURA_09], [BRACIKOWSKI_12].

1.7.4. Choice of method

Looking through the advantages and drawbacks of the above-described methods, it can be concluded that as much the analytical method gains in rapidity as it is less competitive in the accuracy of calculations. This statement is completely opposite when applied to the numerical method. The semi-analytical method is a trade-off solution between these two methods (see Fig.1. 25).

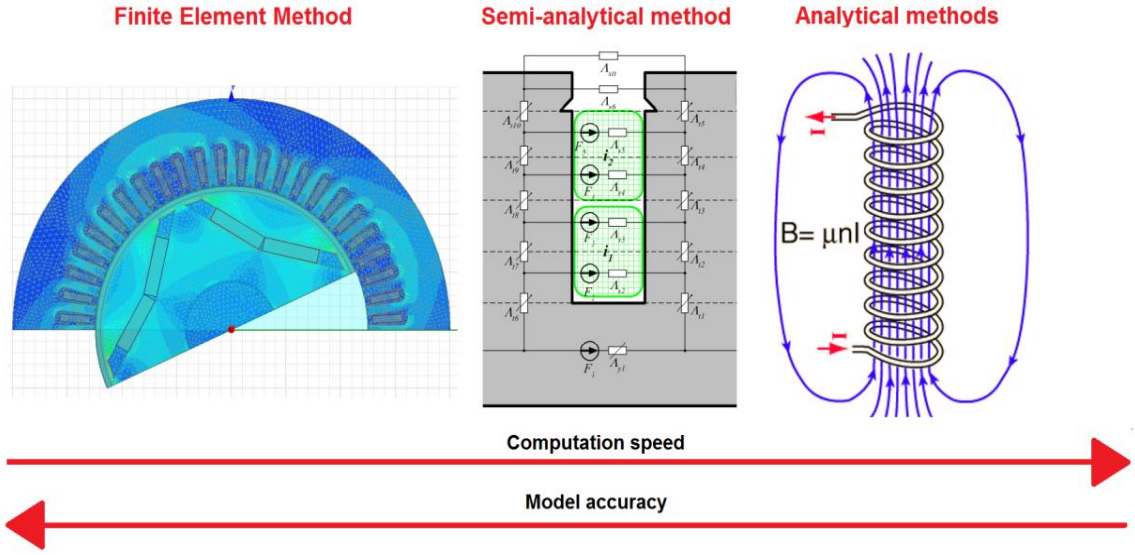

Fig.1. 25 Comparison between the described methods

The main objective of the thesis consists in the developing of a multi-physical generic model fast enough to be integrated into an optimization procedure solving the discrete optimization problem. Normally, the solving of discrete optimization problem is rather cumbersome and takes a lot of time for numerical and even semi-analytical methods. Consequently, the application of the analytical model is more optimal as it promotes the computation rapidity [VENKAT_10].

1.8. Conclusion

Chapter 1 begins with a glance on global warming problem and its connection to the development of energy market. After that, it introduces the evolution of standards adopted by The International Electrotechnical Commission relating to energy efficient motors.

Further, the examination and comparison of different types of electric motors for constant-speed application is described in the dedicated section. It was shown that the line-start permanent magnet synchronous motor has a superiority in terms of performances over the standard induction motor and economic superiority over permanent magnet synchronous motor.

In the following part of the chapter, design challenges applied to different LSPMSM rotor topologies are discussed. Based on this discussion, the three LSPMSM configurations which will be studied along the thesis are chosen (see Fig.1. 21).

Finally, Chapter 1 provides a brief overview of existing methods describing the processes in electrical machines: numerical method, analytical method and permeance network method. The chapter also lists advantages and disadvantage of each methods. Based on this assessment it is decided that analytical methods are most appropriate for the development of a multi-physical generic model being to be used as a base of a pre-design software for the LSPMSM.

1.9. References

[ACC_11] America's Climate Choices. Washington, D.C.: The National Academies Press. 2011. p. 15. ISBN 978-0-309-14585-5

[ALMEIDA_14] De Almeida, A.T.; Ferreira, F.J.T.E.; Quintino, A., «Technical and economic considerations on super high-efficiency three-phase motors», IEEE transactions on industry applications, vol. 50, no. 2, p. 1274-1285, march/april 2014

[BRACIKOWSKI_12] N. Bracikowski « Modélisation multi-physique par modèles à constantes localisées ; Application à une machine synchrone à aimants permanents en vue de son dimensionnement», Dissertation. L'Ecole Centrale de Lille, France, 2012.

[BRISSET_07] S. Brisset, "Démarches et outils pour la conception optimale des machines électriques," Habilitation à Diriger des Recherches, Université des Sciences et Technologies de Lille-Lille I, 2007

[BRUNNER_11] C. Brunner, P. Waide, and M. Jakob, «Harmonized standards for motors and systems-global progress report and outlook», in Proc. 7th EEMODS, Alexandria, VA, USA, 2011, pp. 444–456

[CASSELL_14] J. Cassell, «Disconnect in Equipment Purchasing Costs Manufacturers Billions», HIS, April 30, 2014

[DING_09] T. Ding, N. Takorabet, F.M. Sargos, X. Wang «Design and Analysis of Different Line-Start PM Synchronous Motors for Oil-Pump Applications» IEEE transactions on magnetics, vol. 45, no. 3, march 2009

[DING_11] T. Ding «Etude et optimisation de macines a aimants permanents a demarrage direct sur le reseau», Dissertation. L'Université Henri Poincaré, Nanci I, France, 2011

[DO_10] T. P. Do, "Simulation dynamique des actionneurs et capteurs électromagnétiques par réseaux de réluctances: modèles, méthodes et outils," Thèse de Doctorat, Institut National Polytechnique de Grenoble-INPG, 2010

[[DOGAN_12] H. Dogan, F. Wurtz, L. Garbuio, and A. Foggia, "Optimization of Permanent Magnet Synchronous Machine for Electrical Vehicle Application," in OIPE'12 (International Workshop On Optimization and Inverse Problems in Electromagnetism), 2012, pp. p.230–231

[DUBAS_09] F. Dubas and C. Espanet, "Analytical Solution of the Magnetic Field in Permanent-Magnet Motors Taking Into Account Slotting Effect: No-Load Vector Potential and Flux Density Calculation," Magnetics, IEEE Transactions on, vol. 45, no. 5, pp. 2097–2109, 2009.

[EAMAGNETICS_15] http://www.eamagnetics.com/info_samarium_cobalt_charts01.asp

[EEPOEMDS_11] Energy-Efficiency Policy Opportunities for Electric Motor-Driven Systems, International Energy Agency, 2011

[FASQUELLE_07] A. Fasquelle, "Contribution à la modélisation multi-physique: électo-vibro-acoustique et aérothermique de machines de traction," École Centrale de Lille, France, 2007.

[FCCC/CP/2009] UNFCCC: Copenhagen Accor, 2009

[FENG_12] X. Feng, «Performance Investigation and Comparison of Line Start-up Permanent Magnet Synchronous Motor with Super Premium Efficiency», ICEM 2012

[FODOREAN_05] D. Fodorean, « Conception et réalisation d'une machine synchrone à double excitation : Application à l'entraînement direct. Thèse de Doctorat », Université de Technologie de Belfort-Montbéliard, 2005

[FODOREAN_09] D. Fodorean, A. Miraoui, "Dimensionnement rapide des machines synchrones à aimants permanents (MSAP)", Techniques de l'ingénieur, Nov. 10, 2009

[FUCHSLOCH_08] Fuchsloch. J. F., Finley, W. R., Walter, R. W. : The Next Generation Motor-Designing a New Apporoach to Improve the Energy Efficiency of NEMA Premium Motors, IEEE Ind. Appl. Magazine (Jan/Fab 2008).

[GESY_14] Global Energy Statistical Yearbook 2014

[GIERAS_10] J.F. Gieras, «Permanent Magnet Motor Technology. Design and Application» CRC Press; Third Edition, 2010

[GILLON_09] F. Gillon, "Méthodologies de conception optimale des composants électomagnétiques," Habilitation à Diriger des Recherches, Université des Sciences et Technologies de Lille-Lille I, 2009

[HANSEN_10] Hansen, J., R. Ruedy, M. Sato, and K. Lo, 2010: Global surface temperature change, Rev. Geophys., 48, RG4004, doi:10.1029/2010RG000345

[HASSANPOUR_09] Arash Hassanpour Isfahani, Sadegh Vaez-Zadeh «Line start permanent magnet synchronous motors: Challenges and opportunities», Energy, 34 Issue: 11 (2009-11) Page: 1755-1763

[HEIKKILA_02] T. Heikkila «Permanent magnet synchronous motor for industrial inverter application. Analysis and design», Dissertation. Acta Universitatis Lappeenrantaensis, Finland, 2002.

[HENDERSHOT_10] J.R. Hendershot & T.J.E. Miller, «Design of Brushless Permanent Magnet Machines», Motor Design Books LLC; Second Edition, 2010.

[HO_12] Ho, S.L.; Li, H.L.; Fu, W.N., "A Post-Assembly Magnetization Method of Direct-Start Interior Permanent Magnet Synchronous Motors and Its Finite-Element Analysis of Transient Magnetic Field," Magnetics, IEEE Transactions on , vol.48, no.11, pp.3238,3241, Nov. 2012

[HUANG_08] P. W. Huang , S. H. Mao , M. C. Tsai and C. T. Liu "Investigation of line start permanent magnet synchronous motors with interior magnet rotors and surface magnet rotors", Proc. Int. Conf. Electrical Machines and Systems, ICEMS, pp.1 -5 2008

[HUANG_13] Po-Wei Huang; Mi-Ching Tsai, "Investigation of V-Shaped Line Start Permanent Magnet Motors Based on Reactance Effect," Magnetics, IEEE Transactions on, vol.49, no.5, pp.2311,2314, May 2013

[IEC600034-30_08] Ed. 1: Rotating Electrical Machines—Part 30: Efficiency Classes of Single-Speed, Three-Phase, Cage-Induction Motors (IE-Code), IEC Std.60034-30, 2008.

[IEC600034-30_11] Ed. 2, Draft, Nov. 2011, WG31/2CD: Rotating Electrical Machines—Part 30: Efficiency Classes of Single-Speed, Three-Phase, Cage-Induction Motors (IE-Code), IEC Std. 600-34-30, Nov. 2011

[KWES_14] Key World Energy Statistics. International Energy Agency, 2014

[KURIHARA_04] K. Kurihara, M. Azizur Rahman «High Efficiency Line-Start Interior Permanent Magnet Synchronous Motors», 2004

[LEGRANGER_09] J. Legranger, "Contribution à l'étude des machines brushless à haut rendement dans les applications de moteurs-générateurs embarqués," Thèse de Doctorat, Université de Technologie de Compiègne (UTC), 2009

[LEMENACH_05] G. Albertier, Y.Le Menach, J.-P.Ducreux, F. Piriou, «Comparison of slip surface and moving band techniques for modelling movement in 3d with FEM», European Physical Journal Applied Physics, Vol. 30, N°. 1, pages. 17-21, 4-2005

[MESURES803] «La rentabilité énergétique les entrainements», Mesures 803-Mars 2008, www.mesures.com

[MILLER_84] T.J.E. Miller, «Synchronization Line-Start Permanent Magnet AC Motors», IEEE Trans. On PAS, PAS-103, No.7, July 1984, pp.1822-1828

[MODEER_07] T. Modeer, « Modeling and Testing of Line Start Permanent Magnet Motors », Licentiate Thesis, Stockholm, Sweden 2007

[NAKAMURA_09] K. Nakamura, S. Hisada, K. Arimatsu, T. Ohinata, K. Sakamoto, and O. Ichinokura, "Iron Loss Calculation in a Three-Phase-Laminated-Core Variable Inductor Based on Reluctance Network Analysis," Magnetics, IEEE Transactions on, vol. 45, no. 10, pp. 4781–4784, 2009

[NEJDAR_11] B. Nejdar, "Modélisation basée sur la méthode des réseaux de perméances en vue de l'optimisation de machines synchrones à simple et à double excitation," Thèse de Doctorat, École Normale Supérieure de Cachan-ENS Cachan, 2011

[PETRICHENKO_07] D. Petrichenko, "Contribution la modlisation et la conception optimale des turbo-alternateurs de faible puissance," Ph.D. dissertation, l'École Centrale de Lille, 2007

[PERHO_02] J. Perho, "Reluctance Network for Analysing Induction Machines," Thèse de Doctorat, Helsinki University of Technology, 2002.

[PCT/IB01/02851] A.Worley, K. Black, S.P. Purbrook, «Line start permanent magnet motor», 2002.

[RUAN_11] T. Ruan, H. Pan, Y. Xia « Design and Analysis of Two Different Line-Start PM Synchronous Motors», Artificial Intelligence, Management Science and Electronic Commerce (AIMSEC), 2011

[SOULARD_02] F. Libert, J. Soulard, and J. Engstrom, «Design of a 4-pole line start permanent magnet synchronous motor,» In Proc. ICEM. 2002, Brugge, Belgium.

[UGALE_12] R. T. Ugale «Inset-Consequent and Inset Rotors for Line Start Permanent Magnet Synchronous Motor», ICEM 2012.

[SIEMENS_09] Siemens «Motors. Answers for industry». Manual, 2009

[VENKAT_10] Venkataraman P.: Applied Optimization with Matlab Programming, A Wiley, John Wiley & Sons, New York, 2001

[WIKI_15] Solar variation, http://en.wikipedia.org/wiki/Solar_variation

Design of three LSPMSM rotor topologies

2.1. Introduction

The second chapter begins with a discussion about analytical methods used for LSPMSM transient d-q equivalent circuit. Further, the development of analytical models considering asynchronous and steady -state operations of the LSPMSM will be introduced. It will be discussed how to create a magnetic equivalent circuit for each of three rotor configurations selected in Chapter 1: series, radial magnetized and V-type. The obtained value of the air-gap flux will be used in the calculation of the flux linkage and steady-state performances.

The characteristics of each LSPMSM rotor configuration are described with aid of an analytical model which is verified by numerical software presented in a dedicated paragraph.

Finally, a general definition of the optimization problem is discussed and the results in the form of Pareto frontiers for two variants of rotor cage are shown.

2.2. Analytical method of LSPMSM designing

In Chapter 1 it was concluded, that the most appropriate solution for the replying to the thesis objectives consists on the development of a multi-physical generic model is the usage of an analytical model. In this thesis the analytical model is based on d-q equivalent circuit.

The circuit based model is a good solution for evaluating and analyzing the transient and steady state performances of the LSPMSM. In spite of having calculation time extremely reduced, he analytical model have a comparatively low accuracy. For consolidation of the analytical models the F.E. modelling will be done using finite element models. In this thesis a specialized FEM software Ansoft/Maxwell is used for this purpose.

2.2.1. Park transformation and transient d-q equivalent circuit of LSPMSM

In electrical engineering, Park's transformation is a mathematical direct–quadrature–zero (dq0) transformation that rotates the reference frame of three-phase systems in an effort to simplify the analysis of three-phase circuits.

The dqo transformation in matrix form applied to any three-phase quantities (e.g. voltages, currents, flux linkages, etc.) is given by eq. (2. 1)

$$x_{dqo} = \sqrt{\frac{2}{3}} \cdot \begin{bmatrix} cos\theta & cos(\theta - \frac{2}{3}\pi) & cos(\theta + \frac{2}{3}\pi) \\ -sin\theta & -sin(\theta - \frac{2}{3}\pi) & -sin(\theta + \frac{2}{3}\pi) \\ \frac{\sqrt{2}}{2} & \frac{\sqrt{2}}{2} & \frac{\sqrt{2}}{2} \end{bmatrix} \cdot \begin{bmatrix} x_a \\ x_b \\ x_c \end{bmatrix} \quad (2.1)$$

In three-phase machines we are typically concerned with three self-inductances and six mutual inductances. In matrix form it can be expressed as follows in (2. 2) [HENDERSHOT 10].

$$L_{ABC} = \begin{bmatrix} L_{AA} & L_{AB} & L_{AC} \\ L_{BA} & L_{BB} & L_{BC} \\ L_{CA} & L_{CB} & L_{CC} \end{bmatrix} \quad (2.2)$$

Using the Clarke transformation the column vector of synchronous inductances is

$$\begin{bmatrix} L_d \\ L_q \end{bmatrix} = C^T \cdot L_{ABC} \cdot C \quad (2.3)$$

Where C is

$$C = \frac{2}{3} \begin{bmatrix} cos\theta & -sin\theta \\ cos(\theta - \frac{2}{3}\pi) & -\sin(\theta - \frac{2}{3}\pi) \\ cos(\theta + \frac{2}{3}\pi) & -sin(\theta + \frac{2}{3}\pi) \end{bmatrix} \quad (2.4)$$

where θ is in electrical degrees.

Applying the three-phase sinusoidal voltage source to the stator winding of LSPMSM produces the rotational magnetic field in the air gap of the motor. The permanent magnet poles fixed on the rotor try to align along this rotating field, yielding a synchronous torque on the rotor. During starting, the damping winding (in our case it may be a squirrel cage or an aluminum or copper can) on the rotor generates the asynchronous starting torque, creating a self-starting capacity [MODEER 07], [WANG 07].

The d,q-axis voltages of LSPMSM for are shown in set of equations (2. 5)

$$\begin{cases} u_d = r_1 \cdot I_d + \frac{d\Psi_d}{dt} - \omega_r \cdot \Psi_q \\ u_q = r_1 \cdot I_q + \frac{d\Psi_q}{dt} + \omega_r \cdot \Psi_d \\ u_{2d} = r'_{2d} \cdot i_{2d} + \frac{d\Psi_{2d}}{dt} \\ u_{2q} = r'_{2q} \cdot i_{2q} + \frac{d\Psi_{2q}}{dt} \end{cases} \quad (2.5)$$

Where u_d, u_{2d} are the d-axis voltage of stator and rotor, u_q, u_{2q} are the q-axis voltage of stator and rotor, ω_r is the electrical angle speed and r'_2 is rotor winding resistance

transferred to the stator and depending on the rotor speed. At steady state u_{2d} and u_{2q} can be considered to be zero.

The magnetic flux equations are shown in set of equations (2. 6)

$$\begin{cases} \Psi_d = L_{1d} \cdot I_d + L_{ad} \cdot i_{2d} + \Psi_m \\ \Psi_q = L_{1q} \cdot I_d + L_{aq} \cdot i_{2q} \\ \Psi_{2d} = L_{2d} \cdot i_{2d} + L_{ad} \cdot I_d + \Psi_m \\ \Psi_{2q} = L_{2q} \cdot i_{2q} + L_{aq} \cdot I_q \end{cases} \quad (2.6)$$

By describing the permanent magnet as a current source, the flux linkage Ψ_m can be defined as eq. (2. 7)

$$\Psi_m = L_{ad} \cdot i_{pm} \quad (2.7)$$

In order to be able to simulate the electrical behavior of the LSPMSM in any electrical circuit analysis program the motors equivalent circuit (see Fig.2. 1) is needed. By transforming the drive voltage into d-q parameters and connecting it to its respective d-q equivalent circuit, estimations of the models currents can be done.

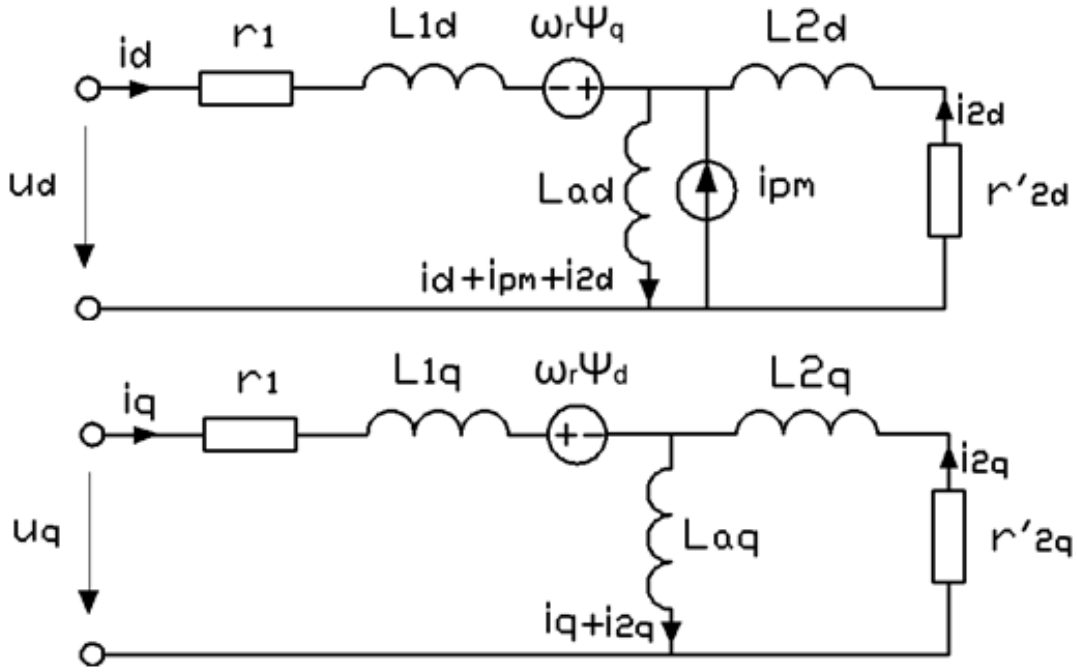

Fig.2. 1 Transient d-q equivalent circuits

The differential equation describing the shaft speed is given by eq. (2. 8)

$$J_{load} \cdot \frac{d\omega_r}{dt} = p \cdot (T_{em} - T_L) \quad (2.8)$$

Where J_{load} is the rotational inertia of the motor and load, T_{em} is electromagnetic torque developed by motor, T_L is the load torque and p is the number of pole pairs.

In [HONSINGER 80] a set of equations describing the transient behavior of LSPMSM is presented below by eq. (2. 9)

$$\begin{cases} \dot{\Psi}_d = u_d - r_1 \cdot I_d + \omega_r \cdot \Psi_q \\ \dot{\Psi}_q = u_q - r_1 \cdot I_q - \omega_r \cdot \Psi_d \\ \dot{\Psi}_d = -r'_2 \cdot i_{2d} \\ \dot{\Psi}_q = -r'_2 \cdot i_{2q} \\ T = \dfrac{3 \cdot p}{2} \cdot (\Psi_d \cdot I_q - \Psi_d \cdot I_d) \end{cases} \quad (2.9)$$

2.2.2. Study of LSPMSM asynchronous operation

When designing an LSPMSM there are two options available. The most popular one found in literature is an IM rotor retooling [SOULARD_02]. Since an LSPMSM can operate with the same stator and winding arrangement as an IM, the IM rotor can be replaced with an LSPMSM rotor [HENDERSHOT_10], [PYRHONEN_08], [DING_11], [HUNG_08], [TAKAHASHI_10]. The simplest way of the rotor modification is the embedding of PMs into the rotor core or onto its surface. This option expels the necessity of machine sizing from zero and permits to start the design process from a well-developed IM sizing procedure. The second option is to do a complete machine design like it has been demonstrated in [SORGDRAGER_14].

In order to reduce the number of discrete parameters and, hence, to limit the computation time, the design algorithm implemented to the LSPMSM models is based on the first method. Fig.2. 2 presents the LSPMSM design procedure proposed in this thesis.

As it has already been mentioned above, for economic reasons, the stator and windings of the LSPMPM are identical to the induction motor of the same power used at present in the electrical applications [SOULARD_02]. As the air-gap flux density contains a large third harmonic due to the rectangular magnet flux density shape the stator winding is star-connected in order to avoid the presence of this third harmonic into the line currents.

In the first step of designing, the data concerning the power (see Fig.2. 2) and the stator of the motor is to be entered. In the same time a user has to choose a configuration of the PMs into the rotor.

The second step is the IM sizing for the same power range. At this stage the same design methodology as for an IM can be applied. This allows to define the stator and winding geometry and the number of rotor bars and to choose a structure of the squirrel cage for a first approximation that gives the value of the rotor cage resistance and the level of saturation in rotor teeth.

As soon as the geometry of the rotor and PMs is known, the d- and q-axis reactances X_d and X_q and the no-load EMF E_0 can be calculated either analytically or computed using FEM. Thanks to these parameters and taking into account the braking torque induced

by the PMs, the start of the LSPMSM can be simulated. If the motor is not able to start, the designer has to go back either to the Stage 2 in order to change the rotor squirrel cage and, hence, to increase the starting torque or to the Stage 3 to resize the PMs and to reduce the breaking torque.

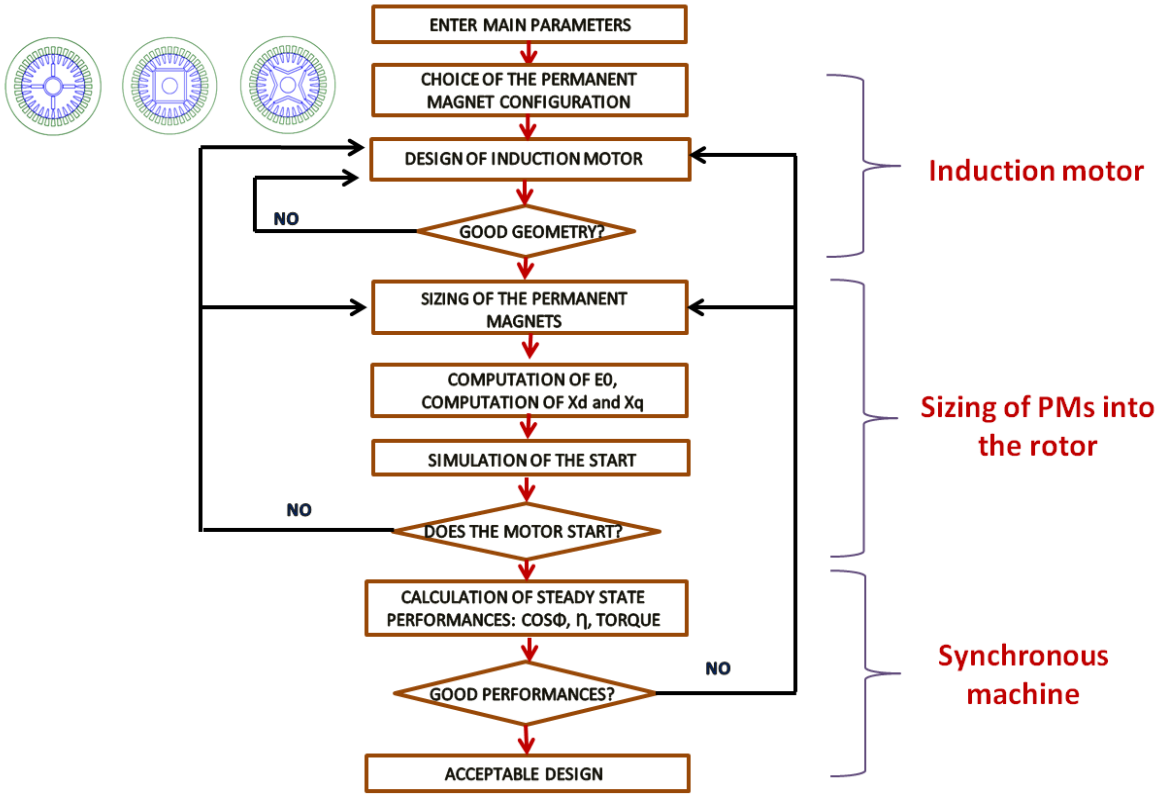

Fig.2. 2 Algorithm summarizing the design procedure

After the successful start of the LSPMSM, performances and steady-state characteristics are calculated and used for finding the optimal solution. Then, the design procedure must be repeated starting from the Stage 2. Every stage of the diagram will be more detailed below.

Algorithm of IM sizing

The LSPMSM contains both IM and PMSM component parts which can be designed separately. As it has been discussed in the previous chapters, once both rotor designs are done they can be combined into one rotor. According to Fig.2. 2, the first step for the design procedure is the sizing of an IM of the same power range that it is required by the specification. The slot number combinations follow the same concerns as in induction motors. Besides, it is generally favorable to have the number of rotor slots divisible by the number of poles, so that the poles are symmetric.

The workflow summarizing the procedure of IM sizing is outlined in Fig.2. 3. Complete description of the analytical approach for IM and an example of calculations are

presented in Appendix B. This approach can be applied for the design of a quite large range of IM. It was compiled using the methodologies proposed in [BOLDEA_10], [KOPILOV_86], [PYRHONEN_08].

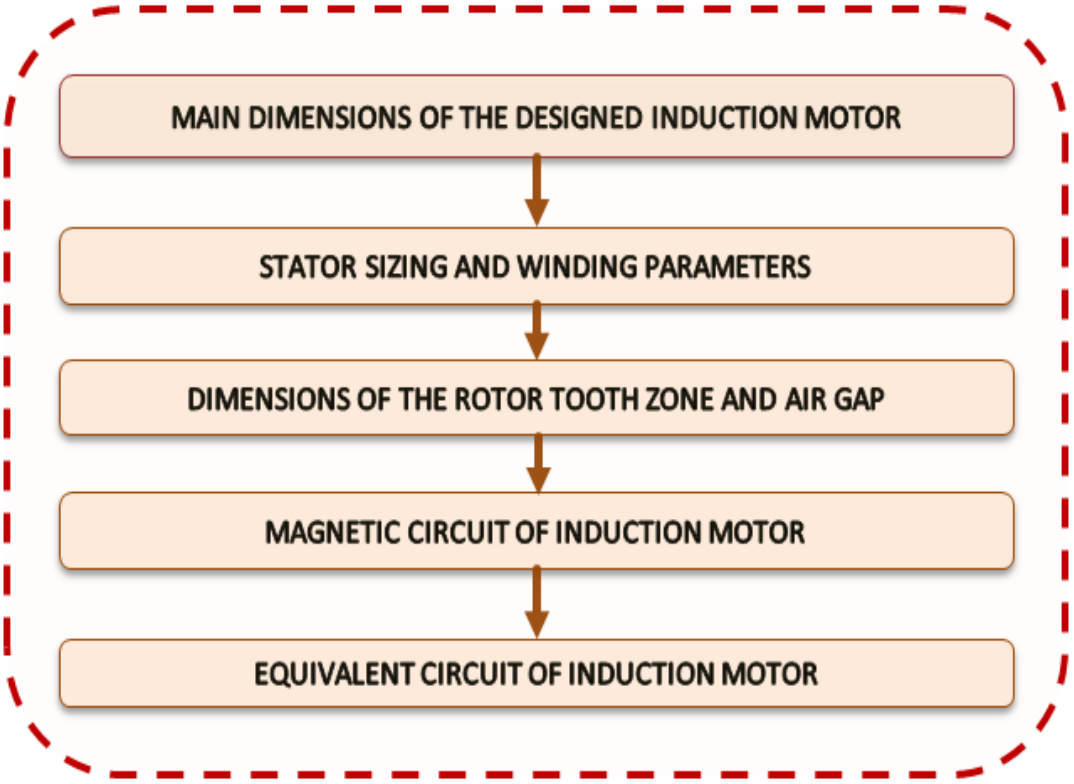

Fig.2. 3 Workflow summarizing the procedure of IM sizing

Results of the analytical design

The principal motor design parameters, obtained from the calculations represent in Appendix B, are given in Table 2. 1.

Table 2. 1 Principal motor design parameters of 4-pole, 7.5 kW IM

Design parameter	Value
Rotor diameter, D_2, mm	148.7
Stator outer diameter, D_a, mm	225
Airgap length, δ, mm	0.7
Number of stator slots, Z1	36
Number of stator slots, Z2	40
Core length, l_δ, mm	110

Fig.2. 4 illustrates the stator topology and windings distribution defined on the basis of the analytical approach. It gives an idea of the motor topology and its parameters in a first approximation. This approach also permits the calculation of starting torque and consequently, the determination of acceptable braking torque.

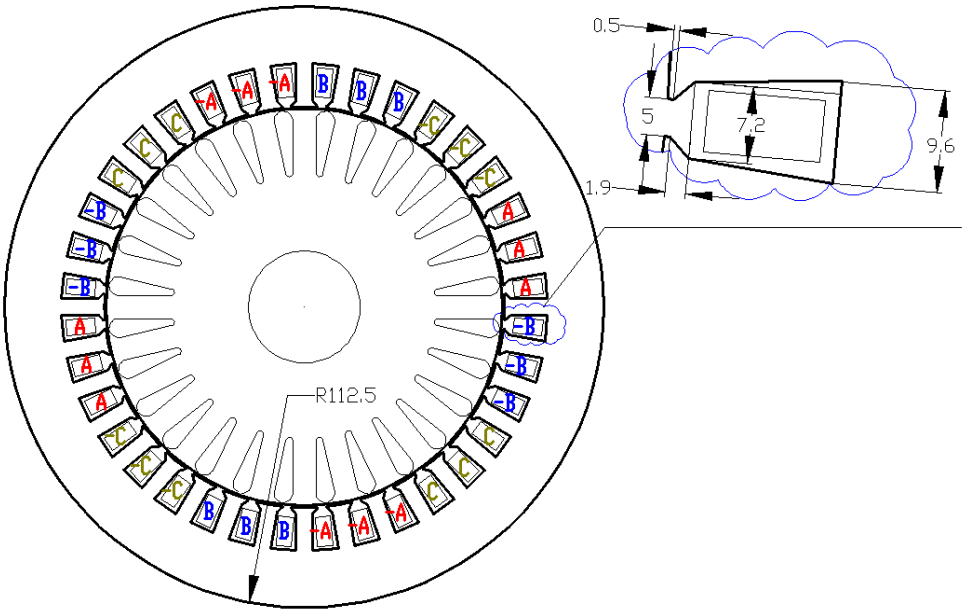

Fig.2. 4 Stator topology, windings distribution and approximate rotor configuration provided for the designing LSPMSM 7.5kW (**see Appendix B**)

Fig.2. 5 shows electrical parameters of T-type equivalent circuit of IM for one configuration: r_1, x_1 are the resistance and reactance of the stator, r_2/s is the equivalent resistance of the rotor, x_2 is the reactance of the rotor, and x_{12} is the magnetic reactance.

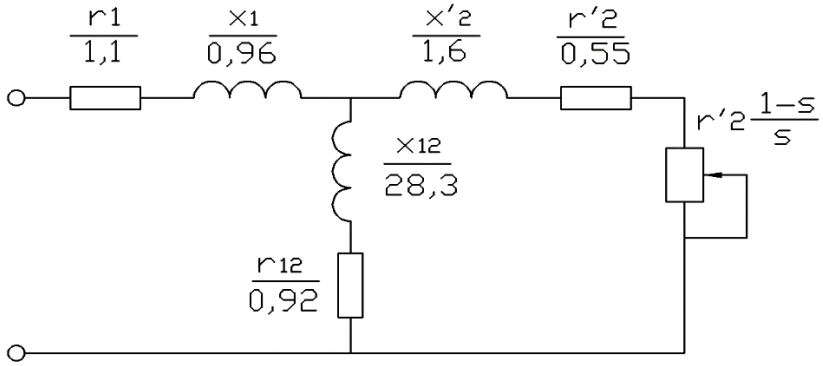

Fig.2. 5 Single-phase T-type equivalent circuit of IM

Table 2. 2 summarizes performances characteristics of 4-pole 7.5 kW IM model represented **in Appendix B**.

Table 2. 2 Performances characteristics of 4-pole 7.5 kW IM (analytical model)

Performances characteristics	Value
Starting current ratio I_{st}/I_{nom}	5.4
Starting torque ratio T_{st}/T_{nom}	1.64
Breakdown torque T_{bd}/T_{nom}	2.54

Fig.2. 6a illustrates the results of analytical modelling for 4-pole 7.5 kW IM. Points of the model are obtained with both high-fidelity industrial simulator ANSYS Maxwell/RMxprt [ZHOU 10] and the applied analytical model. The same approach is applied at the designing the 4-pole 18.5 kW IM (Fig.2. 6b).

On the whole, Fig.2. 6 shows a rather good agreement (maximal deviation is about 5% in the case of designing the 7.5 kW 4-pole IM and 3% in the case of designing the 18.5 kW 4-pole IM) between the results of the analytical calculations and those of the commercial software confirms that the presented method is suitable for the preliminary design and analysis of IM part in the LSPMSM design algorithm. The experimental verification of the model will be done in Chapter 3.

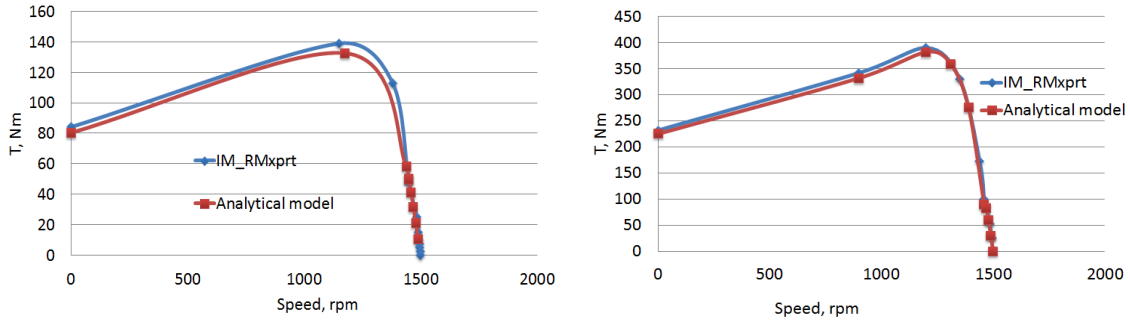

Fig.2. 6 Torque versus speed: (a) 7.5 kW 4-pole IM, (b) 18.5 kW 4-pole IM

2.2.3. Steady-State Model for the LSPMSM design

In steady-state conditions the LSPMSM is normally analyzed in the same way as a PMSM using a d-q model where the d-axis is aligned with the direction of permanent magnet flux. In general, the stator winding has three phase quantities and it can be transformed to rotor reference frame and vice versa by using Park's transformation (2. 1) [MODEER 07].

At a steady-state, the phasor diagram of LSPMSM can be depicted as shown in Fig.2. 7. The no-load phase EMF is

$$\underline{E}_0 = j \cdot E_0 = j \cdot \omega \cdot \Psi_d \quad (2.10)$$

where Ψ_d is the flux linkage due to the fundamental component of d-axis flux produced by the permanent magnet. All the equations in this section are reorganized from the references [STOIA 09], [GIERAS 10].

The voltage equation of LSPMSM motor is:

$$\underline{U} = \underline{E}_0 + r_1 \cdot \underline{I} + j(X_d \cdot \underline{I}_d + X_q \cdot \underline{I}_q) \quad (2.11)$$

Or

$$\underline{U} = \underline{E}_0 + r_1 \cdot \underline{I} + jX_\sigma \cdot \underline{I} + j(X_{ad} \cdot \underline{I}_d + X_{aq} \cdot \underline{I}_q) \quad (2.12)$$

Where X_σ is leakage reactance, X_{ad} and X_{aq} are d-axis and q-axis components of X_d and X_q reactances.

Thanks to the set of equations (2. 11), (2. 12) a vector diagram of LSPMSM can be plotted as shown in Fig.2. 7.

Correspondingly the vector diagram:

$$\underline{U} = \underline{E}_0 + jX_\sigma \underline{I} + \underline{I}_d \cdot (r_1 + jX_{aq}) + \underline{I}_q (r_1 + jX_{ad}) \quad (2.13)$$

$$\underline{E}_f = \underline{U} - r_1 \cdot \underline{I} - jX_\sigma \cdot \underline{I} \quad (2.14)$$

$$\underline{U}_s = \underline{E}_0 + j(X_{ad} \cdot \underline{I}_d + X_{aq} \cdot \underline{I}_q) \quad (2.15)$$

$$\underline{I} = \underline{I}_d + \underline{I}_q = \underline{I}_a + \underline{I}_r \quad (2.16)$$

$$\underline{I}_d = \underline{I} \cdot sin\psi \quad (2.17)$$

$$\underline{I}_q = \underline{I} \cdot cos\psi \quad (2.18)$$

where ψ is power angle.

The input voltage projections on the d-axis and q-axis are

$$U \cdot sin\theta = I_d \cdot r_1 + I_q \cdot X_q \quad (2.19)$$

$$U \cdot cos\theta = \underline{E}_0 - I_d \cdot X_d + I_q \cdot X_q \quad (2.20)$$

where θ is internal angle of the synchronous motor.

Solving eqs. (2. 19), (2. 20) one can find the components of the currents I_d, I_q

$$I_d = \frac{U(X_q cos\theta - r_1 sin\theta) - E_0 X_q}{X_d X_q + r_1^2} \quad (2.21)$$

$$I_q = \frac{U(r_1 cos\theta + X_d sin\theta) - E_0 r_1}{X_d X_q + r_1^2} \quad (2.22)$$

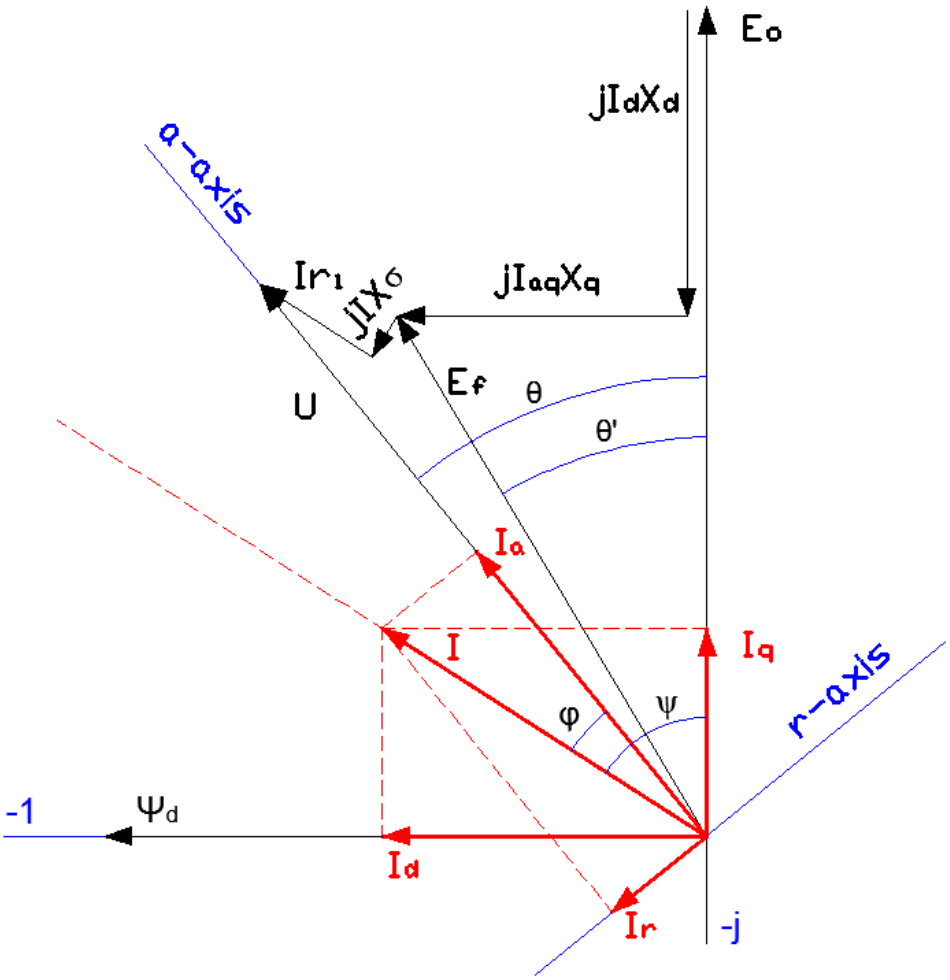

Fig.2. 7 Vector diagram of line-start permanent magnet synchronous motor [STOIA_09]

As it can be seen from the vector diagram, the vector of the input current I can be decomposed in two components, namely the active component I_a and the reactive component I_r.

$$I = \frac{P_{em}}{\sqrt{3}U} = \sqrt{I_a^2 + I_r^2} = \sqrt{I_d^2 + I_q^2} \tag{2. 23}$$

From (2. 21) - (2. 23) it can be deduced

$$\mathrm{I} = \frac{\mathrm{U}}{X_d \cdot X_q + r_1^2} \cdot [(X_q \cdot cos\theta - r_1 \cdot sin\theta - E_0 \cdot X_q)^2 + (r_1 \cdot cos\theta + X_d \cdot sin\theta - E_0 \cdot r_1)^2]^{1/2} \tag{2. 24}$$

By neglecting the armature resistance and the leakage reactance, the components I_a and I_r of the input current are

$$I_a = \left[\frac{E_0}{X_{ad}} - \frac{U}{X_{ad}}\left(1 - \frac{X_{ad}}{X_{aq}}\right)\cdot cos\theta\right] sin\theta \quad (2.25)$$

$$I_r = \left[\frac{U}{X_{ad}} - \frac{E_0}{X_{ad}} - \frac{U}{X_{ad}}\left(1 - \frac{X_{ad}}{X_{aq}}\right)\cdot cos\theta\right] sin\theta \quad (2.26)$$

Electromagnetic torque

The vector diagram in Fig.2. 7 can also be used for determination of the input power:

$$P_{in} = 3 \cdot U \cdot I \cdot cos\varphi = 3 \cdot U \cdot (I_q \cdot cos\theta - I_d \cdot sin\theta) \quad (2.27)$$

From (2. 24)-(2. 27) it follows that input power is

$$P_{in} = 3 \cdot [E_0 \cdot I_q + r_1 \cdot I^2 + I_d \cdot I_q (X_d - X_q)] \quad (2.28)$$

Because of neglected stator core losses, the electromagnetic power given by the terminal power lowered by the stator winding losses:

$$\Delta P_{joule} = 3 \cdot r_1 \cdot I^2 = 3 \cdot r_1 \cdot (I_d^2 + I_q^2) \quad (2.29)$$

$$P_{em} = P_{in} - \Delta P_{joule} = 3 \cdot [E_0 \cdot I_q - I_d \cdot I_q (X_d - X_q)] \quad (2.30)$$

At steady-state synchronous operation, the resulting torque T_{pm} that rotates a LSPMSM combines the permanent magnet alignment torque generated by the PMs and the synchronous reluctance torque Tr. It was found that the synchronous loading capability is deeply influenced by the back EMF and the q-axis current.

When the LSPMSM is designed with different d- and q-axis, an additional provided reluctance torque appears. It is proportional to the difference between the d-axis and the q-axis reactances $X_d - X_q$.

Assume that there are no armature losses, and then the total output torque developed by a salient-pole synchronous motor is

$$T_{em} = T_{PM} + T_r =$$

$$= \frac{P_{em}}{2\pi n_s} = \frac{3}{2\pi n_s}\left[\frac{U \cdot E_0}{X_d} sin\theta + \frac{U^2}{2}\left(\frac{1}{X_d} - \frac{1}{X_q}\right)\cdot sin2\theta\right] \quad (2.31)$$

The total output torque can be also expressed as

$$T_{em} = \frac{3 \cdot E_0 \cdot I}{\Omega} \cdot cos\psi + \frac{3}{2 \cdot \Omega}(X_d - X_q) \cdot I^2 \cdot sin\psi \quad (2.32)$$

Where Ω is the synchronous angular speed and n_s is synchronous speed

$$\Omega = 2 \cdot \pi \cdot n_s \quad (2.33)$$

For the LSPMSM with a surface magnet rotor, L_d is almost the same as L_q, thus the reluctance torque term is insignificant. In a LSPMSM using an embedded magnet rotor, L_d is lower than L_q as the magnetic flux flowing along the d-axis has to cross through

the magnet cavities in addition to the rotor air-gap, while the magnetic flux of the q-axis only crosses the air-gap [HUANG_08].

Eq. (2. 31) shows that the period of the reluctance torque is one half of that of the PM generated torque. Fig.2. 8 proves that an interior magnet type LSPMSM can achieve higher torque than a surface mounted LSPMSM which does not have any reluctant torque component. However, the appearance of the reluctance torque does not mean that the interior magnet type can have higher power density than surface mounted LSPMSM because the magnet flux linkage in LSIPMSM is not the same as that in the surface mounted LSPMSM with the same magnet volume. Eq (2. 32) is another form of the torque equation (2. 31) and suggested by [HENDERSHOT_10] and showing that the total torque of a LSPMSM is increased due to the saliency of the rotor.

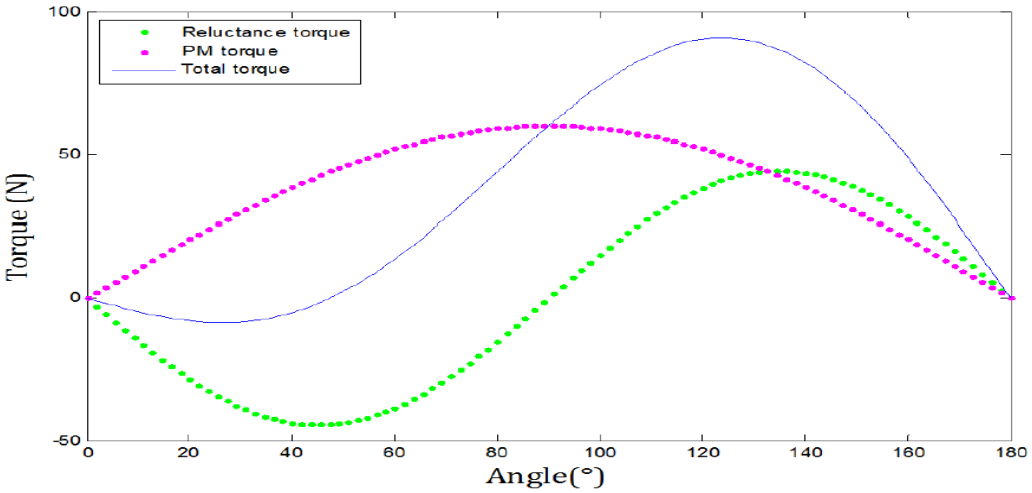

Fig.2. 8 Torque-angle characteristics of a LSPMSM

2.2.4. Analytical calculation of electromagnetic parameters

In Chapter 1 there was chosen 3 LSPMSM rotor configurations meeting the major part of specification requirements and having a high product of power factor and efficiency were preselected in Chapter 1(see Fig.2. 9).

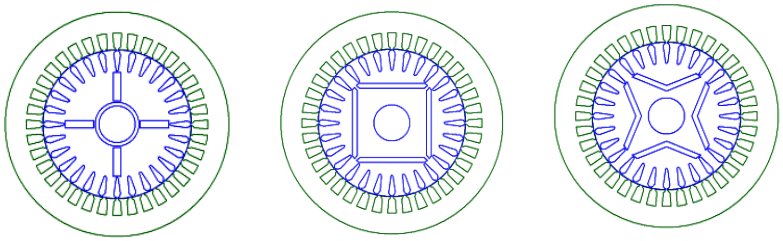

a) b) c)

Fig.2. 9 LSPMSM rotor configurations under study: (a) rotor with radial magnetic circuit structure, (b) rotor with series-type magnetic circuit structure, (c) rotor with V-type magnetic circuit structure

In this paragraph the three analytical models for each LSPMSM rotor topology are developed with the aid of common electromagnetic laws and taking into account geometry of each of motors. The magnetic equivalent circuit will be deduced for each studied rotor shape.

After every section devoted to one of three rotor topologies, the results of analytical models are compared with the results issued from a commercial software and providing from a finite element modeling.

LSPMSM with radial magnetic circuit structure

As it has already been discussed in the previous paragraph, the flux linkage and reluctance are the key parameters to determine the steady-state characteristics of a LSPMSM. Using the magnetic equivalent circuit is the most common method for the determination of these parameters [HENDERSHOT 10], [FODOREAN 09], [HEIKKILA 02], [CARPENTER 12].

Fig.2. 10 shows a simplified one pole scheme of a LSPMSM with a radial magnetic circuit structure.

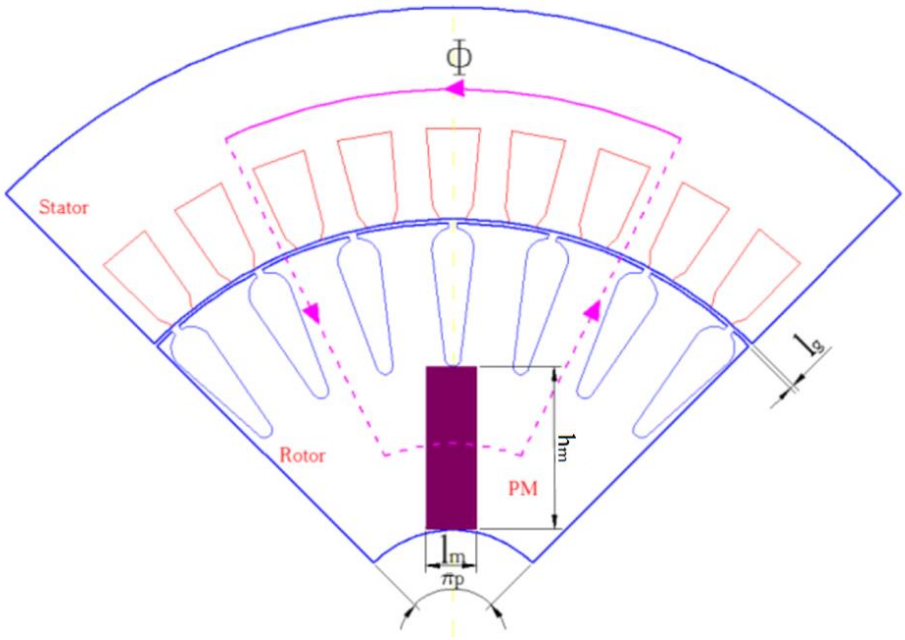

Fig.2. 10 Simplified structure of a LSIPMSM with tangential magnetization

By Gauss's law and neglecting leakage and presence of rotor bar, the total flux from the permanent magnet travels through a half part of the air-gap as shown in eq.(2. 34) [FODOREAN 09], [GIERAS 10].

$$B_m \cdot h_m = B_g \frac{\pi \cdot R_2}{2p} \tag{2. 34}$$

Where R_2 is the rotor radius.

According to Ampere's law

$$l_m \cdot H_m + 2 \cdot l_g \cdot H_g = 0 \tag{2. 35}$$

The linearly approximated equation of demagnetization curve for PM is given by

$$B_m = B_r + \mu_0 \cdot \mu_m \cdot H_m \tag{2. 36}$$

Where B_m is PMs flux density, H_m is magnetic field strength of PMs, μ_0 is the permeability of vacuum, μ_m is relative magnetic permeability. Substituting eq.(2. 36) in eq.(2. 35):

$$\frac{B_m - B_r}{\mu_0 \cdot \mu_r} l_m + 2\frac{B_g}{\mu_0} \cdot l_g = 0 \tag{2. 37}$$

When combining (2. 34) and (2. 37), the air-gap flux density is

$$B_g = \frac{B_r}{\frac{\pi \cdot R_2}{2p} + \frac{2 \cdot \mu_r \cdot l_g}{l_m}} \tag{2. 38}$$

Air-gap flux density (2. 38) can be obtained from the simplified equivalent magnetic circuit (Fig.2. 11). As the magnetic flux from the rotor passes only a half part in the air gap, the air-gap reluctance with one half width of the one pole would be two times of the one pole air-gap reluctance R_g, which is expressed by (2. 39).

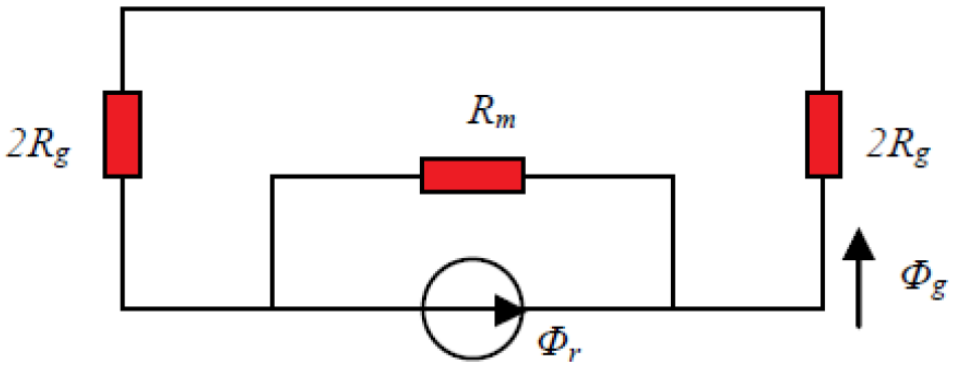

Fig.2. 11 Equivalent magnetic circuit of a LSIPMSM with tangential magnetization (leakage through the bridges are not taken into account)

$$R_g = \frac{k_c \cdot l_g}{\frac{\pi \cdot \mu_0 \cdot R_2 \cdot l_\delta}{p}} \tag{2. 39}$$

Where k_c is the Carter factor which takes into account the increased reluctance due to slotting, l_g is the air gap thickness, l_δ is the active rotor length, l_m is magnet length, h_m is magnet height. The Carter factor can be found according to the algorithm presented in Appendix B.

The PM remanent flux and the PM reluctance are as follows

$$\Phi_r = B_r h_m l_\delta \tag{2. 40}$$

$$R_m = \frac{l_m}{\mu_0 \mu_r H_m l_\delta} \tag{2. 41}$$

Usually the bridges are fully saturated under nominal conditions and behave like the air. Neglecting the leakage through the bridge of the rotor (Fig.2. 11) the air-gap flux density is

$$\Phi_g = \Phi_r \frac{R_m}{R_m + 4R_g} \tag{2. 42}$$

It has been talking above that the magnet fluxes and the EMF could be analytically expressed as function of the studied machine geometry. The magnets produce a flux which is divided into a "useful" component circulating through the stator and which participates in the energy conversion, and a leakage component via the non-ferromagnetic hub and the magnetic shaft, that does not participate in electromechanical conversion. The flux lines are supposed to be purely radial in all air gaps, whose lengths are considered constant. A principle scheme used for analytical model in case of LSPMSM with radial magnet structure is represented in Fig.2. 12.

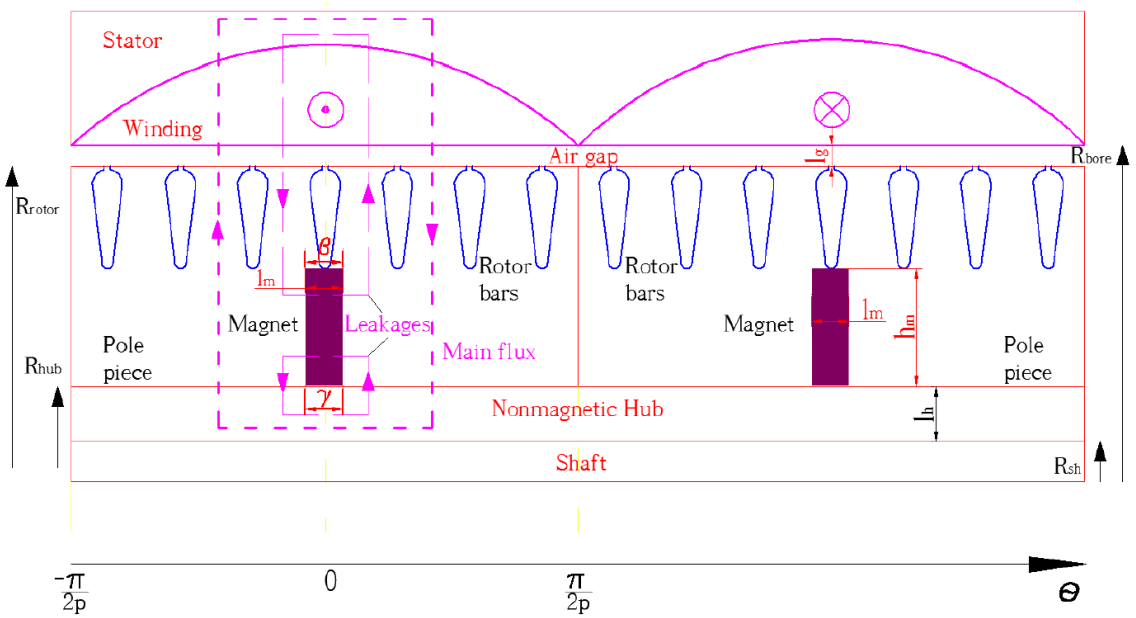

Fig.2. 12 Flux line calculation scheme of magnetic flux density due to PM for a LSPMSM with radial magnet structure [JANNOT_09].

Several assumptions should be made in order to simplify analytical calculations. The magnetic cores are regarded as not saturated, thus the surfaces of the pole pieces are equipotential. Furthermore, the decrease of the magnetic flux density in front of the magnets is considered linear. Besides despite of having the rotor bars the distribution of the magnetic flux in the rotor during the steady state is stated as uniform [JANNOT_09].

Due to assumptions made above and using the flux line calculation scheme (Fig.2. 12) the Ampere's theorem is

$$\begin{cases} h_m \cdot l_m + 2 \cdot H_h \cdot k_c \cdot l_\delta = 0 \\ h_m l_m + 2 \cdot H_g \cdot k_c \cdot l_g = 0 \end{cases} \quad (2.\ 43)$$

The flux conservation law is:

$$\begin{cases} \phi_m = \phi_{sh} + \phi_g \\ \phi_m = B_m \cdot h_m \cdot l_\delta \\ \phi_{sh} = l_\delta \int_0^{\frac{\pi}{2p}-\gamma} B_{sh} \cdot R_{sh} d\theta \\ \phi_g = B_g \cdot R_2 \cdot \beta \cdot l_\delta + l_\delta \int_0^{\frac{\pi}{2p}-\beta} B_g \cdot R_2 d\theta \end{cases} \quad (2.\ 44)$$

Where the *g*, *sh* and *m* subscripts deal, respectively, with the air gap, shaft and magnet quantities. Geometrical coefficients γ and β used in (2. 44) can be calculated as follows in (2. 45):

$$\begin{cases} \gamma = \frac{1}{R_{sh}} \frac{l_m}{2} \\ \beta = \frac{1}{R_2} \frac{l_m}{2} \end{cases} \quad (2.\ 45)$$

Where l_m is magnet width, h_m is magnet height, R_{sh} is external shift radius. It is necessary to add material behavior laws (2. 46) to close the system of Eqs. (2. 43)-(2. 45).

$$\begin{cases} B_m = B_r + \mu_0 \mu_r h_m \\ B_g = \mu_0 H_g \\ B_{sh} = \mu_0 H_{sh} \end{cases} \quad (2.\ 46)$$

Where B_r is remanent magnetization. Combining Eqs. (2. 43), (2. 44) and (2. 46) with geometrical relations (2. 45), the flat-topped value of the flux density waveform, due to magnets, is given in (2. 47) [JANNOT 10].

$$B_g = \frac{2B_r l_m l_h h_m p}{4k_c l_g l_h h_m \mu_m p - 2\gamma k_c l_g l_m p R_{sh} + k_c l_g l_m \pi R_{sh} - 2\beta l_m l_h p R_2 + l_m l_h \pi R_2} \quad (2.\ 47)$$

Appling the fast Fourier transform (FFT) for Eq. (2. 47) the fundamental harmonic of the flux density in the air gap is

$$B_{g1} = \frac{4}{\pi} B_g sin\frac{\alpha\pi}{2} \quad (2.\ 48)$$

where $\alpha = 2/\pi$ is the ratio of the average-to-maximum value of the normal component of the air gap magnetic flux density.

According to the trapezoidal waveform of the flux density and the expression of the top plate Eq. (2. 47) the fundamental of the linkage flux through the stator is directly derived from the set of equations (2. 46) and gives (2. 49).

$$\Psi_1 = \frac{16N_s k_w R_{bore} l_\delta B_r l_m l_h h_m sin(\beta p)}{\beta p \pi \left(l_g(4l_h h_m \mu_m p) + l_m(-2\gamma p + \pi)R_h\right) + l_h h_m \pi R_2} \quad (2.\ 49)$$

where N_s is slot number, k_w is global winding coefficient, R_{bore} is bore radius. To finalize calculations one can apply the Boucherot's formula, which is a special case of Faraday's law. As so the EMF expression is (2. 50).

$$E_0 = \frac{32 f N_s k_w R_{bore} l_\delta B_r l_m l_h h_m sin(\beta p)}{\beta p \pi \left(l_g(4l_h H_m \mu_m p) + l_m(-2\gamma p + \pi)R_h\right) + l_h h_m \pi R_2} \quad (2.\ 50)$$

where f - electric frequency. All the expressions derived in this sub-section incorporate leakage flux in the hub.

In the motor with a such configuration, the resulting armature reaction flux is oriented into the line with the d-axis when PMs are removed from their locus and replaced with non-ferromagnetic material. The magnetic flux flows through the space dedicated to magnets and also through the shaft. After some combinations, the synchronous inductance can be expressed as a function of the machine geometry and winding arrangement could be founded:

$$L_d = \frac{6\mu_0 R_{bore} l_\delta N_s^2 k_{ws}^2}{l_g \pi^2 p^2}\left[-2\beta p + \pi + \frac{4sin(p\beta)^2}{p\beta} - sin(2p\beta) - \right. \\ \left. - \frac{8 l_m l_h R_2 sin(p\beta)}{p\beta(4l_g l_h h_m p + l_h l_m \pi R_2 - 2\gamma l_g l_m p R_h + l_m l_g \pi R_h)}\right] \quad (2.\ 51)$$

The same approach may be used for determination of the q-axis synchronous inductance. Now the resulting armature reaction flux is completely oriented in line with the q-axis. In this position, it is admitted that there is no flux leakage because the magnetic field is almost always circulating in the iron parts of the rotor and the stator.

As for the d-axis, the q-axis synchronous inductance can be calculated as in eq.(2. 52), for all the phases, and is a function of machine geometry and winding arrangement.

$$L_q = \frac{6\mu_0 R_{bore} l_\delta N_s^2 k_{ws}^2}{l_g \pi^2 p^2}[\pi - 2\beta p - sin(2p\beta) + \\ \frac{2(6l_g + \beta\pi R_{bore} - 2(4l_g + \beta\pi R_{bore})cos(\beta\pi) + (2l_g + \beta\pi R_{bore})(cos(\beta\pi) + \beta\pi sin(2p\beta)))}{p\beta(2l_g + \beta\pi R_{bore})l_g\pi^2}] \quad (2.\ 52)$$

Comparison of analytical model with results of commercial software and FE simulations in the case of LSPMSM 7.5kW and 18.5kW with radial magnetic circuit structure

The estimation of the X_{ad},X_{aq} reactances for two LSPMSMs of 7.5kW and respectively 18.5kW with radial magnetic circuit structure has been done using the commercial software ANSYS RMxprt (Fig.2. 13, Fig.2. 15) and by FE analysis accomplished by ANSYS Maxwell software and its **Electric Machines Design Toolkit/** D-Q Solution Calculation Method [MAXWELL 16] (Fig.2. 14. Fig.2. 16). The comparison of the results is summarized in Table 2. 3 and Table 2. 4.

LSPMSM 7.5kW with radial magnetic circuit structure

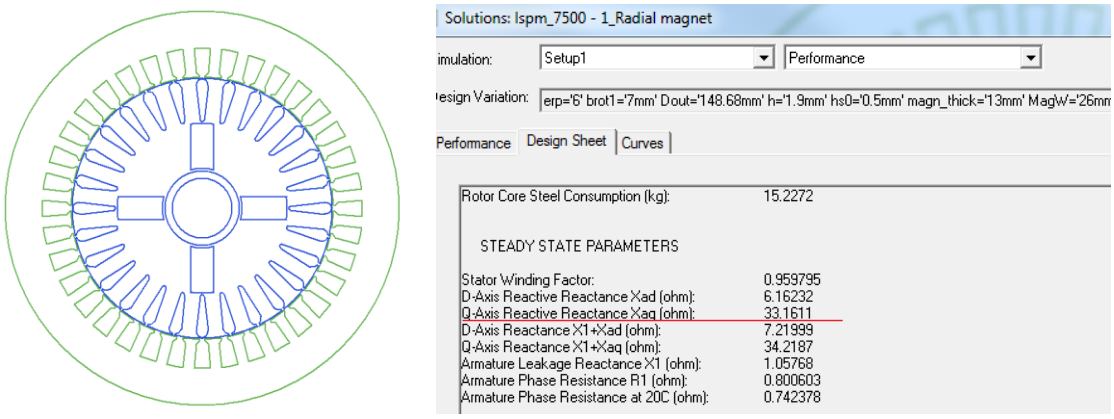

Fig.2. 13 X_{ad}, X_{aq} reactances given by ANSYS RMxprt for LSPMSM 7.5kW with radial magnetic circuit structure

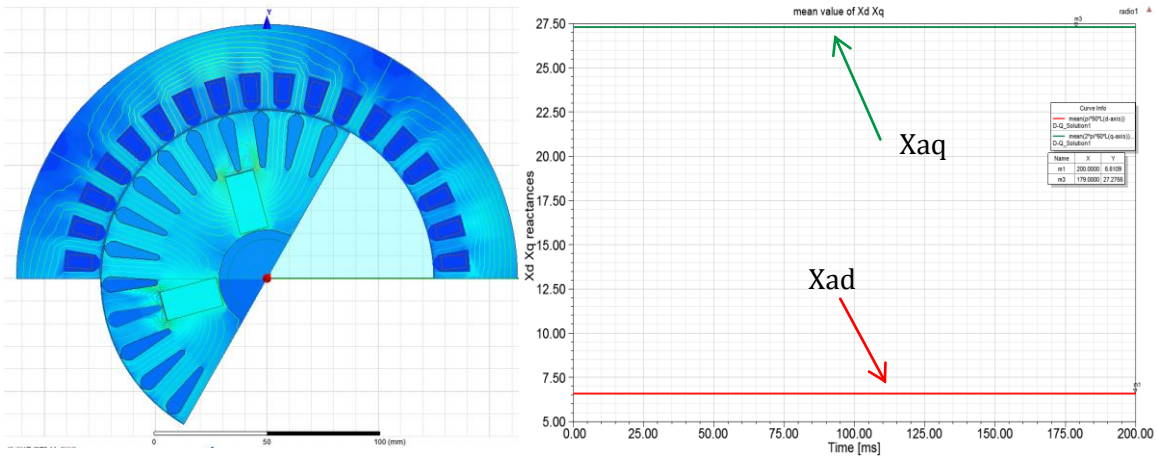

Fig.2. 14 Mean value of X_{ad}, X_{aq} reactances given by ANSYS Maxwell for LSPMSM 7.5kW with a radial magnetic circuit structure

Table 2. 3 Comparison of the results. LSPMSM 7.5kW with a radial magnetic circuit structure

	Parameter				
	Air gap, mm	lm, mm	hm, mm	Xad, Ohm	Xaq, Ohm
Analytical Model	0.7	13	26	7.2	30.9
ANSYS RMxprt	0.7	13	26	6.2	33.2
ANSYS Maxwell	0.7	13	26	6.6	27.3

LSPMSM 18.5kW with radial magnetic circuit structure

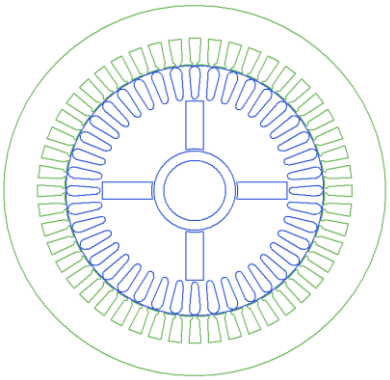

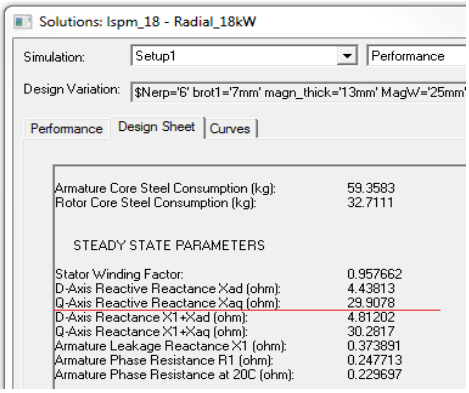

Fig.2. 15 X_{ad}, X_{aq} reactances given by ANSYS RMxprt for LSPMSM 18.5kW with a radial magnetic circuit structure

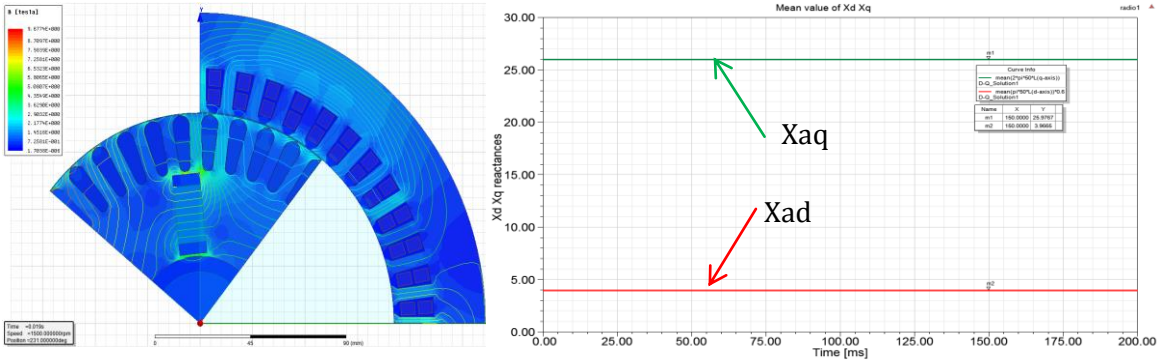

Fig.2. 16 Mean value of X_{ad}, X_{aq} reactances given by ANSYS Maxwell for LSPMSM 18.5kW with a radial magnetic circuit structure

Table 2. 4 Comparison of the results. LSPMSM 18.5kW with a radial magnetic circuit structure

	Parameter				
	Air gap, mm	**l_m, mm**	**h_m, mm**	**Xad, Ohm**	**Xaq, Ohm**
Analytical Model	0.5	13	25	4.1	28.2
ANSYS RMxprt	0.5	13	25	4.4	29.9
ANSYS Maxwell	0.5	13	25	4.0	26.0

LSPMSM with series magnetic circuit structure

The analytical calculations of inductances values for a LSPMSM with series magnetic circuit structure is based on the analytical expressions for the average air gap flux density and the permeance coefficients. Fig.2. 17 shows a cross section of this topology with one half of two magnets, the associated stator and rotor back iron. In this configuration the buried magnets are magnetized across their shorter dimensions along the d-axis.

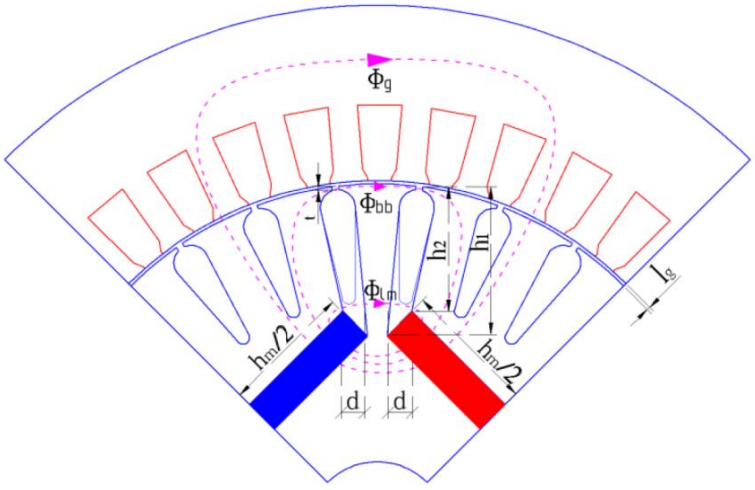

Fig.2. 17 Magnetic flux distributions in the cross section of the LSPMSM with series magnetic circuit structure

The equivalent magnetic circuit is shown in Fig.2. 18, where R_r and R_s are the reluctances of the rotor and stator back irons, respectively, $2R_g$ is the reluctance of the one-half of air gap with compensation for slotting, $2R_m$ is the reluctance of the one-half of a magnet, R_{lm} is the reluctance modelling the flux leakage through the air under the bridge and R_{bb} is the reluctance modelling the flux leakage through the bridge [HADEF 11], [HWANG 02].

Taking as a hypothesis the stator and rotor steel are infinitely permeable everywhere excepting in the bridge between the pole pieces. The flux drops along the stator and rotor yokes can be neglected and the air gap flux Φ_g is related to the remanent magnet flux Φ_r by eq. (2. 53).

$$\Phi_g = \Phi_r \frac{1}{1+\beta(1+2\eta+4\lambda)} \tag{2. 53}$$

In this equation $\beta = R_g/R_m$ is the reluctance ratio, $\eta = R_m/R_{lm}$ and $\lambda = R_m/R_{bb}$ are the leakage flux ratios. The average air gap flux density is given by

$$B_g = B_r \frac{C_\phi}{1+\beta(1+2\eta+4\lambda)} \tag{2. 54}$$

where B_r is remeance of the magnet and $C_\phi = A_m/A_g$ is the flux concentration factor, A_g and A_m are the cross-sectional areas per pole of the air gap and magnet, respectively.

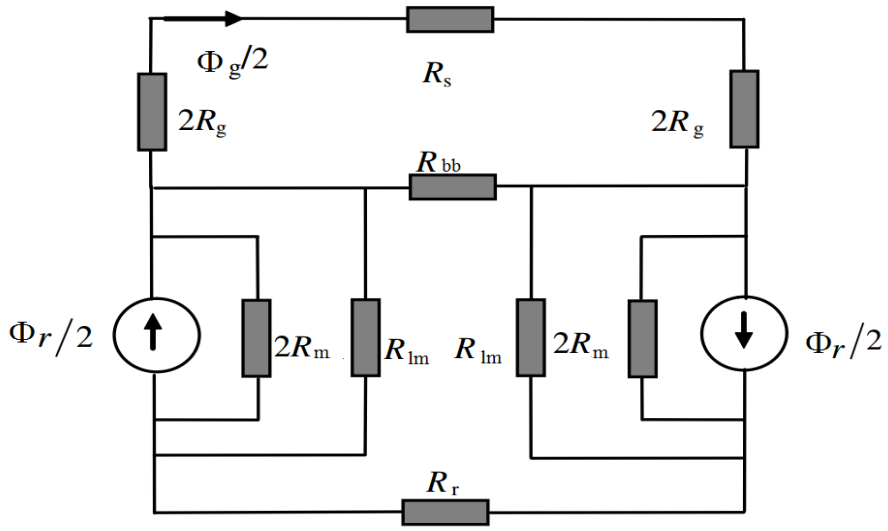

Fig.2. 18 Equivalent circuit of LSPMSM with the series magnetic circuit structure [HWANG 02]

The corresponding magnet flux density B_m in the magnet is determined as

$$B_m = B_r \frac{1+\beta(2\eta+4\lambda)}{1+\beta(1+2\eta+4\lambda)} \tag{2. 55}$$

The leakage flux through the bridge between pole pieces as is illustrated in Fig.2. 18 is given in eq. (2. 56).

$$\Phi_{bb} = \Phi_r \frac{2\beta\lambda}{1+\beta(1+2\eta+4\lambda)} \tag{2. 56}$$

From Eq. (2. 56) the average flux density B_{bdg} within the bridge is

$$B_{bdg} = B_r \frac{\Phi_{bb}}{A_{bdg}} \frac{2\beta\lambda}{1+\beta(1+2\eta+4\lambda)} \frac{A_m}{A_{bdg}} \tag{2.57}$$

where $A_{bdg} = t \cdot R_{st}$ denotes the cross-sectional area of the bridge and t and R_{st} are the bridge width and the stack length respectively. From eq. (2. 57) λ can be expressed as

$$\lambda = \Phi_r \frac{1+1/\beta+2\eta}{2(A_m/A_{bdg})(B_r/B_{bdg})-4} \tag{2.58}$$

If the level of leakage flux through the bridge is limited to the flux density saturation level of B_{sat}, then

$$\lambda \cong \Phi_r \frac{1+1/\beta+2\eta}{2(A_m/A_{bdg})(B_r/B_{sat})-4} \tag{2.59}$$

The air-gap reluctance R_g is expressed as

$$R_g = \frac{l_g k_c}{\mu_0 A_g} \tag{2.60}$$

Consider Fig.2. 18.

$$R_m = \frac{l_m}{\mu_0 \mu_{rec} A_m} \tag{2.61}$$

The reluctance of the air flux barriers under bridge is approximated as follows from

$$R_{lm} = \frac{4d}{\mu_0 l_\delta (h_1+h_2)} \tag{2.62}$$

and hence

$$\eta = \frac{(h_1+h_2)l_m}{4d\mu_{rec}h_m} \tag{2.63}$$

$$\beta = \frac{R_g}{R_{lm}} = \frac{\mu_{rec} l_g k_c}{l_m} C_\phi \tag{2.64}$$

where $A_g = \alpha \cdot R_2 \cdot l_\delta / p$, $A_m = h_m \cdot l_\delta$, α is the pole-arc to pole-pitch ratio.

The amplitude of the fundamental component of the air gap flux due to the magnet acting alone is

$$B_{g1} = k_1 B_g = k_1 B_r \frac{C_\phi}{1+\beta(1+2\eta+4\lambda)} \tag{2.65}$$

where $k_1=4/\pi \sin(\alpha\,\pi/2)$. Hence the amplitude of the fundamental flux per pole is

$$\Phi_{g1} = B_{g1}\frac{D \cdot B_{g1}}{p} \tag{2. 66}$$

For a winding with N_s series turns per phase and a winding factor k_w, the open circuit EMF per phase is

$$E_0 = \frac{2\pi}{\sqrt{2}} k_w N_s \Phi_{g1} f \tag{2. 67}$$

The direct and quadrature synchronous reactances could be found as a function of the machine geometry and winding arrangement:

$$X_d = \frac{12R_b l_\delta f \mu_0 k_w^2 N_s^2}{p^2 l_{gd}^{"}} + X_a \tag{2. 68}$$

$$X_q = \frac{12R_b l_\delta f \mu_0 k_w^2 N_s^2}{p^2 l_{gq}^{"}} + X_a \tag{2. 69}$$

Where the armature reactance X_a is the same as for a cylindrical-rotor synchronous machine,$l_{gd}^{"}$, $l_{gq}^{"}$ are equivalent d- and q-axis air gap thicknesses, k_{1ad}, k_{1aq}, k_{ad} are the factors of the armature reaction

$$X_a = 4m_1\mu_0 f \frac{L_\delta \tau k_w^2 N_s^2}{p\pi l_g} \tag{2. 70}$$

$$l_{gd}^{"} = \frac{k_c l_g}{k_{1ad} - (k_1 k_{ad}/(1 + 2\eta + 4\lambda))} \tag{2. 71}$$

$$l_{gq}^{"} = \frac{k_c l_g}{k_{1aq}} \tag{2. 72}$$

$$k_{1ad} = \alpha + \frac{\sin(\alpha\pi)}{\pi} \tag{2. 73}$$

$$k_{1aq} = \alpha + 0.1 + \frac{\sin(0.1\pi) - \sin(\alpha\pi)}{\pi} \tag{2. 74}$$

$$k_{ad} = \frac{\sin(\alpha\pi/2)}{\alpha\pi/2} \tag{2. 75}$$

Comparison of analytical model with results of commercial software and FE simulations in the case of LSPMSM 7.5kW and 18.5kW with radial magnetic circuit structure

LSPMSM 7.5kW with series magnetic circuit structure

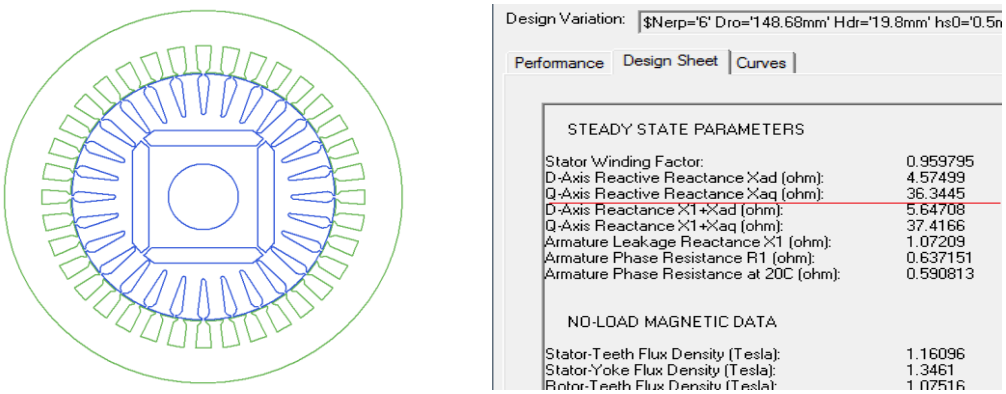

Fig.2. 19 X_{ad}, X_{aq} reactances given by ANSYS RMxprt for LSPMSM 7.5kW with series magnetic circuit structure

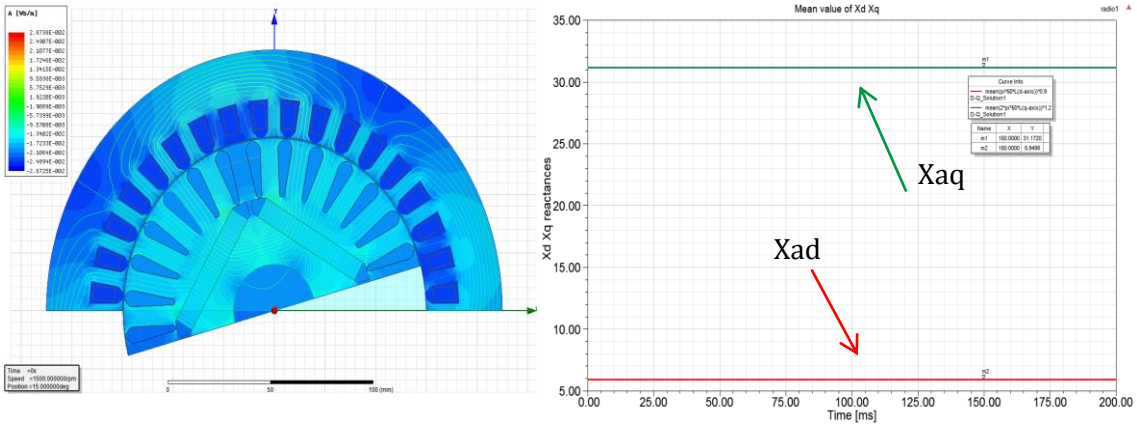

Fig.2. 20 Mean value of X_{ad}, X_{aq} reactances given by ANSYS Maxwell for LSPMSM 7.5kW with series magnetic circuit structure

Table 2. 5 Comparison of the results. LSPMSM 7.5kW with series magnetic circuit structure

	Parameter				
	Air gap, mm	lm, mm	hm, mm	Xad, Ohm	Xaq, Ohm
Analytical Model	0.6	55	9	6.1	36.4
ANSYS RMxprt	0.6	55	9	6.1	40.57
ANSYS Maxwell	0.6	55	9	6.0	31.2

LSPMSM 18.5kW with series magnetic circuit structure

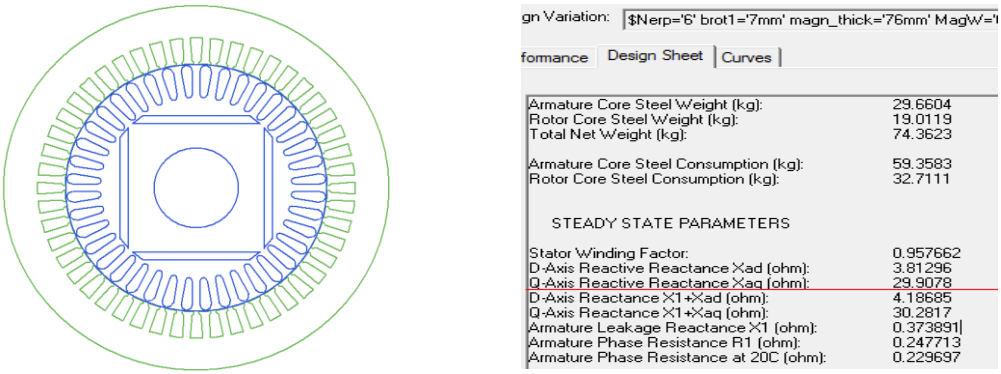

Fig.2. 21 X_{ad}, X_{aq} reactances given by ANSYS RMxprt for LSPMSM 18.5kW with series magnetic circuit structure

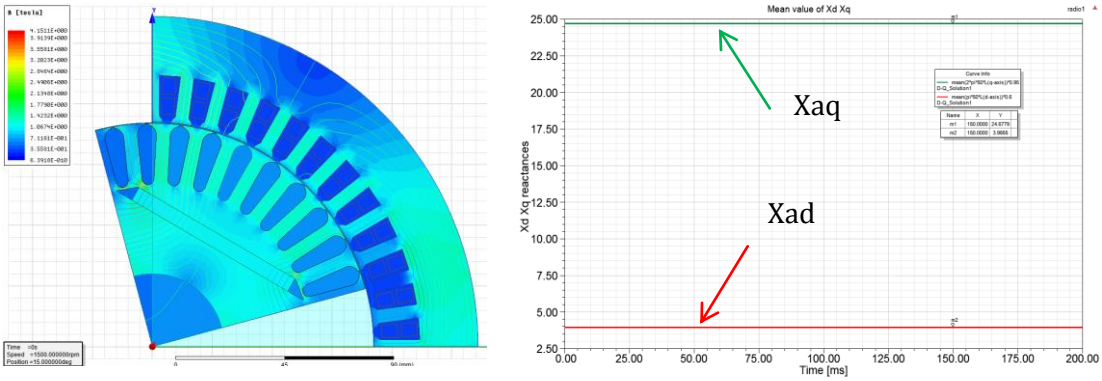

Fig.2. 22 Mean value of X_{ad}, X_{aq} reactances given by ANSYS Maxwell for LSPMSM 18.5kW with series magnetic circuit structure

Table 2. 6 Comparison of the results. LSPMSM 18.5kW with series magnetic circuit structure

	Parameter				
	Air gap, mm	**l_m, mm**	**h_m, mm**	**Xad, Ohm**	**Xaq, Ohm**
Analytical Model	0.5	76	6	4.1	28.2
ANSYS RMxprt	0.5	76	6	3.8	29.9
ANSYS Maxwell	0.5	76	6	4.0	24.7

LSPMSM with V-type magnetic circuit

The analytical model of a LSPMSM with V-type magnetic circuit is more complicated in comparison with two previous types. Fig.2. 23 shows one pole of rotor with V-type PM's

structure. In order to calculate the flux density in the air gap the theory of "Equivalent Magnetic Circuits" has been used in [HEIKKILA_02]. Magneto motive force (MMF) - drops in the rotor and stator iron have been neglected, the rotor slots are assumed to be shaped like a quadrilateral, the air gap flux density is assumed to be rectangular.

The permanent magnet can be considered as a constant MMF-source in series with a constant internal reluctance. The magnitude and the reluctance of the MMF-source can be found from eqns. (2. 41), (2. 42). If the rotor has more than one magnet per pole, e.g. due to flux concentration, eqns. (2. 41) and (2. 42) will still be valid if all the magnets have the same thickness (which normally is the case):

$$l_m = l_{m1} = l_{m2} \tag{2. 76}$$

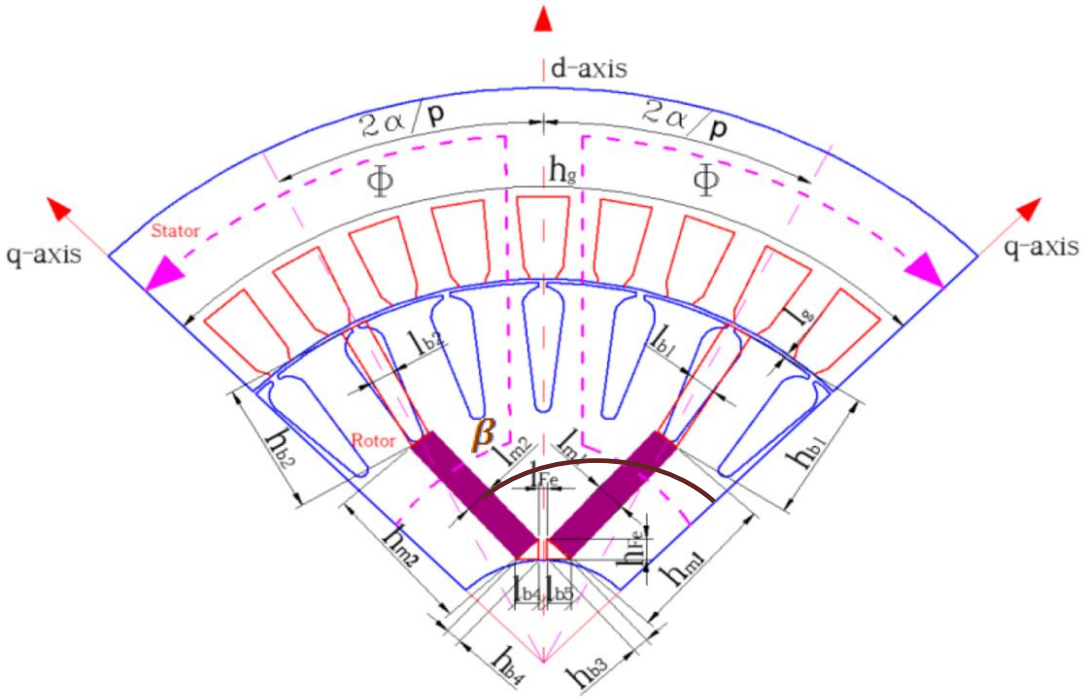

Fig.2. 23 Parameters definition for LSPMSM with V-type magnetic circuit for one pole [HEIKKILA_02]

In this case the magnet width h_m will be the sum of different magnet widths under one pole:

$$h_m = h_{m1} = h_{m2} \tag{2. 77}$$

Due to the tolerances required for inserting the magnets into the slots an extra air gap will be added to the magnetic circuit, see Fig.2. 23. The reluctance of the extra air gap can be expressed as done in (2. 78). The notion of flux barriers includes rotor bars, air-filled slots, the air-filled space between the magnets etc. For simplification all the flux barriers can be regarded as air. The resulting reluctance can be found by connecting all flux barriers under one pole in parallel:

$$R_{bb} = \frac{1}{\mu_0 L_2} \cdot \frac{1}{\sum_{i=1}^{n} \frac{h_{bi}}{l_{bi}}} \tag{2. 78}$$

where l_{bi} is the average length of the route, along which the stray flux has to travel, h_{bi} is the average width of the route, along which the stray flux has to travel. Non-rectangular flux-barriers, for example, an aluminium rotor bar, might be approximated with their average width and average length, see Fig.2. 23. In our case we have two pairs of flux-barriers: at the base and the top of the magnets (Fig.2. 23). Provided that $l_{b1} = l_{b2}$ and $h'_{b1} = h'_{b2} = h_{b1}/2$ the total reluctance of the upper flux-barriers

$$R_{bb1} = R_{\sigma 1} = \frac{1}{\mu_0 L_2} \cdot \frac{1}{2\frac{h'_{b1}}{l'_{b1}}} \tag{2. 79}$$

At the lower part of the magnets it is usually reasonable to use flux barriers in order to avoid a large stray flux (see Fig.2. 23, Fig.2. 24), since then less magnetic material is needed to produce the desired air-gap flux. The free space between the two barriers can be regarded as the iron bridges. The iron bridges are mandatory to keep the rotor together mechanically. At the same time they "short-circuit" some of the flux from the magnets. Depending on the thickness and number of iron bridges the "lost" flux can be quite significant. When the iron bridges are completely saturated they can be considered as air.

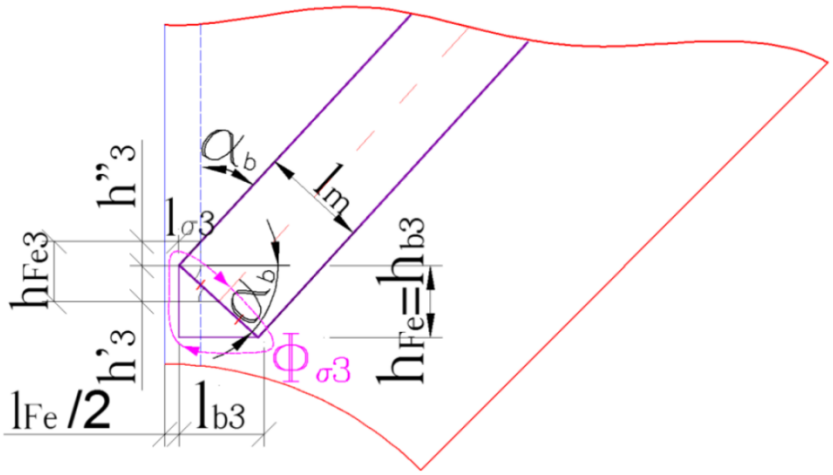

Fig.2. 24 Definition of parameters for leakage reluctance calculation for LSPMSM with V-type magnetic circuit

The length of the saturated bridge h_{Fe3} increases and the width of the flux route l_{fe3} decreases [HEIKKILA_02]. Fig.2. 24 may be used in order to calculate the approximate value of h_{Fe3}.

$$l_{fe3} = \frac{l_{fe}}{2} + l_{\sigma 3} = \frac{l_{fe}}{2} + sin(\alpha_b)\frac{l_m}{4} \tag{2.80}$$

$$h_{fe3} = h_3' + h_3'' \tag{2.81}$$

$$h_3' = sin(\alpha_b)\frac{l_m}{2} \tag{2.82}$$

$$h_3'' = \frac{l_{\sigma 3}}{tag(\alpha_b)} \tag{2.83}$$

Then the stray reluctance $R_{\sigma 3}$ grows, which causes a decreasing of the stray flux $\Phi_{\sigma 3}$. The total reluctance due to the presence of two magnets:

$$R_{bb3} = \frac{1}{2}R_{\sigma 3} = \frac{1}{2\mu_0 L_2} \cdot \frac{l_{Fe3}}{h_{Fe3}} \tag{2.84}$$

Likewise as it was shown shown before the reluctance of the air gap can be expressed

$$R_g = \frac{k_c l_g}{\mu_0 h_g L_2} \tag{2.85}$$

Where h_g is the true circumferential pole width on the rotor surface

$$h_g = 2\alpha R_{rot}\frac{\pi}{180^0}\frac{2}{p} \tag{2.86}$$

where R_{rot} is the rotor radius, α is the electrical angle (in degrees) of half the true pole width on the rotor surface (see Fig.2. 23) and p is the number of poles.

The equivalent magneto motive force of the rotor is the magneto motive force of the permanent magnets minus the product of the saturation flux Φ_{sat} and the reluctance of the permanent magnet with surrounding air-gaps [NEE_00], [THELIN_01].

$$\Theta_2 = \Theta_m - \Phi_{sat}R_m \tag{2.87}$$

The simple equivalent reluctance circuit of one pole is shown in Fig.2. 25.

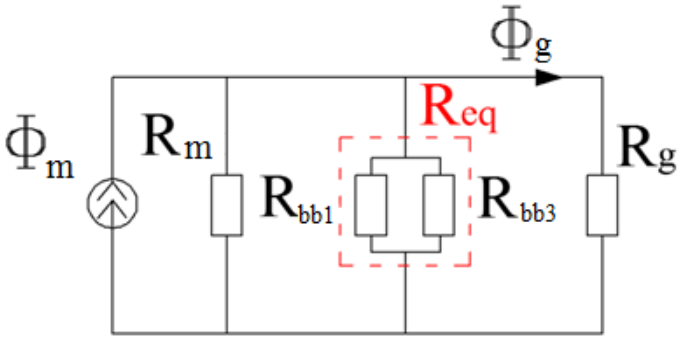

Fig.2. 25 Equivalent reluctance circuit for LSPMSM with V-type magnetic circuit

The equivalent reluctance circuit of the permanent magnet motor consists of the air-gap, the permanent magnets and bridge reluctances and iron reluctances. The air-gap flux Φ_g produced by the permanent magnets is calculated by using the equivalent reluctance circuit as follows in eq. (2. 89)

$$\Phi_g = \frac{\Phi_m R_{bb1} // R_{bb3}}{R_g + R_{bb1} // R_{bb3}} \tag{2. 88}$$

The flat-topped value of the flux density in the air gap is

$$B_g = \frac{\Phi_g}{h_g l_{mg}} \tag{2. 89}$$

Where l_{mg} is the axial length of the magnet, h_g is the true circumferential pole width on the rotor surface. The peak value of the fundamental harmonic of the flux density B_{g1} in the air gap can be calculated as coefficients for the fundamental harmonic of Fourier series.

$$B_{g1} = \frac{4}{\pi} B_g sin\frac{\alpha\pi}{2} \tag{2. 90}$$

Calculation of the d- and q-axis armature reaction reactances is expressed with the aid of form factors of the armature reaction k_{1ad} and k_{1aq} [MILLER 84], [GIERAS 10]:

$$X_{ad} = k_{1ad} X_a \tag{2. 91}$$

$$X_{aq} = k_{1aq} X_a \tag{2. 92}$$

Where the mutual reactance X_a is the same as for a cylindrical-rotor synchronous machine

$$X_a = 4 m_1 \mu_0 f \frac{L_\delta \tau k_w^2 N_s^2}{p\pi l_g} \tag{2. 93}$$

The form factors of the armature reaction are defined as the ratios of the first harmonic amplitudes to the maximum values of normal components of normal components of stator magnetic flux densities in the d-axis and q-axis, respectively:

$$k_{1ad} = \frac{B_{ad1}}{B_{ad}} \tag{2. 94}$$

$$k_{1aq} = \frac{B_{aq1}}{B_{aq}} \tag{2. 95}$$

The peak values of the fundamental harmonics B_{ad1} and B_{aq1} of the stator magnetic flux density can be calculated as coefficients for the fundamental harmonic of Fourier series. In the case of a LSPMSM with a V-type magnetic circuit structure we can apply the same analytical formulation as for inset-type PM motor:

$$k_{1ad} = \frac{1}{\pi}[\alpha\pi + sin(\alpha\pi) + c_g(\pi - \alpha\pi - sin(\alpha\pi)] \tag{2. 96}$$

$$k_{1aq} = \frac{1}{\pi}[\frac{1}{c_g}(\alpha\pi - sin(\alpha\pi)) + \pi(1-\alpha) + sin(\alpha\pi)] \tag{2. 97}$$

$$c_g = 1 + l_m/l_g \tag{2. 98}$$

Where l_m is the depth of the slot for the PMs.

It should be noticed that there is an optimal value of β equals to 140 degrees [HUANG_13] that provides sufficient asynchronous torque while delivering high efficiency at synchronous rotation.

Comparison of analytical model with results of commercial software and FE simulations in the case of LSPMSM 7.5kW and 18.5kW with V-type magnetic circuit

LSPMSM 7.5kW with V-type magnetic circuit

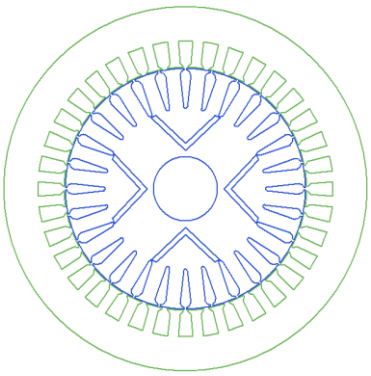

rformance | Design Sheet | Curves

Rotor Core Steel Consumption (kg):	15.1948
STEADY STATE PARAMETERS	
Stator Winding Factor:	0.959795
D-Axis Reactive Reactance Xad (ohm):	7.45223
Q-Axis Reactive Reactance Xaq (ohm):	36.3445
D-Axis Reactance X1+Xad (ohm):	8.52432
Q-Axis Reactance X1+Xaq (ohm):	37.4166
Armature Leakage Reactance X1 (ohm):	1.07209
Armature Phase Resistance R1 (ohm):	0.637151
Armature Phase Resistance at 20C (ohm):	0.590813

Fig.2. 26 X_{ad}, X_{aq} reactances given by ANSYS RMxprt for LSPMSM 7.5kW with V-type magnetic circuit

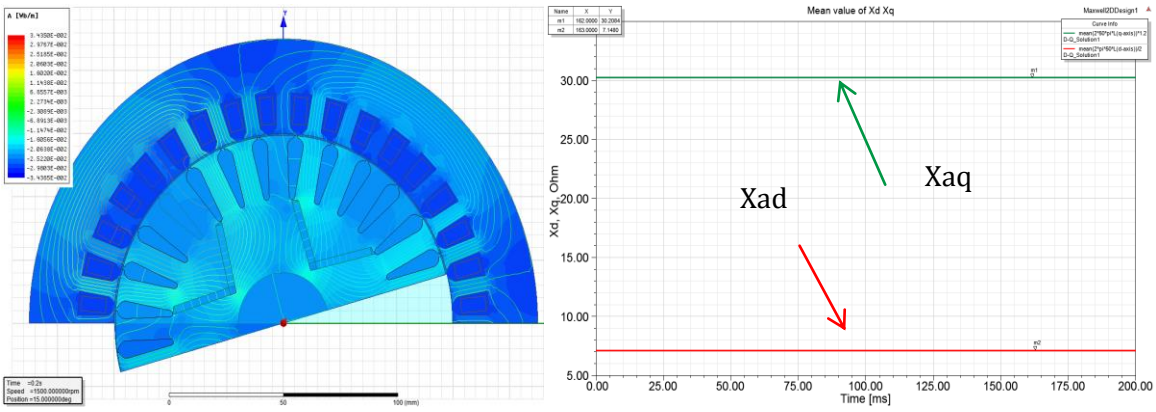

Fig.2. 27 Mean value of X_{ad} , X_{aq} reactances given by ANSYS Maxwell for LSPMSM 7.5kW with V-type magnetic circuit

Table 2. 7 Comparison of the results. LSPMSM 7.5kW with series magnetic circuit structure

	Parameter				
	Air gap, mm	**l_m, mm**	**h_m, mm**	**Xad, Ohm**	**Xaq, Ohm**
Analytical Model	0.7	32.2*2	3	8.4	36,5
ANSYS RMxprt	0.7	32.2*2	3	7,5	36.3
ANSYS Maxwell	0.7	32.2*2	3	7.2	30.2

LSPMSM 18.5kW with V-type magnetic circuit

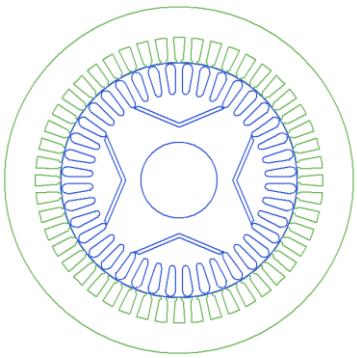

Performance | Design Sheet | Curves

Armature Core Steel Consumption (kg):	59.3583
Rotor Core Steel Consumption (kg):	32.7111
STEADY STATE PARAMETERS	
Stator Winding Factor:	0.957662
D-Axis Reactive Reactance Xad (ohm):	5.73527
Q-Axis Reactive Reactance Xaq (ohm):	29.9078
D-Axis Reactance X1+Xad (ohm):	6.10917
Q-Axis Reactance X1+Xaq (ohm):	30.2817
Armature Leakage Reactance X1 (ohm):	0.373891
Armature Phase Resistance R1 (ohm):	0.247713
Armature Phase Resistance at 20C (ohm):	0.229697

Fig.2. 28 X_{ad} , X_{aq} reactances given by ANSYS RMxprt for LSPMSM 18.5kW with series magnetic circuit structure

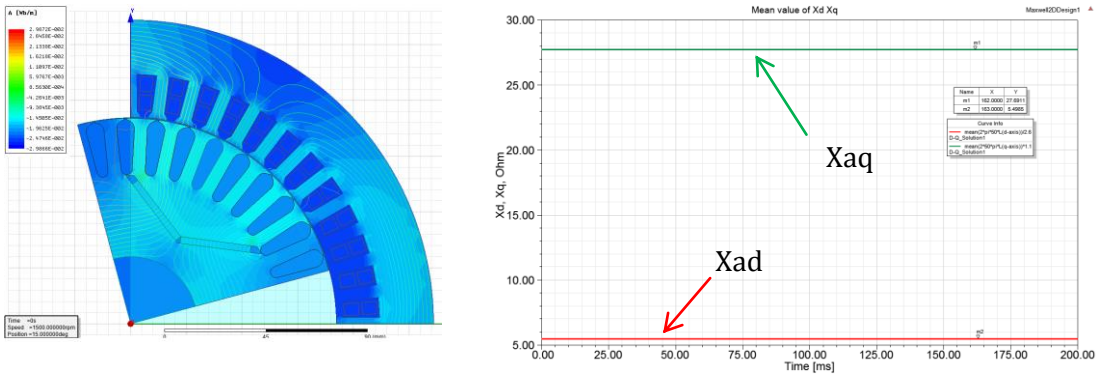

Fig.2. 29 Mean value of X_{ad}, X_{aq} reactances given by ANSYS Maxwell for LSPMSM 18.5kW with series magnetic circuit structure

Table 2. 8 Comparison of the results. LSPMSM 18.5kW with series magnetic circuit structure

	Parameter				
	Air gap, mm	**l_m, mm**	**h_m, mm**	**Xad, Ohm**	**Xaq, Ohm**
Analytical Model	0.5	38	3	6.3	28.2
ANSYS RMxprt	0.5	38	3	5.7	29.9
ANSYS Maxwell	0.5	38	3	5.5	27.5

As it is demonstrated above the analytical models developed for three LSPMSM topologies show a rather good agreement proving the validity of the parameter determination procedures. In the case of two power ratings: 7.5kW and 18.5kW variations between analytically calculated and FE-determined inductances are limited less than 18%. The model deviation can be explained by the fact that the developed analytical models the same as ANSYS RMxprt don't take into account the rotor saturation and deal only with the first harmonics. Though the error is present, such accuracy is considered satisfactory enough and the models can be implemented into the optimization procedure when the medium power LSPMSM is treated.

2.3. Optimization of LSPMSM

The process of design is a complex procedure encompassing a set of factors affecting a final result. For example, the experience of a designer, the technical means, the methods to be used have a considerable impact on the quality of the final product. Therefore, a range of efforts must be allocated for the formalization and synthesis of the existed practices. For that reason optimization is viewed as a mean of aiding designer to make the decisions. In these conditions, finding an appropriate way of resolving an optimization problem is a first challenge being faced by engineers.

Due to manufacturing constraints all of the components of design vector **X** such as the PM's dimensions and the air gap are discontinuous and standardized. The discrete optimization problem is the one for which at least one variable has a discrete finite set. One of the objectives of this work consists in the research of mathematical methods for the class of discrete optimization problems concerning techno-economic criteria and constraints.

2.3.1. Organization of the design process

There are multiple ways of resolving the industrial optimization problems. Often, the set of candidate (already existing) configurations could be used as a support set in the optimization processes. Indeed, the presence of the range of standard configurations is a widely-used measure to increase the customization and decrease the total time of design [ERENS 96], [GOMEZ 08].

Fig.2.30 illustrates four different ways of the design process organization. The methods (a) and (b) have the same core idea which consists in resolving a problem by optimizing each standard configuration separately. In the first case, the procedure of optimization is sequential, whereas in the second is carried out concurrently. Case (c) is different from (a), (b) in the view that the whole standard range of configurations is used in the optimization loop. One example of such workflow is presented in the work [LAN 04]. Case (d) is a common situation when the knowledge base does not contain any configurations with the demanded performance parameters: an inverse problem is resolved without any supporting configurations. In this work, the concept (a) is presumed to be used.

2.3.2. Optimization Problem

The following mathematical optimization problem statement is used throughout this thesis:

$$\begin{cases} \text{minimize } (f_0(\boldsymbol{X}), \dots, f_k(\boldsymbol{X}))^T \\ \text{subject to } g_i(\boldsymbol{X}) \leq b_i, i = 1, \dots, m \\ \qquad\qquad h_j(\boldsymbol{X}) = 0, j = 1, \dots, n \end{cases} \tag{2. 99}$$

Here the vector $\boldsymbol{X} = (x_1, \dots, x_g)$ is the design vector, the functions $f_i : \mathbb{R}^n \to \mathbb{R}, \forall i \in [1, k]$ are the objective functions, the functions g_i, $h_j : \mathbb{R}^n \to \mathbb{R}$ are the inequality and equality constraints. In the following subsections, each item from this definition is considered in more details.

1.3.1.1 Objective functions

Generally, for the problem of techno-economic optimization, two objective functions are taken into account: total costs (in the given case the magnet volume that is the dominant of the motor cost) and losses (*1 –efficiency*) of LSPMSM. Due to the peculiarity of the thesis, there is one of the more objective function considering the braking torque.

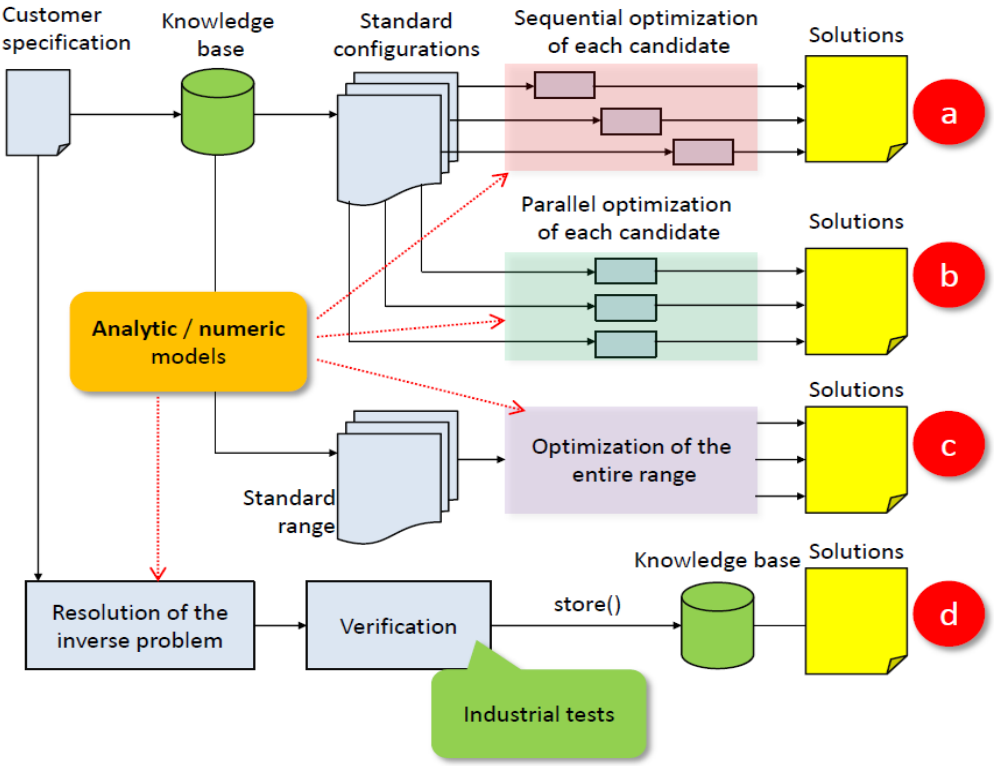

Fig.2. 30 Multiple possible workflows of the design process [SAMARKANOV_12]

1.3.1.2 Parameters

Theoretically, all parameters of problem stay constant during the entire optimization loop as they must be defined in the customer requirement form before the actual optimization process is started.

1. Nominal power (mechanical power shaft delivered): $P_{nom} = 7.5\ kW$
2. Pole number: $2p = 4$
3. Rated torque: $T_{nom} = 47.75\ Nm$
4. Voltage LL: $U_{nom} = 400\ V$
5. Load inertia: $I_{load} = 0.15\ kg \cdot m^2$
6. Ambient temperature: $T_{amb} \in [-10, +40]$
7. Motor axis height : $h_{axis} = 132\ mm$

1.3.1.3 Constraint functions

Generally, for the majority of engineering problems, the entire list of constraints can be separated on two groups: explicit and implicit constraints. The first one unifies all the constraints expressed in the requirement specification while the second consists from the list of domain specific constraints. In this section, both classes are considered for the optimization problem of LSPMSM.

Explicit constraints

These classes of constraints are closely related to the operational characteristics for the demanded motor. In the problem of optimal design of LSPMSM the list of explicit constraints are defined in the requirement specification. For example:

1. The motor should be able to start under 0.9*Un
2. Starting current ratio: $I_{st}/I_{nom} \leq 8$
3. Power factor: $0.8 - cos\varphi \leq 0$
4. Maximal temperature of isolation in the stator slot: $T_s \leq 120\,°C$
5. Overload conditions:$T_{max}/T_{rated} \geq 1.4$
6. Load torque: linearly from zero to nominal speed, starting from $0.8 \cdot T_{nom}$ to T_{nom}
7. EMF at no-load $E_o = 170V$

Implicit constraints

Often, they are closely related to the manufacturing conditions in which the demanded mechanism is produced. As a general rule, customers are not acknowledged about this type of constraints. For the considered problem, the list of implicit constraints is defined in the following way:

1. $(T_{mb} + T_{cage}) - T_{load} > 0$, where T_{mb} is the braking torque, T_{cage} is the cage torque
2. Ratio of the number of poles and number of circuits in parallel: $2p/c_{\|} \in \mathbb{Z}$
3. Ratio of stator coil pitch to number of stator slots: $\tau_p \leq Z_1/(2p+1)$
4. $Z_1/3 \in \mathbb{Z}$, where Z_1 is the number of stator slots
5. $Z_1/2p \in \mathbb{Z}$
6. $b_s < \tau_1/2$, where b_s is the stator slot width, and τ_1 is the stator slot pitch
7. $b_r < \tau_2/2$, where b_r is the stator slot width, and τ_2 is the rotor slot pitch

To sum up, the problem of optimal design of LSPMSM has 14 constraints, 7 for which are explicitly defined by the customer and others are internal, proper for the manufacturing process.

1.3.1.4 Variables

The design vector $\boldsymbol{X} = [x_1, x_2, \ldots, x_n]^T$ identifies the set of design variables. The design variables can be freely varied by the designer to define a designed object [SAMARKANOV 12]. The design vector of the studied problem is composed of 3 or 4 variables depending on the LSPMSM rotor topology: x_1 – length of the air gap; x_2 – magnet height; x_3 – magnet width, x_4-position of magnets over the motor shaft (see fig.

Fig.2. 31). According to analytical models developed below, these parameters directly influence computation of the d- and q-axis reactances X_d and X_q and the back-EMF.

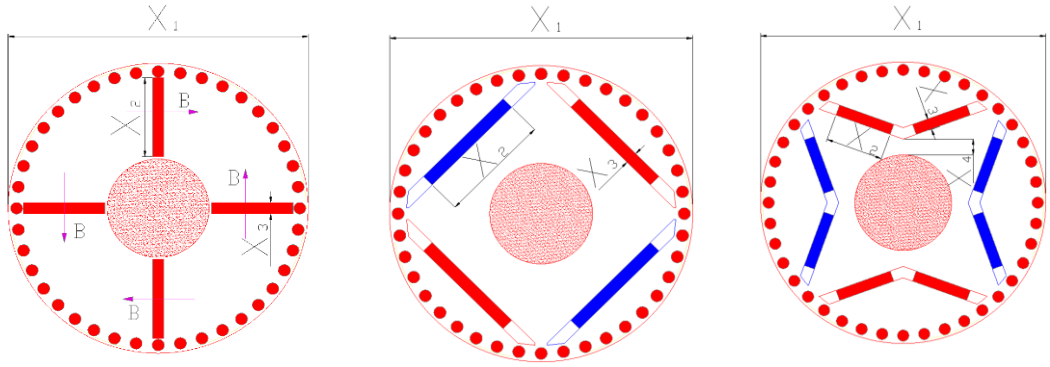

Fig.2. 31 Variable parameters related to configurations under study

2.3.3. Optimization Technique

The model used in optimization process is analytical and the optimization method applied for the considering problem (2. 99) is the exhaustive enumeration (EE) [SAMARKANOV 12], [VENKAT 10]. It is an exact method with evaluations of all possible combinations of the PM dimensions and the air gap length. The method doesn't have any heuristic rules at all.

Because of the presence of several objective functions, the aim of multi-objective evolutionary algorithms is to find compromise solutions rather than a single optimal point as in scalar optimization problems. These tradeoff solutions are usually called Pareto optimal solutions. The EE was applied in order to obtain a genuine Pareto-Front. The method is not pretended to be the best one in terms of total time of calculation, but on the other hand, it gives reliable results [ELISTRATOVA 13].

Conflicting in their nature, objective functions make a designer to undertake the optimal choice in presence of trade-offs. Pareto-front is the set of optimal configurations $\mathcal{R}^*$ and for any configuration belonging to $\mathcal{R}^*$ the following statement can be used (see eq. (2. 100)).

$$f_i(x) \leq f_i(x_i^*) \text{ for } i = 1, \ldots, k \qquad (2.100)$$

$$f_j(x) \leq f_j(x_i^*) \text{ for at least one index } j$$

2.3.4. Functionality of software DEMO-LSPM

Thanks to analytical models developed for the three LSPMSM configurations studied in this thesis, the problem (2. 99) could be treated with use of the design-specialized software DEMO-LSPM developed as part of this thesis. The developed software provides the pre-designing of the three LSPMSM rotor topologies (see Fig.2. 31) and for power range 1.5-32 kW.

DEMO-LSPM is a tool that helps a designer to make a right choice thought the procedure of LSPMSM design taking into account the given datasheet and specification (see Appendix C). The software is implemented on Matlab with a possibility to pass directly to ANSYS Maxwell and use it as a graphical interface and at the same time as a tool of FE analyzing and, thus, an instrument of validation.

Generally, DEMO-LSPM functionality can be described by the three main stages:

1. Treatment of the customer specification form;
2. Identification of a set of most promising (candidate) configurations in the form of Pareto frontier for the submitted customer specification form;
3. Medialization of the chosen configurations on ANSYS RMxprt/Maxwell.

As a result, the application returns a set of optimized configurations and the techno-economical parameters for each solution.

2.3.5. Results of optimization technique in the form of Pareto frontier for two variants of rotor cage

Thanks to the use of DEMO-LSPM three preselected configurations (Fig.2. 31) of LSPMSM 7.5kW were analyzed and all the combinations belonging to the feasible domain and defined by optimization constraints were plotted in the form of Pareto frontier. In Fig.2. 32 the feasible set of solutions using the EE in the form of Pareto frontier is presented.

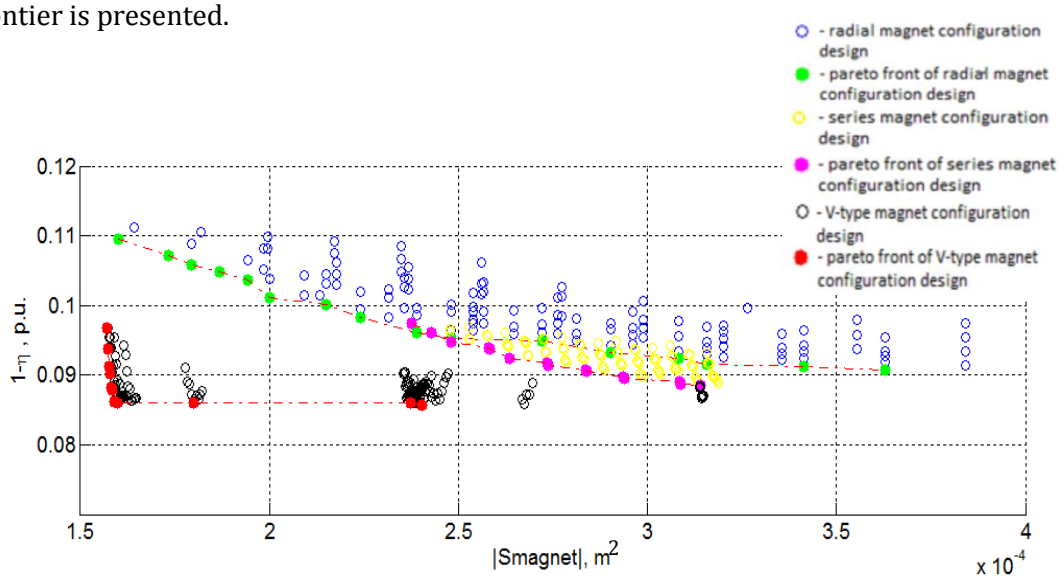

Fig.2. 32 **LSPMSM 7.5kW with classical rotor cage. Pareto frontier of efficiency versus magnet section area:** feasible configurations for radial magnetic circuit structure - blue empty points, Pareto frontier of optimal solutions for radial magnetic circuit structure – green filled points, feasible configurations for series magnetic circuit structure - yellow empty points, Pareto frontier of optimal solutions for series magnetic circuit structure – purple filled points, feasible configurations for V-type magnetic circuit structure – black empty points, Pareto frontier of optimal solutions for V-type magnetic circuit structure – red filled points

After analyzing Fig.2. 32 it may be concluded than the higher is the magnet surface area the less are the losses (*1 –efficiency*). Besides, it can be noticed that the V-type magnetic circuit structure is more performant than the two first LSPMSM configurations: radial magnetic circuit structure and series magnetic circuit structure.

On the other hand as may be seen on Fig.2. 33 the V-type configuration suffers from high braking torque and hence the startup of this motor will be rather long and difficult or even impossible.

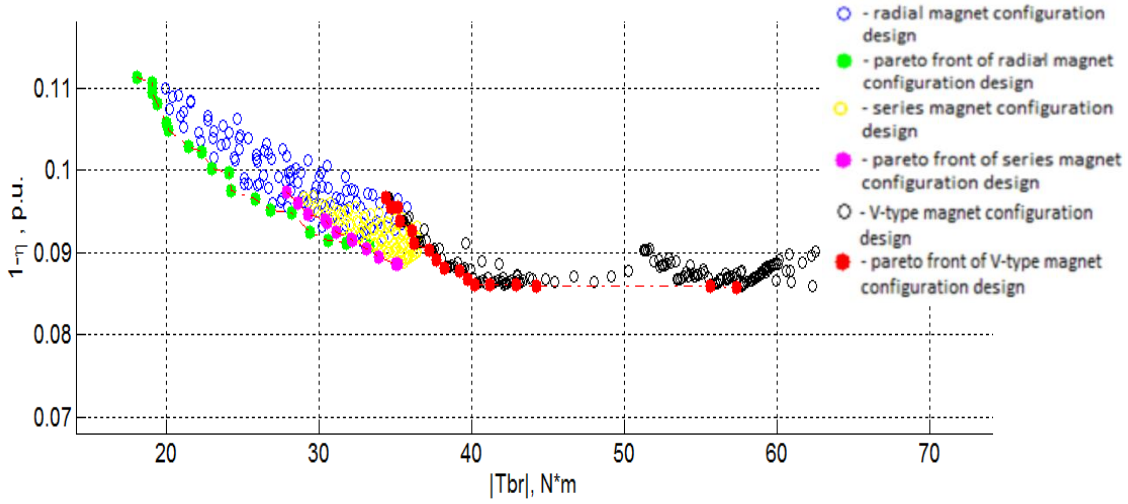

Fig.2. 33 **LSPMSM 7.5kW with classical rotor cage. Pareto frontier of efficiency versus braking torque:** feasible configurations for radial magnetic circuit structure - blue empty points, Pareto frontier of optimal solutions for radial magnetic circuit structure – green filled points, feasible configurations for series magnetic circuit structure - yellow empty points, Pareto frontier of optimal solutions for series magnetic circuit structure – purple filled points, feasible configurations for V-type magnetic circuit structure – black empty points, Pareto frontier of optimal solutions for V-type magnetic circuit structure – red filled points

2.3.6. Advantage of rotor bar reduction

As mentioned previously during the start the LSPMSM behaves as the IM. Fig.2. 32 indicates that there is a proportional relationship between the PM volume and motor efficiency and, hence, it can be interesting to keep more space under PMs. Previous studies on IM theory [BENECKE 11] shows that in the case of startup, e.g. at low rotational speed of rotor which is connected with increased values of rotor current frequency, the current in the rotor bars is cumulatively displaced in radial direction to the air gap like it can be seen in Fig.2. 34.

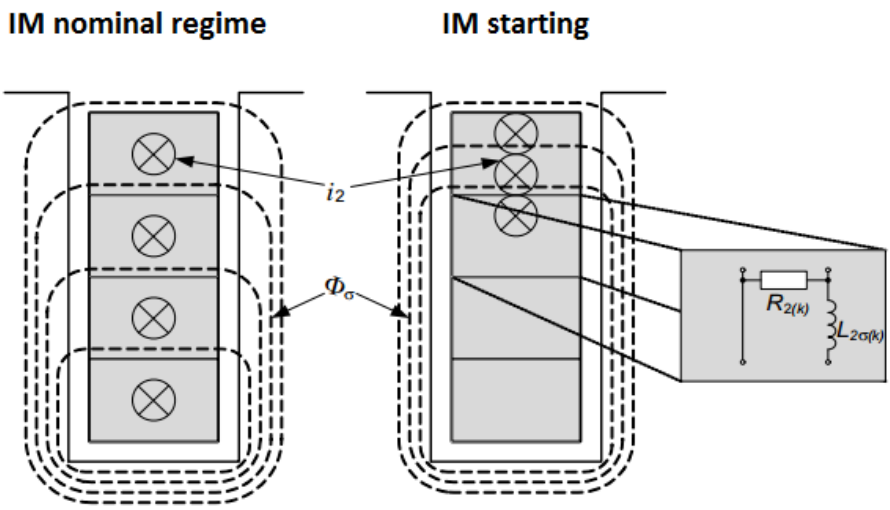

Fig.2. 34 Principle of leakage field distribution in slots of a bar-wound rotor, with s — slip, n — rotational speed, f — electrical frequency (index: 1 — stator, 2 — rotor), i_2 - rotor current, Φσ — leakage flux [BENECKE 11]

Under nominal operating conditions the speed of the LSPMSM rotor equals the speed of the stator field and so the current in the rotor bars and, hence, the rotor losses are zero and the rotor cage is usless. This phenomenon allows reducing of rotor bar section (see Fig.2. 35) and obtaining more space for PMs.

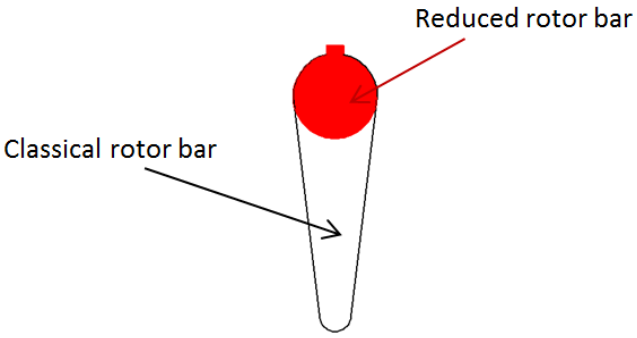

Fig.2. 35 Example of rotor bar reduction

The finite element modeling of LSPMSM for two rotor cage types proves the hypothesis made above and demonstrates almost the same evolution of current in one rotor bar during first 100ms of motor startup. It can be noticed that in both cases rotor currents reach their maximal value $I_{cl\_cage} = 4492\ A$ and $I_{rd\_cage} = 4679\ A$ at time t=9ms (Fig.2. 36, Fig.2. 37).

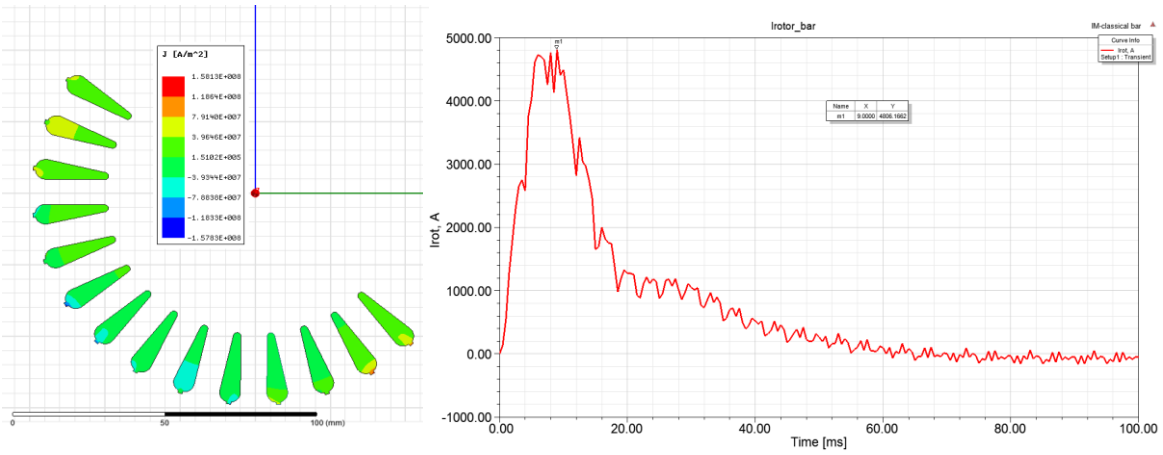

a) b)

Fig.2. 36 Distribution of current in classical rotor cage: (a) Current density in rotor bars at t=9ms, (b) evolution of current in one rotor bar at t=9ms

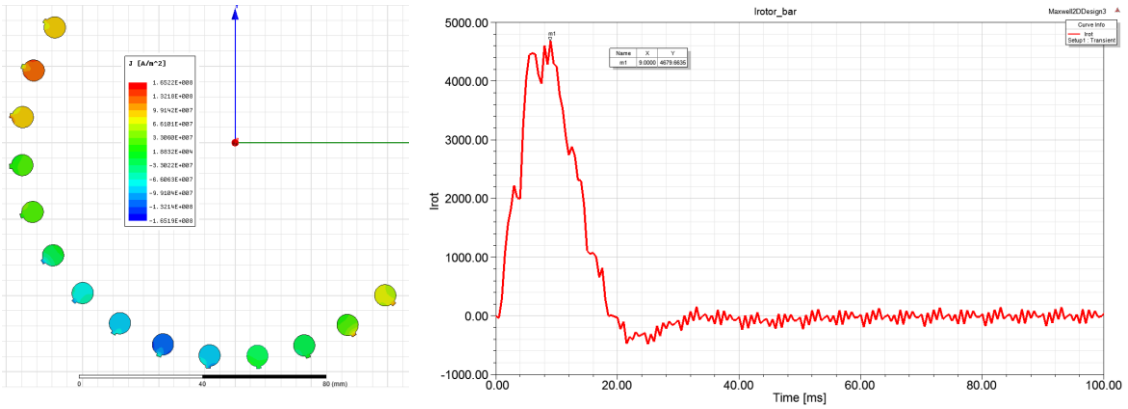

a) b)

Fig.2. 37 Distribution of current in classical rotor cage: (a) Current density in rotor bars at t=9ms, (b) evolution of current in one rotor bar at t=9ms

After reducing the rotor bars (Fig.2. 35, Fig.2. 37) the Pareto frontiers for three studied configurations of LSPMSM 7.5kW (Fig.2. 31) has been plotted. One can notice that they comply with the same trend as demonstrated in Fig.2. 32. At the same time, in terms of efficiency the rotor bars reducing made the LSPMSM with V-type and series magnetic circuit structures more beneficial in comparison with the LSPMSM with radial magnetic circuit structure.

In addition, the reducing of rotor bars significantly improves motor efficiency increasing it in average by 0.1 p.u (see Fig.2. 38). Besides, the space extending under the rotor cage permits to enlarge the number of possible combinations to vary and, thus, multiplying feasible set of solutions to reduce the braking torque created by permanent magnets (Fig.2. 39).

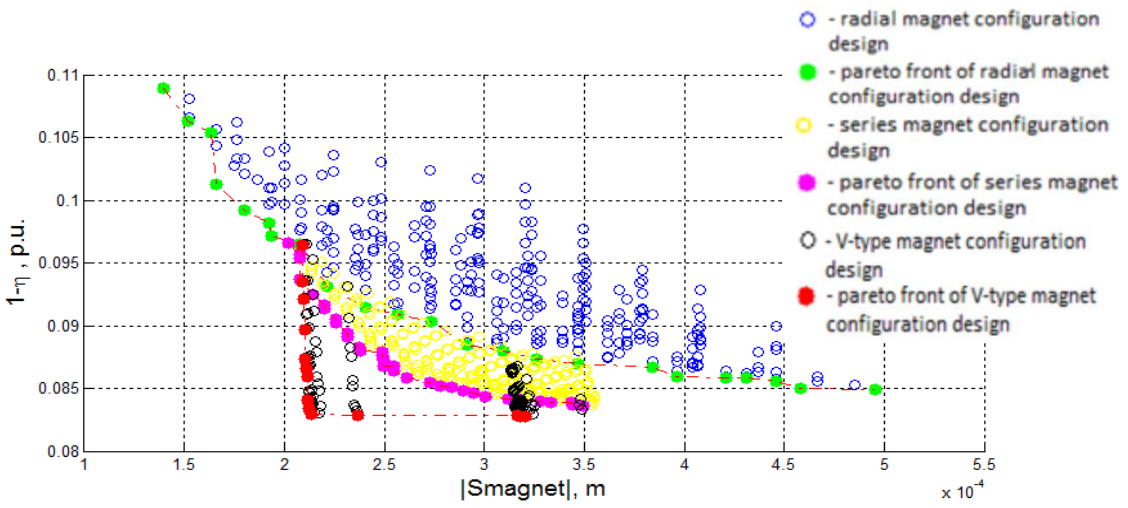

Fig.2. 38 **LSPMSM 7.5kW with reduced rotor cage. Pareto frontier of efficiency versus magnet section area:** feasible configurations for radial magnetic circuit structure - blue empty points, Pareto frontier of optimal solutions for radial magnetic circuit structure – green filled points, feasible configurations for series magnetic circuit structure - yellow empty points, Pareto frontier of optimal solutions for series magnetic circuit structure – purple filled points, feasible configurations for V-type magnetic circuit structure – black empty points, Pareto frontier of optimal solutions for V-type magnetic circuit structure – red filled points

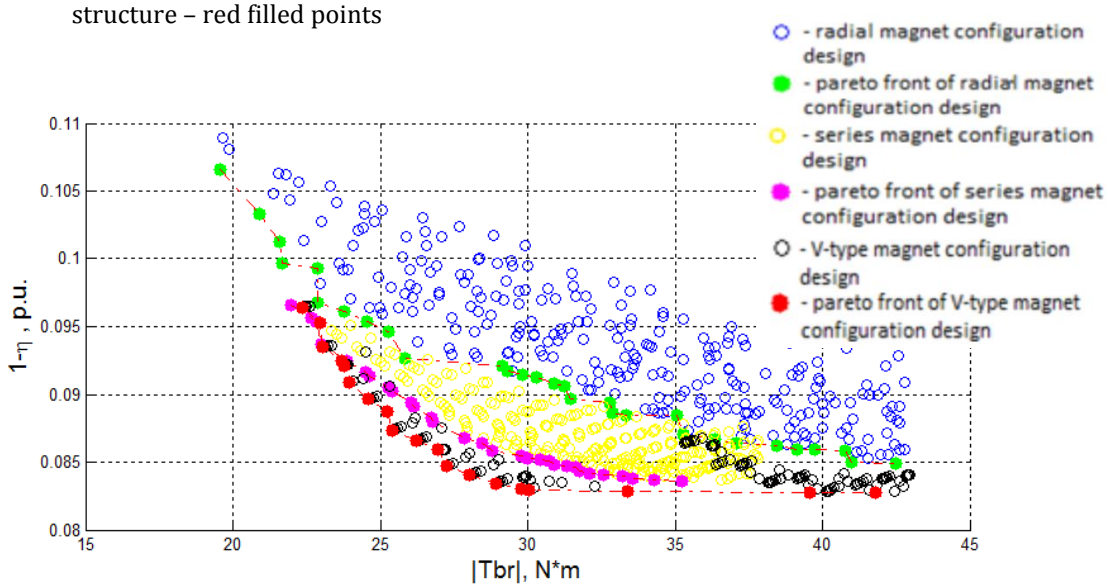

Fig.2. 39 **LSPMSM 7.5kW with reduced rotor cage. Pareto frontier of efficiency versus braking torque:** feasible configurations for radial magnetic circuit structure - blue empty points, Pareto frontier of optimal solutions for radial magnetic circuit structure – green filled points, feasible configurations for series magnetic circuit structure - yellow empty points, Pareto frontier of optimal solutions for series magnetic circuit structure – purple filled points, feasible configurations for V-type magnetic circuit structure – black empty points, Pareto frontier of optimal solutions for V-type magnetic circuit structure – red filled points

2.4. Conclusion

In Chapter 2 the analytical models for each of the three studied LSPMSM rotor configurations are elaborated. Subsequently, the validation of every analytical model with aid of numerical softwares ANSYS RMxprt and ANSYS Maxwell has been realized.

After that a general definition of the optimization problem is given and a study of the constraints and objective functions are provided. Based on analytical models and formulated optimization problem, the design-specialized software DEMO-LSPM was developed and tested. The developed software provides the pre-designing of the three LSPMSM rotor topologies and for power range 1.5-32 kW.

Finally, some results in the form of Pareto frontiers for two rotor cage variants, classical and reduced, were introduced and it was proved that the rotor bars reducing made the LSPMSM with V-type and series magnetic circuit structures more efficient in comparison with the LSPMSM with radial magnetic circuit structure.

In Chapter 3 the results provided by DEMO-LSPM will be used for realization of LSPMSMs prototypes.

2.5. References

[BENECKE_11] M. Benecke , R. Doebbelin , G. Griepentrog , and A. Lindemann, “Skin Effect in Squirrel Cage Rotor Bars and Its Consideration in Simulation of Non-steady-state Operation of Induction Machines”, Progress In Electromagnetics Research Symposium Proceedings, Marrakesh, Morocco, Mar. 20–23, 2011

[BOLDEA_10] I. Boldea, Electric machines, 1st ed. USA: CRC Press, 2010

[CARPENTER_12] D. Carpenter, S. Deleanu, "Parameter determination of synchrnous machine with radial permanent magnets using analytical calculation and standstill tests," Electrical & Computer Engineering (CCECE), 2012 25th IEEE Canadian Conference, vol., no., pp.1,6, April 29 2012-May 2 2012

[DING_11] T. Ding «Etude et optimisation de macines a aimants permanents a demarrage direct sur le reseau», Dissertation. L'Université Henri Poincaré, Nanci I, France, 2011

[ELISTRATOVA_13] V. Elistratova, M. Hecquet, P. Brochet, D. Vizireanu, M, Dessoude, "Analytical approach for optimal design of a line-start internal permanent magnet synchronous motor," Power Electronics and Applications (EPE), 2013 15th European Conference on , vol., no., pp.1,7, 2-6 Sept. 2013

[ERENS_96] F.J. Erens, The synthesis of variety: developing product families, 1996

[FODOREAN_09] D. Fordorean, A. Miraoui, “Dimensionnement rapide des machines synchrones à aimants permanents (MSAP)”, Techniques de l’ingénieur, Nov. 10, 2009

[GIERAS_10] J.F. Gieras, «Permanent Magnet Motor Technology. Design and Application » CRC Press; Third Edition, 2010

[GOMEZ_08] A. Gomez, Optimisation technico-économique multi objectif de systèmes de conversion d'énergie: cogénération électricité-hydrogène à partir d'un réacteur nucléaire de IVème génération, 2008

[HADEF_11] M. Hadef, M. R. Mekideche, A. Djerdir, and A. Miraoui, “An inverse problem approach for parameter estimation of interior permanent magnet synchronous motors,” Progress in Electromagnetics Research B, vol. 31, no. 15, 2011

[HEIKKILA_02] T. Heikkila «Permanent magnet synchronous motor for industrial inverter application. Analysis and design», Dissertation. Acta Universitatis Lappeenrantaensis, Finland, 2002

[HENDERSHOT_10] J.R. Hendershot & T.J.E. Miller, «Design of Brushless Permanent Magnet Machines», Motor Design Books LLC; Second Edition, 2010

[HUANG_13] P-W. Huang; M-C. Tsai, "Investigation of V-Shaped Line Start Permanent Magnet Motors Based on Reactance Effect," Magnetics, IEEE Transactions on, vol.49, no.5, pp.2311,2314, May 2013

[HUANG_08] P-W. Hung, S-H. Mao, and M C Tsai, "Investigation of line start permanent magnet synchronous motors with interior-magnet rotors and surface-magnet rotors," Electrical Machines and Systems, pp. 2888 - 2893, October 2008

[HWANG_02] Hwang, C. C., S. M. Chang, C. T. Pan, and T. Y. Chang, "Estimation of parameters of interior permanent magnet synchronous motors," Journal of Magnetism and Magnetic Materials, Vol. 239, 600–603, 2002

[JANNOT_09] X. Jannot, J.-C. Vannier, J. Saint-Michel, M. Gabsi, C. Marchand and D. Sadarnac «An analytical model for interior permanent-magnet synchronous machine with circumferential magnetization design», IEEE, 2009

[JANNOT_10] X. Jannot , «Modélisation et Optimisation d'un ensemble convertisseur-machine. Application aux systèmes d'entrainement à haute vitesse», Electric power. Supélec, 2010. French

[KOPILOV_86] I. Kopilov, «Electric machines», Energoatomizdat, Moscow, 1986

[LAN_04] Lan, H., Ding, Y., Hong, J., Huang, H. & Lu, B. (2004). A web-based manufacturing service system for rapid product development. Computers in Industry, 54, 51

[MAXWELL_16] Electric Machines Design Toolkit. Customized Solutions, ANSYS, Inc., January 12, 2015

[MODEER_07] T. Modeer «Modeling and Testing of Line Start Permanent Magnet Motors» Dissertation. School of Electrical Engineering, KTH, Sweden 2007

[MILLER_84] T.J.E. Miller «Synchronization Line-Start Permanent Magnet AC Motors», IEEE Trans. On PAS, PAS-103, No.7, July 1984, pp.1822,1828

[NEE_00] H-P. Nee, L. Lefevre, P. Thelin, J. Soulard « Determination of d and q reactances of permanent magnet synchronous motors without measurements of the rotor position, » IEEE Trans. on Industry Applications, Vol. 36, No. 5, 1330-1335, Sep.-Oct. 2000

[PYRHONEN_08] J Pyrhonen, Design of rotating electrical machines, 1st ed. West Sussex, United Kingdom: John Wiley &Sons, Ltd, 2008

[SAMARKANOV_12] D. Samarkanov, F Gillon., P. Brochet, D. Laloy: Optimal design of induction machine using interval algorithms, COMPEL: The International Journal for Computation and Mathematics in Electrical and Electronic Engineering, Vol. 31, N°.5, pages. 1492 - 1502, ISBN. 0332-1649, 8-2012

[SORGDRAGER_14] A.J Sorgdrager, A.J Grobler, R-J Wang « Design procedure of a line-start permanent magnet synchronous machine, » Proceedings of the 22nd South African Universities Power Engineering Conference 2014, pp.307-314

[SOULARD_02] F. Libert, J. Soulard, and J. Engstrom, «Design of a 4-pole line start permanent magnet synchronous motor,» In Proc. ICEM. 2002, Brugge, Belgium

[STOIA_09] D. Stoia, M. Cernat, K. Hameyer, D. Ban «Line-Start Permanent Magnet Synchronous Motors. Analysis And Design», EDPE 2009, October 12-14, 2009, Dubrovnik, Croatia

[TAKAHASHI_10] Takahashi, A.; Kikuchi, S.; Miyata, K.; Wakui, S.; Mikami, H.; Ide, K.; Binder, A., "Dynamic and steady-state performance of line-starting permanent magnet motors,"Electrical Machines (ICEM), 2010 XIX International Conference on , vol., no., pp.1,6, 6-8 Sept. 2010

[THELIN_01] P. Thelin, J. Soulard, H.-P. Nee and C. Sadarangani, "Comparison between different ways to calculate the induced no-load voltage of PM

synchronous motors using Finite Element Methods", 4th International Conference on Power Electronics & Drive Systems 2001, PEDS'01, Bali, Indonesia

[VENKAT_10] Venkataraman P.: Applied Optimization with Matlab Programming, A Wiley, John Wiley & Sons, New York, 2001

[ZHOU_10] Zhou Rui; Wang Qunjing; Li Guoli; Pang Cong; Fang Guanghui, "Optimal design of single-phase induction motor based on MAXWELL 2D Rmxprt," Electrical Machines and Systems (ICEMS), 2010 International Conference on , vol., no., pp.1367,1370, 10-13 Oct. 2010

Prototyping and experimental results

3.1. Introduction

The primary goal of the third chapter is the specification and manufacturing of two LSPMSM prototypes providing verification of the analytical and numerical models described in the second chapter.

The first part of the chapter concerns sizing of two LSPMSM prototypes, specification and prediction of their performances at steady-state and during the motor start and synchronization.

In the second part of the chapter, the experimental validation of asynchronous and synchronous parts in the LSPMSM design methodology is presented. In order to validate the asynchronous part of the LSPMSM design methodology, a commercial 7.5 kW 4-pole squirrel cage induction motor has been purchased.

The second part of the chapter is also dedicated to experimental tests performed on the designed prototypes and on the purchased commercial induction motor. The tests must validate the developed FE models and make a techno-economic comparison between the three studied motors. The study of thermal behavior of the prototypes is also presented in this part and the results are compared with the thermal behavior of the commercial IM.

3.2. LSPMSM prototyping

Previously, it was discussed the economic interest to proceed at the LSPMSM designing from the already existing IM of the same power rating. To follow this strategy it was decided to buy several commercial 7.5kW 4-pole IM (Fig.3. 24b) and rebuilt them for this purpose. Due to limited available funds it has been decided to realize only two prototypes possessing better performances.

In Chapter 3 three motor configurations (Fig.3. 1) were analyzed with the aid of the developed pre-design software DEMO-LSPM (see Chapter 2, Appendix C) and compared. On the basis of this comparison the two topologies of higher performances are chosen. They are motor with series-type magnetic circuit structure rotor and motor with V-type magnetic circuit structure rotor (see Fig.3. 1a, b).

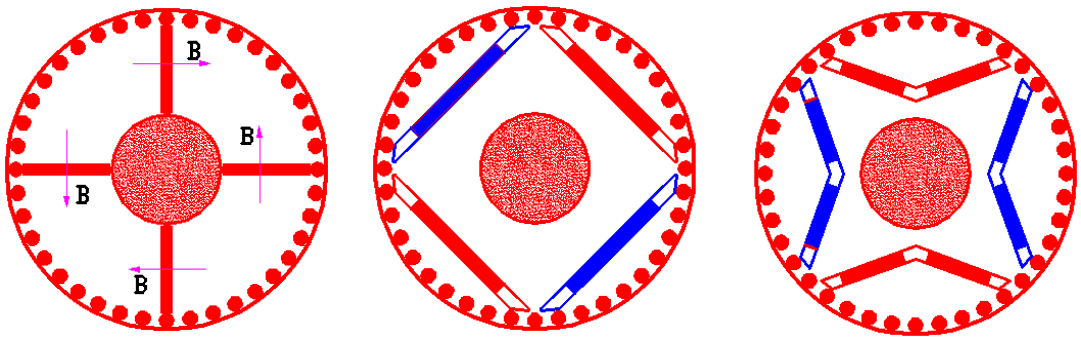

a) b) c)

Fig.3. 1 LSPMSMs rotor configurations studied in Chapter 3: (a) Rotor with radial magnet configuration, (b) Rotor with series magnetic circuit structure, (c) Rotor with V-type magnetic circuit structure

In order to build the selected prototypes, a parametric study taking into account the manufacturing constraints has to be carried out. The study is led by the package Optimetrics of ANSYS Maxwell_RMxprt.

As soon as the prototypes are specified it's necessary to conduct the dynamic analysis in order to be sure that the prototype of chosen configuration is capable to start and to keep its performances under the most difficult conditions of the design specification.

3.3.1. Sizing of two LSPMSM rotors

In this paragraph the strategy of the rotor topology selection is demonstrated. For each configuration the design vector consists of 3 or 4 variable parameters.

Mechanical constraints

In addition to specification requirements (Appendix A), there is also a set of mechanical constraints imposed by the manufacturer of the prototypes. They are:

1. Minimal distance between two rotor bars is equal to the widest part of one tooth, Rib=5mm
2. The distance between the slot of a PM and a rotor bar must be higher than 1.4 mm that fixes the diameter D1 =110 mm
3. Magnet thickness MT vary from 5mm to 6 mm
4. Minimal and maximal distances between the axis and the position of PM is 28 mm and 45mm relatively, and so the parameter O2 may vary from 7mm to 16mm
5. Magnet width MW varies from 44mm to 58mm
6. The rotor cage is made of copper instead of aluminum.

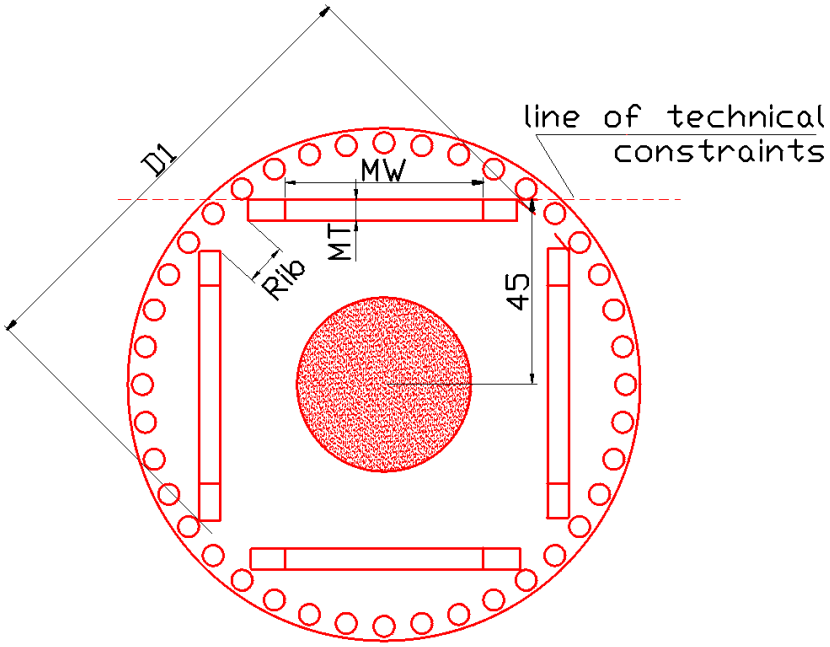

Fig.3. 2 Rotor with series magnetic circuit structure under technical constraints imposed by manufacturer

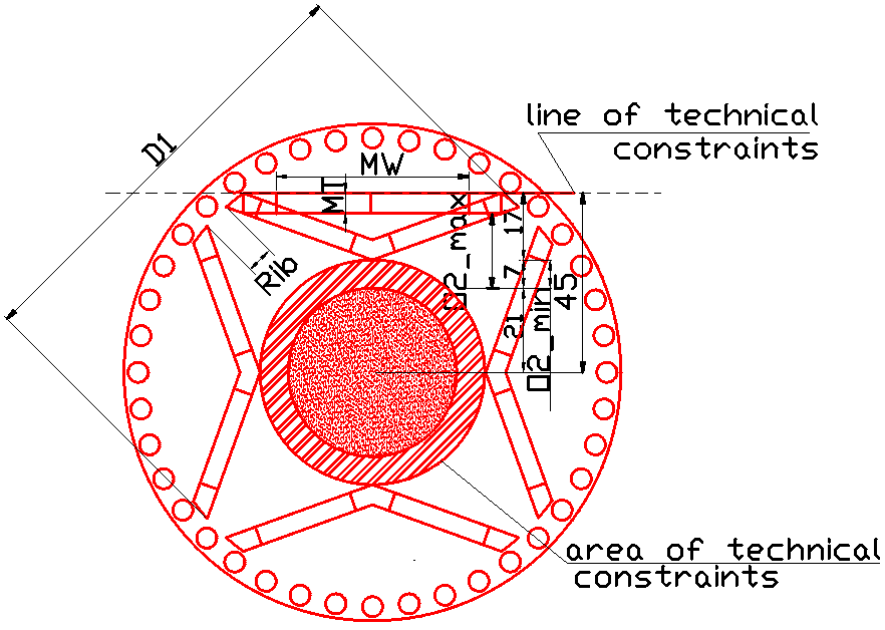

Fig.3. 3 Rotor with V-type magnetic circuit structure under technical constraints imposed by manufacturer

Electrical constraints

The most important conditions sustaining the successfully startup and overcharged capacity during its steady-state are the appropriate value of back electromotive force ($70\% \cdot U_{nom}$ in the given case [SOULARD 02], [STOIA 09]) and the ratio $\frac{T_{max}}{T_{nom}} = 1.4$ (see Appendix A).

A short air gap length maximizes the flux for a given thickness of PMs. On the other hand, it requires more accurate mechanical tolerances and increases cogging torque [HENDERSHOT 10]. Besides, a low air gap augments the braking torque and provokes the magnet demagnetization incited by stator currents during the startup. After finding the compromise between these considerations the air gap length is $l_g = 0.6mm$ [FODOREAN 09], [HEIKKILA 02], [STOIA 09].

3.3.2. Search of the optimal rotor configuration for the LSPMSM with V-type magnetic circuit structure

Varying 3 design variables MT, MW and O2 being the arguments for functions of back-EMF and maximal output power the following dependences are plotted (see Fig.3. 4).

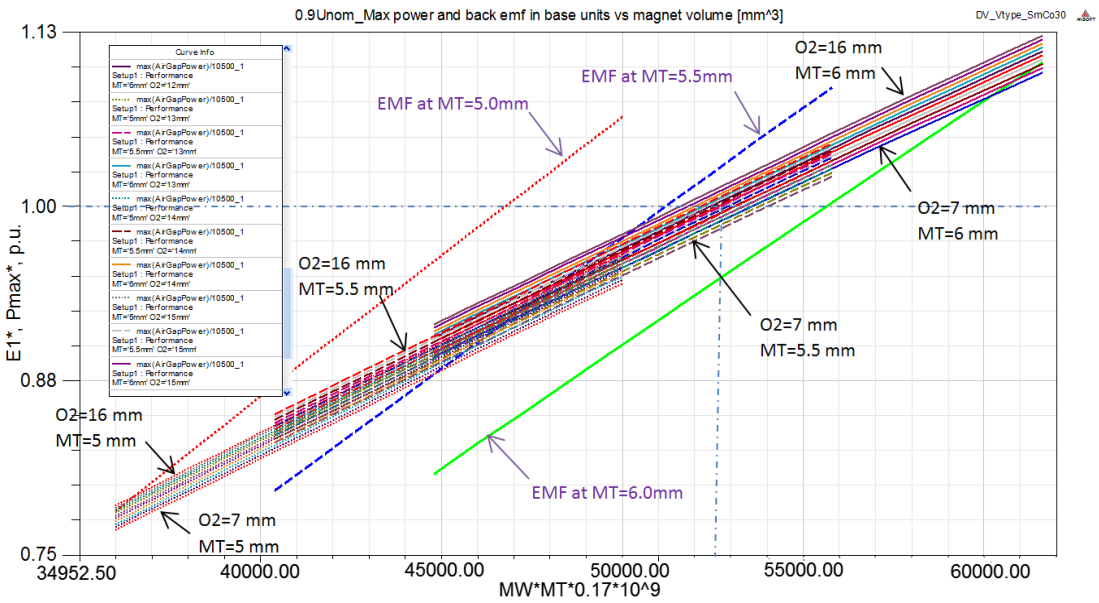

Fig.3. 4 Maximal output power and back-EMF in base units vs. magnet volume (mm^3) at $U=0.9 \cdot U_{nom}$

From Fig.3. 4 one can see that the angle opening O2 has a very little influence on the back-EMF E_0 and has a slight one on the maximal output power P_{max} and efficiency. The parameters which affect E_0 and P_{max} the most are magnet thickness MT and magnet width MW. According to Fig.3. 4, the LSPMSM rotor which satisfies the required values of back-EMF and maximal output power has the following dimensions: MT=6mm, MW=51mm, O2=10mm, optimal volume = $52000mm^3$.

With regard to efficiency, Fig.3. 5 shows that for all the combinations tested above the maximal values of efficiency are located in the rather narrow interval [0.9425÷0.947]p.u. For the configuration MT=6mm, MW=51mm, O2=10mm, optimal volume = $52000mm^3$ the maximal value of efficiency is about 0.9455 p.u, that satisfys the requirements of the specification (see Appendix A)

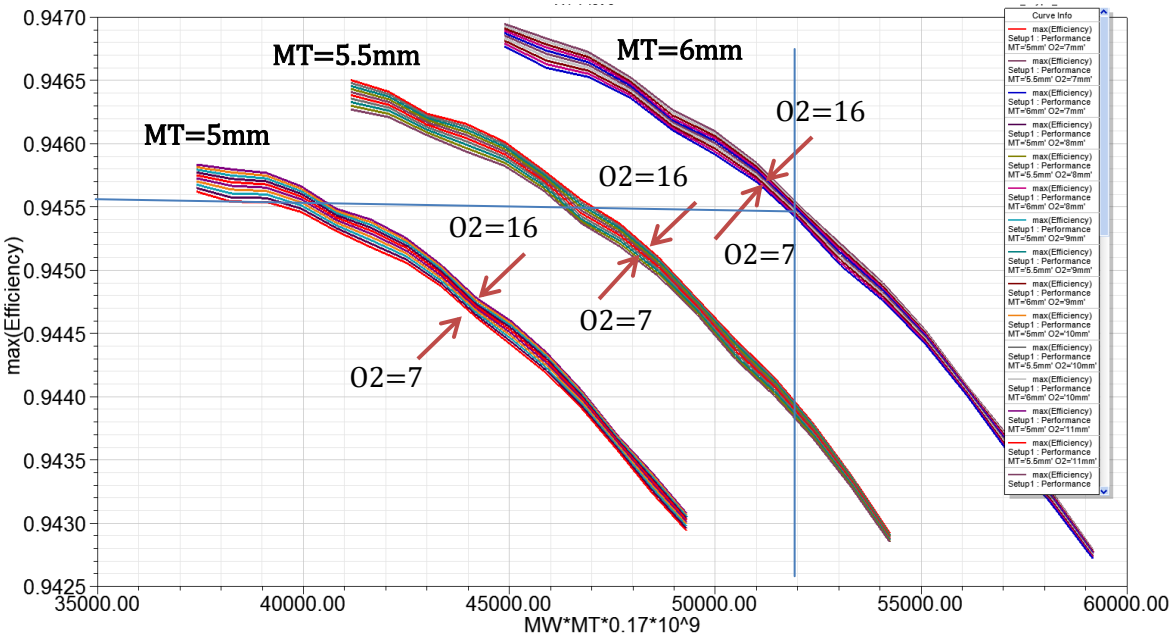

Fig.3. 5 Maximal efficiency in base units vs. magnet volume (mm3) at U=0.9·Unom

The selected configuration has been tested with aide of FE modelling. It is found that between the model analyzed by ANSYS Maxwell_RMxprt and FE model there is an error of 9% as it follows from eq. (3. 1).

	Name	Value	Units	Descrip
1	RMS Fundamental Phase EMF	150.829	V	
2	RMS Line Current	12.0282	A	
3	RMS Phase Current	12.0282	A	
4	Armature Thermal Load	104.899	A^2/mm^3	
5	Specific Electric Loading	22788.3	A_per_meter	
6	Armature Current Density	4603200	A_per_m2	
7	Frictional and Windage Loss	70	W	

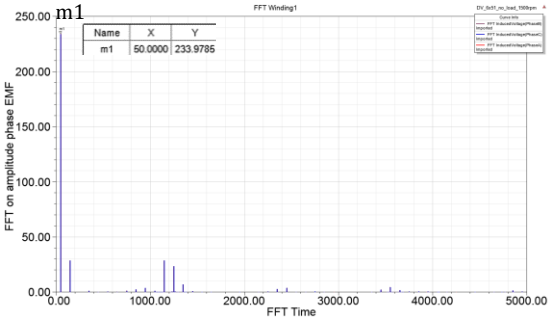

(a) (b)

Fig.3. 6 Comparison of simulation results: (a) RMS value of fundamental phase EMF according to ANSYS Maxwell_RMxprt, (b) Amplitude values of harmonic components of phase EMF according to FE simulation

$$\Delta_1 = \frac{E_{f1.sim} - E_{f1.RM\_xprt}}{E_{f1.sim}} \cdot 100\% = \frac{233.98/\sqrt{2} - 150.83}{233.98/\sqrt{2}} \cdot 100\% = -8.9\% \qquad (3.\ 1)$$

Taking into account the error and considering the FE simulation more precise, the dimensions of new rotor configuration are: MT=6mm, MW=45mm, O2=10mm, volume

= 45900mm^3. Dynamic analysis of the designed LSPMSM with V-type magnetic circuit structure

3.3.3. Dynamic analysis of the designed LSPMSM with V-type magnetic circuit structure

In order to be sure that the motor of chosen configuration is capable to start, its finite element model has been tested under the most difficult conditions: supply voltage U_{start}=90%· U_{nom}, the load torque evolves linearly from zero to nominal speed, starting from 0.8· T_{nom} to T_{nom}, moment of load inertia $J_{load} = 0.15\ kg \cdot m^2$ (Appendix A). In accordance with IEC 60034-1 the capability of 50% overload at U=90%·U_{nom} for 15s in steady-state. The starting characteristics are given in Fig.3. 8 and Fig.3. 9.

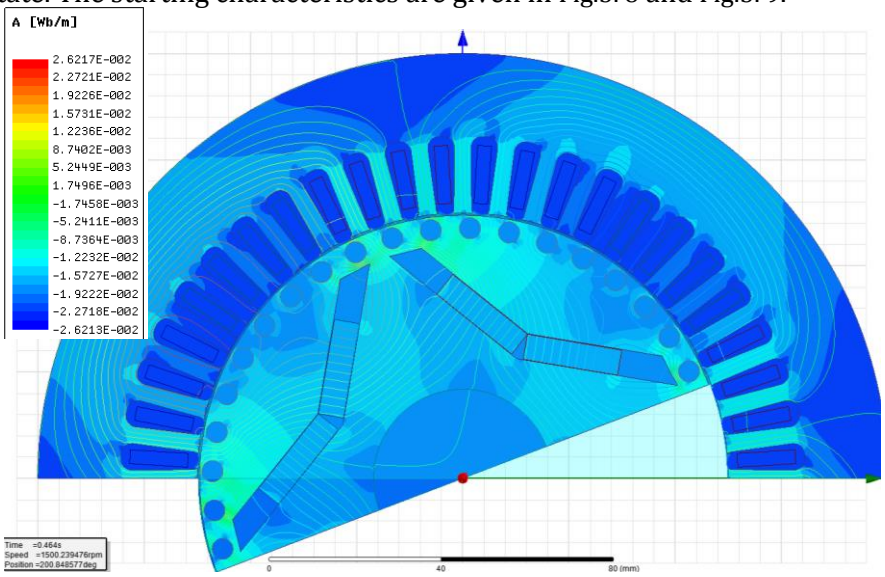

Fig.3. 7 FE model of LSPMSM with V-type magnetic circuit structure and PM surface 6x45 mm^2

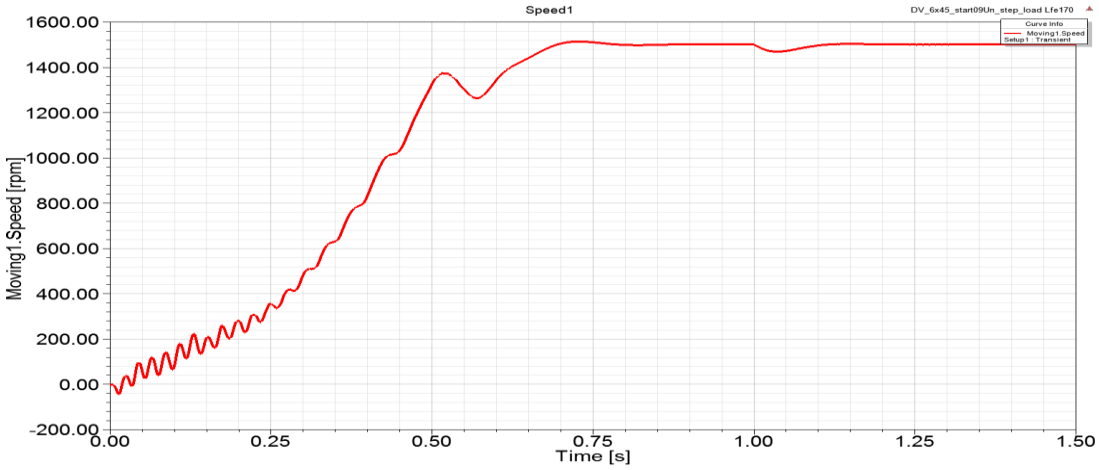

Fig.3. 8 Speed during the synchronization of LSPMSM with V-type magnetic circuit structure and PM surface 6x45 mm^2

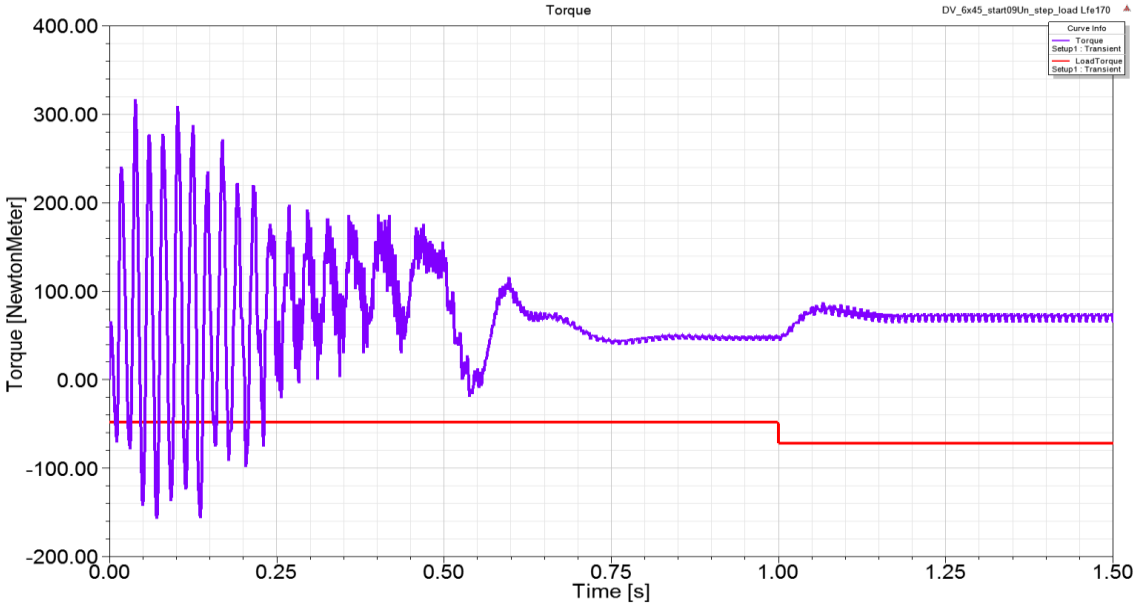

Fig.3. 9 Torque during the synchronization of LSPMSM with V-type magnetic circuit structure and PM surface 6x45 mm^2

The provided analysis of LSPMSM dynamic behavior proves the capability of the prototype with V-type magnetic circuit structure to start-up under the most difficult conditions of the designed specification and to pass an overload test.

3.3.4. Demagnetization of the permanent magnets

The FE model is tested under nominal voltage and nominal load. Fig.3. 11 and Fig.3. 12 show the evolution of average and minimal values of flux density and average and maximal values of magnetic field strength on the PM surfaces during starting and synchronization using the real characteristics of SmCo S30H PMs furnished by the manufacturing company (see Appendix D).

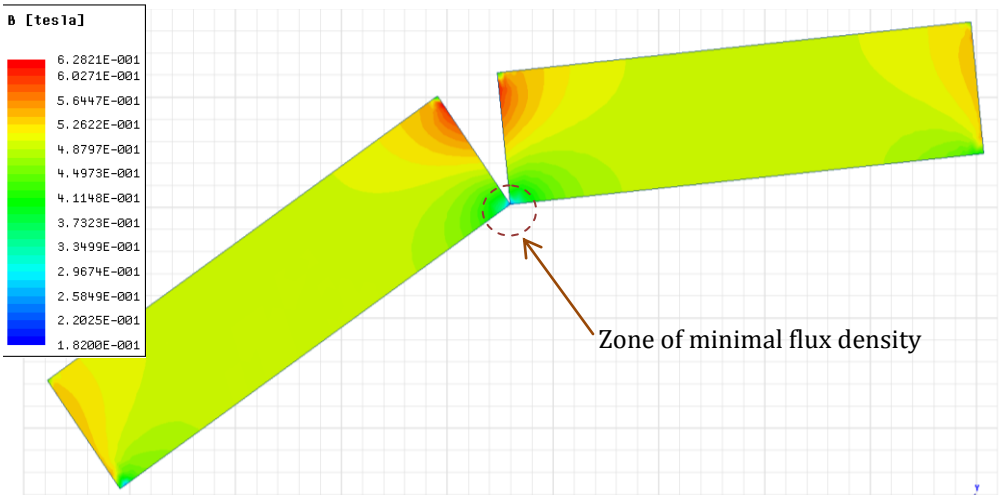

Fig.3. 10 Flux density distribution inside the PMs at time =0.266s

In order to obtain the average value of flux density or magnetic field strength, the surface integral over those scalar fields is found and divided by permanent magnet surface area.

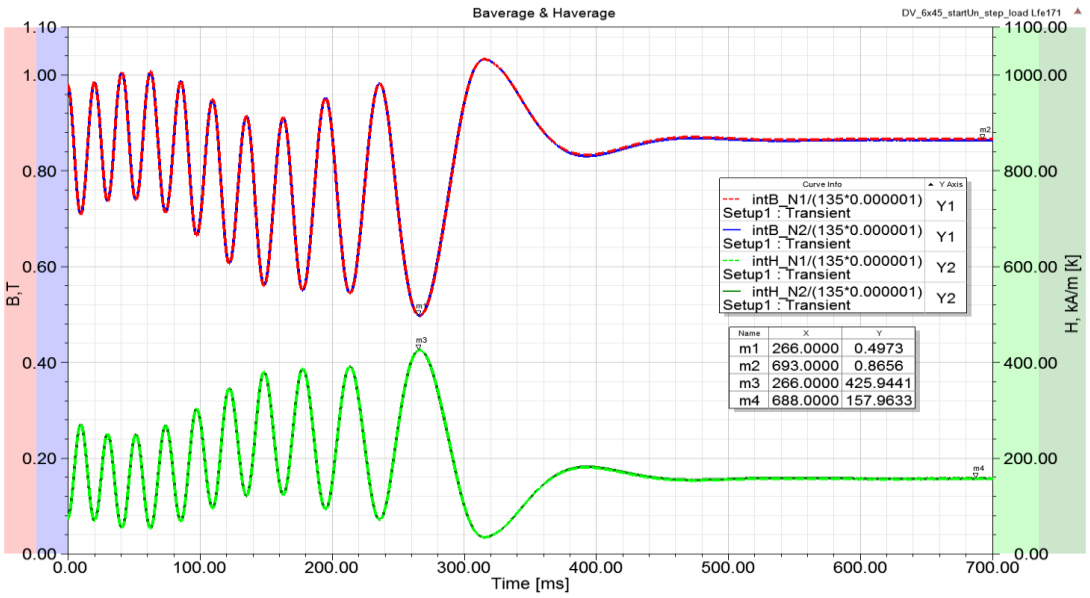

Fig.3. 11 Average values of flux density and magnetic field strength on the PM surfaces during starting and synchronization

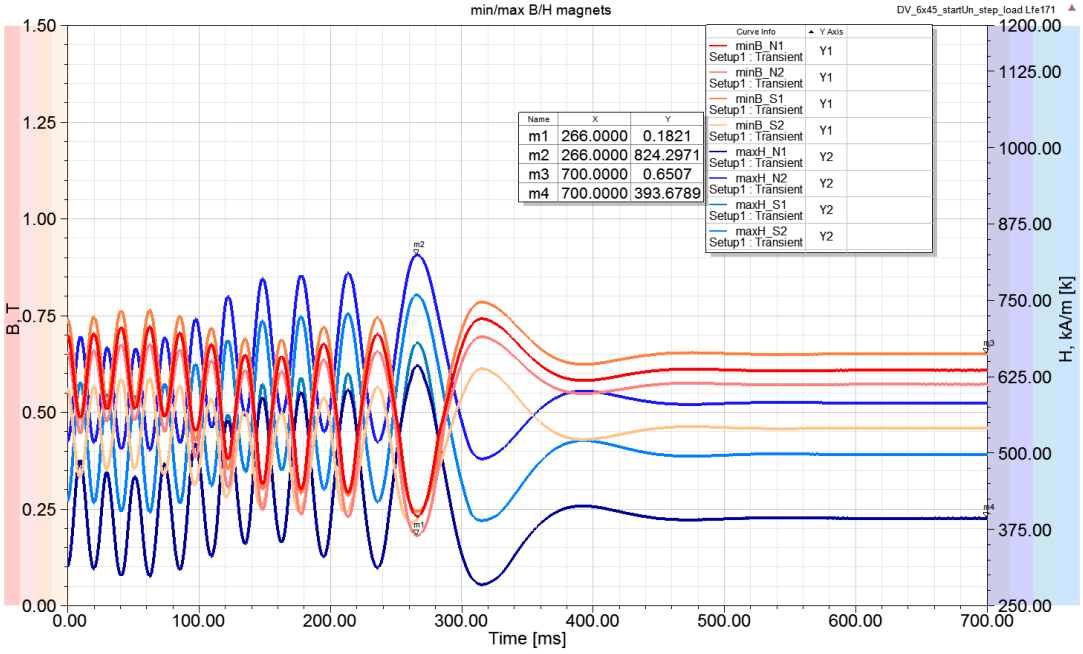

Fig.3. 12 Minimal values of flux density and maximal values of magnetic field strength on the PM surfaces during starting and synchronization

As follows from the figures shown above, even during the starting when the highest winding current giving the largest flux opposing the magnet [DING 11], the minimal and average values of flux density are 0.182T and 0.497T respectively. It means that even in the worst case of the maximal electromagnetic field applied to the SmCo S30H PMs in

the prototype the flux density doesn't shift to the point of irreversible demagnetization of BH curve (see Appendix D). When the synchronization reverts to the steady-state the minimal and average values of flux density grow to 0.65T and 0.866T. Thus, the analysis of FE simulation indicates that even at start the permanent magnets are sufficiently robust in order to withstand the demagnetizing stator current.

3.3.5. Search of the optimal rotor configuration for the LSPMSM with series magnetic circuit structure

The same approach has been applied to the search of optimal configuration in the case of LSPMSM 7.5kW with series magnetic circuit structure. As can be seen from Fig.3. 13, the LSPMSM rotor satisfies the required values of back-EMF and maximal output power when having the following dimensions: MT=5mm, MW=51mm, optimal volume = 42500mm^3.

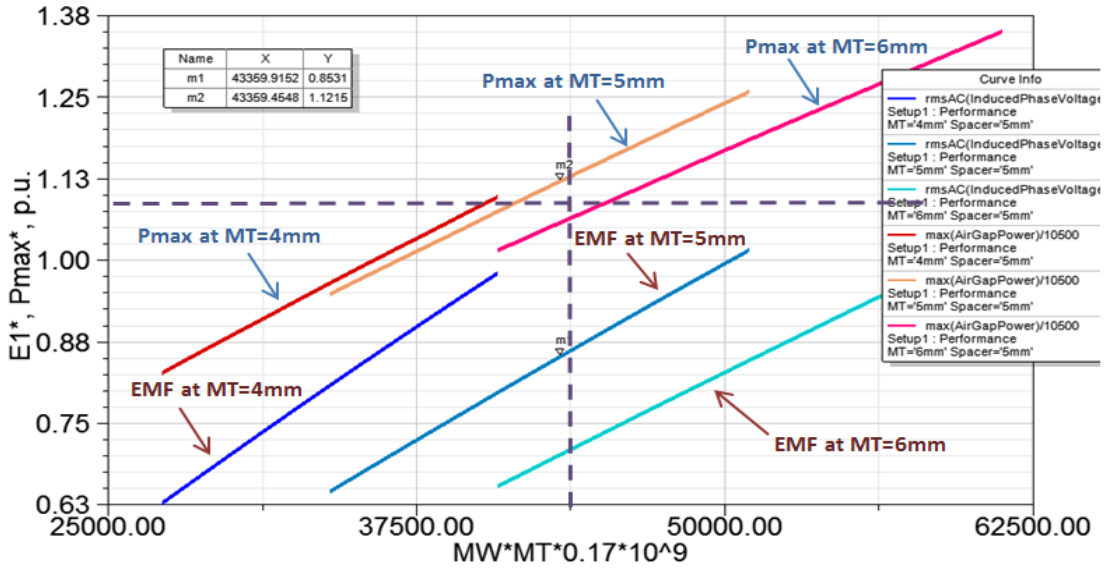

Fig.3. 13 Maximal output power and back-EMF in base units vs. magnet volume (mm^3) at $U=0.9 \cdot U_{nom}$

Fig.3. 14 shows that for the possible combinations tested above maximal values of efficiency are located in the interval [0.946÷0.953]p.u. For the configuration MT=5mm, MW=51mm the maximal value of efficiency is about 0.9455 p.u, that satisfies the requirements of the specification (see Appendix A).

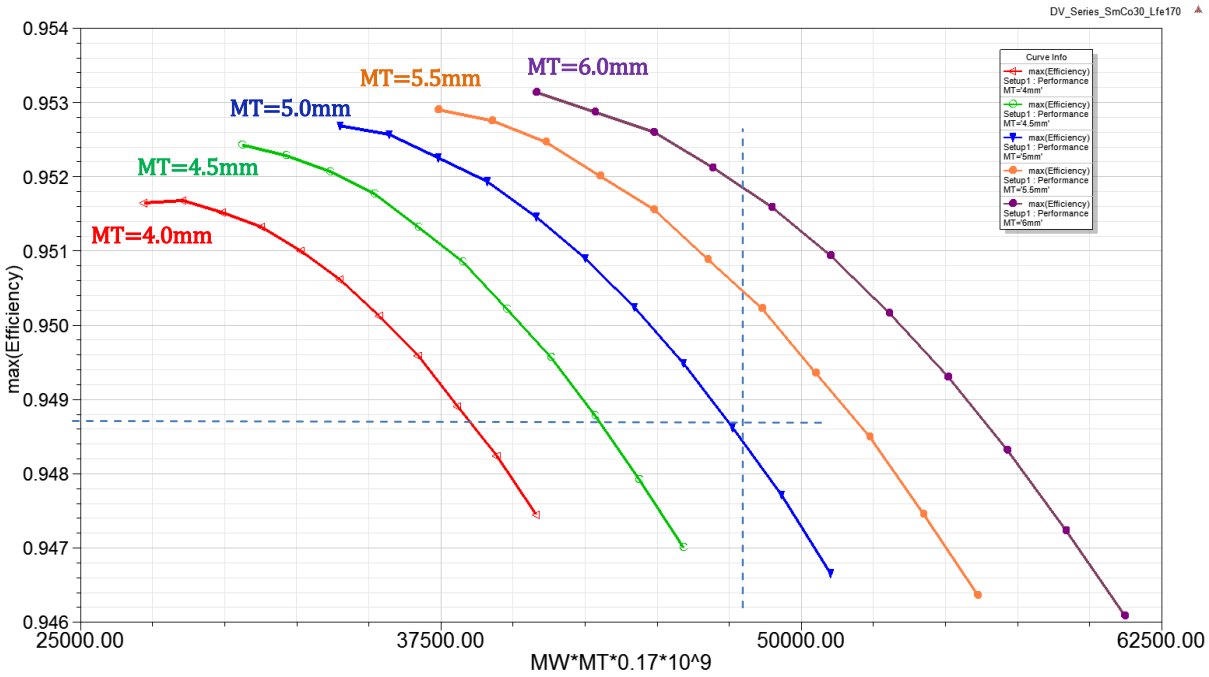

Fig.3. 14 Maximal efficiency in base units vs. magnet volume (mm^3) at U=0.9·Unom

The selected configuration has been tested with aide of FE modelling and it is found that between the model analyzed by ANSYS Maxwell_RMxprt and FE model there is an error of 9% as it follows from eq. (3. 1).

RMS Fundamental Phase EMF	159.93	V
RMS Line Current	13.007	A
RMS Phase Current	13.007	A
Armature Thermal Load	122.667	A^2/mm^3
Specific Electric Loading	24642.8	A_per_meter
Armature Current Density	4977800	A_per_m2
Frictional and Windage Loss	70	W

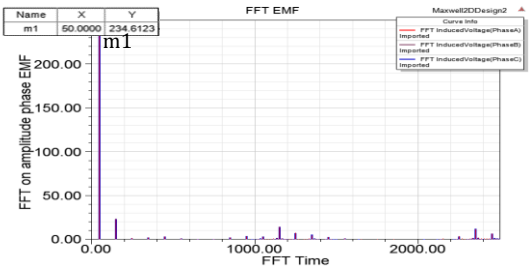

(a) (b)

Fig.3. 15 Comparison of simulation results: (a) RMS value of fundamental phase EMF according to ANSYS Maxwell_RMxprt, (b) Amplitude values of harmonic components of phase EMF according to FE simulation

$$\Delta_1 = \frac{E_{f1.sim} - E_{f1.RM\_xprt}}{E_{f1.sim}} \cdot 100\% = \frac{234.6/\sqrt{2} - 159.93}{234/\sqrt{2}} \cdot 100\% = -8.0\% \qquad (3.\ 2)$$

As a result, the rotor with the following dimensions is chosen: MT=5mm, MW=46mm, volume = 39100mm^3.

3.3.6. Dynamic analysis of the designed LSPMSM with series magnetic circuit structure

The same validation procedure is applied to the LSPMSM with series magnetic circuit structure in order to prove the capability of chosen configuration to start, its finite element model (Fig.3. 16) has been tested under the most unfavorable conditions: supply voltage U_{start}=90%· U_{nom}, the load torque evolves linearly from zero to nominal speed, starting from 0.8· T_{nom} to T_{nom}, moment of load inertia J_{load} =0.15 $kg \cdot m^2$ (Appendix A). In accordance with IEC 60034-1 the capability of 50% overload at U=90%· U_{nom} for 15s in steady-state. The starting characteristics are given in Fig.3. 17 and Fig.3. 18.

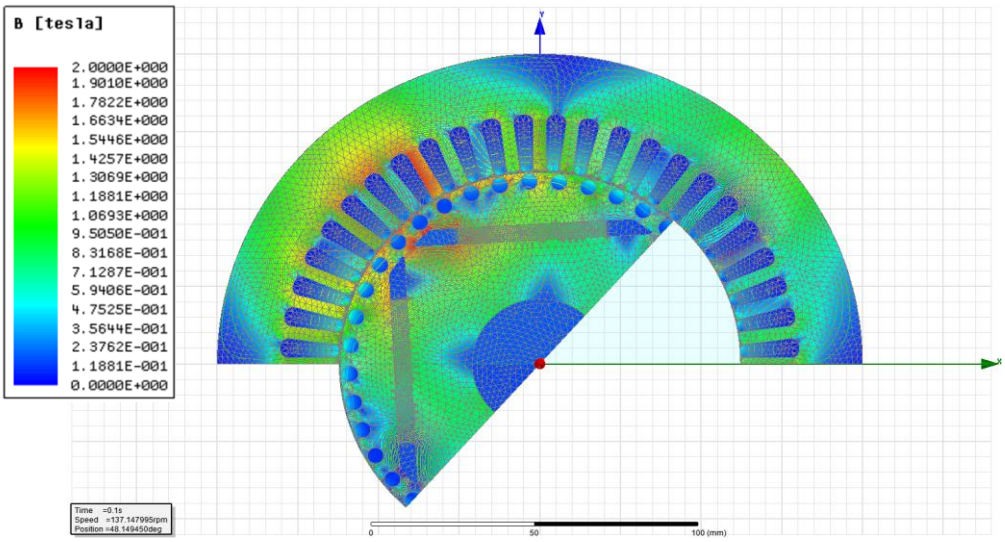

Fig.3. 16 FE model of LSPMSM with series magnetic circuit structure and PM surface 5x46 mm^2

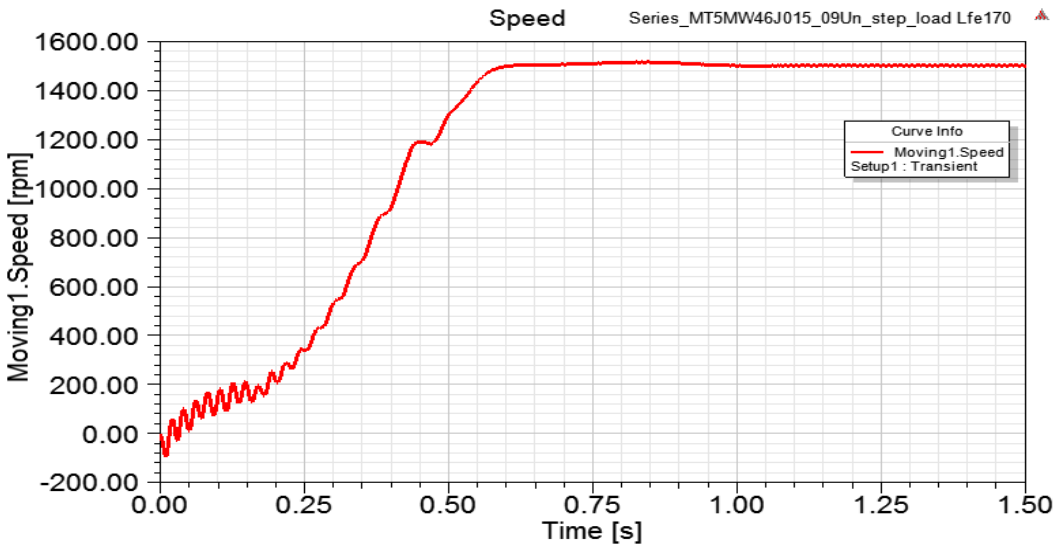

Fig.3. 17 Speed during the synchronization of LSPMSM with series magnetic circuit structure and PM surface 5x46 mm^2

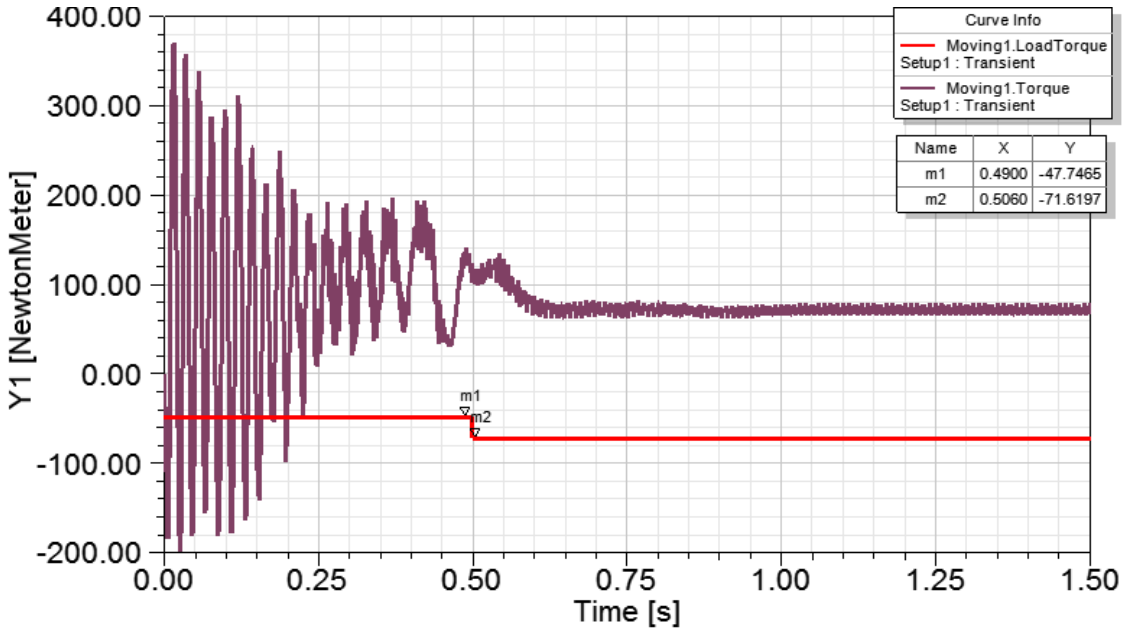

Fig.3. 18 Torque during the synchronization of LSPMSM with series magnetic circuit structure and PM surface 6x45 mm²

The provided dynamic analysis of LSPMSM with series magnetic circuit structure proves that the prototype is able to start-up under the most difficult conditions of the imposed designed specification and to pass an overload test.

3.3.7. Demagnetization of the permanent magnets

Similarly to the study presented in paragraph 3.3.4, the analyzing of demagnetization of LSPMSM with series magnetic circuit structure is based on the finite element computation.

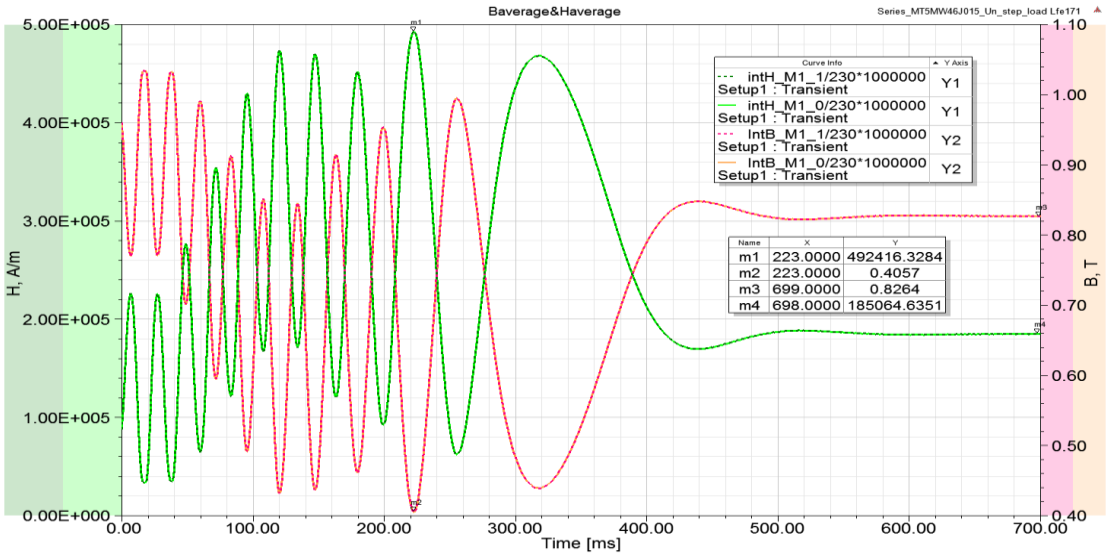

Fig.3. 19 Average values of flux density and magnetic field strength on the PM surfaces during starting and synchronization

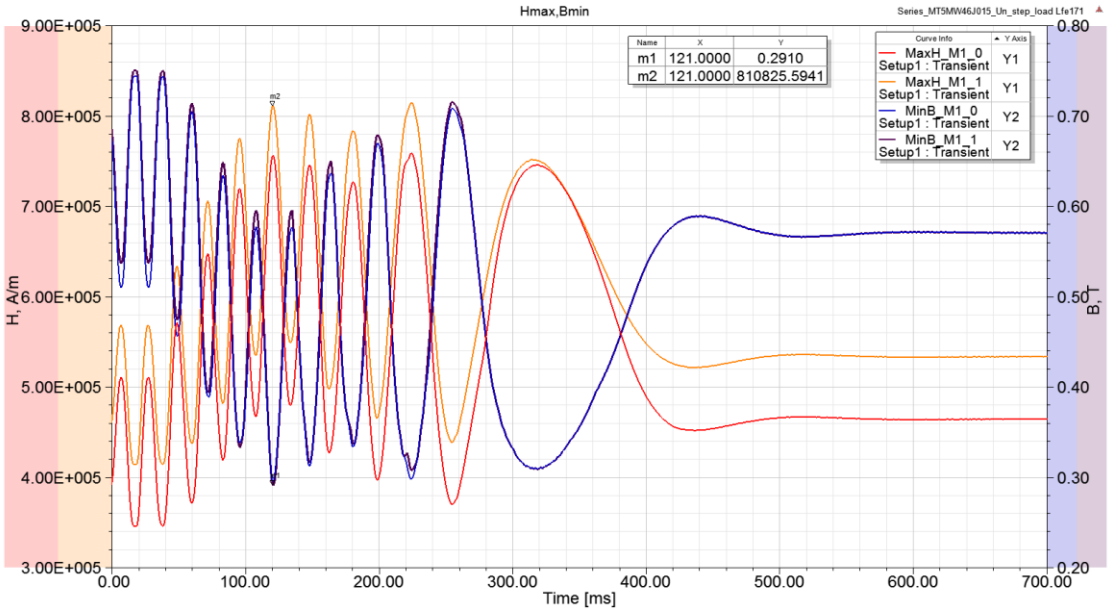

Fig.3. 20 Minimal values of flux density and maximal values of magnetic field strength on the PM surfaces during starting and synchronization

As can be seen from Fig.3. 19 and Fig.3. 20, the minimal and average values of flux density are 0.291T and 0.406T respectively and at steady-state 0.575T and 0.826T. The FE model proves that even whan the maximal electromagnetic field is applied to the SmCo S30H PMs the flux density doesn't shift to the point of irreversible demagnetization of BH curve (see Appendix D). The FE analysis shows that normally the start of the LSPMSM doesn't cause the PMs demagnetization.

3.3.8. Realization of the prototypes

As soon as the rotor geometry for the each of LSPMSMs was specified it was sent to Novelté Système Company in its design office in Belfort, France for further realization.

As it was mentioned above, the stator and the motor frame of the prototypes are those that belong to the purchased industrial 7.5kW 4-pole IMs. Fig.3. 21 provides a partially dissembled view of two commercial IMs dismantling for the following prototyping.

Thus, there are only two principal geometry modifications: insertion of permanent magnets into rotor core and modification (reduction) of rotor bars.

Fig.3. 21 Two commercial IMs dismantling for the following prototyping

Fig.3. 22 shows two shapes of rotor sheets used in the LSPMSM prototypes. Fig.3. 23 presents on example of the prototype with V-type magnetic circuit structure rotor the process of PMs manual embedding into the rotor core slots and their retention with help of special adhesive.

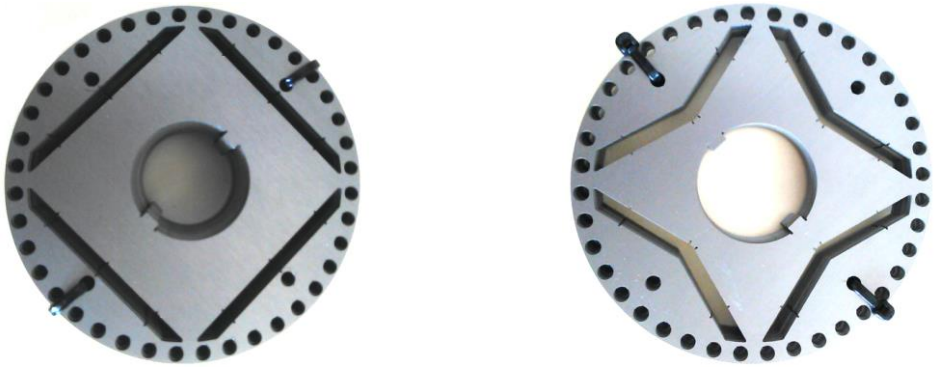

(a) (b)

Fig.3. 22 Rotor sheets of two designed LSPMSM prototypes: (a) Rotor with series magnetic circuit structure, (b) Rotor with V-type magnetic circuit structure

a) b)

Fig.3. 23 Process of PMs embedding into the LSPMSM rotor core: (a) Filling up of a rotor slot with special adhesive, (b) embedding of PM into rotor core

3.3. Experimental results

3.3.1. Test strategy

The primary goal of the experiments is the verification of the analytical and FE models of asynchronous and synchronous parts in LSPMSM design. In the first part, verification of analytical and numerical models for asynchronous design in LSPMSM design presented in Chapter 2 and Appendix B is made using the set of classical laboratory tests (DC resistance test, blocked rotor test, no-load test).

In the second part concerning the synchronous parts in LSPMSM design, the test at no-load is aimed at the estimating and comparing the fluxes produced by the PMs in the realized LSPMSM prototypes with results of FE modeling. The test has to exclude the possibility of the PMs damage and demagnetization during the motor manufacturing. Next, the starting operation and steady state load tests will be realized in order to in verify the starting capability of the designed prototype and the important parameters of interest such as the electromagnetic torque, efficiency and power factor.

3.3.2. Validation of asynchronous part in LSPMSM design

In Chapter 2 an analytical approach for analyzing the asynchronous part of LSPMSM design has been presented and validated using the commercial software **ANSYS Maxwell/RMxprt**. In order to confirm the validity of the analytical and numerical

models, several experiments are carried out on the commercial 7.5 kW 4-pole squirrel cage induction motor.

Comparison of the analytically designed IM and a commercial IM

Fig.3. 24 and Table 3. 1show the difference in main geometrical parameters and material consumption of the analytically designed IM and a commercial IM.

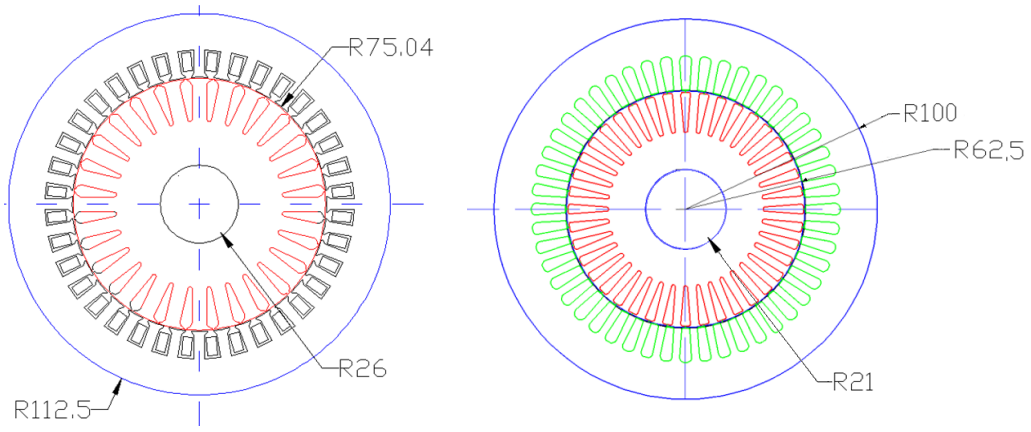

(a) (b)

Fig.3. 24 Geometry comparison: (a) 7.5 kW 4-pole cage analytically designed IM, (b) 7.5 kW 4-pole cage commercial IM

Table 3. 1 Geometry comparison between the analytically designed IM and the commercial IM

	Analytically designed IM 7.5kW	Commercial IM 7.5kW
Motor depth, mm	114	170
Outer stator diameter, mm	225	200
Outer rotor diameter, mm	150	125
Air gap, mm	0.35	0.35
Number of stator slots	36	48
Number of rotor slots	28	40
Armature copper weight, kg	4.8	6.1
Armature core steel Consumption, kg	46	41.3

As it can be seen from the motor comparison, the designed methodology proposed in Chapter 3 and Appendix B gives a motor geometry significantly different from the commercial one. It can be explained by the fact that the commercial motor is designed by the company with the use of its specific design methodology.

After three classic laboratory tests (DC resistance test, blocked rotor test, no-load test) [BOYNOV 08], [DING 11], [ECE 09], [MODEER 07], the impedance parameters of the IM equivalent schema have been determined and compared with those of the equivalent schema of induction motor (Fig.3. 25) analytically designed in Appendix B.

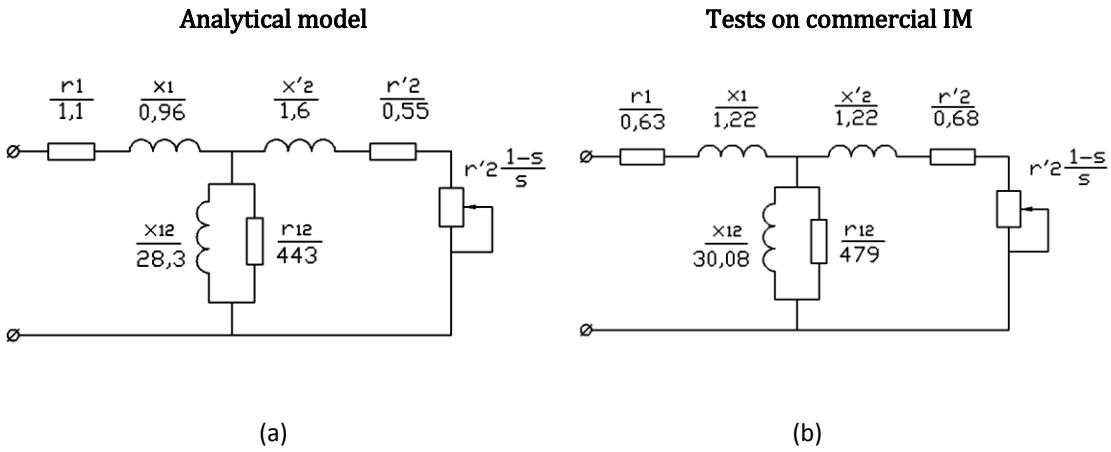

Fig.3. 25 One-phase equivalent schema of 7.5 kW 4-pole cage IM: (a) based on the analytical model, (b) based on the experimental tests realized on a commercial IM

The comparison of one-phase equivalent schema schemes represented on Fig.3. 25 shows a close similarity. The only parameter that is really different is the stator resistance r_1. This fact can be explained by disparity between two IM geometries such as the motor depth and the number of stator and rotor slots (see). Besides, there was no information about the magnetic properties of the rotor and stator electrical materials, thus information on the BH-curves used for analytical design is provided by a reference book [KOPILOV 86].

Though, there is a difference in parameters between the analytically dimensioning model and the real industrial motor, their performances show rather good correlation (Fig.3. 26). So, the proposed approach may be successfully used when the IM is designed. In addition, it can be applied for the dimensioning of the LSPMSM stator and winding and its startup analyzing.

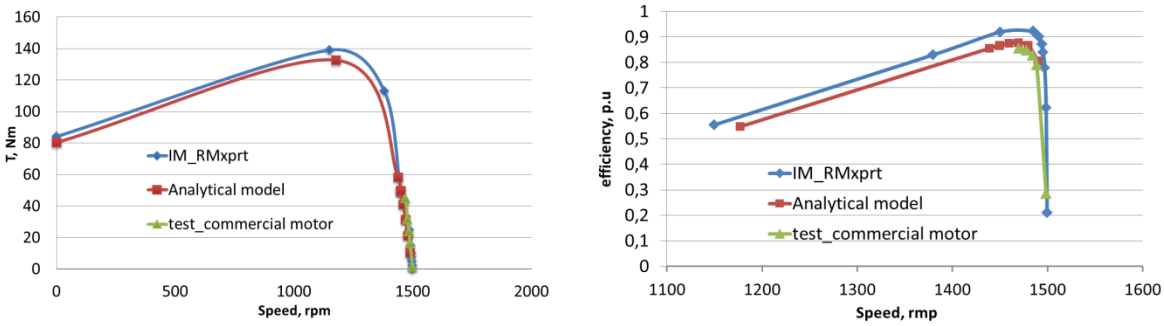

(a) (b)

Fig.3. 26 Comparison of performance characteristics of the 7.5kW 4-pole IM (blue line – numerical model, red line – analytical model, green line – tested commercial motor): (a) Torque versus speed, (b) Efficiency versus speed

Table 3. 2 Nominal regime: Comparison between the analytically designed induction motor and the commercial induction motor

	Analytically designed IM	Commercial IM	|Divergence|, %
Starting torque, Nm	84.5	110	23.2
Nominal speed, rpm	1446	1470	1.6
Nominal current, A	15.5	14.9	4.0
Nominal efficiency, p.u	0.85	0.89	4.5
cos (φ), p.u	0.830	0.835	4.2
Average temperature rise in stator winding, K	67.2	69.3	3.0

Separation of losses in three phase induction motor at no-load test

From IM theory the no load losses are the constant losses which include core loss P_{core}, the Copper losses result from Joule heating P_{joule} and friction and windage loss resulting in so-called mechanical loss P_{mec} as shown in eq. (3. 3)**Erreur ! Source du renvoi introuvable.** [BOYNOV 08], [KOPILOV 86]. The separation between the two losses can be carried out by the no-load test conducted from variable voltage U at rated frequency. When the voltage is decreased below the rated value, the core loss reduces as square of voltage with the mechanical loss remaining constant (Fig.3. 27).

$$P_{no-load} = P_{mec} + P_{joule} + P_{core} = P_{mec} + 3 \cdot I^2 \cdot r_1 + k \cdot U^2 \quad (3.3)$$

As it can bee seen from Fig.3. 27 the mechanical loss P_{mec}=36.4 W. Proceeding from the fact that the stator of the designed LSPMSM protoypes is identical to this of the Leroy-Somer IM, the value of mechanical loss may be kept and reused in all the following computations concering these prototypes.

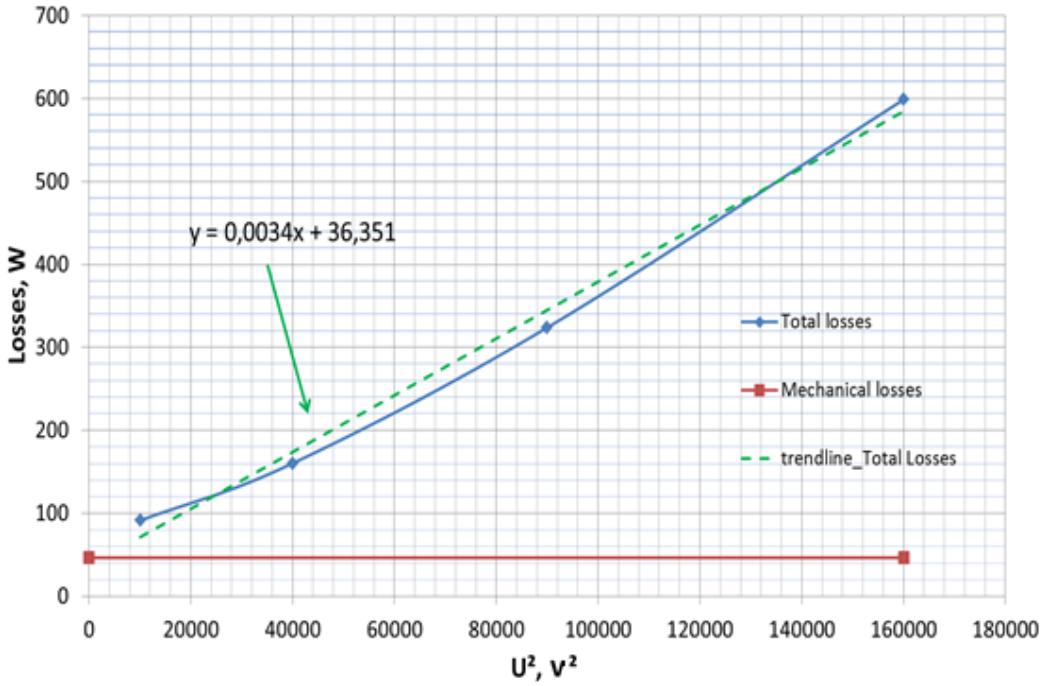

Fig.3. 27 Losses versus square of applied voltage

3.3.3. Validation of synchronous part in LSPMSM design

Prototypes tested at no-load regime

Fig.3. 28 illustrates the experimental workbench setting to obtain the experimental results at no-load for the two designed LSPMSM prototypes and one commercial induction motor 7.5kW [MODEER 07].

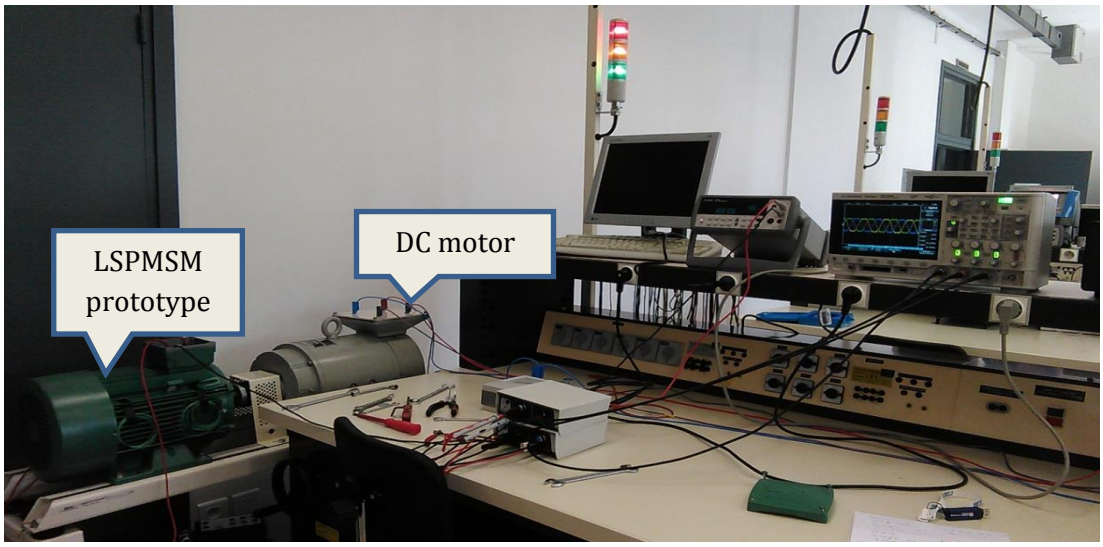

Fig.3. 28 Experimental workbench

The tested prototypes are driven by a DC motor without any load at synchronous speed 1500 rpm. The speed is measured by a speed sensor. The phase EMF is measured by an oscilloscope (see Fig.3. 28).

LSPMSM with series magnetic circuit structure and permanent magnet area 46x5 mm² per pole at no-load

Comparison of two methods (see eqs. (3. 4), (3. 5)) shows that the simulations (Fig.3. 29b, Fig.3. 30a) provide a good agreement with the experimental results (Fig.3. 29a, Fig.3. 30b). The amplitude of the first and the third harmonics is almost the same.

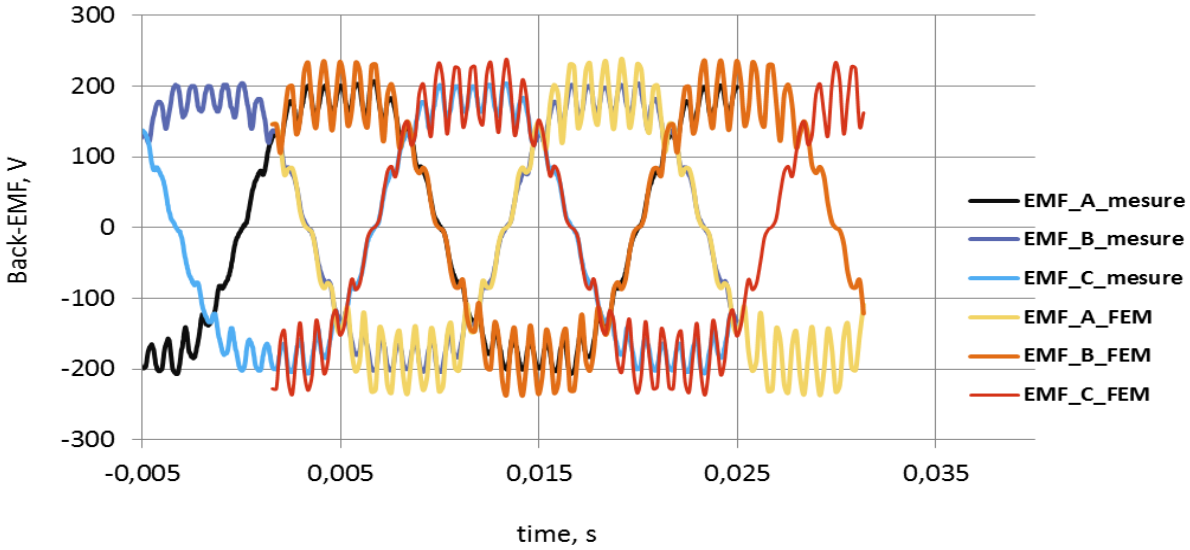

Fig.3. 29 Phase back-EMF comparison: measurement vs 2D FE calculation

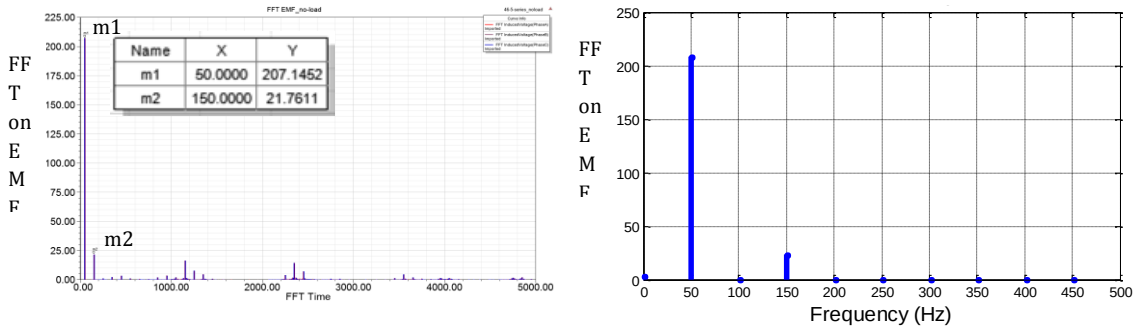

(a) (b)

Fig.3. 30 FFT on one phase A of back-EMF: (a) Simulation results for 1st and 3rd harmonics, (b) Experimental results for 1st and 3rd harmonics

$$\Delta_1 = \frac{E_{f1.sim} - E_{f1.mes}}{E_{f1.sim}} \cdot 100\% = \frac{207.7 - 208.4}{207.7} \cdot 100\% = -0.4\% \quad (3.4)$$

$$\Delta_3 = \frac{E_{f3.sim} - E_{f3.mes}}{E_{f3.sim}} \cdot 100\% = \frac{21.7 - 23.5}{21.7} \cdot 100\% = -8.3\% \quad (3.5)$$

LSPMSM with V-type magnetic circuit structure and permanent magnet area 45-6 mm² per pole at no-load

Using the same analysis which was applied to the LSPMSM with series magnetic circuit structure the performance comparison between the FE model and the tested prototype is realized (see Fig.3. 31 and Fig.3. 32).

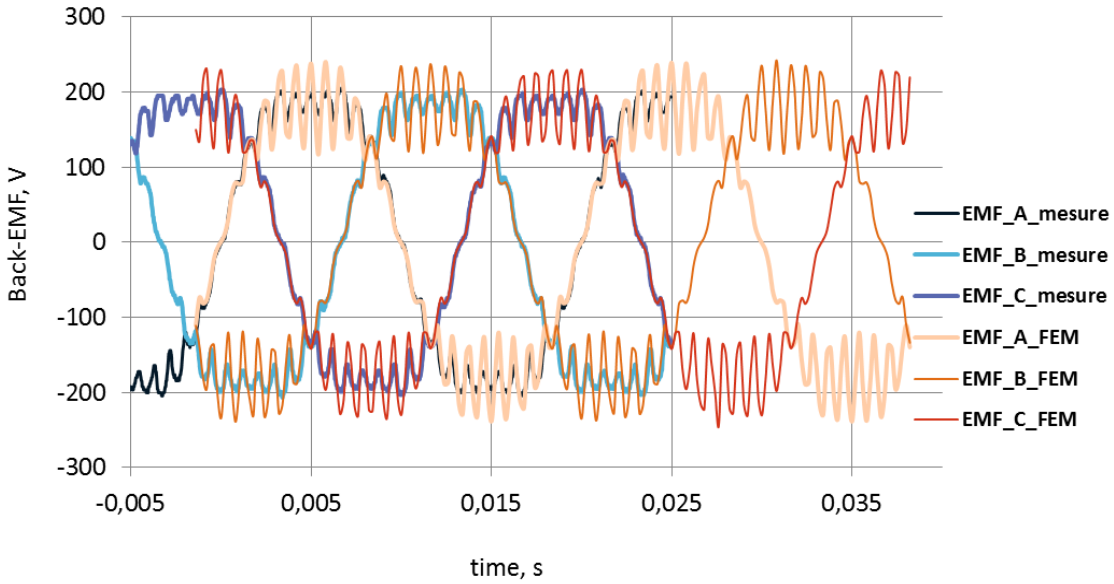

Fig.3. 31 Phase back-EMF comparison: measurement vs 2D FE calculation

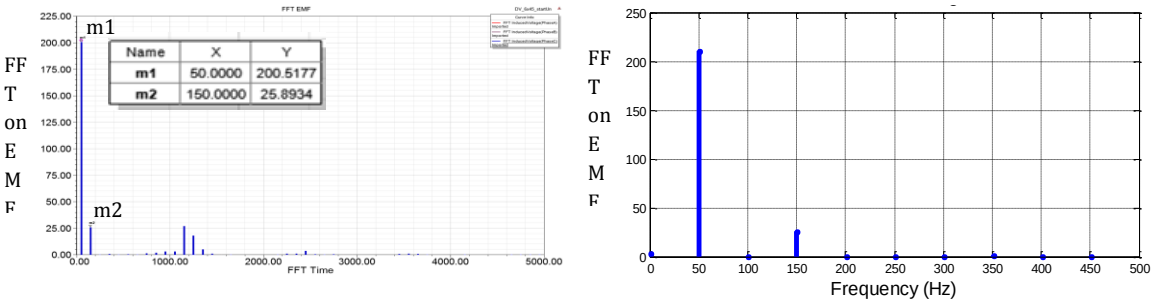

(a) (b)

Fig.3. 32 FFT on one phase A of back-EMF: (a) Simulation results for 1st and 3rd harmonics, (b) Experimental results for 1st and 3rd harmonics

Comparison of two methods shows that the FE model (Fig.3. 32a) provides a good agreement with the experimental results (Fig.3. 32b). The amplitudes of the first and the third harmonics are almost the same.

$$\Delta_1 = \frac{E_{f1.sim} - E_{f1.mesure}}{E_{f1.sim}} \cdot 100\% = \frac{200.5 - 211.1}{200.5} \cdot 100\% = -5.3\% \quad (3.\ 6)$$

$$\Delta_3 = \frac{E_{f3.sim} - E_{f3.mes}}{E_{f3.sim}} \cdot 100\% = \frac{25.9 - 25.7}{25.9} \cdot 100\% = 0.8\% \quad (3.\ 7)$$

Steady-state performances of the two designed prototypes and the commercial induction motor

Fig.3. 33 and Fig.3. 34 present the steady-state performances of two constructed prototypes and the commercial IM under different output power and their comparison with the international norms and the commercial LSPMSM 7.5kW. The experimental results are summarized in Table 3. 3.

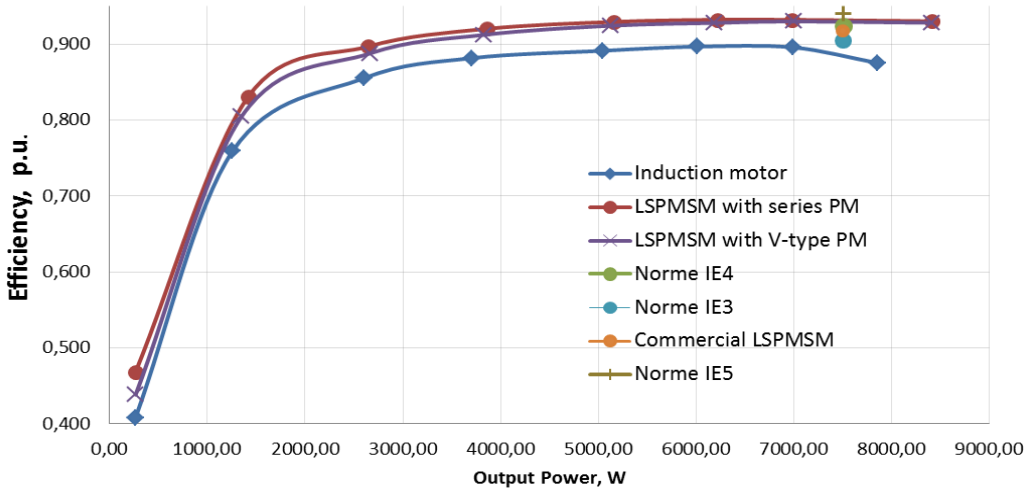

Fig.3. 33 Comparison of three tested motors (blue line – Induction motor, red line – LSPMSM with series PMs, violet line – LSPMSM with V-type PMs): efficiency vs. input power

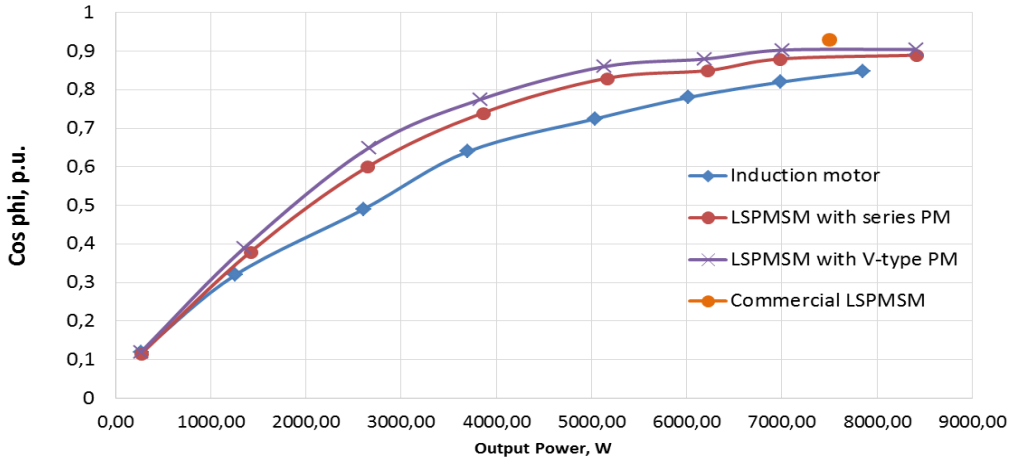

Fig.3. 34 Comparison of three tested motors (blue line – Induction motor, red line – LSPMSM with series PMs, violet line – LSPMSM with V-type PMs): power factor vs. input power

Table 3. 3 Comparison of performance characteristics of the three motors

Induction motor			LSPMSM with series PM			LSPMSM with V-type PM		
Poutput, W	Efficiency, p.u.	Cos phi, p.u.	Poutput, W	Efficiency, p.u.	Cos phi, p.u.	Poutput, W	Efficiency, p.u.	Cos phi, p.u.
265,90	0,408	0,12	267,04	0,468	0,115	267,04	0,438	0,12
1259,82	0,759	0,32	1418,12	0,831	0,38	1352,55	0,805	0,39
2603,81	0,855	0,49	2644,70	0,897	0,6	2663,44	0,888	0,65
3702,44	0,882	0,64	3856,43	0,920	0,74	3831,52	0,912	0,775
5042,81	0,891	0,725	5157,60	0,929	0,83	5129,50	0,924	0,86
6012,42	0,897	0,78	6216,07	0,932	0,85	6191,05	0,928	0,88
6986,75	0,896	0,82	6975,92	0,932	0,88	7001,56	0,930	0,903
7850,44	0,875	0,847	8413,55	0,930	0,89	8408,16	0,928	0,905

From the above comparison it can be seen, that efficiency of the designed LSPMSMs is about 4% higher than that of the commercial induction motor (Fig.3. 33, Table 3. 3) and 1.3% higher than that of commercial LSPMSM 7.5kW [TISON 14]. Besides, under nominal load the tested LSPMSMs possess significantly higher power factor than that of the commercial IM: 0.9p.u for the LSPMSM with V-type magnetic circuit structure, 0.88p.u for the LSPMSM with series magnetic circuit structure and 0.82p.u for the commercial IM (see Table 3. 3). However, the power factor of the commercial LSPMSM is 2.8% higher than that of the designed prototypes.

As it was mentioned before, the high power factor has a lot of techno-economic benefits, besides its high value puts less strain on the electricity grid and so reduces its carbon footprint. Thus, even though the actual price of the designed LSPMSM prototypes is rather high, they are much more ecologically friendly than the standard IM. Moreover, according to IEC 60034-30 [IEC600034-30 11] the efficiency level of the tested

prototypes corresponds to IE4 Super Premium Efficiency Class and so investments in the LSPMSM prototypes may be already justified in the mid-term perspective.

3.4. Thermal study

In LSPMSMs the temperature of the magnets needs to be kept under control, in order to avoid demagnetization. According to the imposed specification (Appendix A) the average stator winding temperature rise shouldn't overpass 80K (hot spot 90K).

Fig.3. 35 shows thermal test measurements applying to the commercial IM and the LSPMSM prototype. The measurement of temperature was realized in two motor parts: in the hottest point of motor frame and the hottest point of the stator winding. Table 3. 4 shows the comparison of experimental measurements with the results of analytical thermal model presented in Appendix B [MEZANI_04], [KOPILOV_86].

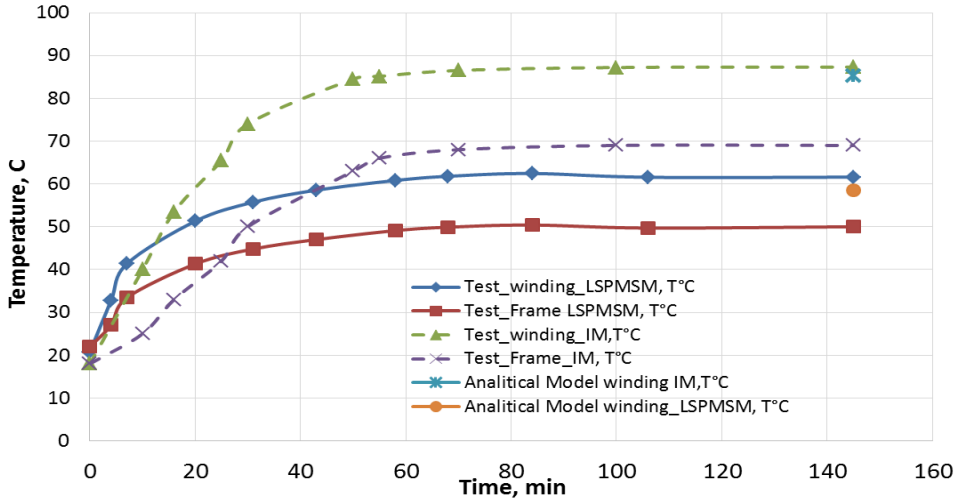

Fig.3. 35 Thermal test measurements applying to the commercial IM and the LSPMSM

Table 3. 4 Comparative results of experimental measurements and analytical model

	Analytical model	Experimental Measurement	|Divergence|, %
Stator winding temperature rise in LSPMSM, K	37.8	40.8	7.3
Stator winding temperature rise in IM, K	67.2	69.3	3

From Fig.3. 35 it can be seen that due to the absence of rotor losses the temperature rise in the winding of the LSPMSM is significantly lower (about 41%) than that of the commercial induction motor.

The estimate of stator winding temperature rise in the LSPMSM prototype is based on the thermal analytical model used for IM stator winding temperature rise prediction as shown in Appendix B. To adapt the analytical model to the LSPMSM prototype the rotor losses are not taken into account. As can be seen from Fig.3. 35 and Table 3. 4 the analytical model shows a good agreement with experimental tests and can be used as a part of multiphysical design model.

3.5. Conclusion

In the third chapter, two LSPMSM prototypes for two rotor structures previously selected in Chapter 2 (rotor with V-type magnetic circuit structure and rotor with series magnetic circuit structure) were sized. After that the prototypes were specified and, according to the elaborated specification, manufactured in the design office of Novelté Company.

The tests performed on the prototypes in the laboratory of Ecole Centrale de Lille validated the synchronous part in the LSPMSM design methodology introduced in Chapter 2 by FE and analytical models. The asynchronous part in the LSPMSM design was confirmed by experimental measurement with aide of the commercial 7.5 kW 4-pole squirrel cage induction motor specially purchased for this purpose.

The experimental results proved that a well-designed LSPMSM shows an absolute superiority over a standard IM in terms of efficiency and power factor and answer the requirements of such high International Efficiency Class as IE4.

In conclusion, the study of thermal behavior of the prototypes was presented and the results were compared with the thermal behavior of the commercial IM. The measurements confirmed that due to the absence of rotor losses the temperature rise of a LSPMSM is significantly lower than that of the standard induction motor.

3.6. References

[BOYNOV_08] K. Boynov, “Efficiency and time-optimal control of fuel cell - compressor - electrical drive systems”, Thesis, Technische Universiteit Eindhoven, 2008

[ECE_09] Electrical and Computer Engineering, “Induction Motor Parameter Measurement”, 2009, http://ece.mst.edu

[DING_11] T. Ding «Etude et optimisation de machines a aimants permanents a demarrage direct sur le reseau», Dissertation. L'Université Henri Poincaré, Nanci I, France, 2011

[FODOREAN_09] D. Fordorean, A. Miraoui, “Dimensionnement rapide des machines synchrones à aimants permanents (MSAP)”, Techniques de l’ingénieur, Nov. 10, 2009

[GIERAS_10] J.F. Gieras, «Permanent Magnet Motor Technology. Design and Application » CRC Press; Third Edition, 2010

[HENDERSHOT_10] J.R. Hendershot & T.J.E. Miller, «Design of Brushless Permanent Magnet Machines», Motor Design Books LLC; Second Edition, 2010

[HEIKKILA_02] T. Heikkila «Permanent magnet synchronous motor for industrial inverter application. Analysis and design», Dissertation. Acta Universitatis Lappeenrantaensis, Finland, 2002

[HUANG_13] P-W. Huang; M-C. Tsai, "Investigation of V-Shaped Line Start Permanent Magnet Motors Based on Reactance Effect," Magnetics, IEEE Transactions on, vol.49, no.5, pp.2311, 2314, May 2013

[IEC600034-30_11] Ed. 2, Draft, Nov. 2011, WG31/2CD: Rotating Electrical Machines—Part 30: Efficiency Classes of Single-Speed, Three-Phase, Cage-Induction Motors (IE-Code), IEC Std. 600-34-30, Nov. 2011

[KOPILOV_86] I. Kopilov, «Electric machines», Energoatomizdat, Moscow, 1986

[MEZANI_04] S. Mezani «Modélisation électromagnétique et thermique des moteurs à induction, en tenant compte des harmoniques d'espace», Dissertation. L'Institut National Polytechnique de Lorraine, France, 2004

[MODEER_07] T. Modeer «Modeling and Testing of Line Start Permanent Magnet Motors» Dissertation. School of Electrical Engineering, KTH, Sweden 2007

[SOULARD_02] F. Libert, J. Soulard, and J. Engstrom, «Design of a 4-pole line start permanent magnet synchronous motor,» In Proc. ICEM. 2002, Brugge, Belgium

[STOIA_09] D. Stoia, M. Cernat, K. Hameyer, D. Ban «Line-Start Permanent Magnet Synchronous Motors. Analysis And Design», EDPE 2009, October 12-14, 2009, Dubrovnik, Croatia

[TISON_14] O. Tison «Rapport d'essais d'un moteur WEG synchrone à aimants permanents à démarrage direct de 7,5 kW», EDF R&D, décembre 2014.

Conclusion

In this work a multiphysics optimization-oriented generic approach for LSPMSM designing was proposed and implemented in specially developed pre-design software called DEMO-LSPM. The software DEMO-LSPM gives flexible possibilities of performance calculation for the three LSPMSM rotor topologies and can be coupled with the commercial finite element modelling software Ansoft/Maxwell.

Chapter 1 begins with a glance on global warming problems and their connection to the development of energy market. After that, the first chapter introduces the evolution of energy efficiency standards adopted by The International Electrotechnical Commission related to electrical motors.

Further, the examination and comparison of different types of electric motors for constant-speed application is described. It is shown that the line-start permanent magnet synchronous motor has superiority in performance over the standard induction motor. Moreover, it is illustrated that the use of those motors is economically reasonable.

In the following part of the chapter, the main design challenges and peculiarities applied to different LSPMSM configurations are discussed. Based on that, the three LSPMSM rotor structures are chosen (see Fig.Conclusion 1):

- LSPMSM with radial magnetic circuit structure of rotor;
- LSPMSM with series magnetic circuit structure of rotor;
- LSPMSM with V-type magnetic circuit of rotor.

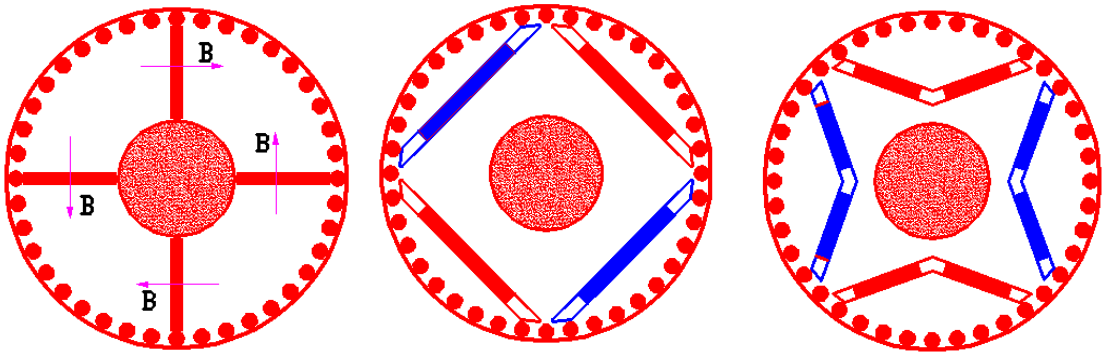

a) b) c)

Fig.Conclusion 1 Three LSPMSMs rotor configurations under study: (a) Rotor with radial magnet configuration, (b) Rotor with series magnetic circuit structure, (c) Rotor with V-type magnetic circuit structure

At the end of Chapter 1 a brief overview of existing methods for describing the processes in electrical machines (numerical, analytical and permeance network) is provided. The chapter also illustrates advantages and drawbacks of each method.

Finally, it is illustrated that the implementation of the analytical methods suits better for the development of a multi-physical generic model being the basis of the pre-design software

In Chapter 2 the analytical model for each of the three studied LSPMSM rotor configurations is elaborated. The analytical models depend on rotor geometries and based on electromagnetic lows. The main goal of this part is to find analytical expressions for d-axis, the q-axis synchronous inductance and electromotive force which are the key-parameters for evaluation of LSPMSM steady-state performances. Subsequently, the validation of every analytical model with aid of numerical softwares ANSYS RMxprt and ANSYS Maxwell has been realized.

After that a general definition of the optimization problem is given and a study of the constraints and objective functions is provided. Based on analytical models and formulated optimization problem, the design-specialized software DEMO-LSPM was developed and tested. The developed software provides the pre-designing of the three LSPMSM rotor topologies and for power range 1.5-32 kW. The results provided by DEMO-LSPM will be used for realization of LSPMSMs prototypes, the manufacturing of which is described in Chapter 3.

Finally, some results in the form of Pareto frontiers for two rotor cage topologies (classical and reduced) were introduced. It was proved that the rotor bars reducing makes the LSPMSM with V-type and series magnetic circuit structures more efficient in comparison with the LSPMSM with radial magnetic circuit structure.

In the third chapter, two LSPMSM prototypes for two of the three rotor structures previously selected in Chapter 2 (rotor with V-type magnetic circuit structure and rotor with series magnetic circuit structure) were sized. After that the prototypes were specified and, according to the elaborated specification, constructed by a manufacturing company.

The experimental tests performed on the prototypes confirmed the synchronous part in the LSPMSM design methodology introduced in Chapter 2 by finite element modelling and analytical models. The asynchronous part in the LSPMSM design was confirmed by experimental measurement with aide of the commercial 7.5 kW 4-pole squirrel cage induction motor specially purchased for this purpose.

The experimental results proved that a well-designed LSPMSM shows an absolute superiority over a standard IM in terms of efficiency (4% higher) and power factor (9.7% higher) and answer the requirements of International Efficiency Class as IE4 (see Fig.Conclusion 1).

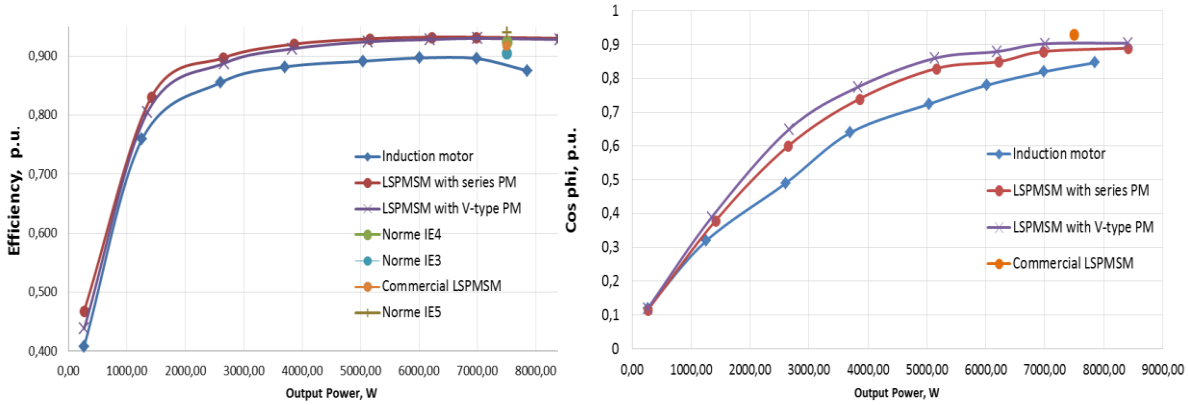

Fig.Conclusion 1 Comparison of three tested motors: (a) efficiency vs. input power; (b) power factor vs. input power

In conclusion, the study of thermal behavior of the prototypes was presented and the results were compared with thermal behavior of the commercial IM. The experimental measurements confirm that due to the absence of rotor losses the temperature rise of a LSPMSM is significantly lower than that of the standard induction motor.

The following points show the perspectives in the near future:

- ✓ Expand the application of the approach and the pre-design software DEMO-LSPM to other types of LSPMSM rotor configurations and to power rangers higher than 32 kW or lower than 1.5kW.
- ✓ In this work at the LSPMSM sizing the stator and winding arrangement are kept the same as of the commercial IM of the same power. To improve the performance characteristics of the designed LSPMSMs in order to answer the requirements of such high International Efficiency Class as IE5, it is necessary to increase the degrees of freedom of the optimization procedure.
  One of the possible solutions may consist in replacing the standard distributed winding with the concentrated one. Due to lower copper consumption, the concentrated winding has lower joule losses and so the overall motor efficiency may be considerably increased.
  The other benefit of the concentrated winding is that its induced emf is greater than that of the distributed winding. This fact can help to save on permanent magnet materials and, thus, to reduce motor price.
  On the other hand, level of harmonics and, thus, level of noise in concentrated winding is higher than that in distributed winding. This problem can be subject to optimization procedure.
- ✓ Refine the thermal model by taking into account the transients and to couple the developed multiphysics generic model to other models describing such phenomena as mechanical and vibroacoustic.

Appendix A. LS-PMSM Specification requirements and constraints for the considered industrial problem:

Specification requirements:

Nominal power: 7.5 kW (mechanical power shaft delivered)

Pole number: 4

Voltage LL: 400V

Rated speed 1500 rpm

Rated torque: 47.75 Nm

Rated voltage LL 400V Y connection

Rated frequency 50 Hz

Specification constraints:

Efficiency at rated power, rated voltage and rated frequency – at least IE3 level (90.4%)

Voltage variation in steady state (given by 60034-1 Std): 400V +/- 5%

Voltage variation for short time (given by 60034-1 Std): 400V +/- 10%

Protection degree: IP54 (to take into consideration for thermal design)

Maximal ambient temperature: 40 °C

Min. ambient temperature: -10 °C

Stator winding temperature rise average : 80K (hot spot 90K)

Outer fan

Motor axis height : 132mm max

Overload conditions : 1.6 times nominal torque for 30 sec

In-rush currents during start-up $<$ 8 pu

Load inertia : 0.15 kg*m^2 (given by 60034-1 Std)

Load torque: linearly from zero to nominal speed, starting from 0.8 p.u. to 1 p.u.

The motor should be able to start to start under 0.9*Un (given by 60034-1 Std):

Three consecutive start-up from “cold” state

Two consecutive start-up from “hot” state

6 start-up / hour

Appendix B. An example of the IM design

Specification requirements

Nominal power: 7.5 kW (mechanical power shaft delivered)

Rated voltage LL: 400V

Pole number: 4

Number of phases: 3

Rated speed 1500 rpm

Rated torque: 47.75 Nm

Motor axis height: 132 mm

Rated voltage LL 400V Y connection

Rated frequency 50 Hz

Main technical parameters of the induction motor

1. Synchronous rotational speed:

$$n_1 = 60\frac{f}{p} = 60\frac{50}{2} = 1500 \text{ rpm}$$

2. For the axis height h=132 mm the stator outer diameter is

$$D_a = 225 \text{ mm}$$

3. Inner diameter of the stator

$D = K_d \cdot D_a = 0.667 \cdot 0.225 = 0.15$ m where the coefficient $K_d \in [0.64 \div 0.68]$

[KOPILOV 86] (see Table B. 1)

Table B. 1 Coefficient K_D

2p	2	4	6	8-12
K_D	0.52-0.57	0,64-0,68	0,70-0,72	0,74-0,77

4. Expected levels for efficiency and power factor

$$\eta = 86\%, \cos\varphi = 0.86 \text{ p. u.}$$

5. Pole pitch

$$\tau = \frac{D \cdot \pi}{2p} = \frac{0.15 \cdot \pi}{4} = 0.118 \text{ m}$$

6. Active apparent power

$$P' = P_2 \frac{k_e}{\eta \cdot \cos\varphi} = 7500 \frac{0.97}{0.86 \cdot 0.86} = 9.84 \text{ kW}$$

where coefficient k_e is a ratio between the back EMF and the voltage.

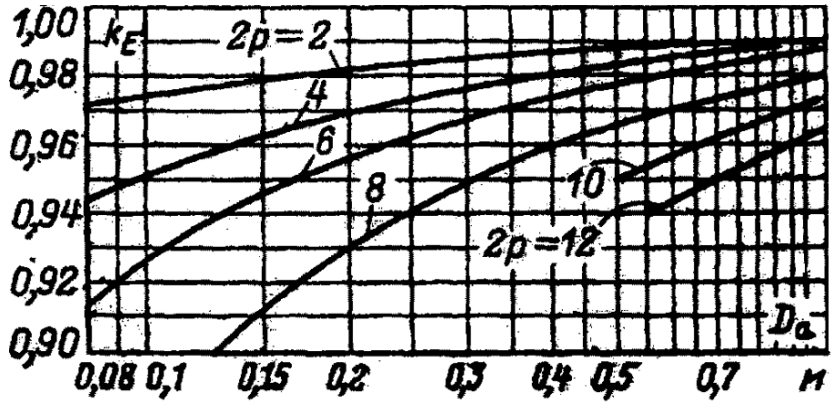

Fig. B. 1 Coefficient k_e [KOPILOV_86]

7. According to Fig. B. 2 and Fig. B. 3 the expected electromagnetic load and the air gap flux density for the motor axis height 132mm and IP54:

$$A = 27*10^3 \text{ A/m}; \quad B_\delta = 0.89 \text{ T}$$

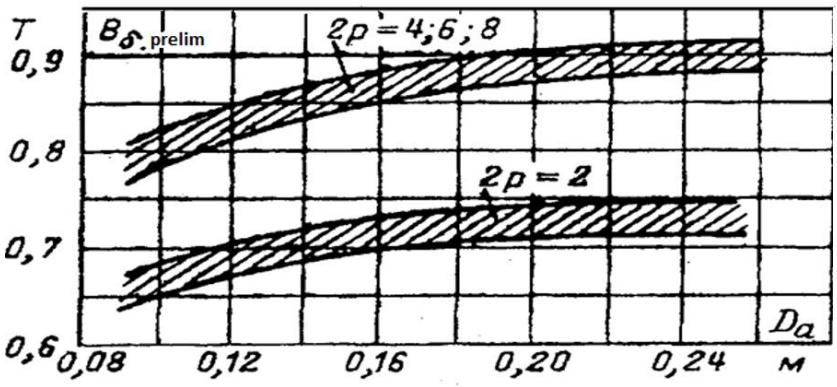

Fig. B. 2 Preliminary values of the air gap flux density versus the stator outer diameter [KOPILOV_86]

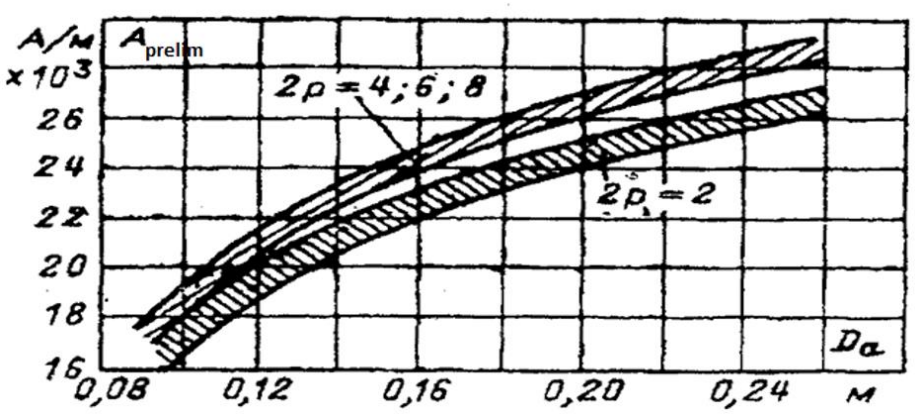

Fig. B. 3 Preliminary value of the electrical loading versus the stator outer diameter [KOPILOV_86]

8. Winding factor for single-layer winding:

$$k_{w1} = 0.95$$

9. Active length of the magnetic core

$$l_\delta = \frac{P'}{1.11 \cdot D^2 \cdot \Omega \cdot k_{w1} \cdot A \cdot B_\delta} = \frac{9.8364 \cdot 10^3}{1.11 \cdot 0.15^2 \cdot 157 \cdot 0.95 \cdot 27 \cdot 10^3 \cdot 0.89} = 0.11 \text{ m},$$

where $\Omega = \frac{2 \cdot \pi \cdot n_1}{60} = 157$ rad/s

10. Geometrical main machine dimensional criteria

$$\lambda = \frac{l_\delta}{\tau} = 0.93$$

which is situated within recommended limits (0.8÷1.3).

Determination of the slot number, number of turns per winding and a cross section of the stator winding

1. According to [KOPILOV_86] the limit values for the stator tooth pitch $t_1 \in [0.11 \div 0.13]$ mm for the motor axis height 132mm.

2. Number of stator slots

$$Z_{1min} = \frac{\pi \cdot D}{t_{1max}} = \frac{\pi \cdot 0.15}{0.13} = 36$$

$$Z_{1max} = \frac{\pi \cdot D}{t_{1min}} = \frac{\pi \cdot 0.15}{0.11} = 42$$

Chose $Z_1 = 36$, then the number of stator slots per pole and per phase $q = \frac{Z_1}{2p \cdot m} = \frac{36}{4 \cdot 3} = 3$ slots. In this case the number of rotor slots $Z_2 = 40$.

3. Tooth stator pitch

$$t_1 = \frac{D \cdot \pi}{2p \cdot m \cdot q} = \frac{0.15 \cdot \pi}{2 \cdot 2 \cdot 3 \cdot 3} = 13.1\,\text{mm}$$

4. Preliminary value of the stator phase current

$$I_{1n} = \frac{P_2}{3 \cdot U_{1n} \cdot \eta \cdot \cos\varphi} = \frac{7500}{3 \cdot 231 \cdot 0.86 \cdot 0.86} = 14.63\,\text{A}$$

5. Number of effective conductors in one slot

$$u_{s1} = \frac{\pi \cdot D \cdot A}{I_{1n} \cdot Z_1} = \frac{\pi \cdot 0.15 \cdot 27000}{14.63 \cdot 36} \cong 24$$

6. Chose the number of parallel branches in one stator winding $a = 1$, then

$$U_s = a \cdot u_{s1} = 1 \cdot 24 = 24$$

7. Number of turns per winding

$$W_1 = \frac{U_s \cdot Z_1}{2 \cdot 3 \cdot a} = \frac{24 \cdot 36}{2 \cdot 3 \cdot 1} = 144\ \text{turn}$$

8. Adjusted electromagnetic loading value

$$A = \frac{2 \cdot 3 \cdot I_{1n} \cdot W_1}{\pi \cdot D} = \frac{2 \cdot 3 \cdot 14.63 \cdot 144}{\pi \cdot 0.15} = 26.815 \cdot 10^3\,\text{A/m}$$

9. Adjusted magnetic flux

$$\Phi = \frac{k_e \cdot U_{1n}}{4 \cdot 1.11 \cdot W_1 \cdot k_{w1} \cdot f} = \frac{0.97 \cdot 231}{4 \cdot 1.11 \cdot 144 \cdot 0.95 \cdot 50} = 0.0073\,\text{Wb}$$

10. Adjusted magnetic flux density

$$B_\delta = \frac{p \cdot \Phi}{D \cdot l_\delta} = \frac{2 \cdot 0.0073}{0.15 \cdot 0.11} = 0.885\ \mathrm{T}$$

11. Estimated value of the current density in the stator windings

$$J_1 = \frac{A \cdot J_1}{A} = 7.0 \cdot 10^6 \frac{A}{m^2} \rightarrow A \cdot J_1 = 188 \cdot 10^9 A^2/m^3$$

12. Cross-section of one effective conductor

$$q_{ef} = \frac{I_{1n}}{a \cdot J_1} = \frac{14.63}{1 \cdot 7 \cdot 10^6} = 2.09\ \mathrm{mm}^2$$

13. Assume that where is 2 elementary conductors in one effective $n_{el} = 2$, then the cross-sectional area of the standard uninsulated wire chosen using a list of standardized values is

$$q_{el} = \frac{q_{ef}}{n_{el}} = \frac{2.09}{2} \cong 0.985\ \mathrm{mm}^2$$

14. Using a list of standardized values of wires, it has been chosen

$d_{el} = 1.12\ \mathrm{mm}-$ diameter of uninsulated wire

$q_{ef} = q_{el} \cdot n_{el} = 0.985 \cdot 2 = 1.97\ \mathrm{mm}^2,$

$d_i = 1.2\ \mathrm{mm}-$ diameter of insulated wire

15. Adjusted value of Current density in the stator windings

$$J_1 = \frac{I_{1n}}{a \cdot q_{el} \cdot n_{el}} = \frac{14.63}{1 \cdot 0.985 \cdot 2} \cong 7.43\ \mathrm{A/mm}^2$$

16. Normally the stator yoke flux density $B_a \in [1.4 \div 1.6]$ T and stator teeth flux density $B_{z1} \in [1.6 \div 1.9]$. Chose $B_a = 1.6\ \mathrm{T}, B_{z1} = 1.9\ \mathrm{T}$.

17. Preliminary value of the stator teeth width

$$b_{z1} = \frac{B_\delta \cdot t_1}{B_{z1} \cdot 0.97} = \frac{0.885 \cdot 0.0131}{1.9 \cdot 0.97} \cong 6.29\ \mathrm{mm}$$

$$h_{a1} = \frac{\Phi}{1.94 \cdot B_a \cdot l_\delta} = \frac{0.0073}{1.94 \cdot 1.6 \cdot 0.11} \cong 21.4\,\text{mm}$$

18. Slot stamp dimensions (see Fig. B. 4):

h_{slit} = 0.5 mm - height of the stator slot slit

b_{slit} = 3.5 mm - mean value of the stator slot

$\Delta b_s = \Delta h_s$ =0.1 mm - width and height of stator slot allowances

b_i = 0.35 mm one-sided thickness of slot insulation

$$h_{s1} = \frac{(D_a - D)}{2} - h_{a1} = \frac{0.225 - 0.15}{2} - 0.0214 = 16.1\,\text{mm}$$

$$b_{2(s)} = \frac{\pi \cdot (D + 2 \cdot h_{s1})}{Z_1} - b_{z1} = \frac{(0.15 + 2 \cdot 0.0161)}{36} - 0.00629 = 9.6\,\text{mm}$$

$$b_{1(s)} = \frac{\pi \cdot (D + 2 \cdot h_{slit} - b_{slit}) - Z_1 \cdot b_{z1}}{Z_1 - \pi} = \\ = \frac{\pi \cdot (0.15 + 2 \cdot 0.0005 - 0.0035) - 36 \cdot 0.00629}{36 - \pi} = 7.2\,\text{mm}$$

$h_{w(s)} = 0.5 \cdot (b_{1(s)} - b_{slit}) = 0.5 \cdot (7.2 - 3.5) = 1.9\,\text{mm}$ - height of the stator slot wedge

$h_{s.k.(s)} = h_{s1} - (h_{slit} + h_{w(s)})$=16.1-(0.5+1.9) =13.7 mm - height of the stator slot for wires laying

$h_{z(1)} = h_{s1} = 16.1\,\text{mm}$

19. Slot stamp dimensions taking into account assembly allowances

$$b'_{1(s)} = b_{1(s)} - \Delta b_s = 7.2 - 0.1 = 7.1\,\text{mm}$$

$$b'_{2(s)} = b_{2(s)} - \Delta b_s = 9.6 - 0.1 = 9.5\,\text{mm}$$

$$h'_{s.k.(s)} = h_{s.k.(s)} - \Delta h_s = 13.7 - 0.1 = 13.6\,\text{mm}$$

20. Cross-sectional area of the stator slot insolation

$$S_i = b_i(2 \cdot h_{s1} + b_{1(s)} + b_{2(s)}) = 0.35 \cdot (2 \cdot 16.1 + 7.2 + 9.6) = 17.15\,\text{mm}^2$$

21. Stator slot cross-sectional area designed for the placement of winding conductors

$$S'_s = \frac{b'_{1(s)} + b'_{2(s)}}{2} \cdot h'_{s.k.(s)} - S_i = \frac{7.1 + 9.5}{2} \cdot 13.6 - 17.15 = 95.73\,mm^2$$

22. Slot fill factor

$$k_{fill} = \frac{d_i^2 \cdot U_s \cdot n_{el}}{S'_s} = \frac{1.2^2 \cdot 24 \cdot 2}{95.73} = 0.722$$

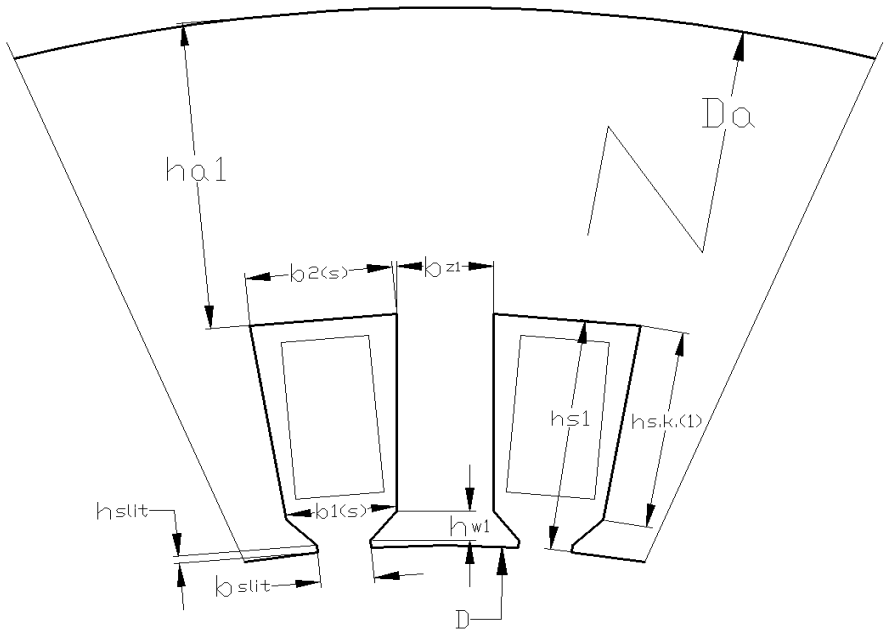

Fig. B. 4 Stator tooth zone

Dimensions of the rotor tooth zone

1. According to design of experiments accomplished for the LSPMSM steady state regime the air gap is chosen equal to δ=0.7mm.

2. Number of the rotor slots for 2p = 4 and Z1 = 36 equals to Z2 = 40

3. Rotor diameter D_2 =D – 2δ =150-2·0.7 ≅ 148.7 mm

4. Active rotor length $l_2 = l_\delta = 110\,mm$

5. Tooth rotor pitch

$$t_2 = \frac{\pi \cdot D_2}{Z_2} = \frac{\pi \cdot 148.7}{40} = 11.68\ \text{mm}$$

6. Shaft diameter

$$D_j = D_{sh} = k_{sh} \cdot D_a = 0.23 \cdot 0.225 \cong 50\ \text{mm}$$

where $k_{sh} = 0.23$, for the axis height h = 132 mm and 2p = 4

7. Calculation of current in rotor bars

$K_I = 0.2 + 0.8 \cdot \cos\varphi = 0.2 + 0.8 \cdot 0.86 = 0.888$ - coefficient taking into account the influence of the magnetizing current

$$\upsilon_I = \frac{2 \cdot 3 \cdot W_1 \cdot k_W}{Z_2} = \frac{2 \cdot 3 \cdot 144 \cdot 0.96}{40} = 20.7 - \text{reduction coefficient}$$

$I_{2n} = K_I \cdot \upsilon_I \cdot I_{1n} = 0.888 \cdot 20.7 \cdot 14.63 = 269.4\ \text{A}$ - estimated value of the nominal rotor phase current

8. Cross-sectional area of one rotor bar

$$q_b = \frac{I_{2n}}{J_2} = \frac{269.4}{3.3} = 81.6\ \text{mm}^2$$

Where $J_2 \in [2.5 \div 3.5]\ \text{A/mm}^2$ - current density in the rotor bar for IP 54

9. Normally the rotor teeth flux density $B_{z2} \in [1.7 \div 1.95]$. Chose $B_{z2} = 1.75\ \text{T}$.

10. Preliminary value of the rotor teeth width

$$b_{z2} = \frac{B_\delta \cdot t_2}{0.97 \cdot B_{z2}} = \frac{0.885 \cdot 0.01168}{0.97 \cdot 1.75} = 6.09\ \text{mm}$$

11. If the motor axis height is less than 160 mm normally it is used trapezoidal semi-closed bars. For this case width of the slit $b_{slit2} = 1.5\ \text{mm}$, height of the slit $h_{slit2} = 0.75\ \text{mm}$, then the diameter of the curvature of the upper part of the rotor slot is

$$b_{1(r)} = \frac{\pi \cdot (D_2 - 2 \cdot h_{slit2}) - Z_2 \cdot b_{z2}}{\pi + Z_2} = \frac{\pi \cdot (148.7 - 2 \cdot 0.75) - 40 \cdot 6.09}{\pi + 40} = 5.0\ \text{mm}$$

12. Adjustment of the preliminary rotor bar current density

$$\Delta q_b = \left(\frac{Z_2}{\pi} + \frac{\pi}{2}\right) \cdot b_{1(r)}^2 - 4 \cdot q_b = \left(\frac{40}{\pi} + \frac{\pi}{2}\right) \cdot 5.0^2 - 4 \cdot 81.6 = 41.13\ \text{mm}^2$$

13. Diameter of the curvature of the rotor bar lower part

$$b_{2(r)} = \sqrt{\frac{\Delta q_b}{\frac{Z_2}{\pi} - \frac{\pi}{2}}} = \sqrt{\frac{41.13}{\frac{40}{\pi} + \frac{\pi}{2}}} = 2.0\ \text{mm}$$

14. Distance between the centers of the upper and lower circles of the rotor bar

$$h_{1(r)} = \left(b_{1(r)} - b_{2(r)}\right) \cdot \frac{Z_2}{\pi} = (5.0 - 2.0) \cdot \frac{40}{\pi} = 20.2\ \text{mm}$$

15. Height of the rotor slot

$$h_{s(r)} = h_{1(r)} + \frac{b_{1(r)}}{2} + \frac{b_{2(r)}}{2} + h_{slit2} = 19.4 + \frac{5.0}{2} + \frac{2.0}{2} + 0.75 = 24.4\ \text{mm}$$

16. Cross-sectional area of the rotor bar

$$q_b = \frac{\pi}{8}\left(b_{1(r)}^2 + b_{2(r)}^2\right) + \frac{\left(b_{1(r)} + b_{2(r)}\right)}{2} \cdot h_{1(r)}$$

$$= \frac{\pi}{8}(5.0^2 + 2.0^2) + \frac{(5.0 + 2.0)}{2} \cdot 19.7 = 81.9\ \text{mm}^2$$

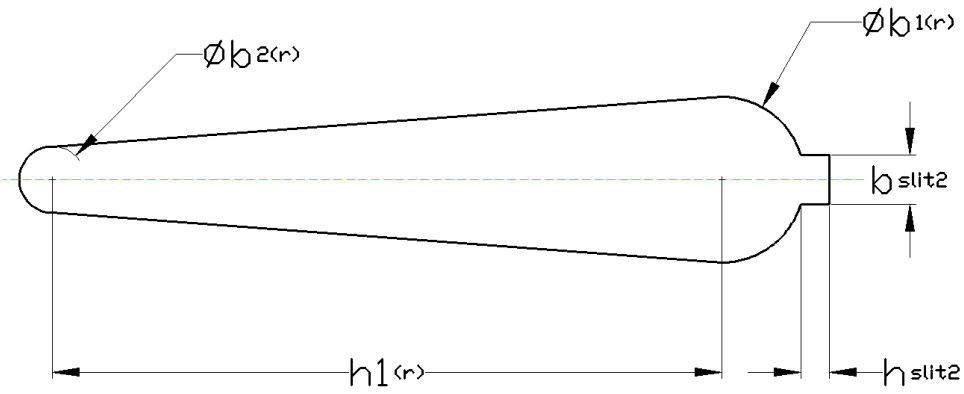

Fig. B. 5 Rotor slot configuration

17. Adjusted current density in the rotor bar

$$J_2 = \frac{I_{2n}}{q_b} = \frac{269.4}{81.9} = 3.29\ \text{A/mm}^2$$

18. Current density in the end ring of the short-circuited rotor

$$J_{rg} = 0.85 \cdot J_2 = 0.85 \cdot 3.29 = 2.8\ \text{A/mm}^2$$

19. Ratio of the current in the bars to the current in the end-ring

$$\Delta = 2 \cdot \sin\left(2p \cdot \frac{\pi}{Z_2 \cdot 2}\right) = 2 \cdot \sin\left(4 \cdot \frac{\pi}{40 \cdot 2}\right) = 0.31$$

20. Current in the end ring

$$I_{rg} = \frac{I_{2n}}{\Delta} = \frac{269.4}{0.31} = 861.02\ \text{A}$$

21. Cross-sectional area of the end ring

$$q_{rg} = \frac{I_{rg}}{J_{rg}} = \frac{861.02}{2.8} = 308\text{mm}^2$$

22. Cross-sectional height of the end ring

$$h_{rg} = 1.25 \cdot h_{s(r)} = 1.25 \cdot 24{,}4 = 30.5\ \text{mm}$$

23. Width of the end ring

$$b_{rg} = \frac{q_{rg}}{h_{rg}} = \frac{308}{30.5} = 10.1\ mm$$

24. Average diameter of the end ring

$$D_{rg.av} = D_2 - 0.001 \cdot h_{rg} = 148.7 - 0.001 \cdot 30.5 = 118.18\ mm$$

Calculation of the magnetizing current

1. Flux densities in the stator and rotor teeth and stator and rotor yoke correspondingly are $B_{Z1} = 1.88\ T,\ B_{Z2} = 1.75\ T, B_a = 1.6T, B_j = 1.10\ T$

2. Rated height of the rotor yoke at 2p=4

$$h_j' = \left(2 + \frac{2p}{2}\right) \cdot \frac{\frac{D_2}{2} - 0.001 \cdot h_{s(r)}}{3.2 \cdot \frac{2p}{2}} = 4 \cdot \frac{\frac{148.7}{2} - 0.001 \cdot 24.4}{3.2 \cdot 2} = 30.7\ mm$$

3. Computation of the Carter's factor k_δ

$$\gamma_1 = \frac{(b_{slit}/\delta)^2}{5 + \frac{b_{slit}}{\delta}} = \frac{(3.5/0.7)^2}{5 + \frac{3.5}{0.7}} = 2.5$$

$$\gamma_2 = \frac{(b_{slit}/\delta)^2}{5 + \frac{b_{slit}}{\delta}} = \frac{(1.5/0.7)^2}{5 + \frac{1.5}{0.7}} = 0.64$$

$$k_{\delta 1} = \frac{t_1}{(t_1 - \gamma_1 \cdot \delta)} = \frac{13.1}{(13.1 - 2.5 \cdot 0.7)} = 1.154$$

$$k_{\delta 2} = \frac{t_2}{(t_2 - \gamma_2 \cdot \delta)} = \frac{11.68}{(11.68 - 0.64 \cdot 0.7)} = 1.04$$

$$k_\delta = k_{\delta 1} \cdot k_{\delta 2} = 1.154 \cdot 1.04 = 1.2$$

4. Magnetic voltage in the air gap

$$F_\delta = \frac{2}{\mu_0} \cdot B_\delta \cdot k_\delta \cdot \delta = \frac{2}{4\pi \cdot 10^{-7}} \cdot 0.885 \cdot 1.2 \cdot 0.7 = 1183.3\ A$$

5. Magnetic voltage in the stator tooth zone

$$F_{z1} = 2 \cdot h_{s1} \cdot H_{z1} = 0.002 \cdot 16.1 \cdot 1950 = 62.79\ A$$

6. Magnetic voltage in the rotor tooth zone

$$F_{z2} = 2 \cdot h_{s(r)} \cdot H_{z2} = 0.002 \cdot 24.4 \cdot 1330 = 64.4\,\text{A A}$$

where H_{z1} and H_{z2} are taken from the data-sheet for applied electric steel

7. Saturation coefficient of the induction motor tooth zone

$$k_z = 1 + \frac{F_{z1} + F_{z2}}{F_\delta} = 1 + \frac{62.79 + 64.4}{1183.3} = 1.11$$

8. Height of the stator yoke

$$h_a = 0.5 \cdot (D_a - D) - h_{s1} = 0.5 \cdot (225 - 150) - 16.1 = 21.4\,\text{mm}$$

9. Height of the rotor yoke

$$h_j = 0.5 \cdot (D_2 - D_j) - h_{s(r)} = 0.5 \cdot (148.7 - 50) - 24.4 = 24.0\,\text{mm}$$

10. Magnetic voltages in the stator and rotor yokes respectively

$$F_a = L_a \cdot H_a = 0.16 \cdot 750 = 120\,\text{A}$$

$$F_j = L_j \cdot H_j = 0.06 \cdot 221 = 13.2\,\text{A}$$

where H_a and H_j are taken from the data-sheet for applied electric steel and L_a and L_j are lengths of the average magnetic field line in the stator ant rotor yokes respectively

$$L_a = \frac{\pi \cdot (D_a - h_a)}{2p} = \frac{\pi \cdot (225 - 21.4)}{4} = 0.16\,\text{m}$$

$$L_j = \frac{\pi \cdot (D_j + h_j)}{2p} = \frac{\pi \cdot (50 - 23.1)}{4} = 0.059\,\text{m}$$

11. Total magnetic voltage of the induction motor magnetic circuit for one pair (Fig. B. 6).

$$F_\mu = F_\delta + F_{z1} + F_{z2} + F_a + F_j = 1183.3 + 62.8 + 64.4 + 120 + 13.2 = 1443.6\,\text{A}$$

12. Magnetic circuit saturation factor

$$k_\mu = \frac{F_\mu}{F_\delta} = \frac{1437.2}{1166.9} = 1.23$$

13. Magnetizing current

$$I_\mu = \frac{p \cdot F_\mu}{0.9 \cdot 3 \cdot W_1 \cdot k_w} = \frac{2 \cdot 1437.2}{0.9 \cdot 3 \cdot 144 \cdot 0.96} = 7.7\ A$$

14. Magnetizing current in per unit values

$$I_\mu^* = \frac{I_\mu}{I_{1n}} = \frac{7.7}{14.63} = 0.53\ p.u.$$

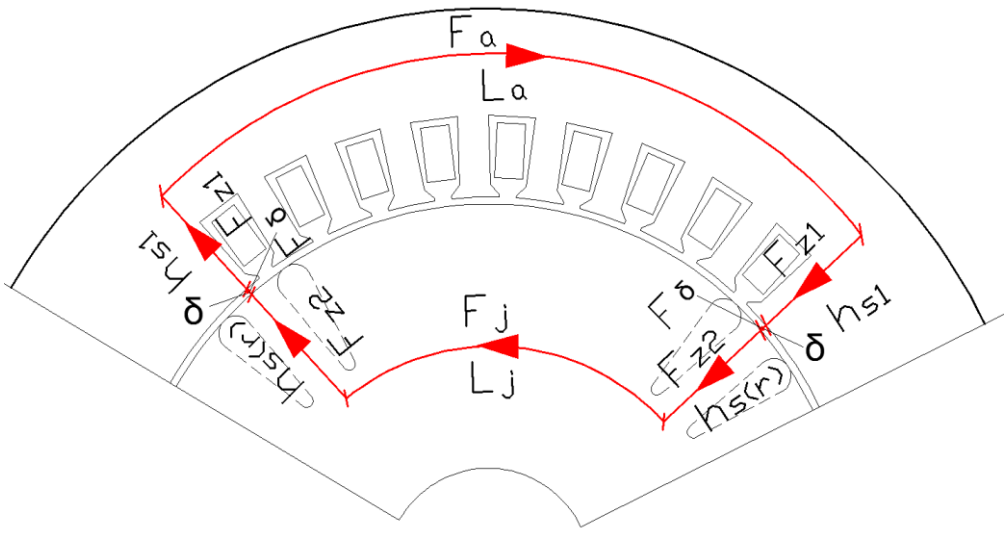

Fig. B. 6 Magnetic circuit scheme of the magnetic flux circulation

Characteristics of IM at nominal operating mode

1. Average coil width

$$b_{coil} = \pi \cdot (D + h_{s1}) \cdot \frac{\beta_1}{2p} = \pi \cdot (0.15 + 0.016) \cdot \frac{1}{2p} = 0.1305\ m$$

Where β_1 is relative winding pitch

2. Overhang of the end-winding (see Fig. B. 7)

$$L_{ov} = K_{ov} \cdot b_{coil} + B = 0.5 \cdot 0.1305 + 0.01 = 0.075 \text{ m}$$

Where B is length of the straight part of the coil overhang, K_{ov} is coefficient for insulated end-windings.

3. Length of the end parts of the coil

$$L_{end} = K_{end} \cdot b_{coil} + 2 \cdot B = 1.55 \cdot 0.1305 + 2 \cdot 1.55 = 0.22 \text{ m}$$

Where K_{end} is coefficient for insulated end-windings.

4. Average length of one coil turn

$$L_{av} = 2 \cdot (l_{\delta} + L_{end}) = 2 \cdot (0.11 + 0.22) = 0.66 \text{ mm}$$

5. Total length of the phase stator windings conductor

$$L_1 = L_{av} \cdot W1 = 0.66 \cdot 144 = 95.05 \text{ m}$$

6. Active resistance of one phase in the stator winding at steady-state nominal temperature 115ºC

$$r_1 = \rho_{115} \cdot \frac{L_1}{a \cdot n_{el} \cdot q_{el} \cdot 0.000001} = \frac{95.05}{43 \cdot 10^{-6} \cdot 1 \cdot 2 \cdot 0.985 \cdot 10^{-6}} = 1.105 \text{ Ohm}$$

where ρ_{115} is electrical resistivity of copper

7. Active resistance of the phase stator winding in per units

$$r_1^* = r_1 \cdot \frac{I_{1n}}{U_{1n}} = 1.15 \cdot \frac{14.63}{231} = 0.07 \text{ p.u.}$$

8. Resistance of the end ring segment between two neighboring bars

$$r_{rg} = \rho_{rg} \cdot \pi \cdot \frac{D_{rg.av}}{Z_2 \cdot 10^{-6} \cdot q_{rg}} = \pi \cdot \frac{117.1}{20.5 \cdot 28 \cdot 10^{-6} \cdot 308} = 1.47 \cdot 10^{-6} \text{ Ohm}$$

where ρ_{rg} is electrical resistivity of aluminium in the rotor at steady-state nominal temperature 115ºC

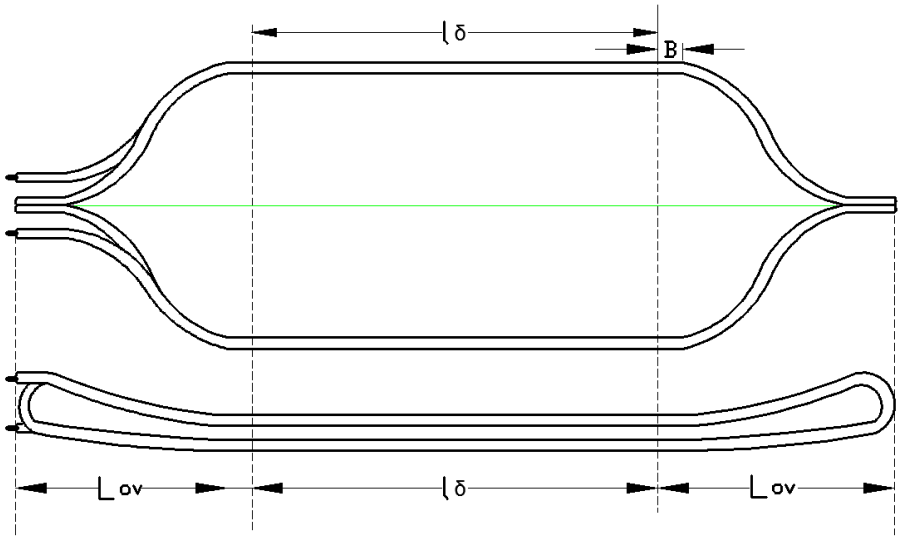

Fig. B. 7 Double layer coil of stator field winding

9. Rotor bar resistance

$$r_b = \rho_b \cdot \frac{l_\delta}{10^{-6} \cdot q_b} = \frac{0.11}{20.5 \cdot 81.9} = 6.55 \cdot 10^{-5}\ \text{Ohm}$$

where ρ_b is electrical resistivity of aluminium in the rotor at steady-state nominal temperature 115ºC

10. Active resistance of the phase rotor winding

$$r_2 = r_b + 2 \cdot \frac{r_{rg}}{\Delta^2} = 6.55 \cdot 10^{-5} + 2 \cdot 1.7 \cdot \frac{10^{-06}}{0.48^2} = 9.55 \cdot 10^{-5}\ \text{Ohm}$$

11. Active resistance of one phase rotor winding referred to the stator

$$r_2' = r_2 \cdot \frac{4 \cdot 3 \cdot (W_1 \cdot k_w)^2}{Z_2} = \frac{12 \cdot (144 \cdot 0.96)^2}{40} = 0.55\ \text{Ohm}$$

12. Active resistance of one phase rotor winding referred to the stator in per unit values

$$r_2'^* = r_2' \cdot \frac{I_{1n}}{U_{1n}} = 0.551 \cdot \frac{14.63}{231} = 0.035\ \text{p. u.}$$

13. Ratio of the rotor and stator teeth divisions

$$\Delta t_z = \frac{t_2}{t_1} = \frac{11.68}{13.1} = 0.89$$

14. Height of stator slot taking into account insulation thickness and mechanical allowances

$$h_{2(s)} = h_{s.k.(s)} - \Delta h_s - 2 \cdot b_i = 13.7 - 0.1 - 2 \cdot 0.35 = 12.9 \text{ mm}$$

Where the thickness of one-side stator slots insulation $b_i = 0.25$ mm

15. Stator slot leakage coefficient

$$\lambda_{S(1)} = \frac{h_{2(s)}}{3 \cdot b_{1(s)}} + 3 \cdot \frac{3 \cdot h_{w1}}{b_{1(s)} + 2 \cdot b_{1slit}} + \frac{h_{1slit}}{b_{1slit}} = \frac{12.9}{3 \cdot 7.2} + 3 \cdot \frac{3 \cdot 1.9}{7.2 + 2 \cdot 3.5} + \frac{0.5}{3.5} = 1.14$$

16. Stator end leakage coefficient

$$\lambda_{end(1)} = 0.34 \cdot q \cdot \frac{L_{end} - 0.64 \cdot \beta_1 \cdot \tau}{l_\delta} = 0.34 \cdot 3 \cdot \frac{0.22 - 0.64 \cdot 1 \cdot 0.117}{0.11} = 1.36$$

17. Calculation of the permeance of the stator winding differential leakage

$$\xi_1 = 2 \cdot 1.45 - (k_w \cdot \Delta t_z)^2 = 2.9 - (0.96 \cdot 0.89)^2 = 2.17$$

18. Stator differential leakage coefficient

$$\lambda_{diff(s)} = t_1 \cdot \frac{\xi_1}{12 \cdot k_\delta \cdot \delta} = 13.096 \cdot \frac{2.17}{12 \cdot 1.2 \cdot 0.7} = 2.82$$

19. Stator leakage reactance for one phase

$$x_1 = 15.8 \frac{f_1}{100} \cdot \frac{2 \cdot l_\delta}{2 \cdot p \cdot q} \left(\lambda_{S(1)} + \lambda_{end(1)} + \lambda_{diff(s)}\right) \left(\frac{W_1}{100}\right)^2 = 15.8 \frac{50}{100} \cdot \frac{2 \cdot 0.11}{2 \cdot 2 \cdot 3} (1.14 + 1.36 + 2.82) \left(\frac{144}{100}\right)^2 = 1.6 \text{ Ohm}$$

20. Phase stator leakage reactance per units

$$x_1^* = x_1 \frac{I_{1n}}{U_{1n}} = 1.6 \cdot \frac{14.63}{231} = 0.1 \text{ p.u.}$$

21. Dimensional factors of the rotor tooth zone

$$\Delta b_{\delta 2} = \frac{b_{slit2}}{\delta} = \frac{1.5}{0.7} = 2.14$$

$$\Delta b_{t2} = \frac{b_{slit2}}{t_2} = \frac{1.5}{11.68} = 0.13$$

22. Estimated height of the rotor slot

$$h_{0(r)} = h_{1(r)} + 0.4 \cdot b_{2(r)} = 20.2 + 0.4 \cdot 1.9 = 20.96\,\text{mm}$$

23. Rotor slot leakage coefficient

$$\lambda_{2(r)} = \left(\frac{h_{0(r)}}{3 \cdot b_{1(r)}} \cdot \left(1 - \frac{\pi \cdot b_{1(r)}^2}{8 \cdot q_b}\right) + 0.66 - \frac{b_{2slit}}{2 \cdot b_{1(r)}} + \frac{h_{2slit}}{b_{2slit}}\right)$$
$$= \left(\frac{20.96}{3 \cdot 5.1} \cdot \left(1 - \frac{\pi \cdot 5.0^2}{8 \cdot 81.9}\right) + 0.66 - \frac{1.5}{2 \cdot 5.0} + \frac{0.75}{1.5}\right) = 2.07$$

24. Leakage coefficient of the rotor end-rings

$$\lambda_{end(2)} = 2.3 \cdot \frac{D_{rg.av}}{(Z_2 \cdot l_\delta \cdot \Delta^2)} \cdot \lg\left(\frac{4.7 \cdot D_{rg.av}}{0.001 \cdot (h_{rg} + 2 \cdot b_{rg})}\right) =$$
$$= 2.3 \cdot \frac{0.12}{(40 \cdot 0.11 \cdot 0.31^2)} \cdot \lg\left(\frac{4.7 \cdot 0.12}{0.001 \cdot (30.5 + 2 \cdot 10.1)}\right) = 0.66$$

25. Calculation of the permeance of the rotor differential leakage

$$\xi_2 = 1 + 0.2 \cdot \left[\left(\frac{\pi \cdot 2p}{2 \cdot Z_2}\right)^2 - \frac{\Delta z}{\left(1 - \left(\frac{2p}{2 \cdot Z_2}\right)\right)^2}\right] = 1 + 0.2 \cdot \left[\left(\frac{\pi \cdot 2p}{2 \cdot 40}\right)^2 - \frac{0.02}{\left(1 - \left(\frac{2p}{2 \cdot 40}\right)\right)^2}\right]$$
$$= 0.99$$

where Δz can be found from **Erreur ! Source du renvoi introuvable.**.

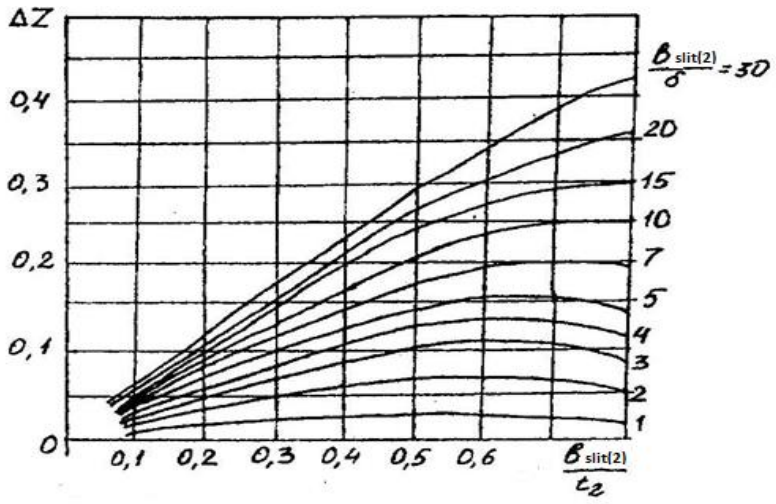

Fig. B. 8 Coefficient Δz [KOPILOV_86]

26. Rotor differential leakage coefficient

$$\lambda_{diff(r)} = t_2 \cdot \frac{\xi_2}{12 \cdot k_\delta \cdot \delta} = 11.68 \cdot \frac{0.99}{12 \cdot 1.2 \cdot 0.7} = 1.14$$

27. Rotor leakage reactance for one phase

$$x_2 = 7.9 \cdot f_1 \cdot l_\delta \cdot 0.000001 \cdot \left(\lambda_{S(r)} + \lambda_{end(r)} + \lambda_{diff(r)}\right) =$$
$$= 7.9 \cdot 50 \cdot 0.11 \cdot 0.000001 \cdot (2.07 + 0.66 + 1.14) = 0.00017 \text{ Ohm}$$

28. Phase rotor leakage reactance referred to the stator

$$x_2' = x_2 \cdot 12 \cdot \frac{(W_1 \cdot k_w)^2}{Z_2} = 0.00017 \cdot 12 \cdot \frac{(144 \cdot 0.96)^2}{40} = 0.96 \text{ Ohm}$$

29. Phase rotor leakage reactance referred to the stator in per unit values

$$x_{2*}' = x_2' \cdot \frac{I_{1n}}{U_{1n}} = 0.96 \cdot \frac{14.63}{231} = 0.061 \text{ p. u.}$$

Losses in the induction motor

1. Mass of the steel stator yoke

$$m_a = \pi \cdot (D_a - 0.001 \cdot h_a) \cdot k_c \cdot \gamma_c \cdot l_\delta \cdot 0.001 \cdot h_a$$
$$= \pi \cdot (0.225 - 0.001 \cdot 21.4) \cdot 0.97 \cdot 7800 \cdot 0.11 \cdot 0.001 \cdot 21.4$$
$$= 11.4 \text{ kg}$$

Where

$k_c = 0.97$ – stator core filling factor, $\gamma_c = 7800 \frac{kg}{m^3}$ – specific weight of steel

2. Mass of stator teeth

$$m_{Z(s)} = 0.001 \cdot h_{Z(1)} \cdot 0.001 \cdot b_{Z(1)} \cdot Z_1 \cdot l_\delta \cdot k_c \cdot \gamma_c =$$
$$= 0.001 \cdot 16.1 \cdot 0.001 \cdot 6.31 \cdot 36 \cdot 0.11 \cdot 0.97 \cdot 7800 = 3.044 \text{ kg}$$

3. Fundamental losses of in the stator core

$$\Delta p_{c.fund} = P_{0.1/50} \cdot \left(k_{DA} \cdot m_a \cdot B_a^2 + k_{DZ} \cdot m_{Z(s)} \cdot B_{Z(1)}^2\right) \cdot \left(\frac{f_1}{50}\right)^\beta$$
$$= 2.5 \cdot (1.6 \cdot 114.4 \cdot 1.6^2 + 1.8 \cdot 3.044 \cdot 1.89^2) \cdot \left(\frac{50}{50}\right)^\beta = 165.84 \text{ W}$$

Where β=1,3÷1,5 - coefficient taking into account the dependence of the losses in the steel on the frequency of magnetization reversal, k_{DA}=1,6, k_{DZ}=1,8 -coefficients taking into account the effect of magnetic flux uneven distribution on the core losses, $P_{0,1/50}$=2.5 W/kg - specific losses in the utilized steel.

4. Active resistance, which characterizes magnetic losses in the equivalent circuit

$$r_{12} = \frac{\Delta p_{c.fund}}{3 \cdot I_\mu{}^2} = \frac{165.84}{3 \cdot 7.7^2} = 0.92 \text{ Ohm}$$

5. Active resistance in per units

$$r_{12}^* = r_{12} \cdot \frac{I_{1n}}{U_{1n}} = 0.92 \cdot \frac{14.63}{231} = 0.059 \text{ Ohm}$$

6. Reactance of mutual stator and rotor inductances

$$x_{12} = \frac{U_{1n}}{I_\mu} - x_1 = \frac{231}{7.7} - 1.6 = 28.3 \text{ Ohm}$$

7. Reactance of mutual stator and rotor inductances in per unit values

$$x_{12}^{*} = x_{12} \cdot \frac{I_{1n}}{U_{1n}} = 28.3 \cdot \frac{14.63}{231} = 1.79 \text{ Ohm}$$

Erreur ! Source du renvoi introuvable. shows a T-type electrical equivalent ircuit of the studied IM

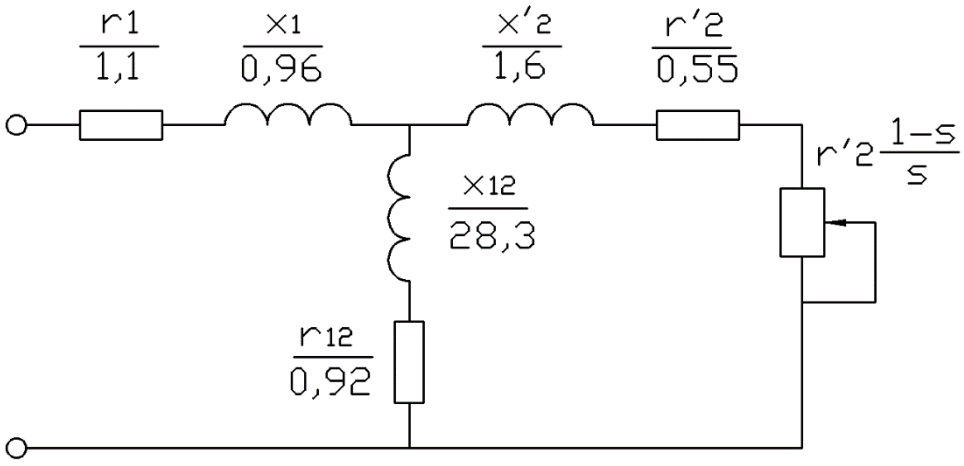

Fig. B. 9 T-type equivalent circuit of IM

8. Ratio of the slit width to the air gap

$$\Delta b_{\delta 1} = \frac{b_{slit1}}{\delta} = \frac{3.5}{0.7} = 5$$

$$\Delta b_{\delta 2} = \frac{b_{slit2}}{\delta} = \frac{1.5}{0.7} = 2.14$$

9. Amplitude of the flux density pulsations in the air gap on the crowns of teeth of the stator and rotor (Fig. B. 10)

$$B_{0(s)} = \beta_{0(1)} \cdot k_{\delta} \cdot B_{\delta} = 0.3 \cdot 1.2 \cdot 0.88 = 0.32 \text{ T}$$

$$B_{0(r)} = \beta_{0(2)} \cdot k_{\delta} \cdot B_{\delta} = 0.1 \cdot 1.2 \cdot 0.88 = 0.11 \text{ T}$$

Where the coefficients could be found from Fig. B. 10.

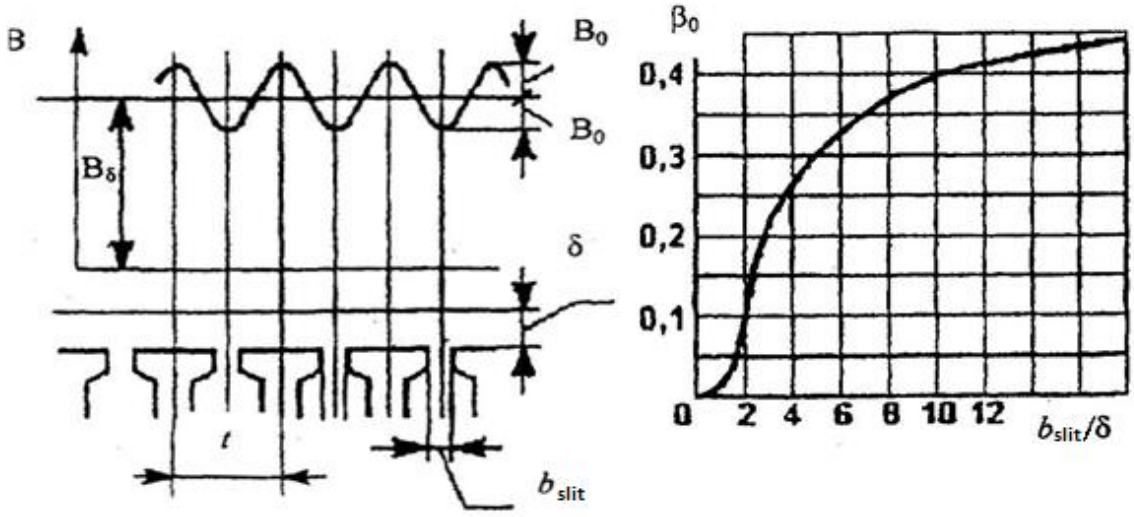

Fig. B. 10 For calculation of surface losses: representation of flux density pulsation in the air gap and the plot $\beta_0=f(b_{slit}/\delta)$ [KOPILOV 86]

10. At the no-load regime the rotational speed is taken as the speed of magnetic field rotation

$$n = 60 \cdot \frac{f_1}{2p} = 60 \cdot \frac{50}{4} = 1500 \text{ rpm}$$

11. Specific surface losses in stator and rotor crowns

$$p_{surf(s)} = 0.75 \cdot \left(Z_2 \cdot \frac{n}{10000}\right)^{1.5} \cdot \left(B_{0(s)} \cdot t_2\right)^2$$
$$= 0.75 \cdot \left(40 \cdot \frac{1500}{10000}\right)^{1.5} \cdot (0.32 \cdot 11.68)^2 = 152.6 \text{ W/m}^2$$

$$p_{surf(r)} = 0.75 \cdot \left(Z_1 \cdot \frac{n}{10000}\right)^{1.5} \cdot \left(B_{0(r)} \cdot t_1\right)^2$$
$$= 0.75 \cdot \left(36 \cdot \frac{1500}{10000}\right)^{1.5} \cdot (0.11 \cdot 13.1)^2 = 18.2 \text{ W/m}^2$$

12. Total surface losses

$$\Delta p_{surf(s)} = p_{surf(s)} \cdot 0.001 \cdot (t_1 - b_{slit1}) \cdot Z_1 \cdot l_\delta$$
$$= 152.6 \cdot 0.001 \cdot (13.096 - 3.5) \cdot 36 \cdot 0.11 = 5.8 \text{ W}$$

$$\Delta p_{surf(r)} = p_{surf(r)} \cdot 0.001 \cdot (t_2 - b_{slit2}) \cdot Z_2 \cdot l_\delta$$
$$= 18.2 \cdot 0.001 \cdot (11.68 - 1.5) \cdot 40 \cdot 0.11 = 0.82 \text{ W}$$

13. Amplitude of the flux density pulsations in the middle cross sections of teeth

$$B_{pul(1)} = \gamma_2 \cdot \delta \cdot \frac{B_{Z(s)}}{2 \cdot t_1} = 0.64 \cdot 0.7 \cdot \frac{1.89}{2 \cdot 13.096} = 0.033\ T$$

$$B_{pul(2)} = \gamma_1 \cdot \delta \cdot \frac{B_{Z(r)}}{2 \cdot t_2} = 2.5 \cdot 0.7 \cdot \frac{1.75}{2 \cdot 11.68} = 0.13\ T$$

14. Mass of rotor teeth steel

$$m_{Z(r)} = Z_2 \cdot h_{Z(r)} \cdot b_{Z(r)} \cdot l_\delta \cdot k_c \cdot \gamma_c = 40 \cdot 0.0241 \cdot 0.00609 \cdot 0.11 \cdot 0.97 \cdot 7800 = 4.91\ kg$$

15. Pulsation losses in teeth

$$\Delta p_{pul(s)} = 0.11 \cdot m_{Z(s)} \cdot \left(Z_2 \cdot n \cdot \frac{B_{pul(1)}}{1000}\right)^2 = 0.11 \cdot 3.044 \cdot \left(40 \cdot 1500 \cdot \frac{0.033}{1000}\right)^2 = 1.27\ W$$

$$\Delta p_{pul(r)} = 0.11 \cdot m_{Z(r)} \cdot \left(Z_1 \cdot n \cdot \frac{B_{pul(2)}}{1000}\right)^2 = 0.11 \cdot 4.91 \cdot \left(36 \cdot 1500 \cdot \frac{0.13}{1000}\right)^2 = 27.0\ W$$

16. Sum of additional losses at no-load

$$\Delta p_{c.ad} = \Delta p_{surf(s)} + \Delta p_{surf(r)} + \Delta p_{pul(s)} + \Delta p_{pul(r)} = 5.8 + 0.82 + 1.27 + 27.0 = 34.88\ W$$

17. Total magnetic losses of induction motor

$$\Delta p_c = \Delta p_{c.ad} + \Delta p_{c.fund} = 34.88 + 165.84 = 200.72\ W$$

18. Mechanical and ventilation losses

$$\Delta p_{mec} = K_T'' \cdot \left(\frac{n}{10}\right)^2 \cdot D_a^4 = 1.0075 \cdot \left(\frac{1500}{10}\right)^2 \cdot 0.225^4 = 58.1\ W$$

19. Electrical losses in the stator at no-load mode

$$\Delta p_{el.0} = 3 \cdot r_1 \cdot I_\mu^2 = 3 \cdot 1.1 \cdot 7.7^2 = 198.3\ W$$

20. Active component of the no-load current

$$I_{0.a} = (\Delta p_c + \Delta p_{mec} + \Delta p_{el.0}) \cdot (3 \cdot U_{1n}) = 0.66\,A$$

21. No-load current

$$I_0 = \sqrt{I_{0.a}^2 + I_\mu^2} = \sqrt{0.66^2 + 7.7^2} = 7.765\,A$$

22. No-load power factor

$$\cos\varphi_0 = \frac{I_{0.a}}{I_0} = \frac{7.7}{7.765} = 0.0$$

23. Losses which do not depend on the slip

$$\Delta p_{const} = 0.001 \cdot (\Delta p_c + \Delta p_{mec}) = 0.001 \cdot (200.72 + 58.1) = 0.26\,kW$$

24. Calculation of components of the complex coefficient C_1

Active component:

$$C_{1a} = \frac{(r_{12} \cdot (r_1 + r_{12}) + x_{12} \cdot (x_1 + x_{12}))}{r_{12}^2 + x_{12}^2} = \frac{(0.92 \cdot (1.104 + 0.92) + 28.26 \cdot (1.6 + 28.26))}{0.92^2 + 28.26^2} = 1.06$$

Reactive component:

$$C_{1r} = \frac{(r_1 \cdot x_{12} - r_{12} \cdot x_1)}{r_{12}^2 + x_{12}^2} = \frac{(1.04 \cdot 28.26 - 0.92 \cdot 1.6)}{0.92^2 + 28.26^2} = 0.037$$

25. Magnitude of the complex coefficient

$$C_1 = \sqrt{C_{1a}^2 + C_{1r}^2} = \sqrt{1.06^2 + 0.037^2} = 1.06$$

26. Complex coefficient

$$|\gamma| = \operatorname{arctg}\left(\frac{C_{1r}}{C_{1a}}\right) = \operatorname{arctg}\left(\frac{0.037}{1.06}\right) = 2.01^\circ$$

27. Determination of constant coefficients

$$a' = C_{1a}^2 - C_{1r}^2 = 1.06^2 - 0.037^2 = 1.12$$

$$b' = 2 \cdot C_{1a} \cdot C_{1r} = 2 \cdot 1.12 \cdot 0.037 = 0.08$$

$$a_0 = C_{1a} \cdot r_1 + C_{1r} \cdot x_1 + b' \cdot x_2' = 1.12 \cdot 1.04 + 0.037 \cdot 1.6 + 0.08 \cdot 0.96 = 1.3 \text{ Ohm}$$

$$b_0 = C_{1a} \cdot x_1 - C_{1r} \cdot r_1 + a' \cdot x_2' = 1.12 \cdot 1.6 - 0.037 \cdot 1.04 + 1.12 \cdot 0.96 = 2.73 \text{ Ohm}$$

28. Preliminary value of the nominal slip

$$s_{n.cr} = r_2'^* = 0.035$$

29. Components of the magnetization circuit complex impedance

$$R_m = C_{1a} \cdot r_{12} + C_{1r} \cdot x_{12} = 1.12 \cdot 0.92 + 0.037 \cdot 28.26 = 2.03 \text{ Ohm}$$

$$X_m = C_{1a} \cdot x_{12} + C_{1r} \cdot r_{12} = 1.12 \cdot 28.26 + 0.037 \cdot 0.92 = 29.86 \text{ Ohm}$$

$$Z_m = \sqrt{R_m^2 + X_m^2} = \sqrt{2.03^2 + 29.86^2} = 29.93 \text{ Ohm}$$

$$\cos\varphi_0 = \frac{R_m}{Z_m} = \frac{2.03}{29.93} = 0.068$$

$$\sin\varphi_0 = \frac{X_m}{Z_m} = \frac{29.86}{29.93} = 0.998$$

30. No-load current

$$I_0 = \frac{U_{1n}}{Z_m} = \frac{231}{29.93} = 7.72 \text{ A}$$

$$I_{0a} = I_0 \cdot \cos\varphi_0 = 7.72 \cdot 0.068 = 0.52 \text{ A}$$

$$I_{0r} = I_0 \cdot \sin\varphi_0 = 7.72 \cdot 0.998 = 7.7 \text{ A}$$

31. Rotor resistance and reactance depending on the slip

$$R_s = a_0 + a' \cdot \frac{r_2'}{s_{n.cr}} = 1.3 + 1.12 \cdot \frac{0.55}{0.035} = 18.95 \text{ Ohm}$$

$$X_s = b_0 + b' \cdot \frac{r_2'}{s_{n.cr}} = 0.08 + 2.73 \cdot \frac{0.55}{0.035} = 1.49 \text{ Ohm}$$

$$Z_s = \sqrt{R_s^2 + X_s^2} = \sqrt{18.95^2 + 1.49^2} = 19.0 \text{ Ohm}$$

$$\cos\varphi_2' = \frac{R_s}{Z_s} = \frac{18.95}{19.0} = 0.997$$

$$\sin\varphi_2' = \frac{X_s}{Z_s} = \frac{1.49}{19.0} = 0.078$$

32. Rotor current reduced to the stator

$$I_2'' = \frac{U_{1n}}{Z_s} = \frac{231}{19} = 12.15 \text{ A}$$

$$I_{2a}'' = I_2'' \cdot \cos\varphi_2' = 12.15 \cdot 0.997 = 12.12 \text{ A}$$

$$I_{2r}'' = I_2'' \cdot \sin\varphi_2' = 12.15 \cdot 0.078 = 0.95 \text{ A}$$

33. Active and reactive components of the stator phase current

$$I_{1a} = I_{0a} + I_{2a}'' = 0.52 + 12.12 = 12.64 \text{ A}$$

$$I_{1r} = I_{0r} + I_{2r}'' = 7.7 + 0.95 = 8.65 \text{ A}$$

34. Module of the phase stator current

$$I_1 = \sqrt{I_{1a}^2 + I_{1r}^2} = \sqrt{12.64^2 + 8.65^2} = 15.32 \text{ A}$$

35. Rotor current reduced to the stator

$$I_2' = C_1 \cdot I_2'' = 1.06 \cdot 12.15 = 12.87 \text{ A}$$

36. Active power at the input of the induction motor

$$P_1 = 3 \cdot U_{1n} \cdot I_{1a} = 3 \cdot 231 \cdot 12.64 = 8.76 \text{ kW}$$

37. Electrical losses in the windings of the stator and rotor

$$\Delta p_{el(s)} = 3 \cdot I_1^2 \cdot r_1 = 3 \cdot 15.32^{\,2} \cdot 1.04 = 0.78 \text{ kW}$$

$$\Delta p_{el(r)} = 3 \cdot I_2'^2 \cdot r_2' = 3 \cdot 12.87^{\,2} \cdot 0.55 = 0.27\ \text{kW}$$

38. Additional losses in the motor

$$\Delta p_{ad} = 0.005 \cdot P1 = 0.005 \cdot 8.76 \cdot 10^3 = 0.044\ \text{kW}$$

39. Total losses in the induction motor

$$\sum \Delta p = \Delta p_{el(s)} + \Delta p_{el(r)} + \Delta p_{fund} + \Delta p_{ad} = 0.78 + 0.27 + 0.26 + 0.044 = 1.35\ \text{kW}$$

40. Useful power

$$P_2 = P_1 - \sum \Delta p = 8.76 - 1.35 = 7.41\ \text{kW}$$

41. Efficiency of the induction motor

$$\eta = 1 - \sum \Delta p / P_1 = 1 - \frac{7.41}{8.76} = 0.846$$

42. Power factor

$$\cos\varphi = \frac{I_{1a}}{I_1} = \frac{12.64}{15.32} = 0.83$$

43. Electrical rotor speed

$$\Omega_2 = 4 \cdot \pi \cdot f_1 \cdot \frac{1 - s}{2p} = 4 \cdot \pi \cdot 50 \cdot \frac{1 - 0.035}{2p} = 151.63\text{rad/s}$$

44. Output electromagnetic torque

$$T_{nom} = 1000 \cdot \frac{P_2}{\Omega_2} = 1000 \cdot \frac{7.41}{151.63} = 48.86\ \text{Nm}$$

Calculation of induction motor starting characteristics

1. Geometrical dimensions of the rotor slot

$$h_{b(r)} = h_{1(r)} + 0.5 \cdot b_{1(r)} + 0.5 \cdot b_{2(r)} = 20.2 + 0.5 \cdot 5.0 + 0.5 \cdot 1.9 = 23.685\ \text{mm}$$

$$h_{0(r)} = h_{1(r)} + 0.4 \cdot b_{2(r)} = 20.2 + 0.4 \cdot 1.9 = 20.96\ \text{mm}$$

2. Minimum and maximum depths of the current penetration in the rotor bar

$$h_{r(1)} = 0.5 \cdot b_{1(r)} = 0.5 \cdot 5.0 = 2.5 \text{ mm}$$

$$h_{r(2)} = h_{1(r)} + 0.5 \cdot b_{1(r)} = 20.2 + 0.5 \cdot 5.0 = 22.7 \text{ mm}$$

3. Current reduction coefficient for a short-circuited rotor winding

$$\upsilon_i = 6 \cdot W_1 \cdot \frac{k_w}{Z_2} = 6 \cdot 144 \cdot \frac{0.96}{40} = 20.73$$

4. Rotor nominal phase current

$$I_{2n} = \upsilon_i \cdot I'_{2n} = 20.73 \cdot 13.1 = 271.63 \text{ A}$$

5. Dimensional factor of stator and rotor teeth zones

$$C_N = 0.64 + 2.5 \cdot \sqrt{\delta \cdot (t_1 + t_2)} = 0.64 + 2.5 \cdot \sqrt{0.7 \cdot (13.1 + 11.68)} = 1.06$$

6. When the slip S=1, the mutual reactance is assumed to be

$$x_{12st} = k_\mu \cdot x_{12} = 1.22 \cdot 28.26 = 34.47 \text{ Ohm}$$

7. Rotor bare equivalent height

$$\xi = 0.001 \cdot 63.61 \cdot h_{b(r)} \cdot \sqrt{S} = 0.001 \cdot 63.61 \cdot 23.685 \cdot \sqrt{1} = 1.5 \text{ m}$$

8. If $1 \leq \xi \leq 4$, than φ is determined from Fig. B. 11.

$$\varphi = 0.34$$

9. Depth of current penetration into the rotor bar

$$h_r = \frac{h_{b(r)}}{1 + \varphi} = \frac{23.685}{1 + 0.34} = 17.68 \text{ mm}$$

10. Area of the current penetration into one rotor bar

$$q_r = \pi \cdot \frac{b_{1(r)}^2}{8} + \left(h_r - \frac{b_{1(r)}}{2}\right) \cdot \frac{b_{1(r)} + b_r}{2} = \pi \cdot \frac{5.0^2}{8} + \left(17.68 - \frac{5.0}{2}\right) \cdot \frac{5.0 + 2.69}{2}$$

$$= 68.87 \text{ mm}^2$$

Where $b_r = b_{1(r)} - \left(h_r - \frac{b_{1(r)}}{2}\right) \cdot \frac{b_{1(r)} - b_{2(r)}}{h_{1(r)}} = 5.0 - \left(17.68 - \frac{5.0}{2}\right) \cdot \frac{5.0 - 1.9}{20.2} = 2.69$

11. Coefficient taking into account increase of the rotor bar resistance under the influence of skin effect phenomenon

$$k_r = \frac{q_{b(r)}}{q_r} = \frac{81.9}{68.87} = 1.19$$

12. Coefficient taking into account increase in the rotor phase resistance

$$K_R = 1 + \frac{r_b \cdot (k_r - 1)}{r_2} = 1 + \frac{6.55 \cdot 10^{-11} \cdot (1.19 - 1)}{9.55 \cdot 10^{-11}} = 1.13$$

13. Value of the rotor phase resistance reduced to the stator one

$$r'_{2\xi} = K_R \cdot r'_2 = 1.13 \cdot 0.547 = 0.62 \text{ Ohm}$$

14. If $0 \leq \xi \leq 4$, the nonlinear function φ' is determined in Fig. B. 12.

Chose $\varphi' = 0.89$

15. Constant component of the rotor slot leakage coefficient

$$\lambda_{2(r)} = \frac{h_{0(r)}}{3 \cdot b_{1(r)}} \cdot \left(1 - \frac{\pi \cdot b_{1(r)}^2}{8 \cdot q_b}\right)^2 + 0.66 - \frac{b_{2slit}}{2 \cdot b_{1(r)}} =$$

$$= \frac{20.96}{3 \cdot 5.1} \cdot \left(1 - \frac{\pi \cdot 7.5^2}{8 \cdot 81.9}\right)^2 + 0.66 - \frac{1.5}{2 \cdot 5.0} = 1.57$$

16. Predicted multiplication factor of the initial starting current

$$I^*_{st.prelim} = 7 \text{ p.u.}$$

17. Predicted value of current at the motor start-up

$$I_2 = I^*_{st.prelim} \cdot I_{2n} \cdot e^{-\frac{0.05}{s}} = 7 \cdot 271.63 \cdot e^{-\frac{0.05}{1}} = 1808.7 \text{ A}$$

18. Rotor slot leakage coefficient taking into account the skin effect phenomenon

$$\lambda_{2\xi(r)} = \lambda'_{2(r)} \cdot \varphi' + \frac{h_{slit2}}{b_{slit2}} + 1.12 \cdot \frac{h'_{slit2}}{I_2} = 1.57 \cdot 0.89 + \frac{0.75}{3.5} + 1.12 \cdot \frac{0}{1808.7}$$

$$= 1.9$$

19. Change in the rotor leakage reactance caused by the skin effect phenomenon

$$K_x = \frac{\lambda_{2\xi(r)} + \lambda_{end(r)} + \lambda_{dif(r)}}{\lambda_{2(r)} + \lambda_{end(r)} + \lambda_{dif(r)}} = \frac{1.9 + 0.66 + 1.14}{2.07 + 0.66 + 1.14} = 0.955$$

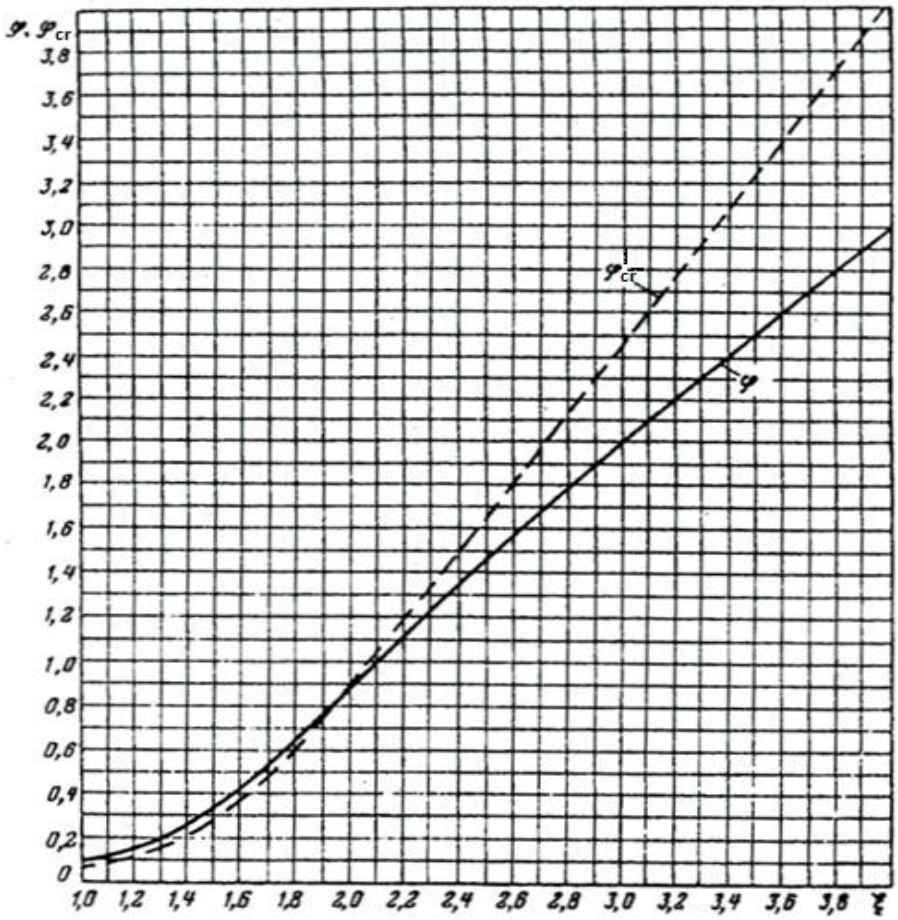

Fig. B. 11 Graphe of relations between φ , φcr and the rotor bare equivalent height ξ [KOPILOV_86]

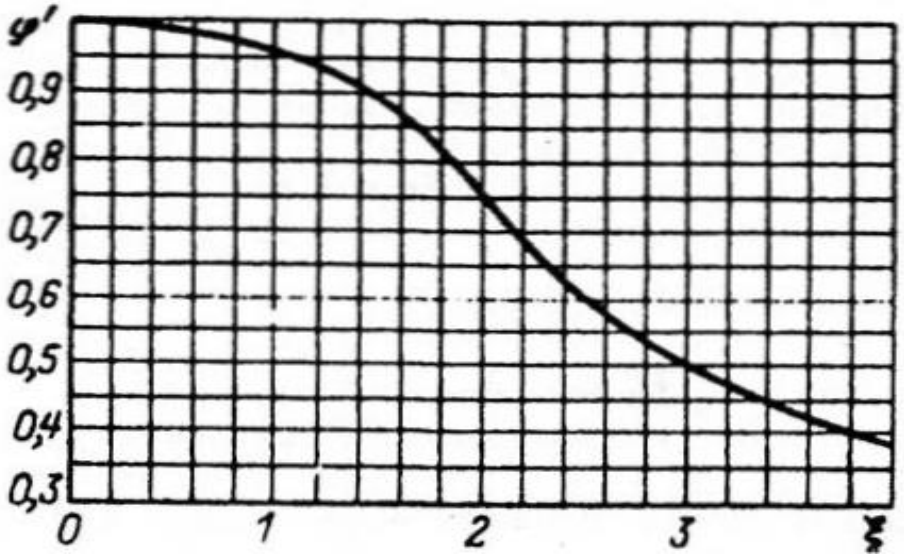

Fig. B. 12Relations between φ' and the rotor bare equivalent height ξ [KOPILOV_86]

20. Rotor leakage reactance caused by the skin effect phenomenon

$$x'_{2\xi} = K_x \cdot x'_2 = 0.955 \cdot 0.96 = 0.92 \text{ Ohm}$$

21. Calculation of the stator phase current based on the induction motor simplified equivalent circuit taking into account the skin effect phenomenon

$$a_\xi = C_{1a} \cdot r_1 + C_{1r} \cdot x_1 + b' \cdot x'_{2\xi} = 1.12 \cdot 1.04 + 0.037 \cdot 1.6 + 0.08 \cdot 0.92 = 1.3 \text{ Ohm}$$

$$b_\xi = C_{1a} \cdot x_1 - C_{1r} \cdot r_1 + a' \cdot x'_{2\xi} = 1.12 \cdot 1.6 - 0.037 \cdot 1.04 + 1.12 \cdot 0.92 = 2.68 \text{ Ohm}$$

$$R_{S\xi} = a_\xi + a' \cdot \frac{r'_{2\xi}}{S} = 1.3 + 1.12 \cdot \frac{0.62}{1} = 1.99$$

$$X_{S\xi} = b_\xi + b' \cdot \frac{r'_{2\xi}}{S} = 2.68 + 0.037 \cdot \frac{0.62}{1} = 2.63 \text{ Ohm}$$

$$Z_{S\xi} = \sqrt{R_{S\xi}^2 + X_{S\xi}^2} = \sqrt{1.99^2 + 2.63^2} = 3.3 \text{ Ohm}$$

$$\cos\varphi'_{S\xi} = \frac{R_{S\xi}}{Z_{S\xi}} = \frac{1.99}{3.3} = 0.6$$

$$\sin\varphi'_{S\xi} = \frac{X_{S\xi}}{Z_{S\xi}} = \frac{2.63}{3.3} = 0.8$$

$$I''_{S\xi} = \frac{U_{1n}}{Z_{S\xi}} = \frac{231}{3.3} = 70.0 \text{ A}$$

$$I''_{2a\xi} = I''_{S\xi} \cdot \cos\varphi'_{S\xi} = 70.0 \cdot 0.6 = 42.25 \text{ A}$$

$$I''_{2r\xi} = I''_{S\xi} \cdot \sin\varphi'_{S\xi} = 70.0 \cdot 0.8 = 55.82 \text{ A}$$

$$I_{1a\xi} = I_{0a} + I''_{2a\xi} = 0.52 + 42.25 = 42.77 \text{ A}$$

$$I_{1r\xi} = I_{0r} + I''_{2r\xi} = 7.7 + 55.82 = 63.52 \text{ A}$$

$$I_{1\xi} = \sqrt{I_{1a\xi}^2 + I_{1r\xi}^2} = \sqrt{42.77^2 + 63.52^2} = 76.58 \text{ A}$$

22. Initial prediction of the saturation ratio for the value of the slip S=1 can be made based on the total stator slot current

$$I_{slot} = I_{1st} \cdot \frac{u_{s1}}{a} = 76.58 \cdot \frac{24}{1} = 1837.92 \text{ A}$$

23. If $I_{slot} \approx 1400 \div 1900$ A at S=1, then $k_{st(1)} = 1.25 \div 1.35$

    Chose the saturation ratio $k_{sat(1)} = 1.35$

24. Predicted value of the stator phase current at start-up taking into account skin effect phenomenon

$$I_{1st.pred} = k_{st(1)} \cdot I_{1\xi} = 1.35 \cdot 76.58 = 103.4 \text{ A}$$

25. Average MMF of one winding, referred to one stator slot

$$F_{s.av} = 0.7 \cdot \left(1 + k_w \cdot \frac{Z_1}{Z_2}\right) \cdot I_{1st.pred} \cdot \frac{u_{s1}}{a} = .7 \cdot \left(1 + 0.96 \cdot \frac{36}{40}\right) \cdot 103.4 \cdot \frac{24}{1}$$

$$= 3237.1 \text{ A}$$

26. Value of the fictitious leakage flux density in the air gap

$$B_{\Phi\delta} = 0.001 \cdot \frac{F_{s.av}}{1.6 \cdot \delta \cdot C_N} = 0.001 \cdot \frac{3237.1}{1.6 \cdot 0.7 \cdot 1.06} = 2.73 \text{ T}$$

27. The value of the nonlinear function χ_δ, which characterizes relations between the leakage flux in saturated motor and the leakage flux in unsaturated motor, is determined in Fig. B. 13.

    Take $\chi_\delta = 0.78$.

28. Value of the additional stator slot opening

$$C_{e1} = (t_1 - b_{slit1}) \cdot (1 - \chi_\delta) = (13.1 - 3.5) \cdot (1 - 0.78) = 2.11 \text{ mm}$$

29. Decrease in the coefficient of the stator slot leakage permeance

$$\Delta\lambda_{S(1).st} = C_{e1} \cdot \frac{h_{slit1} + 0.58 \cdot h_{w(1)}}{b_{slit1} \cdot (C_{e1} + 1.5 \cdot b_{slit1})} = 2.11 \cdot \frac{0.5 + 0.58 \cdot 1.9}{3.5 \cdot (2.11 + 1.5 \cdot 3.5)} = 0.13$$

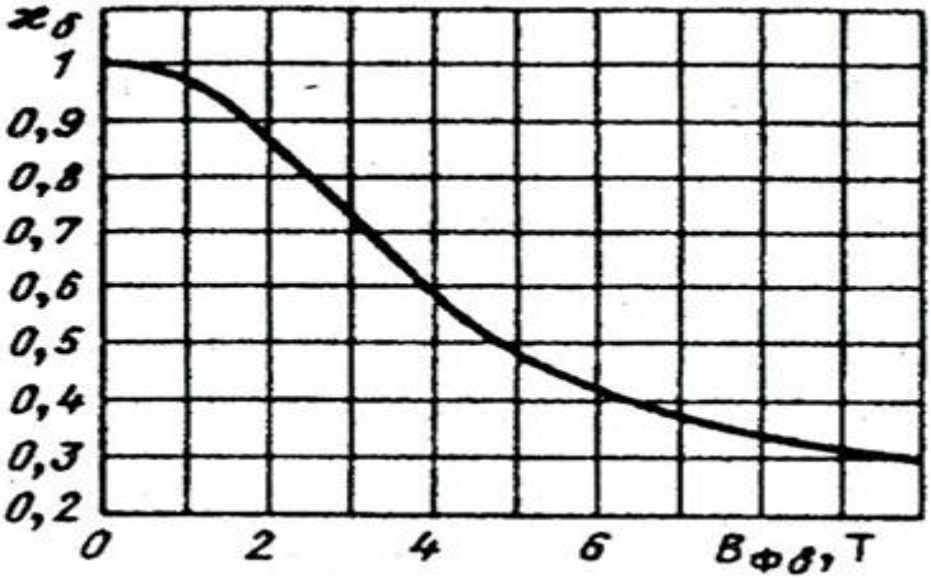

Fig. B. 13 Relations between χ_δ and $B_{\Phi\delta}$ [KOPILOV_86]

30. Stator slot leakage coefficient when motor is saturated

$$\lambda_{S(1).st} = \lambda_{S(1)} - \Delta\lambda_{S(1).st} = 1.15 - 0.13 = 1.02$$

31. Stator differential leakage coefficient when motor is saturated

$$\lambda_{diff(s).st} = \chi_\delta \cdot \lambda_{diff(s)} = 0.78 \cdot 2.82 = 2.2$$

32. Phase stator leakage reactance taking into account the saturation effect

$$x_{1st} = x_1 \cdot \frac{\lambda_{S(1).st} + \lambda_{end(s)} + \lambda_{diff(s).st}}{\lambda_{S(1)} + \lambda_{end(s)} + \lambda_{diff(s)}} = 1.6 \cdot \frac{1.02 + 1.36 + 2.2}{1.15 + 1.36 + 2.82} = 1.37 \text{ Ohm}$$

33. Relative value of the phase stator leakage reactance taking into account the saturation effect

$$x_{1st}^* = \frac{x_{1.st}}{x_1} = \frac{1.37}{1.6} = 0.86 \text{ p.u.}$$

34. The same way one can calculate the phase rotor leakage reactance, taking into account the skin and saturation effects

$$C_{e2} = (t_2 - b_{slit2}) \cdot (1 - \chi_\delta) = (11.68 - 1.5) \cdot (1 - 0.78) = 2.24 \text{ mm}$$

$$\Delta\lambda_{S(2).st} = C_{e2} \cdot \frac{h_{slit2}}{b_{slit2} \cdot (C_{e2} + b_{slit2})} = 2.24 \cdot \frac{0.75}{1.5 \cdot (2.24 + 1.5)} = 0.3$$

$$\lambda_{S(2)\xi.st} = \lambda_{2\xi(r)} - \Delta\lambda_{S(2).st} = 1.9 - 0.3 = 1.6$$

$$\lambda_{diff(r).st} = \chi_\delta \cdot \lambda_{diff(r)} = 0.78 \cdot 1.14 = 0.89$$

$$x'_{2\xi st} = x'_2 \cdot \frac{\lambda_{S(2)\xi.st} + \lambda_{end(r)} + \lambda_{diff(r).st}}{\lambda_{S(r)} + \lambda_{end(r)} + \lambda_{diff(r)}} = 0.96 \cdot \frac{1.6 + 0.66 + 0.89}{2.07 + 0.66 + 1.14} = 0.78 \text{ Ohm}$$

$$x'^{*}_{2\xi sat} = \frac{x'_{2\xi st}}{x'_2} = \frac{0.78}{0.96} = 0.81 \text{ p. u.}$$

35. Active and reactive components of the coefficient C_{1st} taking into account the saturation

$$C_{1a.st} = \frac{(r_{12} \cdot (r_1 + r_{12}) + x_{12.st} \cdot (x_{1st} + x_{12st}))}{r_{12}^2 + x_{12.st}^2}$$
$$= \frac{(0.92 \cdot (1.104 + 0.92) + 34.47 \cdot (1.37 + 34.47))}{0.92^2 + 34.47^2} = 1.04$$

$$C_{1r.st} = \frac{(r_1 \cdot x_{12st} - r_{12} \cdot x_{1st})}{r_{12}^2 + x_{12.st}^2} = \frac{(1.04 \cdot 34.47 - 0.92 \cdot 1.37)}{0.92^2 + 34.47^2} = 0.031$$

45. Magnitude of the complex coefficient

$$C_{1.st} = \sqrt{C_{1a.st}^2 + C_{1r.st}^2} = \sqrt{1.04^2 + 0.031^2} = 1.04$$

The value of the stator phase current during start-up is calculated using the induction motor simplified equivalent circuit (Fig. B. 14)

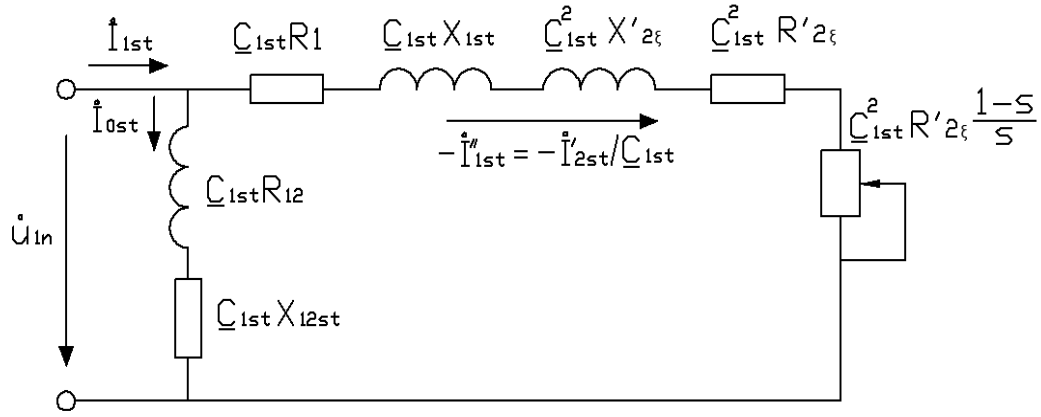

Fig. B. 14 Induction motor simplified equivalent circuit taking into account the skin and saturation effects

46. Following calculations are made in accordance with the already known methodology

$$a'_{st} = C^2_{1a.st} - C^2_{1r.st} = 1.04^2 - 0.031^2 = 1.08$$

$$b'_{st} = 2 \cdot C_{1a.st} \cdot C_{1r.st} = 2 \cdot 1.04 \cdot 0.031 = 0.064$$

$$a_{st} = C_{1a.st} \cdot r_1 + C_{1r.st} \cdot x_{1st} + b'_{st} \cdot x'_{2\xi st}$$
$$= 1.04 \cdot 1.104 + 0.031 \cdot 1.37 + 0.064 \cdot 0.078 = 1.24 \text{ Ohm}$$

$$b_{st} = C_{1a.st} \cdot x_{1.st} - C_{1r} \cdot r_1 + a'_{st} \cdot x'_{2\xi st}$$
$$= 1.104 \cdot 1.37 - 0.031 \cdot 1.104 + 1.08 \cdot 0.078 = 2.24 \text{ Ohm}$$

47. Components of the magnetization circuit complex impedance taking into account the saturation

$$R_{m.st} = C_{1a.st} \cdot r_{12} + C_{1r.st} \cdot x_{12.st} = 1.04 \cdot 0.92 + 0.031 \cdot 34.47 = 2.03 \text{ Ohm}$$

$$X_{m.st} = C_{1a.st} \cdot x_{12.st} + C_{1r.st} \cdot r_{12} = 1.04 \cdot 34.47 + 0.031 \cdot 0.92 = 35.85 \text{ Ohm}$$

$$Z_{m.st} = \sqrt{R^2_{m.st} + X^2_{m.st}} = \sqrt{2.03^2 + 35.85^2} = 35.9 \text{ Ohm}$$

$$\cos\varphi_{0.st} = \frac{R_{m.st}}{Z_{m.st}} = \frac{2.03}{35.9} = 0.056$$

$$\sin\varphi_{0.st} = \frac{X_{m.st}}{Z_{m.st}} = \frac{35.85}{35.9} = 0.998$$

48. No-load current taking into account the saturation effect

$$I_{0.st} = \frac{U_{1n}}{Z_{m.st}} = \frac{231}{35.9} = 6.43\ A$$

$$I_{0a.st} = I_{0.st} \cdot \cos\varphi_{0.st} = 6.43 \cdot 0.056 = 0.36\ A$$

$$I_{0r.st} = I_{0.st} \cdot \sin\varphi_{0.st} = 6.43 \cdot 0.998 = 6.42\ A$$

49. Rotor resistance and reactance depending on the slip taking into account the saturation effect

$$R_{s.st} = a_{st} + a'_{st} \cdot \frac{r'_{2\xi}}{S} = 1.24 + 1.08 \cdot \frac{0.62}{1} = 1.9\ Ohm$$

$$X_{s.st} = b_{st} + b'_{st} \cdot \frac{r'_{2\xi}}{S} = 2.24 + 0.064 \cdot \frac{0.62}{1} = 2.2\ Ohm$$

$$Z_{s.st} = \sqrt{R_{s.st}^2 + X_{s.st}^2} = \sqrt{1.9^2 + 2.2^2} = 2.92\ Ohm$$

$$\cos\varphi'_{2.st} = \frac{R_{s.st}}{Z_{s.st}} = \frac{1.9}{2.92} = 0.66$$

$$\sin\varphi'_{2.st} = \frac{X_{s.st}}{Z_{s.st}} = \frac{2.2}{2.92} = 0.76$$

50. Rotor current reduced to the stator taking into account the saturation effect

$$I''_{2.st} = \frac{U_{1n}}{Z_{s.st}} = \frac{231}{2.92} = 79.2\ A$$

$$I''_{2a.st} = I''_{2.st} \cdot \cos\varphi'_{2.st} = 79.2 \cdot 0.66 = 51.18\ A$$

$$I''_{2r.st} = I''_{2.st} \cdot \sin\varphi'_{2.st} = 79.2 \cdot 0.76 = 59.82\ A$$

51. Active and reactive components of the stator phase current taking into account the saturation effect

$$I_{1a.st} = I_{0a.st} + I''_{2a.st} = 0.36 + 51.18 = 52.2\ A$$

$$I_{1r.st} = I_{0r.st} + I''_{2r.st} = 6.42 + 59.82 = 66.24\ A$$

52. Module of the phase stator current taking into account the saturation effect

$$I_{1.st} = \sqrt{I_{1a.st}^2 + I_{1r.st}^2} = \sqrt{52.2^2 + 66.24^2} = 84.4\ A$$

53. Relative value of the stator current at start-up taking into account the saturation effect

$$I^*_{1.st} = \frac{I_{1.st}}{I_{1n}} = \frac{84.4}{15.53} = 5.4$$

54. Electromagnetic torque at start-up taking into account the saturation effect

$$T_{st} = 3 \cdot \frac{p}{2 \cdot \pi \cdot f_1} \cdot (C_{1.st} \cdot I''_{2.st})^2 \cdot \frac{r'_{2\xi}}{S} = 3 \cdot \frac{2}{2 \cdot \pi \cdot 50} \cdot (1.04 \cdot 79.2)^2 \cdot \frac{0.62}{1} = 80.3\ Nm$$

55. Relative value of the electromagnetic torque at start-up

$$T^*_{st} = \frac{T_{st}}{T_{nom}} = \frac{80.3}{48.86} = 1.64\ p.u.$$

56. After a set of repetitive calculations for different values of the slip, the breakdown torque can be calculated as

$$T_{bd} = 3 \cdot \frac{p}{2 \cdot \pi \cdot f_1} \cdot (C_{1.st} \cdot I''_{2.st})^2 \cdot \frac{r'_{2\xi}}{S_{cr}} = 3 \cdot \frac{2}{2 \cdot \pi \cdot 50} \cdot (1.04 \cdot 47.9)^2 \cdot \frac{0.62}{0.204} = 128.74\ Nm$$

57. Relative value of the breakdown torque

$$T^*_{bd} = \frac{T_{bd}}{T_{nom}} = \frac{128.7}{48.86} = 2.54\ p.u.$$

Thermal analysis

Calculations are based on the thermal equivalent circuit presented on Fig. B. 15 the elements of the circuit will be detailed below in the course of paragraph.

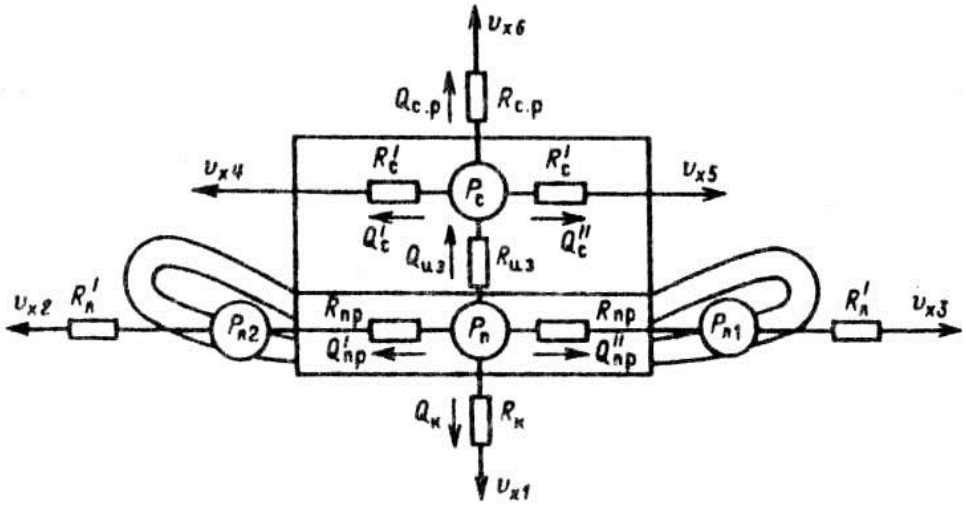

Fig. B. 15 Thermal equivalent circuits [KOPILOV 86]

1. Electrical losses in the slot of the stator winding

$$\Delta p'_{es(s)} = 1.07 \cdot \Delta p_{el(s)} \cdot 2 \cdot \frac{l_\delta}{L_{av}} = 1.07 \cdot 780 \cdot 2 \cdot \frac{0.11}{0.66} = 282.9\ W$$

2. Electrical losses in the end parts of the stator winding

$$\Delta p'_{e.end(s)} = 1.07 \cdot \Delta p_{el(s)} \cdot 2 \cdot \frac{L_{end}}{L_{av}} = 1.07 \cdot 780 \cdot 2 \cdot \frac{0.22}{0.66} = 571.7\ W$$

3. Temperature rise in the inner surface of the stator core over the air temperature inside the motor

$$\Delta V_{sf.1} = K \cdot \frac{\Delta p'_{es(s)} + \Delta p_{c.fund}}{\pi \cdot D \cdot l_\delta \cdot \alpha_1} = 0.2 \cdot \frac{282.9 + 165.84}{\pi \cdot 0.15 \cdot 0.11 \cdot 105} = 16.48\ ^0C$$

Where K=0.2 is the coefficient for the number of poles 2p=4 and α_1 is heat transfer coefficient can be found from Fig. B. 16

4. Ratio of diameter of the standard uninsulated wire to the diameter of the standard insulated wire

$$\Delta d = \frac{d}{d_i} = \frac{1.12}{1.2} = 0.93$$

5. Estimated perimeter of the stator slot cross-section

$$\Pi_{s1} = 2 \cdot h_{s.k.1} + b_{1(s)} + b_{2(s)} = 2 \cdot 13.7 + 7.2 + 9.6 = 44.2\,\text{mm}$$

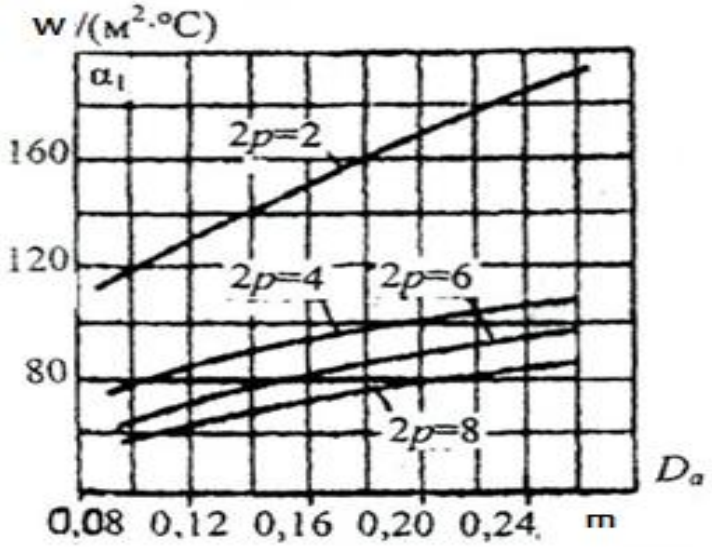

Fig. B. 16 Average value of the heat transfer coefficient for induction moors IP44 and axes height h<160 mm [KOPILOV_86]

6. Temperature surplus in the stator slot insulation

$$\Delta V_{i.s1} = \Delta p'_{es(s)} \cdot \frac{\left(0.5 \cdot \frac{b_i}{\lambda_{eq}} + \frac{b_{1(s)}+b_{2(s)}}{16 \cdot \lambda'_{eq}}\right)}{Z_1 \cdot l_\delta \cdot \Pi_{s1}} = 282.9 \cdot \frac{\left(0.5 \cdot \frac{0.35}{0.16} + \frac{7.2+9.6}{16 \cdot 1.1}\right)}{36 \cdot 0.11 \cdot 44.2} = 5.08^0\text{C}$$

Where $\lambda_{eq} = 0.16 \frac{W}{m \cdot {}^\circ C}$ is average equivalent thermal conductivity of slot insulation for insulation classes B, F, H, $\lambda'_{eq} = 1.1 \frac{W}{m^2 \cdot {}^\circ C}$ is average value of thermal conductivity of the internal insulation found from Fig.B. 1.

7. Temperature surplus through the insulation thickness in the stator end-windings

$$\Delta V_{i.end1} = \Delta p'_{e.end(s)} \cdot \left(0.5 \cdot \frac{d_i - d}{\lambda_{eq}} + \frac{\frac{h_{s.k1}}{12 \cdot \lambda'_{eq}}}{2 \cdot Z_1 \cdot L_{end} \cdot \Pi_{s1}}\right) =$$

$$= 571.7 \cdot \left(0.5 \cdot \frac{1.2 - 1.12}{0.16} + \frac{\frac{13.7}{12 \cdot 1.1}}{2 \cdot 36 \cdot 0.22 \cdot 44.2}\right) = 1.04^0$$

8. Temperature rise in the outer surface of the stator end-winding insulation over the air temperature inside the motor

$$\Delta V_{sf.end1} = K \cdot \frac{\Delta p'_{e.end(s)}}{2 \cdot \pi \cdot D \cdot L_{ov} \cdot \alpha_1} = K \cdot \frac{571.7}{2 \cdot \pi \cdot 0.15 \cdot 0.075 \cdot 105} = 15.35^0 C$$

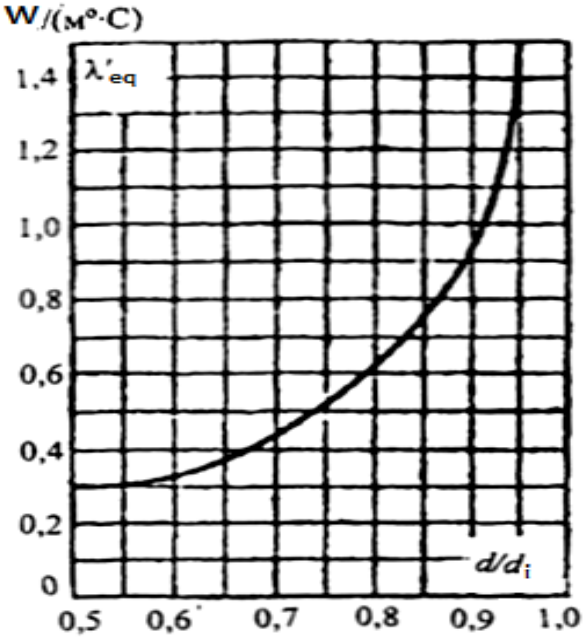

Fig.B. 1. Average values of thermal conductivity λ'eq of the internal insulation [KOPILOV_86]

9. Average temperature rise in the stator winding over the air temperature inside the motor

$$\Delta V'_1 = \frac{(\Delta V_{sf.1} + \Delta V_{is1}) \cdot 2 \cdot l_\delta + (\Delta V_{i.end1} + \Delta V_{sf.end1}) \cdot 2 \cdot L_{end}}{L_{av}} = \\ = \frac{(16.48 + 5.08) \cdot 2 \cdot 0.11 + (1.04 + 15.35) \cdot 2 \cdot 0.22}{0.665} = 18.1^0 C$$

10. Total losses in the rotor at nominal speed and temperature 120°C

$$\sum \Delta p' = \sum \Delta p + 0.3 \cdot \left(\Delta p_{el(s)} + \Delta p_{el(r)}\right) = 1.35 + 0.07 \cdot (0.78 + 0.27) \\ = 1.46 \text{ kW}$$

11. Equivalent cooling surface of the motor case

$$S_{case} = (\pi \cdot D_a + 8 \cdot \Pi_r) \cdot (l_\delta + 2 \cdot L_{ov}) \\ = (\pi \cdot 0.225 + 8 \cdot 0.32) \cdot (0.11 + 2 \cdot 0.075) = 0.85 \text{ m}^2$$

Where $\Pi_r = 0.32\text{m}$ is cross-sectional perimeter of ribs in the motor case for the motor axis height $0.32\ \text{mm}$ (see Fig. B. 17).

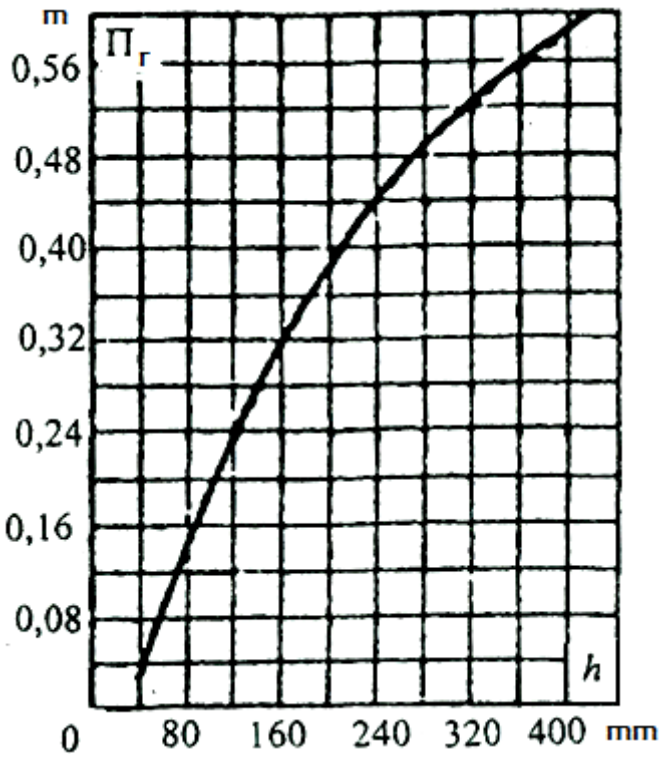

Fig. B. 17 Average value for cross-sectional perimeter of case ribs for induction motor [KOPILOV_86]

12. Sum of losses related to air inside the motor

$$\sum \Delta p'_{air} = \sum \Delta p' - (1 - K) \cdot \left(\Delta p'_{es(s)} + \Delta p_{c.fund}\right) - 0.9 \cdot \Delta p_{mec} =$$

$$= 1.46 - (1 - 0.2) \cdot (282.9 + 165.84) - 0.9 \cdot 58.1 = 1.048\ \text{kW}$$

13. Increase of the air temperature inside the motor over the ambient temperature

$$\Delta V_{air} = \frac{\sum \Delta p'_{air}}{S_{case} \cdot \alpha_{air}} = \frac{1.048}{0.85 \cdot 25} = 49.1^0\text{C}$$

Where α_{air} is the air heat transfer coefficient, which can be found from **Erreur ! Source du renvoi introuvable.**.

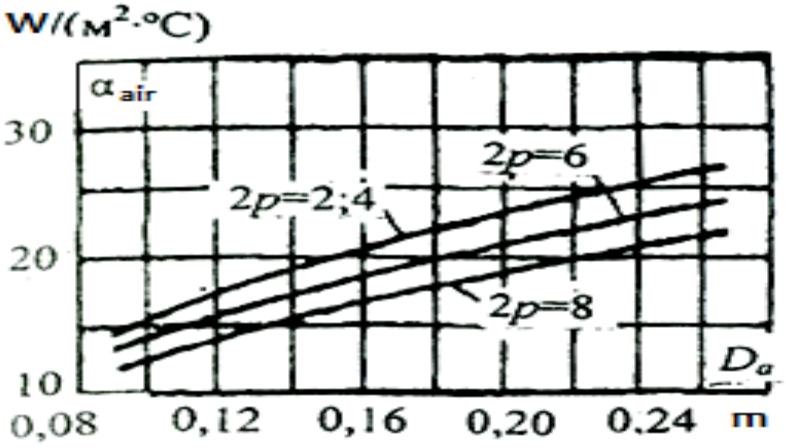

Fig. B. 18Average value of the air heat transfer coefficient αair for induction motors with degree protection IP54 and axis height h<160mm [KOPILOV_86]

14. Average increase of the stator winding temperature over the ambient temperature

$$\Delta V_1 = \Delta V'_1 + \Delta V_{air} = 18.1 + 49.1 = 67.2^0C$$

Appendix C. DEMO-LSPM: graphical user interface

```
%% DEMO-LSPM
%-----Nominal power----%
P2n=7.5; %kW
%----Number of stator winding phases---%
m1=3;
%-----Rated phase voltage of the stator winding---%
U1n=220; % V
%----- Number of poles 2p  -----%
doublep=4;
%----Stator frequency----%
f1=50; %Hz
%----Ambient temperature---%
Tbob=40;   %cel
%----Magnet properties-----%
mum=1.1; %Relative recoil permeability
Br=1.10; %Remanent flux-dencity
%----skewing-----%
skewing=0;
%-------specification constraints-----%
cosfi=0.70; %---Minimal value of cos(fi)
RatioT=1.4; %---Minimal value of ratio Tmax/Tnom
```

Fig. C. 1: DEMO-LSPM: specification form

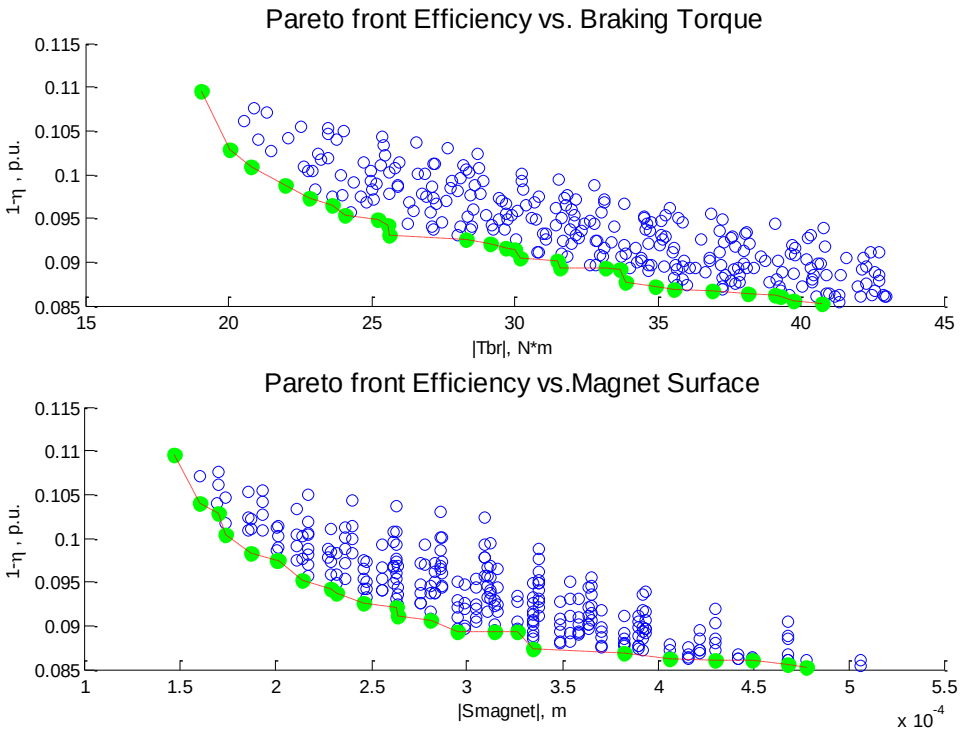

Fig. C. 2 DEMO-LSPM: solutions plot

V-type magnet configuration Pareto points Efficiency vs. Braking Torque

N_element	eta	Tbr22	cosf	em22	hm22	eag22	angle	Xd	Xq	Tmax/Tnom
1.0000	0.9181	30.3928	0.9968	0.0314	0.0034	0.0007	65.6000	12.2012	34.8120	1.5737
2.0000	0.9178	28.2587	0.9925	0.0292	0.0034	0.0007	77.8000	11.8346	34.8120	1.5651
3.0000	0.9170	27.3689	0.9869	0.0292	0.0034	0.0008	77.8500	11.1122	30.8737	1.5953
4.0000	0.9162	26.4684	0.9793	0.0291	0.0034	0.0009	77.8500	10.5149	27.7748	1.6270
5.0000	0.9093	23.0795	0.9277	0.0288	0.0034	0.0013	78.0000	8.8368	19.9728	1.6881
6.0000	0.9013	20.9169	0.8741	0.0287	0.0034	0.0016	78.1000	7.9900	16.5847	1.7172
7.0000	0.9183	37.8180	0.9965	0.0290	0.0052	0.0011	77.9500	8.0601	23.1987	2.1110
8.0000	0.9133	24.3866	0.9551	0.0286	0.0034	0.0011	81.9667	9.5169	23.1987	1.6697
9.0000	0.9000	20.6606	0.8727	0.0283	0.0034	0.0016	82.0667	7.9515	16.5847	1.6904
10.0000	0.9185	39.0630	1.0000	0.0287	0.0052	0.0009	81.9000	8.8116	27.7748	2.0273
11.0000	0.9000	20.5609	0.8713	0.0282	0.0034	0.0016	84.0500	7.9382	16.5847	1.6955
12.0000	0.9187	39.6203	0.9995	0.0287	0.0052	0.0008	83.9250	9.3055	30.8737	1.9854
13.0000	0.9000	20.5099	0.8705	0.0281	0.0034	0.0016	85.2400	7.9320	16.5847	1.6980
14.0000	0.9000	20.4794	0.8701	0.0281	0.0034	0.0016	86.0333	7.9287	16.5847	1.6994
15.0000	0.9066	21.8270	0.9055	0.0282	0.0034	0.0014	86.5857	8.4570	18.6901	1.7079
16.0000	0.9000	20.4593	0.8698	0.0281	0.0034	0.0016	86.6000	7.9266	16.5847	1.7003
17.0000	0.9000	20.4452	0.8696	0.0281	0.0034	0.0016	87.0250	7.9253	16.5847	1.7009
18.0000	0.9000	20.4348	0.8695	0.0281	0.0034	0.0016	87.3556	7.9244	16.5847	1.7014
19.0000	0.9173	27.5317	0.9904	0.0286	0.0034	0.0007	87.5600	11.7237	34.8120	1.5511
20.0000	0.9164	26.6802	0.9841	0.0285	0.0034	0.0008	87.5700	11.0085	30.8737	1.5808
21.0000	0.9155	25.8098	0.9760	0.0285	0.0034	0.0009	87.5700	10.4170	27.7748	1.6123
22.0000	0.9146	24.9475	0.9658	0.0284	0.0034	0.0010	87.5800	9.9151	25.2690	1.6455
23.0000	0.9122	24.1088	0.9530	0.0284	0.0034	0.0011	87.5900	9.4807	23.1987	1.6418
24.0000	0.9110	23.3015	0.9387	0.0283	0.0034	0.0012	87.6000	9.0990	21.4580	1.6766
25.0000	0.9083	22.5293	0.9230	0.0282	0.0034	0.0013	87.6000	8.7593	19.9728	1.6729
26.0000	0.9053	21.7929	0.9064	0.0282	0.0034	0.0014	87.6100	8.4538	18.6901	1.6692
27.0000	0.9035	21.0922	0.8874	0.0281	0.0034	0.0015	87.6200	8.1768	17.5706	1.7055
28.0000	0.9000	20.4268	0.8693	0.0281	0.0034	0.0016	87.6200	7.9238	16.5847	1.7017

V-type Pareto points Efficiency vs. Magnet Surface

N_element	eta	Tbr22	cosf	em22	hm22	eag22	angle	Xd	Xq	Tmax/Tnom
1.0000	0.9181	30.3928	0.9968	0.0314	0.0034	0.0007	65.6000	12.2012	34.8120	1.5737
2.0000	0.9178	28.2587	0.9925	0.0292	0.0034	0.0007	77.8000	11.8346	34.8120	1.5651
3.0000	0.9187	39.6203	0.9995	0.0287	0.0052	0.0008	83.9250	9.3055	30.8737	1.9854
4.0000	0.9000	20.4794	0.8701	0.0281	0.0034	0.0016	86.0333	7.9287	16.5847	1.6994
5.0000	0.9066	21.8270	0.9055	0.0282	0.0034	0.0014	86.5857	8.4570	18.6901	1.7079
6.0000	0.9000	20.4593	0.8698	0.0281	0.0034	0.0016	86.6000	7.9266	16.5847	1.7003
7.0000	0.9000	20.4452	0.8696	0.0281	0.0034	0.0016	87.0250	7.9253	16.5847	1.7009
8.0000	0.9000	20.4348	0.8695	0.0281	0.0034	0.0016	87.3556	7.9244	16.5847	1.7014
9.0000	0.9173	27.5317	0.9904	0.0286	0.0034	0.0007	87.5600	11.7237	34.8120	1.5511
10.0000	0.9164	26.6802	0.9841	0.0285	0.0034	0.0008	87.5700	11.0085	30.8737	1.5808
11.0000	0.9155	25.8098	0.9760	0.0285	0.0034	0.0009	87.5700	10.4170	27.7748	1.6123
12.0000	0.9146	24.9475	0.9658	0.0284	0.0034	0.0010	87.5800	9.9151	25.2690	1.6455
13.0000	0.9122	24.1088	0.9530	0.0284	0.0034	0.0011	87.5900	9.4807	23.1987	1.6418
14.0000	0.9110	23.3015	0.9387	0.0283	0.0034	0.0012	87.6000	9.0990	21.4580	1.6766
15.0000	0.9083	22.5293	0.9230	0.0282	0.0034	0.0013	87.6000	8.7593	19.9728	1.6729
16.0000	0.9053	21.7929	0.9064	0.0282	0.0034	0.0014	87.6100	8.4538	18.6901	1.6692
17.0000	0.9035	21.0922	0.8874	0.0281	0.0034	0.0015	87.6200	8.1768	17.5706	1.7055
18.0000	0.9000	20.4268	0.8693	0.0281	0.0034	0.0016	87.6200	7.9238	16.5847	1.7017

Calculations are done

Fig. C. 3 DEMO-LSPM: consolidate table of results of Pareto plot (Fig. C. 2)

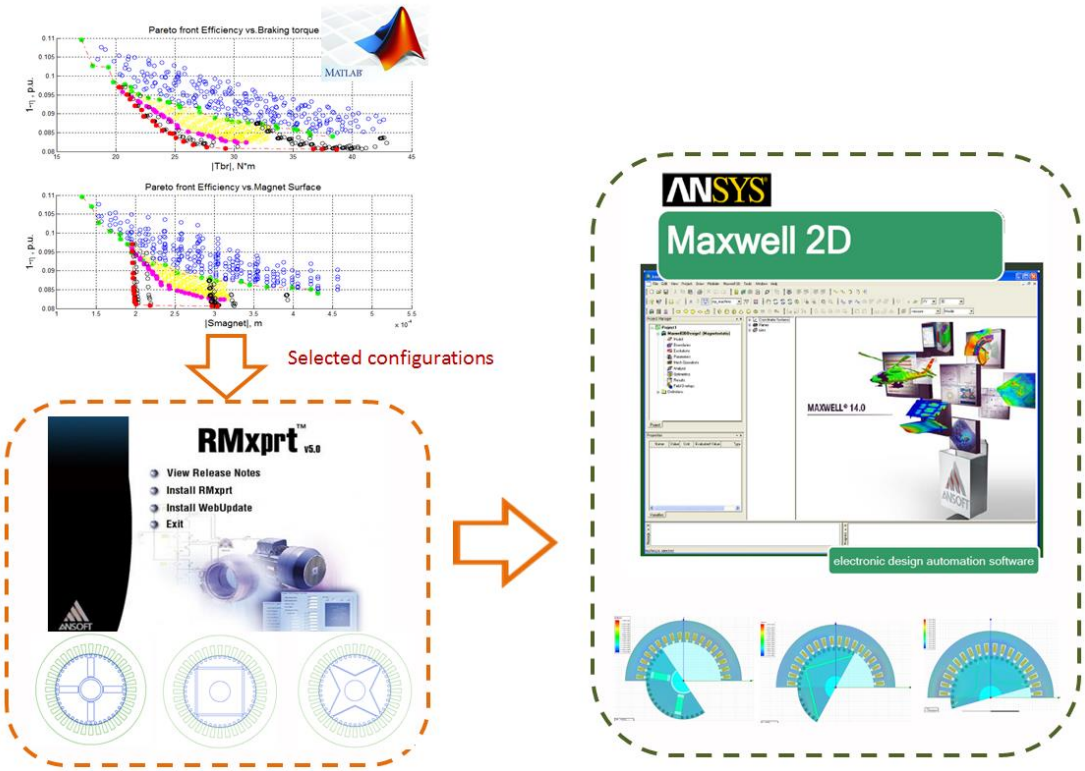

Fig. C. 4 DEMO-LSPM: Scheme of coupling between Matlab script and ANSYS Maxwell

Appendix D. Characteristics of PM SmCo S30H

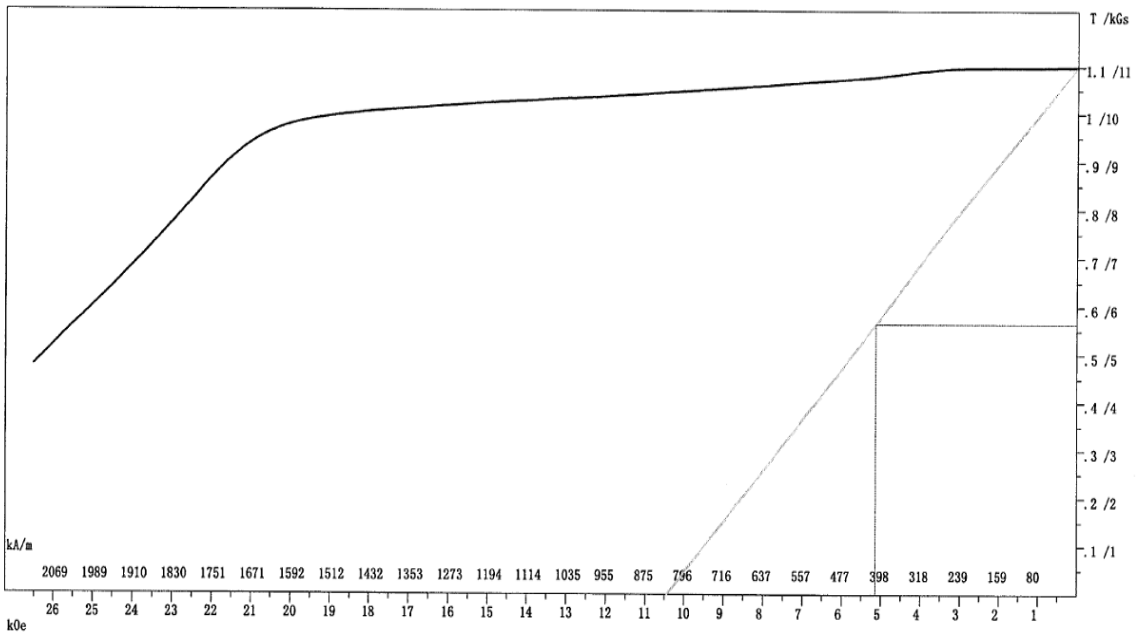

Br	= 1.099	T	10.99	kGs
Hcb	= 831	kA/m	10.44	kOe
Hcj	> 2110	kA/m	26.52	kOe
(BH)max	= 230.94	kJ/m^3	29.02	MGOe
Hk	= 1537	kA/m	19.32	kOe
Hd	= 409	kA/m	5.14	kOe
Bd	= .564	T	5.64	kGs
Hk/Hcj	< 72.9%			

Material Type:	SmCo
Patch No:	2:17
Sample No:	t1
Test Date:	
Sample Shape:	Column
Size(mm):	7.24
Document No:	100410925
SampleT(℃):	20

Appendix E. List of symbols

Latin symbols

$\boldsymbol{A}$	vector magnetic potential	[Wb/m]
A_{bdg}	cross-sectional area of a bridge	[m^2]
A_g	air gap cross-sectional area	[m^2]
A_m	magnet cross-sectional area	[m^2]
B_{bdg}	average flux density within the bridge	[T]
B_g	air gap flux density	[T]
B_{g1}	fundamental of the air gap flux density	[T]
B_m	PMs flux density	[T]
B_r	remanent magnetization	[T]
B_{sat}	flux density saturation level	[T]
B_{sh}	flux density in shaft	[T]
C	three-phase current transform matrix	[-]
C_ϕ	flux concentration factor	[-]
c_g	silency factor	
D1	diameter of PMs circumcircle	[mm]
E_0	phase back-EMF	[V]
E_{f1}	first harmonic of the phase back-EMF	[V]
E_{f3}	third harmonic of the phase back-EMF	[V]
f	frequency	[Hz]

H	magnetic field strength	[A/m]
H_g	magnetic field strength in the air gap	[A/m]
H_m	magnetic field strength in the magnets	[A/m]
H_{sh}	magnetic field strength in the shaft	[A/m]
h_g	circumferential pole width on the rotor surface	[m]
h_m	magnet height	[m]
l_m	magnet length	[m]
I_{nom}	nominal stator current	[A]
I_a	active component of stator current	[A]
I_r	reactive component of stator current	[A]
i_d	stator d-axis current	[A]
i_q	stator q-axis current	[A]
i_{2d}	rotor d-axis current	[A]
i_{2q}	rotor q-axis current	[A]
$\boldsymbol{J}$	current density	[A/m^2]
J_{load}	moment of load inertia	[kg· m^2]
k_{1ad}	d- axis form factor of the armature reaction	[-]
k_{1aq}	q- axis form factors o the armature reaction	[-]
k_{ad}	form factors of the armature reaction	[-]
k_c	Carter's factor	[-]
k_w	global winding coefficient	[-]

L_{1d}	stator d-axis leakage inductance	[H]
L_{1q}	stator q-axis leakage inductance	[H]
L_{2d}	rotor d-axis leakage inductance	[H]
L_{2q}	rotor q-axis leakage inductance	[H]
L_{ABC}	matrix of self-inductances and mutual inductances	[H]
L_{ad}	d-axis synchronous inductance	[H]
L_{aq}	q-axis synchronous inductance	[H]
l_g	air gap length	[m]
$l_{gd}^{"}$	air gap length referred to the d-axis	[m]
$l_{gq}^{"}$	air gap length referred to the q-axis	[m]
l_h	length of the non-magnetic hub	[m]
l_{mg}	axial length of the magnet	[m]
l_δ	active length of the magnetic core	[m]
M	magnetization	[A/m]
MT	magnet thickness	[mm]
MW	magnet width	[mm]
N_s	slot number	[-]
n_s	synchronous speed	[round/s]
O2	angle opening	[mm]
P_{core}	core losses	[W]
P_{in}	input power	[W]
P_{joule}	copper losses	[W]

P_{max}	maximal output power	[W]
P_{mec}	mechanical losses	[W]
p	pole number	[-]
R_2	rotor radius	[m]
R_{bb}	reluctance of the bridge	[H^{-1}]
R_{bore}	bore radius	[m]
R_h	radius of the non-magnetic hub	[m]
R_g	air gap reluctance	[H^{-1}]
R_{lm}	reluctance of air under the bridge	[H^{-1}]
R_m	PM reluctance	[H^{-1}]
R_r	rotor reluctance	[H^{-1}]
R_s	stator reluctance	[H^{-1}]
R_{sh}	shaft radius	[m]
R_{st}	stack length	[m]
R_σ	stray reluctance	[H^{-1}]
r_1	stator resistance	[Ω]
r'_2	rotor winding resistance	[Ω]
s	slip	[-]
t	time, bridge width	[s], [m]
T_{bd}	breakdown torque	[Nm]
T_{cage}	asynchronous torque developed by winding damper	[Nm]
T_{em}	electromagnetic torque	[Nm]

T_L	load torque	[Nm]
T_{max}	maximal output torque	[Nm]
T_{mb}	braking torque	[Nm]
T_{nom}	nominal load torque	[Nm]
T_{pma}	permanent magnet alignment torque	[Nm]
T_{rel}	synchronous reluctance torque	[Nm]
T_{tot}	total torque	[Nm]
U	phase voltage	[V]
U_{nom}	nominal phase voltage	[V]
u_d	d-axis voltage of stator	[V]
u_{2d}	d-axis voltage of rotor	[V]
u_q	q-axis voltage of stator	[V]
u_{2q}	q-axis voltage of rotor	[V]
X_d	d- axis synchronous reactance	[Ω]
X_q	q- axis synchronous reactance	[Ω]
X_σ	leakage reactance	[Ω]
X_a	per-phase leakage reactance	[Ω]
x_1	stator reactance	[Ω]
x_2	rotor reactance	[Ω]
x_{12}	magnetic reactance	[Ω]

Greek symbols

α	pole-arc to pole-pitch ratio	[-]
β	geometrical coefficient, reluctance ratio	[-]
γ	geometrical coefficient, reluctance ratio	[-]
η	reluctance ratio, efficiency	[-]
Θ_m	magneto motive force of the PMs	[A·turn]
Θ_2	magneto motive force of the rotor	[A·turn]
θ	internal angle of the synchronous motor	[rad]
λ_{PM}	Permanent magnet flux linkage	[Wb]
μ	magnetic permeability	[H/m]
μ_0	permeability of vacuum	[H/m]
μ_m	Relative permeability	[-]
σ	electrical conductivity	[S/m]
Φ_{bb}	Flux in the bridge	[Wb]
Φ_g	air-gap flux	[Wb]
Φ_{g1}	Fundamental of the air-gap flux	[Wb]
Φ_r	PM remanent flux	[Wb]
Φ_{sat}	saturation flux	[Wb]
ϕ_{sh}	flux in the shaft	[Wb]
ϕ_σ	stray flux	[Wb]
φ	power factor angle, phase angle between voltage and current	[rad]

Ψ_1	fundamental of the stator linkage flux	[Vs]
Ψ_{2d}	rotor d-axis flux linkage	[Vs]
Ψ_{2q}	rotor q-axis flux linkage	[Vs]
Ψ_d	stator d-axis flux linkage	[Vs]
Ψ_q	stator q-axis flux linkage	[Vs]
Ψ_m	flux linkage	[Vs]
ψ	Power angle	[rad]
Ω	geometrical synchronous angular speed	[rad/s]
ω_r	synchronous angular frequency	[rad/s]

Publications during this thesis

4 international conferences

[1] “Analytical Approach for Optimal Design of a Line-Start Internal Permanent Magnet Synchronous Motor”, EPE’13 ECCE Europe Power Electronics and Adjustable Speed Drives, 9-2013

Vera ELISTRATOVA, Michel HECQUET, Pascal BROCHET, Darius VIZIREANU, Maxime DESSOUDE

[2] “Optimal Design of a Line-Start Permanent Magnet Synchronous Motor”, ISEF 2013 - XVI International Symposium on Electromagnetic Fields in Mechatronics, Electrical and Electronic Engineering, 9-2013

Vera ELISTRATOVA, Michel HECQUET, Pascal BROCHET, Darius VIZIREANU, Maxime DESSOUDE

[3] “Design Approach for a Line-Start Internal Permanent Magnet Synchronous Motor”, 15th International IGTE Symposium on Numerical Field Calculation in Electrical, pages. 78-83, 9-2012

Vera ELISTRATOVA, Michel HECQUET, Pascal BROCHET, Darius VIZIREANU, Maxime DESSOUDE

[4] “Design of a Line-Start Internal Permanent Magnet Synchronous Motor”, Vera ELISTRATOVA, Michel HECQUET, Pascal BROCHET, Pr Shirinskii, REEPE – 2013 au MPEI de Moscou, 5th congrès de recherche à Moscou, 2013

1 national conference

[1] « Conception d’un moteur à démarrage direct”, Véra ELISTRATOVA, CRIEC 2013, communication nationale, Colloque de Recherche inter-Ecoles Centrale, 19eme édition, Lyon 2013.

Titre en français: Conception optimale d'une gamme de moteurs synchrones à démarrage direct à haute performance énergétique

Résumé en français:

Ce travail a pour objectif de développer un outil analytique multi-physiques de dimensionnement d'une gamme de moteurs « hybrides » à démarrage direct, intégrant les avantages des deux technologies : l'auto-démarrage de la technologie asynchrone et les bonnes performances énergétique en régime permanent de la technologie synchrone à aimants permanents en répondant aux nouveaux enjeux d'efficacité énergétique et en ajoutant à cela les aspects économiques.
La validation de cet outil est effectuée par des modèles éléments finis créés avec un logiciel commercial ANSYS/Maxwell et par des essais expérimentaux réalisés à l'aide de deux prototypes LSPMSM 7.5kW.

Mots-clefs: moteur LSPM, modèle de dimensionnement, modélisation éléments finis, énumération exhaustive, modèle analytique, validation expérimentale.

Titre en anglais: Optimal design of line-start permanent magnet synchronous motors of high efficiency

Résumé en anglais:

This work aims to develop a multi-physical generic model (and a pre-design software) for a range of LSPMSMs which would integrate the advantages of both technologies: self-start asynchronous technology and good energy performance of synchronous permanent magnet technology.
The validation of this model is carried out by finite element commercial software ANSYS / Maxwell and by experimental tests using two 7.5kW.LSPMSM prototypes.

Keywords: LSPM motor, analytical model, pre-design software, finite element modelling, exhaustive enumeration, experimental tests